Optimization of acoustic, optical and optoelastic devices

Dühring, Maria Bayard; Sigmund, Ole; Jensen, Jakob Søndergaard

Publication date:
2009

Document Version
Publisher's PDF, also known as Version of record

Optimization of acoustic, optical and optoelastic devices

PhD Thesis

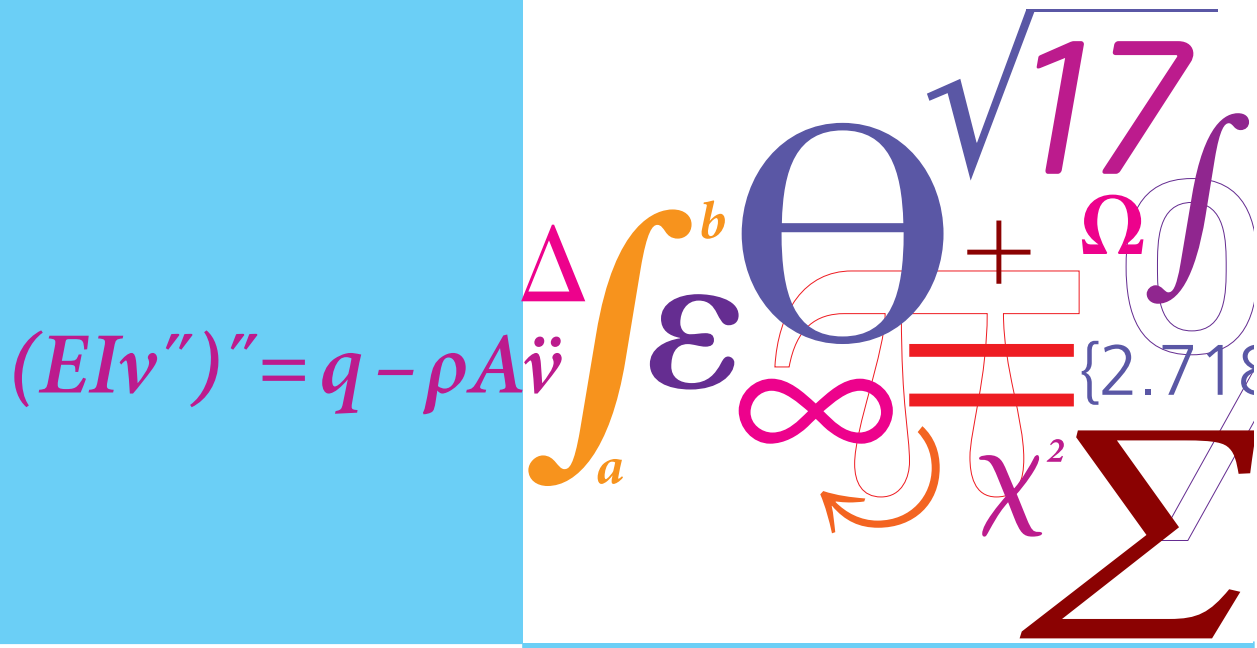

Maria Bayard Dühring
DCAMM Special Repport No. S109
July 2009

DTU Mechanical Engineering
Department of Mechanical Engineering

Optimization of acoustic, optical and optoelastic devices

by

Maria Bayard Dühring

DEPT. OF MECHANICAL ENGINEERING
Solid Mechanics

TECHNICAL UNIVERSITY OF DENMARK

Title of the thesis:
Optimization of acoustic, optical and optoelastic devices

Ph.D. student:
Maria Bayard Dühring
E-mail: mbd@mek.dtu.dk

Supervisors:
Ole Sigmund
E-mail: sigmund@mek.dtu.dk

Jakob Søndergaard Jensen
E-mail: jsj@mek.dtu.dk

Address:
Department of Mechanical Engineering, Solid Mechanics
Technical University of Denmark
Nils Koppels Allé, Building 404, 2800 Kgs. Lyngby, Denmark

Preface

This thesis is submitted in partial fulfillment of the requirements for obtaining the degree of Ph.D. in mechanical engineering at the Technical University of Denmark (DTU). The Ph.D. project was funded by DTU and carried out at the Department of Mechanical Engineering, Solid Mechanics, at DTU in the period February 1st 2006 - July 31st 2009. Supervisors on the project were Professor Dr.techn. Ole Sigmund and Associate Professor Ph.D. Jakob Søndergaard Jensen from the department.

I am very grateful to my two supervisors for their inspiring support and for always taking their time to discuss the work and the results during the project. I would also like to thank Martin P. Bendsøe, who was my co-supervisor until January 1st 2009, for our beneficial collaboration.

I would like to express my gratitude to the partners from the joint research group *Photonic Switches and Modulators based on Surface Acoustic Waves* of ePIXnet - *the European Network of Excellence on Photonic Integrated Components and Circuits* Paulo V. Santos and Markus Beck from Paul-Drude-Institut für Festkörperelektronik, Berlin, Germany, and Mike van der Poel, Elaine C. Saraiva Barretto and Peter De Heyn from Department of Photonics Engineering, DTU, for the successful collaboration and for the help to understand the experimental aspects related to my theoretical work.

A part of this work was carried out with Vincent Laude and Abdelkrim Khelif at Institute FEMTO-ST, Besançon, France, during my 5 month stay in autumn 2007 and winter 2008. I am very grateful that the stay was made possible and for the new academic input in a friendly and welcoming atmosphere. During my 6 months leave in the spring 2008 I worked with Thomas Feurer at the Institute of Applied Physics, University of Bern, Switzerland, and would like to thank him for his support and inspiration related to the work about photonic-crystal fibers.

I am thankful to Krister Svanberg at Royal Institute of Technology, Sweden, who has granted me permission to use the MMA-code. The support form the Eurohorcs/ESF European Young Investigator Award (EURYI, www.esf.org/euryi) through the grant "Synthesis and topology optimization of optomechanical systems" and from the Danish Center for Scientific Computing is also gratefully acknowledged.

I finally wish to thank my colleagues in the TopOpt Group, at the section of Solid Mechanics and in particular the other phd-students for creating a cheerful and inspiring working environment.

Kgs. Lyngby, July 31st 2009.

Maria Bayard Dühring

Resumé (in Danish)

Forskningsområdet, der omhandler elastiske og optiske bølger, er ekspanderet kraftigt i løbet af det sidste århundrede, og dette har resulteret i mange betydningsfulde anvendelser. Det er derfor blevet vigtigt at simulere og optimere bølgestrukturer. I denne afhandling bliver tre forskellige bølgeproblemer simuleret, og bølgestrukturer optimeres enten vha. topologioptimering eller parameterstudier af geometrien.

Det første bølgeproblem omhandler akustiske bølger, som udbreder sig i luft. Topologioptimering bliver her anvendt til at designe strukturer, der reducerer støjen fra en punktkilde i et fastlangt område. Metodens potentiale bliver illustreret ved at optimere formen af støjmure langs en vej, der virker bedre end de konventionelle lige og T-formede støjmure for både en enkelt frekvens og et frekvensinterval.

Topologioptimeringsmetoden bliver herefter udvidet til at designe tværsnittet af fotoniske krystal fibre med en hul kerne. Det bliver vist, at energistrømningen gennem kernen kan forøges i det optimerede design, fordi overlappet mellem det magnetiske felt og det absorberende materiale, som omgiver kernen, reduceres.

I den sidste problemstilling undersøges interaktionen mellem akustiske overfladebølger og optiske bølger i bølgeledere. Først bliver en Rayleigh-bølge genereret i et piezoelektrisk materiale vha. tynde elektroder, og et parameterstudie af den optiske bølgeleders geometri viser, at interaktionen kan forbedres med en størrelsesorden, fordi de mekaniske spændinger i bølgelederen forøges. Det bliver desuden vist, at ved at benytte topologioptimering kan der dannes en struktur af lufthuller under bølgelederen, der omdirigerer Rayleigh-bølgen og forøger interaktionen. Til sidst undersøges akustiske overfladebølger, der genereres vha. elektroder med stor højde i forhold til bredden. Antallet af akustiske bølgeformer stiger, når højden af elektroderne forøges. Det vises, at interaktionen mellem disse nye typer af akustiske overfladebølger og en optisk bølge kan forøges med mere end to størrelsesordener i forhold til interaktionen med overfladebølger genereret vha. konventionelle tynde elektroder.

Abstract

The field of research dealing with propagating elastic and optical waves has expanded during the last century and that has resulted in many significant applications. It has therefore become important to simulate and optimize wave devices. In this work three different types of wave propagation problems are simulated and wave structures are improved by either topology optimization or parameter studies of their geometry.

The first wave problem treats acoustic waves propagating in air. Topology optimization is applied to design structures such that noise from a point source is reduced in a fixed area. The strength of the method is validated by optimizing the shape of sound barriers along a road, which perform better than conventional straight and T-shaped barriers for both a single driving frequency and a frequency interval.

The method of topology optimization is then extended to design the cross section of a photonic-crystal fiber with a hollow core. It is shown that the energy flow in the core can be increased in the optimized design because the overlap between the magnetic field and the lossy cladding material is reduced.

The acousto-optical interaction between surface acoustic waves and optical waves in channel waveguides is investigated in the last problem. First a Rayleigh wave is generated in a piezoelectric material by conventional thin electrodes, and a parameter study of the waveguide geometry show that the acousto-optical interaction can be improved with an order of magnitude because of increased mechanical stress concentrations. It is furthermore demonstrated, that topology optimization can be employed to create a pattern of air holes that traps the Rayleigh wave below the waveguide such that the interaction is improved. Finally, the generation of surface acoustic waves by high aspect ratio electrodes is studied. Several confined acoustic modes exist for increasing aspect ratio. It is demonstrated, that the interaction between these new types of waves and an optical wave in a waveguide can be increased with more than two orders of magnitude compared to interaction with surface waves generated by conventional thin electrodes.

Publications

The following publications are part of the thesis

[P1] M. B. Dühring, J. S. Jensen and O. Sigmund, Acoustic design by topology optimization, *Journal of Sound and Vibration*, 317, 557-575, 2008.

[P2] M. B. Dühring, O. Sigmund and T. Feurer, Design of photonic-bandgap fibers by topology optimization, submitted, 2009.

[P3] M. van der Poel, M. Beck, M. B. Dühring, M. M. de Lima, L. H. Frandsen, C. Peucheret, O. Sigmund, U. Jahn, J. M. Hvam and P. V. Santos, Surface acoustic wave driven light modulation, proceedings of the European Conference on Integrated Optics and Technical Exhibition, Copenhagen, Denmark, 25-27 April, 2007.

[P4] M. B. Dühring and O. Sigmund, Improving the acousto-optical interaction in a Mach-Zehnder interferometer, *Journal of Applied Physics*, 105, 083529, 2009.

[P5] M. B. Dühring, Design of acousto-optical devices by topology optimization, proceedings of WCSMO-8, 8th World Congress on Structural and Multidisciplinary Optimization, LNEC, Lisbon, Portugal, June 1-5, 2009.

[P6] M. B. Dühring, V. Laude and A. Khelif, Energy storage and dispersion of surface acoustic waves trapped in a periodic array of mechanical resonators, *Journal of Applied Physics*, 105, 093504, 2009.

[P7] M. B. Dühring, V. Laude and A. Khelif, Improving surface acousto-optical interaction by high aspect ratio electrodes, submitted, 2009. The paper has received positive review from *Journal of Advances in Engineering Software*, but in order to reach a broader audience the paper has been withdrawn from this journal and resubmitted to Journal of Applied Physics.

Contents

Chapter 1
Introduction

1.1 Aim of the thesis

The study of elastic and optical waves has obtained great importance during the last century. Waves with different kinds of properties have been discovered, which combined with an intense research in materials and fabrication techniques have allowed for the fabrication of structures down to nano scale, resulting in a range of important applications from sonar, ultrasound scanning over lasers, optical fibers and integrated optics. The field of research is continuously expanding and opening up for new and promising applications. It has therefore become essential to simulate and understand wave propagation in order to design wave devices.

The aim of this thesis is to study propagating elastic and optical waves, which are described on a time-harmonic form, and to optimize wave devices either by varying different geometry parameters or by topology optimization. The method of topology optimization is a gradient based optimization method that has proven efficient for optimizing static and dynamic problems in engineering and is here extended to three new wave propagation problems with increasing complexity. First acoustic waves that are propagating in air are studied and topology optimization is employed to design sound barriers such that the noise is reduced behind the barrier. Then optical waves are simulated in photonic-crystal fibers and the energy flow through the core is maximized by designing the cross section of the fiber by use of topology optimization. Finally, surface acoustic waves are simulated in piezoelectric materials and their interaction with optical waves in channel waveguides is investigated. This study is both based on a parametric investigation of the geometry as well as topology optimization in order to improve the acousto-optical interaction. The different wave problems are all governed by second order differential equations that can be discretized and solved in a similar way by the finite element program Comsol Multiphysics with Matlab.

1.2 Structure of the thesis

This thesis is a common introduction to the work done during the Ph.D. study. It gives an overview of the results presented in the seven publications [P1]-[P7] together with a few additional results related to the three different wave propagation problems that are simulated and optimized by parameter studies and topology optimization.

The three wave problems are connected to each other through the two introductory chapters 2 and 3. Chapter 2 is a general introduction to elastic and optical

waves. The characteristics of the two wave types are explained and the development in their practical applications during the last century is summarized. It is furthermore explained that the different types of waves can be modeled by time-harmonic second order differential equations, and that they in this work are discretized and solved in a similar way by the finite element method.

The concept of topology optimization is introduced in chapter 3 and an overview of the wave propagation problems that have been optimized using this method is presented. In this thesis, the topology optimization method is extended to the three new wave problems. As they can be optimized by the method in the same way with similar expressions for the objective function, the optimization problems are stated on a common form in this chapter together with the corresponding sensitivity analysis. The different approaches to obtain well-defined and mesh-independent designs for the wave problems are summarized.

The subsequent three chapters are each concerned with one of the wave propagation problems for which the subject is further explained and results are presented. Chapter 4 deals with the work from publication [P1], which is about acoustic waves propagating in air. A method to design structures by topology optimization in order to minimize noise is presented. The method is demonstrated by two examples where outdoor sound barriers are designed for a single frequency and a frequency interval, respectively.

In chapter 5 optical waves propagating in photonic-crystal fibers are considered. Topology optimization is here applied to design the cross section around the hollow core of a holey fiber such that the energy flow through the core is maximized and the overlap with the lossy cladding material is reduced. The chapter is a summary of the work presented in [P2].

The most complicated wave problem of the thesis is presented in chapter 6 where an acousto-optical model is introduced in order to simulate the interaction between surface acoustic waves and optical waves confined in channel waveguides. Both a parameter study of the geometry and topology optimization are employed to optimize the acousto-optical interaction between a Rayleigh wave and optical waves in ridge waveguides. This gives an overview of the results from [P3]-[P5]. The numerical model is furthermore utilized to study the properties of high aspect ratio electrodes, which is work presented in [P6] and [P7]. The acousto-optical interaction between surface acoustic waves generated by these electrodes and an optical wave in a buried waveguide is investigated and compared to results for conventional thin electrodes.

Finally, some common conclusions for the project are drawn in chapter 7 and further work is suggested.

Chapter 2
Time-harmonic propagating waves

In this chapter elastic and optical waves are introduced and it is explained how they can be modeled by time-harmonic second order differential equations and solved by the finite element method.

2.1 Elastic and optical waves

The two wave phenomena known as elastic and electromagnetic waves are studied in this work. They both consist of disturbances that vary in time and space. Elastic waves propagate in a material medium (a fluid or a solid) by displacing material particles from their equilibrium position, which are brought back by restoring forces in the medium. Electromagnetic waves can propagate in both a medium and in vacuum and are composed of an electric and a magnetic field. Despite their different physical origins, elastic and electromagnetic waves have many similarities. They can be described by similar mathematical equations and they both exhibit properties as reflection, diffraction, dispersion, superposition etc. During the last one and a half century the different types of elastic and electromagnetic waves have been studied and methods to model, control and guide them have been developed. This has led to a range of important applications from the early sonar to today's transport of information by optical fibers as outlined in the following subsections.

2.1.1 Elastic waves

Elastic waves propagating in a fluid are referred to as acoustic waves for the lower, audible frequencies and ultrasonic waves for higher frequencies [1]. Because fluids consist of freely-moving particles, there is no shear motion and the waves are only polarized in the longitudinal direction. Their material properties are therefore scalars (as the density and bulk modulus) and the analysis can be done by a scalar equation with a single property (for instance pressure) as the dependent variable.

Elastic waves in solid crystals are more complicated and the materials are described by tensors with rank up to four [2, 3]. The waves can have both longitudinal and shear components and must in general be described by vector equations. Bulk waves propagate through the bulk material, whereas surface acoustic waves (SAW) are confined to the material surface with exponential decay into the bulk. Different types of SAWs exist and the most popular is the almost non-dispersive Rayleigh wave, which consists of a longitudinal and a vertical transverse component. The Love wave and the Bleustein-Gulyaev wave are both polarized in the transverse horizontal direction, the first propagates in a thin film on a substrate and the other

propagates near the surface of a half space. The Lamb wave is a type of wave that propagates in plates. The solid crystals are in general anisotropic such that their properties, as elastic, thermal, electric and optical properties, depend on the crystal direction. If the material is piezoelectric the elastic wave will be accompanied by an electric field. Apart from direct mechanical impact the elastic waves can be generated in different ways, for instance by the thermal-elastic effect by laser pulses, or by applying an electric field to transducers connected to a piezoelectric material were a wave is generated by the inverse piezoelectric effect.

Audible waves were the first known types of waves. At the end the 19th century, it was known that seismic waves can propagate as bulk waves in the earth and in 1885 it was discovered by Lord Rayleigh that also surface waves are generated by seismic activity [4]. The piezoelectric effect was discovered in 1880 [5] and it was employed in the first sonar that were tested during the 1st World War. The waves were generated by transducers and launched in the water to detect submarines. This was the first application of elastic waves and they have ever since been studied in both fluids and structures. An increasing number of applications have emerged such as oscillators, filters, delay lines and ultrasound scanning in medicine and non-destructive testing. An important condition for realizing these applications and making them efficient was the intensive study of new piezoelectric materials and their fabrication, as ceramics and single crystals, that started in the middle of the 20th century. This made it possible to transform electric energy efficiently into acoustic energy through bulk wave transducers for high frequencies around 1 GHz. In 1965 it was shown by White and Voltmer [6] that Rayleigh waves can be excited by interdigital transducers, which consist of arrays of electrode fingers deposited on the surface of a piezoelectric material. The electrode fingers define the wavelength and the width of the wave beam. This method is now the most common way to generate and detect acoustic waves, and Rayleigh waves are used extensively in electromechanical bandpass filters and resonators in telecommunication, television and mobile phones [7] as well as in oscillators and sensors [8, 9, 10]. With the modern fabrication techniques it is possible to make interdigital transducer that generates SAWs with frequencies up to a few GHz. A new application of SAWs is in optoelastic devices where optical waves are modulated, see subsection 2.1.3.

2.1.2 Optical waves

The other type of waves treated here are electromagnetic waves, which can propagate both in vacuum and in solid media, see [11] for an introduction to this field. The electric and magnetic fields have the same phase and are polarized perpendicular to each other and perpendicular to the propagation direction. Electromagnetic waves were first suggested by Maxwell in the 1860s [12], where he combined the laws of electricity and magnetism in Maxwell's equations. Electromagnetic waves are fully described by these vector equations, which give the electric and the magnetic fields for general elliptic polarized waves in structured medias. They can be reduced

to scalar equations in order to treat the simpler in-plane transverse electric and magnetic waves, respectively. Since it was discovered that light is electromagnetic waves, optics has been considered as a subfield of electromagnetism and covers the behavior of infrared, visible and ultraviolet light.

The intense study of materials and structures to control and guide optical waves, that started in the 20th century, has led to many applications in everyday life such as the radar, laser, lens design and fabrication of optical components [13]. Already from the middle of the 19th century it was known that light can be guided by refraction, which has been used in the study of slab and channel waveguides where light can be guided, split and bent. These components are the building blocks in modern integrated optics, where a number of guided wave devices are combined on a common substrate to build complex optical circuits with small dimensions. This offers a way to guide and process information carried by optical waves and has applications as interferometers and sensors. The guidance of waves by refraction has also been applied in optical fibers where light is guided in a core material surrounded by a cladding with lower refractive index. The research started in the mid 1960s and the propagation loss in the fibers has since then been reduced significantly. Optical fibers are now employed to carry information over long distances with low loss and dispersion, which has revolutionized the field of telecommunication.

An alternative way to guide and control optical waves is by photonic crystals. They are periodically structured dielectric materials in one, two or three dimensions that prohibit the propagation of electromagnetic waves at certain frequencies such that band gaps are created. Line and point defects can be introduced to guide and localize optical waves. The concept gained importance after the two papers [14, 15] were published in 1987. Since then, photonic crystals have been studied theoretically and experimentally in an increasing number of publications, and the first 2D photonic crystal was fabricated for optical wavelengths in 1996 [16]. Applications are in filters, splitters and resonant cavities and an introduction to the field is found in [17]. An important application of the 2D photonic crystal is the photonic-crystal fiber developed in the beginning of the 1990s. In contrast to the conventional optical fiber the optical wave is here guided in a core region surrounded by a periodic structure of air holes, which confine the wave by the band-gap effect, see [18, 17] for an overview. The first photonic-crystal fibers were produced for commercial purposes in 2000 and are fabricated by a drawing process. Compared to conventional optical fibers, photonic-crystal fibers have advantages as higher power flow, better confinement and a possibility to enhance or avoid dispersion and nonlinear effects.

2.1.3 Acousto-optical interaction

The properties of an optical wave can be changed in different ways by applying external fields to the material in which the wave travels, see [13]. This will change the optical properties of the material and hence the properties of the optical wave. One example is the electro-optic effect where an external electric field applied to the

medium can change the phase velocity of the optical wave because of higher order effects. Another example is the photoelastic effect where the refractive index can be changed by applying an external stress field. The change in refractive index is related to the stress or the strain through the stress-optical or strain-optical relation, respectively, where the stress-optical and strain-optical coefficients are collected in second-rank tensors. By utilizing this effect it is possible to change an isotropic material to an optically anisotropic material by applying a stress field. This stress-induced birefringence was first studied in 1816 by Brewster. If an elastic wave is propagating in a medium, the refractive index will change periodically because of the photoelastic effect. The phenomenon is known as the acousto-optical effect. The acousto-optical interaction was first investigated in 1922 by Brillouin in order to diffract an optical beam [19]. Experiments that confirmed the effect were performed in 1932 [20]. Further investigation of the effect showed that elastic waves can be used to change properties as intensity, frequency and direction of optical waves. The other way around, optical waves can be used to measure characteristics of elastic waves as attenuation and radiation patterns. This research led to the development of spectrum analyzers, tunable optical filters and variable delay lines, where it is used that the velocity of the elastic wave is typically 10^5 times smaller than for electromechanical waves. One of the most popular devices is the acousto-optical modulator that is used for instance in laser printers.

As SAWs are confined to a material surface they have a potential in integrated optics where they can interact efficiently with optical waves in waveguides close to the surface. This concept is currently being invested for fast and compact devices where optical waves are modulated by SAWs for signal generation in semiconductor structures. An introduction is given in [21], where the concepts for SAW generation and the mechanisms for the acousto-optical interaction in different structures are reviewed. In [22] experimental results for a compact and monolithic modulator consisting of a SAW driven Mach-Zehnder interferometer (MZI) are presented, and the device is modified for more efficient modulation in [23]. The concept of acousto-optical multiple interference devices are suggested in [24] where several MZIs are combined in parallel or series in order to design ON/OFF switching, pulse shapers and frequency converters. In [25] the working principle of a SAW driven optical frequency shifter based on a multi-branch waveguide structure is presented. These devices are expected to be very compact and compatible with integrated optics based on planar technology for different material systems.

2.2 Modeling of wave problems

In this work, three different types of wave propagating problems with increasing complexity are investigated. The first is about propagation of acoustic waves in air and the next treats optical waves propagating in a photonic-crystal fiber. In the last problem the propagation of SAWs in piezoelectric materials and their interaction with optical waves in waveguides are studied. All the different types of waves vary

in space and time and can be described in a similar way by second order differential equations. In the case of elastic waves in a solid material, the displacement u_i of a point with the coordinates x_k varies with time t, such that $u_i = u_i(x_k, t)$. By combining Newton's second law with Hooke's law for a solid inhomogeneous material the wave equation is obtained [3]

$$\frac{\partial}{\partial x_j}\left(c_{ijkl}\frac{\partial u_l}{\partial x_k}\right) - \rho\frac{\partial^2 u_i}{\partial t^2} = 0, \tag{2.1}$$

where c_{ijkl} are the stiffness constants and ρ is the mass density, which all depend on the position x_k. The expression in (2.1) is a system of three second order differential equations for an anisotropic, inhomogeneous material in 3D. In the case of a fluid the wave equation has the scalar form

$$\frac{\partial}{\partial x_i}\left(\alpha_1\frac{\partial u}{\partial x_i}\right) - \alpha_2\frac{\partial^2 u}{\partial t^2} = 0, \tag{2.2}$$

where u is the pressure, α_1 is the inverse of the mass density and α_2 is the inverse of the bulk modulus. If u describes the out of plane displacements in a solid material, α_1 is the shear modulus and α_2 denotes the mass density, equation (2.2) models the behavior of elastic shear waves. In a similar way, the electromagnetic waves can be described by a system of three second order differential equations in the general case, which can be reduced to the scalar equation (2.2) for the special cases of in-plane modes. In the case of transverse electric modes u describes the electric field, α_1 is the inverse of the dielectric constant and α_2 is the product of the vacuum permittivity and the vacuum permeability.

In many situations it can be assumed that the forces, and thus the waves, are varying harmonically in time with the angular frequency ω. It is therefore convenient to eliminate the time-dependency in the equations. In the case of for instance a fluid, the field variable is described on the complex exponential form $u(x_k, t) = \hat{u}(x_k)e^{i\omega t}$, where $\hat{u}$ describes the complex amplitude and the phase indirectly. The exponential represents the time variation. This means that the operator $\frac{\partial^2}{\partial t^2}$ can be written as $-\omega^2$ and when $\hat{u}e^{i\omega t}$ is introduced in the wave equation (2.3) and the hat is omitted it reduces to the simpler form

$$\frac{\partial}{\partial x_i}\left(\alpha_1\frac{\partial u}{\partial x_i}\right) + \omega^2\alpha_2 u = 0. \tag{2.3}$$

This equation is known as the Helmholtz equation and is valid for the field oscillating at the single frequency ω. The real physical value of u is found by taking the real part of the complex solution to the problem. The conversion from a time dependent to a time-harmonic problem can be done in an equivalent way for the other wave problems and only these types of problems are considered in this work.

A solution to a wave problem can be found by applying a set of boundary conditions that give information about free and clamped surfaces and interfaces between

different materials. In cases where an unbounded structure is considered, it is necessary to apply boundary conditions that do not reflect the waves in order to limit the modeling domain. In simple cases as in wave propagation in fluids, a condition as the Sommerfeld radiation condition can be applied [1]. In more complicated cases as for elastic wave propagation in solid structures and for non-perpendicular waves, it is more accurate to employ perfectly matched layers, which are employed for time-harmonic elastodynamic problems in [26]. In this case an extra layer is applied at the boarders where the disturbances are absorbed gradually before they reach the outer boundaries. In all the wave problems considered in this work the driving forces are applied as harmonic varying boundary conditions. If a unit cell is considered where periodic boundary conditions connect opposite boundaries, the problem can be solved as an infinite periodic structure.

2.3 Discretizing and solving wave problems

Analytical solutions exist for simple problems as spherical acoustic waves propagating in an infinite domain in 3D or Rayleigh waves propagating in a homogeneous half space. For more complex geometries and material distributions the problems must be solved numerically. In this work the finite element method is employed. The dependent variables u_j in a problem are collected in a field vector defined as $\mathbf{u} = [u_1, u_2, ..., u_j, ..., u_J]$ and are discretized using sets of finite element basis functions $\{\phi_{j,n}(\mathbf{r})\}$

$$u_j(\mathbf{r}) = \sum_{n=1}^{N} u_{j,n}\phi_{j,n}(\mathbf{r}), \tag{2.4}$$

where $\mathbf{r}$ is the position vector. The degrees of freedom corresponding to each field are assembled in the vectors $\mathbf{u}_j = \{u_{j,1}, u_{j,2}, ..., u_{j,n}, ...u_{j,N}\}^T$. In the problems considered here, a triangular element mesh is employed and for the physical fields either vector elements or second order Lagrange elements are used depending on the problem. The governing equations are discretized by a standard Galerkin method [27]

$$\sum_{j=1}^{J} \mathbf{S}_{kj}\mathbf{u}_j = \sum_{j=1}^{J} \left(\mathbf{K}_{kj} + i\omega\mathbf{C}_{kj} - \omega^2\mathbf{M}_{kj}\right)\mathbf{u}_j = \mathbf{f}_k, \tag{2.5}$$

where the system matrix $\mathbf{S}_{kj}$ has contributions from the stiffness matrix $\mathbf{K}_{kj}$, the damping matrix $\mathbf{C}_{kj}$ and the mass matrix $\mathbf{M}_{kj}$. $\mathbf{f}_k$ is the load vector. When material damping or absorbing boundary conditions are employed the damping matrix is different from zero and the problem gets complex valued. The material damping can be introduced to make the problems behave more realistically and can in some cases be necessary in order to avoid ending up in a local optimum during an optimization process, see chapter 3.

The implementation of the wave propagation problems is done using the high-level programming language Comsol Multiphysics with Matlab [28]. This software is designed to model scientific and engineering problems described by partial differential equations and solve them by the finite element method. It is furthermore possible to combine different physical models and solve multiphysics problems, as for instance an elastic and an optical model in order to investigate the acousto-optical effect. The models can be defined by the user by writing conventional differential equations and it is also possible to use the application modes, which are templates for specific physical problems with the appropriate equations and variables predefined. In this work the elastic wave problems are implemented in the general form where the governing equations and boundary conditions are written on divergence form. The optical problems are solved using the perpendicular waves, hybrid-mode waves, application mode. When solving wave problems enough elements must be used in order to resolve the waves, which typically means that at least 5 second order elements per wavelength must be employed. In Comsol Multiphysics the discretized problem in (2.5) is solved as one system and direct solvers based on LU factorization of the system matrix are utilized.

Chapter 3
Topology optimization applied to time-harmonic propagating waves

In the previous chapter, wave propagation problems for time-harmonic elastic and optical waves have been introduced. It has been explained that they are governed by second order differential equations and can be solved in a similar way by the finite element method. As discussed, different kinds of wave propagation is utilized in an increasing number of applications and it is therefore important to improve the performance for a certain frequency or frequency range. The aim is either to hinder wave propagation, for instance minimization of the sound power at a certain position in a room, or waveguiding, as maximization of the power flow through a point of a structure. To optimize these kinds of problems different types of optimization methods can be applied. There are at least two fundamentally different approaches to solve an optimization problem. The simplest strategy is to take the best solution from a number of trial solutions, perhaps generated by stochastic methods or simply from a parameter study where one or more parameters are varied. The other approach is to use an iterative method where an intermediate solution is obtained in each iteration step, which finally converges to an optimum. This can be done by a variety of algorithms suitable for different types of problems, for example for linear or nonlinear, constrained or unconstrained problems. To determine the direction and the length of the next step in the iteration, information from the objective and constraint functions as function values, gradient and curvature information can be employed.

In this work, wave propagation problems are either investigated by parameter studies, where geometry parameters are varied, or by topology optimization, which is an iterative optimization method based on repeated sensitivity analysis of the objective and constraint functions and mathematical programming steps. In the following, the method of topology optimization is introduced and a description of the way it is applied to the wave propagation problems studied in this work is given.

3.1 Topology optimization and propagating waves

By the method of topology optimization, material is freely distributed in a design domain and the aim is to get a structure that consists of well defined regions of solid material and void such that the objective function is optimized. Thus, the layout of the structure with the number, position and shape of the holes is determined. The method therefore offers higher design freedom than other known methods as size and shape optimization, which are restricted to a predefined number of holes in the

structure.

The method was first introduced by Bendsøe and Kikuchi in 1988 [29] as a computer based method for continuum structures with the purpose of minimizing the compliance for a limited amount of material by a homogenization approach. Since then, topology optimization has been developed further and the theory is thoroughly explained in [30]. A typical topology optimization procedure is to define the design domain for the structure, the boundary conditions and the load case. The structure is then discretized by finite elements and the design variables are the material density in each element that in the final design should correspond to either solid material or void. The density is then related to the different physical parameters that describe the material in the problem considered. In the original case, where the static compliance of structures is minimized, the physical parameter is the stiffness. Many different methods to solve the topology optimization problem have been suggested in the literature. As described in [30], the SIMP-model (Solid Isotropic Material with Penalization) is a very efficient method to get optimized designs in structural mechanics. This method is based on continuous design variables that can take on any value of the densities between void and solid material. Material interpolation functions that penalize the intermediate densities are employed to force the design to consist of areas of either void or solid material in the final design. As it was possible to get structures with better performance than those obtained from size and shape optimization, topology optimization got increasingly popular and has been used in aero and automotive industries. Today topology optimization tools are provided for the industry by commercial software systems [31].

By relating the density to other material parameters than stiffness, topology optimization can be applied to other types of engineering and scientific problems. In [30] many applications as different as compliant mechanism design, heat and flow problems are presented. Next to minimization of static compliance, one of the first type of applications the method was applied to was dynamic problems, a research field that is continuously developing. Either eigenvalue optimization for free vibrations was considered [32, 33, 34] or the optimization of the dynamic response, as the dynamic compliance, for a structure for a given driving frequency or frequency range [35, 36, 37, 38]. Thus, optimization methods were developed for structures subjected to time-harmonic loads.

In the beginning of this decade the method was furthermore extended to elastic wave propagation problems and first phononic-bandgap materials and structures were studied in 2003 [39]. Later the method was applied to periodic plate structures [40, 41] and theoretical and experimental results are compared in [41]. In [42] non-periodic plate structures are designed for vibration suppression and energy transport. One-dimensional layered structures for longitudinal wave propagation are studied in [43] and in [44] minimization of transmission and absorption through slaps is examined. SAW propagation is considered in [45] where filters and waveguides in elastic materials are optimized. Topology optimization has recently been applied to acoustic wave propagation problems in air such as acoustic horns [46],

reflection chambers [47], sound barriers designed by genetic algorithms [48] and acoustic-structure interaction [49]. These optimization problems usually result in non-intuitive designs with holes in the structures and parts not attached to each other, which would not be possible by size and shape optimization.

Parallel to the work about elastic wave propagation, topology optimization methods concerning propagating optical waves appeared. First planar electromagnetic waves were studied for photonic-bandgap materials in [50, 51] and then structures such as bends and splitters [52, 53, 54, 55] based on band-gap materials were designed for single frequencies or frequency intervals. Planar photonic-crystal waveguide components with low loss as well as high bandwidth and transmission have been fabricated and characterized in various papers [56, 57, 58]. The tailoring of dispersion properties are considered in [59] for photonic-crystal waveguides and for optical fibers in [60]. In [61] a coupled magnetomechanical analysis is carried out in order to use topology optimization to maximize the elastic wave transduction of a magnetostrictive patch-type transducer. Lately, the method of topology optimization has been extended to transient wave propagation for one-dimensional problems [62, 63] and the concept can be applied to both elastic and optical waves.

Topology optimization is now a well established method and has been employed to improve problems in a range of different fields. However, when the method is applied to a new type of problem it takes some trial and error to obtain applicable designs and overcome problems as badly defined boundaries of the designs, appearance of intermediate densities and non-unique solutions. It is first of all important to formulate the optimization problem with the objective function and constraints such that the wanted physical effect is obtained. In order to obtain mesh-independent designs and reduce the appearance of intermediate materials, filtering methods and appropriate interpolation functions must be employed. For problems with non-unique solutions, convergence to a local optima can be prevented by continuation methods. Finally, it is important to interpret the optimized designs physically and compare them with intuitive designs.

In the present work, the method of topology optimization is extended to three new types of wave propagation problems. The first is mathematically the simplest and the aim is to minimize noise from acoustic waves in air by designing structures as sound barriers. The next is concerned with optical waves and here the purpose is to maximize the energy flow in a hollow photonic-crystal fiber. Finally, the method is applied to propagating surface acoustic waves in a piezoelectric material in order to improve the acousto-optical interaction with an optical wave in a waveguide. The three different problems are governed by similar equations and the way topology optimization is applied to them is therefore essentially the same. In the following sections, a generic optimization problem for the wave propagation problems is introduced with design variables, objective and constraint functions as well as the sensitivity analysis. The different initiatives applied to prevent problems as intermediate materials and mesh-dependent solutions are explained.

3.2 Design variables and material interpolation

Topology optimization is here employed to design structures for propagating waves. A domain Ω is exited by a harmonic input force and the aim is to find a distribution of air and solid material in the design domain Ω_d such that the objective function Φ is optimized in the output domain Ω_o. The concept is sketched in figure 3.1. The optimization problem is discrete as there should be either air or solid material in each point of the design domain. However, in order to allow for efficient gradient-based optimization the problem is formulated with continuous material properties that can take any value in between the values for air and solid material. To control the material properties a continuous material indicator field $0 \leq \xi(\mathbf{r}) \leq 1$ is introduced, where $\xi = 0$ corresponds to air and $\xi = 1$ to solid material. If μ describes the material parameters in the physical model, see section 2.2, introducing the design variable means that

$$\mu(\xi) = \begin{cases} \mu_\mathrm{a}, & \xi = 0 \\ \mu_\mathrm{s}, & \xi = 1 \end{cases}, \tag{3.1}$$

where μ_a represents the material values for air and μ_s the material values for solid material. Although ξ is continuous, the final design should be as close to discrete ($\xi = 0$ or $\xi = 1$) as possible in order to be well defined. To ease this, different interpolations functions as well as filtering and penalization methods can be employed. Here a morphology-based filter is used, as described in section 3.5, and interpolation functions, where the material parameters or their inverse are interpolated linearly between the two material phases, are employed

$$\mu(\xi) = \mu_\mathrm{a} + \xi(\mu_\mathrm{s} - \mu_\mathrm{a}). \tag{3.2}$$

This function satisfies the condition in (3.1), but does not necessarily result in a discrete optimal solution. A discrete design is referred to as a 0-1 design in the following.

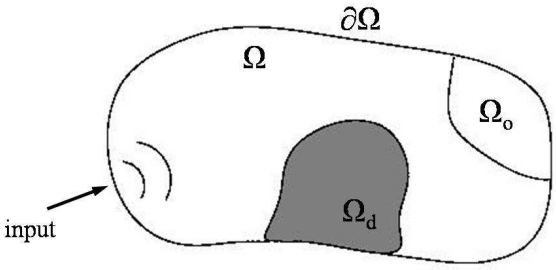

Figure 3.1 The concept of topology optimization applied to wave propagation problems. Air and solid material must be distributed in the design domain Ω_d in order to optimize the objective function in the output domain Ω_o.

3.3 The optimization problem

The purpose of the topology optimization is to optimize the objective function Φ. For the three wave propagation problems considered Φ has a similar form and depends on the field variables u_j or their derivatives with respect to x_j, which in both cases will be denoted w_j. The functions w_j are in general complex valued so in order to get a positive and real valued objective function it is the squared absolute value of w_j or a sum of these that is optimized. The generic formulation of the optimization problem where the response has to be minimized takes the form

$$\min_{\xi} \quad \Phi = \int_{\Omega_\mathrm{o}} \sum_{j=1}^{J} |w_j(\mathbf{r}, \xi(\mathbf{r}))|^2 \mathrm{d}\mathbf{r}, \qquad \text{objective function} \tag{3.3}$$

$$\text{subject to } \frac{1}{\int_{\Omega_\mathrm{d}} \mathrm{d}\mathbf{r}} \int_{\Omega_\mathrm{d}} \xi(\mathbf{r}) \mathrm{d}\mathbf{r} - \beta \leq 0, \qquad \text{volume constraint} \tag{3.4}$$

$$0 \leq \xi(\mathbf{r}) \leq 1 \quad \forall\ \mathbf{r} \in \Omega_\mathrm{d}, \qquad \text{design variable bounds} \tag{3.5}$$

$$\sum_{j=1}^{J} \mathbf{S}_{kj} \mathbf{u}_j - \mathbf{f}_k = 0, \qquad \text{governing equations} \tag{3.6}$$

The only constraint that is employed in the optimization problems considered is the volume constraint (3.4). It can be included in the formulation to put a limit on the amount of material distributed in the design domain Ω_d. The parameter β indicates the fraction of the volume that is allowed to contain solid material and it takes values between 0 and 1, where $\beta = 1$ corresponds to no limit. When the problem considered has several local minima the optimized designs will be strongly dependent on the choice of β.

With the objective function (3.3) the problem is optimized for one driving frequency. But for wave propagation problems it is often relevant to optimize for a frequency interval in order to get a broadband solution. The objective function can therefore be changed such that the objective is to minimize the sum of responses for a number of target frequencies ω_i in the interval considered, as explained in [53]. The chosen interval is divided into M equally sized subintervals. The target frequency in each subinterval, which results in the highest value of Φ, is determined by approximating Φ as function of the frequency using Padé expansions, see [64]. The problem is then optimized for the new objective function Ψ, which is the sum of Φ evaluated at the determined target frequencies and divided by the number of intervals M to get the average value

$$\min_{\xi} \quad \Psi = \frac{\sum_{\omega_1,\ldots,\omega_M} \max_{\omega_i \in I_i}(\Phi(\omega_i))}{M}, \quad I_1 = [\omega_1; \omega_2[, \ldots, I_M =]\omega_M; \omega_{M+1}]. \tag{3.7}$$

Here $\omega_{M+1} - \omega_1$ is the entire frequency interval and I_i are the equally sized subintervals. By this procedure, Φ is minimized at all the target frequencies, which are updated at regular intervals during the optimization.

3.4 Sensitivity analysis

The design variables are updated by a gradient based optimization algorithm, see section 3.5, and the derivatives with respect to the design variables of the objective and the constraint functions must be evaluated. They indicate how much the function will change if a certain design variable is changed an infinitesimal quantity. These derivatives can be calculated as the design variable is introduced as a continuous field. The design variable field ξ is discretized using finite element basis functions $\{\phi_{J+1,n}(\mathbf{r})\}$ in a similar way as for the dependent variables

$$\xi(\mathbf{r}) = \sum_{n=1}^{N_d} \xi_n \phi_{J+1,n}(\mathbf{r}). \tag{3.8}$$

The degrees of freedom are assembled in the vector $\boldsymbol{\xi} = \{\xi_1, \xi_2, ...\xi_{N_d}\}^T$, and typically zero or first order Lagrange elements are used.

The complex field vector $\mathbf{u}_k$ is via (2.5) an implicit function of the design variables, which is written as $\mathbf{u}_k(\boldsymbol{\xi}) = \mathbf{u}_k^R(\boldsymbol{\xi}) + i\mathbf{u}_k^I(\boldsymbol{\xi})$, where $\mathbf{u}_k^R$ and $\mathbf{u}_k^I$ denote the real and the imaginary parts of $\mathbf{u}_k$. Thus the derivative of the objective function $\Phi = \Phi(\mathbf{u}_k^R(\boldsymbol{\xi}), \mathbf{u}_k^I(\boldsymbol{\xi}), \boldsymbol{\xi})$ is given by the following expression found by the chain rule

$$\frac{\mathrm{d}\Phi}{\mathrm{d}\boldsymbol{\xi}} = \frac{\partial\Phi}{\partial\boldsymbol{\xi}} + \sum_{k=1}^{J} \left(\frac{\partial\Phi}{\partial\mathbf{u}_k^R}\frac{\partial\mathbf{u}_k^R}{\partial\boldsymbol{\xi}} + \frac{\partial\Phi}{\partial\mathbf{u}_k^I}\frac{\partial\mathbf{u}_k^I}{\partial\boldsymbol{\xi}} \right). \tag{3.9}$$

As $\mathbf{u}_k$ is an implicit function of $\boldsymbol{\xi}$ the derivatives $\partial\mathbf{u}_k^R/\partial\boldsymbol{\xi}$ and $\partial\mathbf{u}_k^I/\partial\boldsymbol{\xi}$ are not known directly. The sensitivity analysis is therefore done by employing an adjoint method where the unknown derivatives are eliminated at the expense of determining adjoint and complex variable fields [65]. From equation (2.5) it is known that $\sum_{j=1}^{J} \mathbf{S}_{kj}\mathbf{u}_j - \mathbf{f}_k = 0$, and therefore equation $\sum_{j=1}^{J} \bar{\mathbf{S}}_{kj}\bar{\mathbf{u}}_j - \bar{\mathbf{f}}_k = 0$ is also valid. The overbar denotes the complex conjugate. It is assumed that the load does not depend on the design variables such that the derivative of $\sum_{j=1}^{J} \mathbf{S}_{kj}\mathbf{u}_j$ and $\sum_{j=1}^{J} \bar{\mathbf{S}}_{kj}\bar{\mathbf{u}}_j$ with respect to $\boldsymbol{\xi}$ are also zero. When they are multiplied with the adjoint variable fields $\frac{1}{2}\boldsymbol{\lambda}_k$ and $\frac{1}{2}\bar{\boldsymbol{\lambda}}_k$, respectively, and added to (3.9) it does not change the value of the derivative

$$\begin{aligned}\frac{\mathrm{d}\Phi}{\mathrm{d}\boldsymbol{\xi}} =& \frac{\partial\Phi}{\partial\boldsymbol{\xi}} + \sum_{k=1}^{J} \left(\frac{\partial\Phi}{\partial\mathbf{u}_k^R}\frac{\partial\mathbf{u}_k^R}{\partial\boldsymbol{\xi}} + \frac{\partial\Phi}{\partial\mathbf{u}_k^I}\frac{\partial\mathbf{u}_k^I}{\partial\boldsymbol{\xi}} \right) \\ &+ \sum_{k=1}^{J} \left(\frac{1}{2}\boldsymbol{\lambda}_k^T \frac{\mathrm{d}}{\mathrm{d}\boldsymbol{\xi}} \left(\sum_{j=1}^{J} \mathbf{S}_{kj}\mathbf{u}_j \right) + \frac{1}{2}\bar{\boldsymbol{\lambda}}_k^T \frac{\mathrm{d}}{\mathrm{d}\boldsymbol{\xi}} \left(\sum_{j=1}^{J} \bar{\mathbf{S}}_{kj}\bar{\mathbf{u}}_j \right) \right).\end{aligned} \tag{3.10}$$

The two last derivatives are expanded as follows

$$\frac{\mathrm{d}}{\mathrm{d}\boldsymbol{\xi}}\left(\sum_{j=1}^{J}\mathbf{S}_{kj}\mathbf{u}_j\right)=\sum_{j=1}^{J}\left(\frac{\partial\mathbf{S}_{kj}}{\partial\boldsymbol{\xi}}\mathbf{u}_j^R+\mathbf{S}_{kj}\frac{\partial\mathbf{u}_j^R}{\partial\boldsymbol{\xi}}+i\frac{\partial\mathbf{S}_{kj}}{\partial\boldsymbol{\xi}}\mathbf{u}_j^I+i\mathbf{S}_{kj}\frac{\partial\mathbf{u}_j^I}{\partial\boldsymbol{\xi}}\right), \tag{3.11}$$

$$\frac{\mathrm{d}}{\mathrm{d}\boldsymbol{\xi}}\left(\sum_{j=1}^{J}\bar{\mathbf{S}}_{kj}\bar{\mathbf{u}}_j\right)=\sum_{j=1}^{J}\left(\frac{\partial\bar{\mathbf{S}}_{kj}}{\partial\boldsymbol{\xi}}\mathbf{u}_j^R+\bar{\mathbf{S}}_{kj}\frac{\partial\mathbf{u}_j^R}{\partial\boldsymbol{\xi}}-i\frac{\partial\bar{\mathbf{S}}_{kj}}{\partial\boldsymbol{\xi}}\mathbf{u}_j^I-i\bar{\mathbf{S}}_{kj}\frac{\partial\mathbf{u}_j^I}{\partial\boldsymbol{\xi}}\right). \tag{3.12}$$

When (3.11) and (3.12) are inserted into (3.10) the derivative of the objective function takes the form

$$\begin{aligned}\frac{\mathrm{d}\Phi}{\mathrm{d}\boldsymbol{\xi}}=\frac{\partial\Phi}{\partial\boldsymbol{\xi}}&+\sum_{k=1}^{J}\left(\frac{1}{2}\boldsymbol{\lambda}_k^T\sum_{j=1}^{J}\frac{\partial\mathbf{S}_{kj}}{\partial\boldsymbol{\xi}}\mathbf{u}_j+\frac{1}{2}\bar{\boldsymbol{\lambda}}_k^T\sum_{j=1}^{J}\frac{\partial\bar{\mathbf{S}}_{kj}}{\partial\boldsymbol{\xi}}\bar{\mathbf{u}}_j\right)\\&+\sum_{k=1}^{J}\left(\frac{\partial\Phi}{\partial\mathbf{u}_k^R}+\sum_{j=1}^{J}\left(\frac{1}{2}\boldsymbol{\lambda}_j^T\mathbf{S}_{jk}+\frac{1}{2}\bar{\boldsymbol{\lambda}}_j^T\bar{\mathbf{S}}_{jk}\right)\right)\frac{\partial\mathbf{u}_k^R}{\partial\boldsymbol{\xi}}\\&+\sum_{k=1}^{J}\left(\frac{\partial\Phi}{\partial\mathbf{u}_k^I}+\sum_{j=1}^{J}\left(\frac{1}{2}i\boldsymbol{\lambda}_j^T\mathbf{S}_{jk}-\frac{1}{2}i\bar{\boldsymbol{\lambda}}_j^T\bar{\mathbf{S}}_{jk}\right)\right)\frac{\partial\mathbf{u}_k^I}{\partial\boldsymbol{\xi}}.\end{aligned} \tag{3.13}$$

The terms $\frac{\partial\mathbf{u}_k^R}{\partial\boldsymbol{\xi}}$ and $\frac{\partial\mathbf{u}_k^I}{\partial\boldsymbol{\xi}}$ are derivatives of implicitly given functions and these terms can be eliminated by choosing the adjoint variable fields $\boldsymbol{\lambda}_j$ such that the following equations are satisfied

$$\sum_{j=1}^{J}\left(\boldsymbol{\lambda}_j^T\mathbf{S}_{jk}+\bar{\boldsymbol{\lambda}}_j^T\bar{\mathbf{S}}_{jk}\right)=-2\frac{\partial\Phi}{\partial\mathbf{u}_k^R}, \tag{3.14}$$

$$\sum_{j=1}^{J}\left(i\boldsymbol{\lambda}_j^T\mathbf{S}_{jk}-i\bar{\boldsymbol{\lambda}}_j^T\bar{\mathbf{S}}_{jk}\right)=-2\frac{\partial\Phi}{\partial\mathbf{u}_k^I}. \tag{3.15}$$

If equation (3.15) is multiplied by i and subtracted from (3.14) the following relation is obtained

$$\sum_{j=1}^{J}\boldsymbol{\lambda}_j^T\mathbf{S}_{jk}=-\frac{\partial\Phi}{\partial\mathbf{u}_k^R}+i\frac{\partial\Phi}{\partial\mathbf{u}_k^I}. \tag{3.16}$$

Another relation is obtained by again multiplying (3.15) by i and then adding it to (3.14)

$$\sum_{j=1}^{J}\bar{\boldsymbol{\lambda}}_j^T\bar{\mathbf{S}}_{jk}=-\frac{\partial\Phi}{\partial\mathbf{u}_k^R}-i\frac{\partial\Phi}{\partial\mathbf{u}_k^I}. \tag{3.17}$$

The two expressions (3.16) and (3.17) are equivalent, which is seen by taking the complex conjugate on both sides of expression (3.17). This means that when $\boldsymbol{\lambda}_j$ is computed by equation (3.16) it will also fulfill equation (3.17). Equation (3.16) is transposed and it is used that $\mathbf{S}_{kj}$ is symmetric

$$\sum_{j=1}^{J} \mathbf{S}_{kj}\boldsymbol{\lambda}_j = \left(\frac{\partial \Phi}{\partial \mathbf{u}_k^R} - i\frac{\partial \Phi}{\partial \mathbf{u}_k^I}\right)^T. \tag{3.18}$$

The expression in (3.18) can be solved as one system in a similar way as the discretized problem in (2.5). In the case where w_k in the objective function (3.3) is equal to the field variable u_k the right hand side of equation (3.18) is found by the expression

$$\begin{aligned}\frac{\partial \Phi}{\partial \mathbf{u}_{k,n}^R} - i\frac{\partial \Phi}{\partial \mathbf{u}_{k,n}^I} &= \int_{\Omega_\mathrm{o}} \left(\frac{\partial \Phi}{\partial \mathbf{u}_k^R}\frac{\partial \mathbf{u}_k^R}{\partial \mathbf{u}_{k,n}^R} - i\frac{\partial \Phi}{\partial \mathbf{u}_k^I}\frac{\partial \mathbf{u}_k^I}{\partial \mathbf{u}_{k,n}^I}\right) \mathrm{d}\mathbf{r} \\ &= \int_{\Omega_\mathrm{o}} (2u_k^R - i2u_k^I)\phi_{k,n}\mathrm{d}\mathbf{r}. \end{aligned} \tag{3.19}$$

In the case where w_k indicates the derivative $\frac{\partial u_k}{\partial x_k}$ the right hand side of equation (3.18) is found by

$$\begin{aligned}&\frac{\partial \Phi}{\partial \mathbf{u}_{k,n}^R} - i\frac{\partial \Phi}{\partial \mathbf{u}_{k,n}^I} = \int_{\Omega_\mathrm{o}} \left(\frac{\partial \Phi}{\partial w_k^R} - i\frac{\partial \Phi}{\partial w_k^I}\right)\frac{\partial \phi_{k,n}}{\partial x_k}\mathrm{d}\mathbf{r} \\ &= \int_{\Omega_\mathrm{o}} \left(2w_k^R - i2w_k^I\right)\frac{\partial \phi_{k,n}}{\partial x_k}\mathrm{d}\mathbf{r} = \int_{\Omega_\mathrm{o}} \left(2\frac{\partial u_k^R}{\partial x_k} - i2\frac{\partial u_k^I}{\partial x_k}\right)\frac{\partial \phi_{k,n}}{\partial x_k}\mathrm{d}\mathbf{r}. \end{aligned} \tag{3.20}$$

The derivatives $\frac{\partial u_k}{\partial x_k}$ can be calculated automatically by Comsol Multiphysics. The adjoint variable fields are now determined such that the two last terms in (3.13) vanish and the derivative of the objective function reduces to

$$\frac{\mathrm{d}\Phi}{\mathrm{d}\boldsymbol{\xi}} = \frac{\partial \Phi}{\partial \boldsymbol{\xi}} + \sum_{k=1}^{J}\left(\frac{1}{2}\boldsymbol{\lambda}_k^T\sum_{j=1}^{J}\frac{\partial \mathbf{S}_{kj}}{\partial \boldsymbol{\xi}}\mathbf{u}_j + \frac{1}{2}\bar{\boldsymbol{\lambda}}_k^T\sum_{j=1}^{J}\frac{\partial \bar{\mathbf{S}}_{kj}}{\partial \boldsymbol{\xi}}\bar{\mathbf{u}}_j\right), \tag{3.21}$$

and can be rewritten in the form

$$\frac{\mathrm{d}\Phi}{\mathrm{d}\boldsymbol{\xi}} = \frac{\partial \Phi}{\partial \boldsymbol{\xi}} + \sum_{k=1}^{J}\Re\left(\boldsymbol{\lambda}_k^T\sum_{j=1}^{J}\frac{\partial \mathbf{S}_{kj}}{\partial \boldsymbol{\xi}}\mathbf{u}_j\right). \tag{3.22}$$

Finally, the derivative of the constraint function with respect to one of the design variables is

$$\frac{\partial}{\partial \xi_n}\left(\frac{1}{\int_{\Omega_\mathrm{d}}\mathrm{d}\mathbf{r}}\int_{\Omega_\mathrm{d}}\xi(\mathbf{r})\mathrm{d}\mathbf{r} - \beta\right) = \frac{1}{\int_{\Omega_\mathrm{d}}\mathrm{d}\mathbf{r}}\int_{\Omega_\mathrm{d}}\phi_{J+1,n}(\mathbf{r})\mathrm{d}\mathbf{r}. \tag{3.23}$$

The mentioned vectors $\partial\Phi/\partial\boldsymbol{\xi}$, $\int_{\Omega_\mathrm{o}}(2u_k^R - i2u_k^I)\phi_{k,n}\mathrm{d}\mathbf{r}$, $\int_{\Omega_\mathrm{o}}\left(2\frac{\partial u_k^R}{\partial x_k} - i2\frac{\partial u_k^I}{\partial x_k}\right)\frac{\partial \phi_{k,n}}{\partial x_k}\mathrm{d}\mathbf{r}$ and $\int_{\Omega_\mathrm{d}}\phi_{J+1,n}(\mathbf{r})\mathrm{d}\mathbf{r}$ as well as the matrix $\partial\mathbf{S}_{kj}/\partial\boldsymbol{\xi}$ are assembled in Comsol Multiphysics as described in [66].

3.5 Practical implementation

The actual update of the design variables in each step is done by employing the Method of Moving Asymptotes (MMA) by Svanberg 2002, see [67]. This is an efficient mathematical programming method to solve the type of smooth problems (meaning that the objective and constraint functions should at least belong to C^1) with the high number of degrees of freedom found in topology optimization. It is an algorithm that employs information from the previous iteration steps as well as gradient information - plus second order information if it is available.

In order to get optimization problems that behave well during the optimization and to obtain applicable 0-1 designs, the optimization problems can be modified in different ways. First of all material damping can be applied such that the resonance frequencies are damped, which make the problems more realistic and well behaving during the optimization. When the mesh size is decreased, the optimization will in general result in mesh-dependent solutions with small details, which make the design inconvenient to manufacture. To avoid these problems a filter is employed. The filter makes the material properties of an element dependent on a function of the design variables in a fixed neighborhood around the element such that the optimized design is mesh-independent. In the present work, a close-type Heaviside morphology-based filter is applied to the problems, which has proven efficient for wave propagation problems [68]. The method results in designs where all holes below the size of the filter radius have been eliminated. To get a numerically stable optimization, the filter must usually be implemented as a continuation scheme where the property of the filter is gradually changed from a density filter to a morphology-based filter. A further advantage of these filter-types is that they tend to eliminate gray elements in the transition zone between solid and air regions.

The problems studied here are non-unique with a number of local optima that typically originate from local resonance effects. To prevent convergence to these local optima a continuation method can be applied where the original problem is modified to a smoother problem. For wave problems it has been shown that a strong artificial damping will smoothen the response [39, 53], hence this method is applied to some of the problems in this project. A strong material damping is applied in the beginning of the optimization and after convergence of the modified problem or after a fixed number of iterations the problem is gradually changed back to the original one with a realistic damping. The continuation scheme of the filter has a similar effect.

The iterative optimization procedure including the filter can finally be written in the pseudo code:

1. Choose target frequencies ω_i and initialize the design variable vector $\boldsymbol{\xi}$, the counter iter = 0, the tolerance tol=0.01 and change=1.
2. for iter = 1:1000
3. Calculate filtered densities $\tilde{\boldsymbol{\xi}}$ by the chain rule.
4. Calculate the material values and solve the FE problem based on $\tilde{\boldsymbol{\xi}}$.
5. Compute the objective function Ψ and the sensitivities based on $\tilde{\boldsymbol{\xi}}$.
6. Calculate filtered sensitivities.
7. Update the design variables $\boldsymbol{\xi}_{\text{new}}$ by the MMA-algorithm.
8. Compute change=max($||\boldsymbol{\xi}_{\text{new}}$ -$\boldsymbol{\xi}||$).
9. If mod(iter,50) == 0 | change $<$ tol, then update target frequencies, the material damping or the filter as appropriate and set change=0.5.
10. Break if change $<$ tol.
11. end
12. Postprocess and display the results.

The optimized designs are in general sensitive to the choice of driving frequency or frequency interval as well as other factors such as the volume fraction β, the initial guess and the filter size. It is therefore recommended to choose the driving frequency or the frequency interval carefully and to perform more optimizations with several parameter combinations to obtain the best possible design.

Chapter 4
Design of sound barriers by topology optimization [P1]

The first type of wave problem considered in the present work, is the propagation of acoustic waves in air, where topology optimization is employed to optimize the distribution of materials in structures to reduce noise. This chapter is a summary of the work presented in publication [P1].

It is essential to control acoustic properties in a wide range of problems such as in the design of loudspeakers, the layout of rooms for good speech conditions or in noise reduction where sound waves can have a damaging effect on humans or electronic equipment. Reduction of sound is important for indoor situations as in open offices, staircases as well as in car and airplane cabins or for outdoor problems, for instance along roads with heavy traffic. The most common way to reduce noise is by passive noise control where structures as sound barriers are employed to screen from the sound or where absorbers as resonators, porous absorbing material or membranes are used to absorb the acoustic waves. Both experimental and theoretical work has been employed in order to design for noise reduction. Scale models of sound barriers with different shapes are for instance investigated in [69, 70], and numerical results for sound barriers are obtained with a boundary element method in [71, 72]. In both cases the T-shaped barrier tends to give the largest noise reduction. Different kinds of optimization methods have been applied to acoustic problems as shape optimization, see [73], and in [48] a systematic way to design barriers with genetic algorithms is suggested. Lately, topology optimization has been applied to control sound by different structures such as acoustic horns, plate and shell structures or reflection champers as outlined in section 3.1.

In [P1] the method of topology optimization is extended to problems were noise is reduced by passive noise control for a single driving frequency or a frequency interval for 2D and 3D problems. It is first applied to room acoustics where the structure of the ceiling is optimized in order to reduce the sound in a certain part of the room. This concept was first presented by the author in [74] and extended with more examples in [P1]. The objective function is minimized because of the forming of cavities acting as Helmholtz resonators, or by moving natural frequencies, that are close to the diving frequency, to lower or higher values by redistributing material at the nodal planes or at the high pressure amplitudes, respectively. It is also shown that the method is suitable to find optimized distributions of absorbing material along the walls. Finally, the method is applied to design outdoor sound barriers and two examples for a single frequency and a frequency interval, respectively, are presented in the following to show the performance of the method.

4.1 Method

The aim of the presented method is to design sound barriers by redistribution of air and solid material (aluminum) in the design domain Ω_d such that the noise is reduced in the output domain Ω_o behind the barrier. This is illustrated by figure 4.1. The sound source, which is placed to the left of Ω_d, is emitting harmonic waves with the vibrational, particle velocity U. The ground is reflecting and the outer boundary in the air is absorbing. The governing equation for a driving angular frequency ω is the Helmholtz equation [1]

$$\frac{\partial}{\partial x_i}\left(\rho^{-1}\frac{\partial p}{\partial x_i}\right)+\omega^2\kappa^{-1}p=0, \tag{4.1}$$

where p is the complex sound pressure amplitude, ρ is the mass density and κ is the bulk modulus, which all depend on the position $\mathbf{r}$. The design variable ξ takes the value 0 for air and 1 for the solid material. The inverse density and bulk modulus are interpolated linearly between the two material phases. The objective function Φ is the average of the squared sound pressure amplitude in the output domain, Ω_o. The formulation of the optimization problem thus takes the form

$$\min_{\xi} \ \log(\Phi)=\log\left(\frac{1}{\int_{\Omega_\mathrm{o}}\mathrm{d}\mathbf{r}}\int_{\Omega_\mathrm{o}}|p(\mathbf{r},\xi(\mathbf{r}))|^2\mathrm{d}\mathbf{r}\right), \qquad \text{objective function} \tag{4.2}$$

$$\text{subject to } \frac{1}{\int_{\Omega_\mathrm{d}}\mathrm{d}\mathbf{r}}\int_{\Omega_\mathrm{d}}\xi(\mathbf{r})\mathrm{d}\mathbf{r}-\beta\leq 0, \qquad \text{volume constraint} \tag{4.3}$$

$$0\leq\xi(\mathbf{r})\leq 1 \quad \forall\ \mathbf{r}\in\Omega_\mathrm{d}, \qquad \text{design variable bounds} \tag{4.4}$$

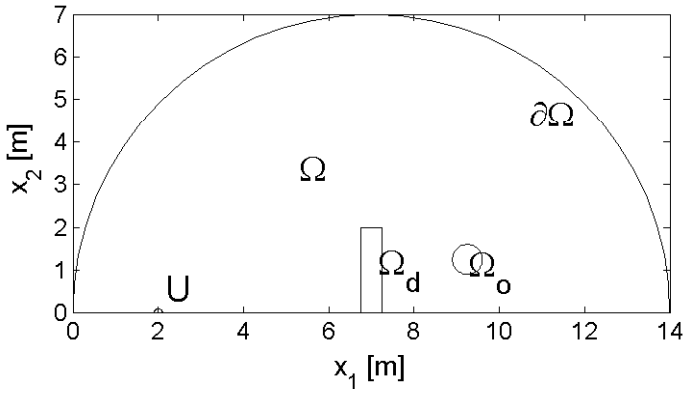

Figure 4.1 The geometry employed for the sound barrier topology optimization problem with the design domain Ω_d, the output domain Ω_o and the point source with the vibrational velocity U.

To obtain better numerical scaling in the optimization process the logarithm is taken to the objective function, and the sensitivities hence have to be adjusted by dividing them with Φ. The volume constraint imposes a limit on the amount of material distributed in Ω_{d} given by the volume fraction β in order to save material. The initial guess for the optimization is a uniform distribution of solid material in Ω_{d} with the volume fraction β. A small amount of mass-proportional damping is added to the problem and the morphology-based filter described in section 3.5 is applied. Second order Lagrange elements are used for the complex pressure amplitude and the design variables are discretized by first order Lagrange elements.

4.2 Results

In the first example, the sound barrier is optimized for the octave band center frequency $f = 125$ Hz (where $f = \omega/2\pi$) and the volume fraction $\beta = 0.9$. The performance of the optimized design obtained from the topology optimization is compared to the performance of a straight and a T-shaped barrier. The two conventional barriers are centered in the design domain and they both have the same height as Ω_{d} and the T-shaped barrier has the same width. The increase of the objective function $\Delta\Phi$ for the T-shaped barrier and the optimized design is given in table 4.1 compared to Φ for the straight barrier. It is observed that the T-shaped barrier reduces the noise slightly more than the straight barrier, which is in agreement with the literature. The table shows that the objective function for the optimized design is reduced with more than 9 dB compared to the straight barrier. The optimized barrier is indicated in figure 4.2(a) and is close to a 0-1 design. The distribution of the sound pressure amplitude for the optimized design is seen in figure 4.2(b). The sound pressure amplitude is high in the cavity connected to the right surface, which is acting as a kind of a Helmholtz resonator.

It is also possible to design the sound barrier for a frequency interval using Padé approximations as described in section 3.3. The next example is thus optimized for the interval between the two center band frequencies [63;125] Hz with 7 target frequencies. The volume factor is again $\beta = 0.9$ and the objective function Ψ is reduced from 71.4 dB for the initial guess to 64.4 dB for the optimized design. The barrier is seen in figure 4.3(a) and it has a cavity on both vertical edges that can act as Helmholtz resonators. In figure 4.3(b), the value of Φ is plotted as a function of the frequency f for the optimized design as well as for the straight and the T-shaped

Table 4.1 The increase of the objective function $\Delta\Phi$ for the T-shaped and the optimized barrier compared to Φ for the straight barrier for $f = 125$ Hz.

frequency f [Hz]	straight Φ [dB]	T-shape $\Delta\Phi$ [dB]	optimized $\Delta\Phi$ [dB] $\beta = 0.90$
125	70.02	-0.90	-9.13

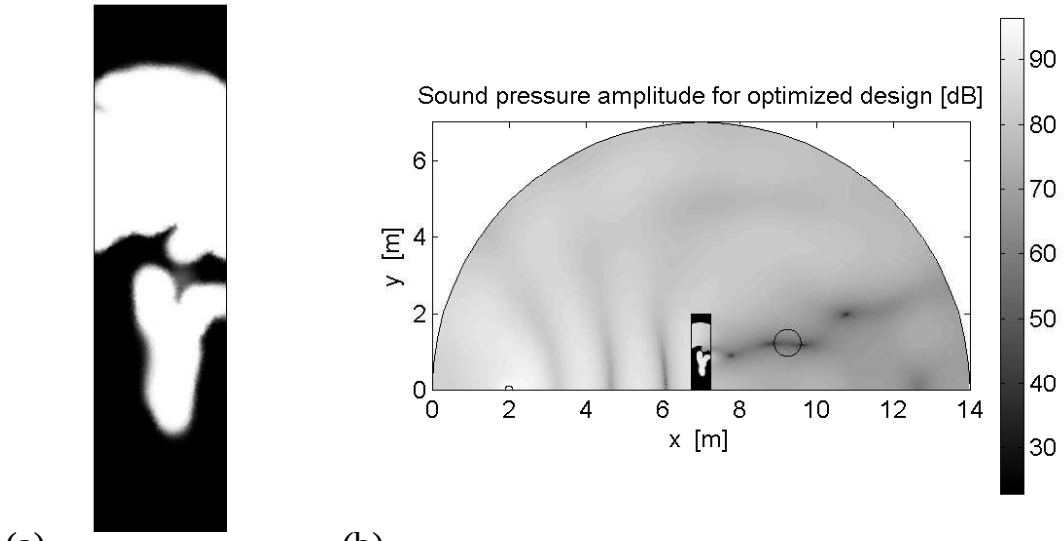

Figure 4.2 Results of the optimization for the target frequency $f = 125$ Hz and β=0.9. (a): The optimized design where black is solid material and white is air. (b): The distribution of the sound pressure amplitude around the optimized design.

barriers. The optimized design performs better than the two other barriers in the entire frequency interval and the T-shaped barrier is better than the straight barrier. However, Φ is not reduced with as many dB for the single frequencies as in the first example, but it is decreased with around 2 dB in the entire interval compared to the straight barrier.

These examples show that the method of topology optimization presented here is suitable to design sound barriers in outdoor situations for both a single frequency and a frequency interval. In [P1] it is also shown that Φ can be reduced with up to 30 dB when a barrier on each side of the source are utilized. In this case the optimized barriers are displaced compared to each other such that a destructive wave pattern decreases the objective function. By displacing T-shaped barriers in a similar way a reduction of almost 10 dB is obtained, which shows that the method can be employed to find a good position of conventional barriers such that the noise is reduced. The method is suited for low frequencies, but for frequencies higher than $f = 125$ Hz problems start to appear due to the more complicated distribution of the sound pressure amplitude and because of many local minima.

In the future, the method should be tested for more complicated problem settings with complex geometries, several sound sources and bigger output areas. In the outdoor situation sources from several parallel lanes should be included as well as larger objects along the road. Finally, the described method could be employed to optimize other acoustic properties such as the reverberation time or the sound power

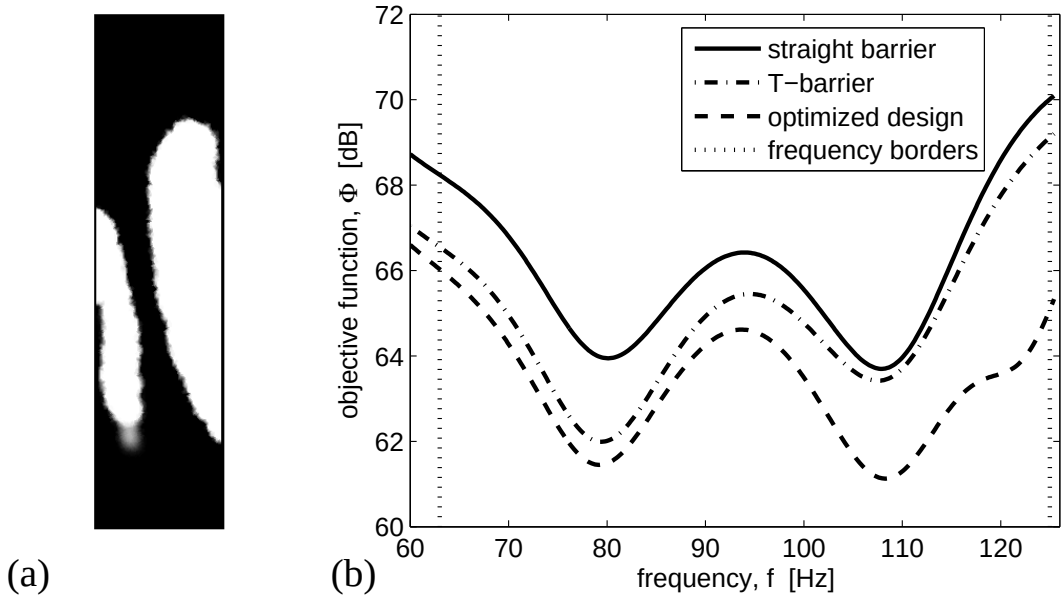

Figure 4.3 Results of the optimization for the frequency interval [63;125] Hz with 7 target frequencies and $\beta = 0.9$. (a): The optimized design where black indicates solid material and white is air. (b): The value of Φ as function of the frequency f for the straight, T-shaped and optimized sound barriers.

into an area or through an opening between coupled rooms.

Chapter 5
Design of photonic-crystal fibers by topology optimization [P2]

The second type of wave problem is studied in this chapter and is about optical waves propagating in hollow core photonic-crystal fibers. The method of topology optimization is used to maximize the energy flow by redistributing air and silica material around the core, such that the overlap of the magnetic field in the lossy silica cladding is decreased. The chapter is a summary of publication [P2].

One- or two-dimensional photonic crystals are employed to confine optical waves in the core region of photonic-crystal fibers, which were first studied in the 1990s [75, 76]. A holey fiber consists of a hollow core, which is surrounded by a two dimensional periodic pattern of air holes that confine the wave by the band-gap effect [17]. Thus, a part of the optical wave propagates in air for this type of fiber, and therefore losses as well as unwanted dispersion and nonlinear effects from the cladding material can be reduced. Another part of the wave propagates in the cladding, which is usually silica. For optical wavelengths in general, silica is a lossy material and will absorb a part of the energy. For most wavelengths holey fibers will therefore not be convenient for long fiber links, but rather for short distance applications as for instance in laser surgery. Compared to conventional laser surgery with reflecting mirrors fibers gives the possibility to do operations inside the body without the need to open it. A first application of photonic-crystal fibers for medical purposes is found in [77] where a fiber is employed successfully in laryngeal and airway surgery. In order to get a high energy flow in the fiber it is important to design the cross section such that the overlap between the optical mode and the cladding is as small as possible. This problem is considered in a number of papers [78, 79, 80], where geometry parameters such as the core size, the thickness and the shape of a solid core boundary as well as the size of the fingers pointing towards the core have been varied. In this chapter topology optimization, which has already been applied to design photonic crystals [50, 53, 54, 56], is employed to increase the energy flow in a holey fiber. First the method is presented and then an example of its performance is shown for an optical wavelength relevant for medical purposes.

5.1 Method

The purpose of the presented method is to distribute air and silica material in the design domain Ω_d around the fiber core such that the energy flow in the core region Ω_c is maximized. The initial design of the holey fiber is given in figure 5.1. The pitch is $\Lambda = 3.1$ μm, the hole diameter over the pitch ratio is $d/\Lambda = 0.92$ and the

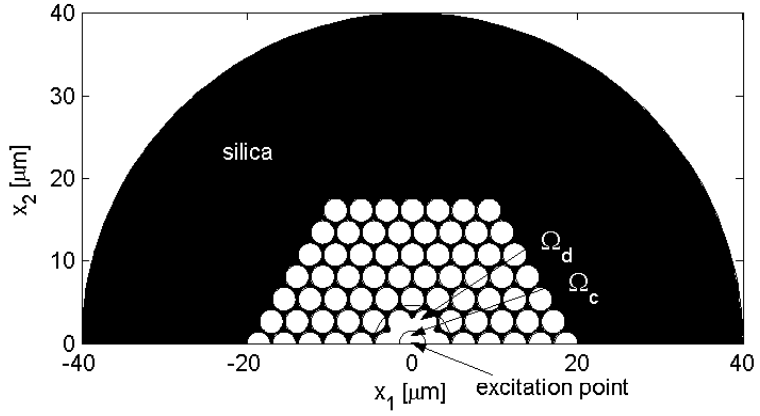

Figure 5.1 Geometry of the photonic crystal fiber used in the optimization. Black indicates silica and white is air. The design domain is Ω_d and Ω_c is the core region where the objective function is optimized.

radius of the air core in the center is $R = \Lambda$. The boundary condition along all the borders is the perfect electric conductor. The chosen optical wavelength in free space is $\lambda_0 = 2$ μm and the refractive indexes for this wavelength are $n_\mathrm{a} = 1$ for air and $n_\mathrm{s} = 1.43791 + 0.0001i$ for silica. The imaginary part of n_s indicates the absorbing coefficient α_s. It is assumed that the propagating optical modes have harmonic solutions on the form

$$H_{p,\nu}(x_1, x_2, x_3) = H_{p,\nu}(x_1, x_2)e^{-i\beta_\nu x_3}, \tag{5.1}$$

where $H_{p,\nu}$ is the magnetic field of the optical wave and β_ν is the propagation constant for a given optical mode ν. This is entered into the time-harmonic wave equation

$$e_{ijk}\frac{\partial}{\partial x_j}\left(b_{kl}b_{lm}e_{mnp}\frac{\partial H_{p,\nu}}{\partial x_n}\right) - k_0^2 H_{i,\nu} = 0, \tag{5.2}$$

where $k_0 = 2\pi/\lambda_0$ is the free space propagation constant, e_{ijk} is the alternating symbol and $b_{ik}n_{kj} = \delta_{ij}$. For the problem considered in this chapter the materials are assumed to be isotropic and therefore $b_{kl}b_{lm}$ reduces to n^{-2}. For the given value of k_0 the propagation constant β_ν for the possible modes are found by solving the wave equation as an eigenvalue problem. In order to define the problem for the topology optimization, the propagation constant for the guided mode β_1 is calculated. The wave equation is then solved in a way where both k_0 and β_1 are fixed, and the guided mode is excited by applying a magnetic source term in the center of the fiber, which is directed in the horizontal direction. The design variable ξ takes the value 0 for air and 1 for silica and the refractive index is interpolated linearly between the two material phases. The objective function Φ is an energy measure and is defined as

the sum of the squared magnetic field amplitudes in the x_1- and x_2-direction in the core area, Ω_c. Hence, the optimization problem is given as

$$\max_{\xi} \ \log(\Phi) = \log \int_{\Omega_c} \sum_{j=1}^{2} |H_j(\mathbf{r}, \xi(\mathbf{r}))|^2 \mathrm{d}\mathbf{r}, \qquad \text{objective function} \tag{5.3}$$

$$\text{subject to } 0 \leq \xi(\mathbf{r}) \leq 1 \quad \forall\ \mathbf{r} \in \Omega_d, \qquad \text{design variable bounds} \tag{5.4}$$

The morphology-based filter described in section 3.5 is applied to avoid mesh-dependent solutions and to enforce 0-1 designs. To prevent convergence to a local optima a continuation method is applied where α_s has a big value from the beginning of the optimization such that the problem is modified to a smoother problem. During the optimization α_s is gradually reduced to its more realistic value. Vector elements are used for H_1 and H_2 in order to avoid spurious modes. Lagrange elements of second order are used for H_3 and of zero order for ξ.

5.2 Results

An example of the optimization is shown in figure 5.2(a) and 5.2(b) where the initial and the optimized designs are plotted, respectively. The distribution of the energy measure from the objective function normalized with its maximum value for the initial design, Φ_{max}, is indicated with the contour lines. The objective function is increased 3.75 times for the optimized design. All parts are connected in the optimized geometry and it is close to be a 0-1 design. The symmetry around the vertical axis is kept in the optimized design, but the 60 degree symmetry from the initial design has vanished. The objective function in the optimized design has been redistributed such that the modes shape is extending more in the vertical direction

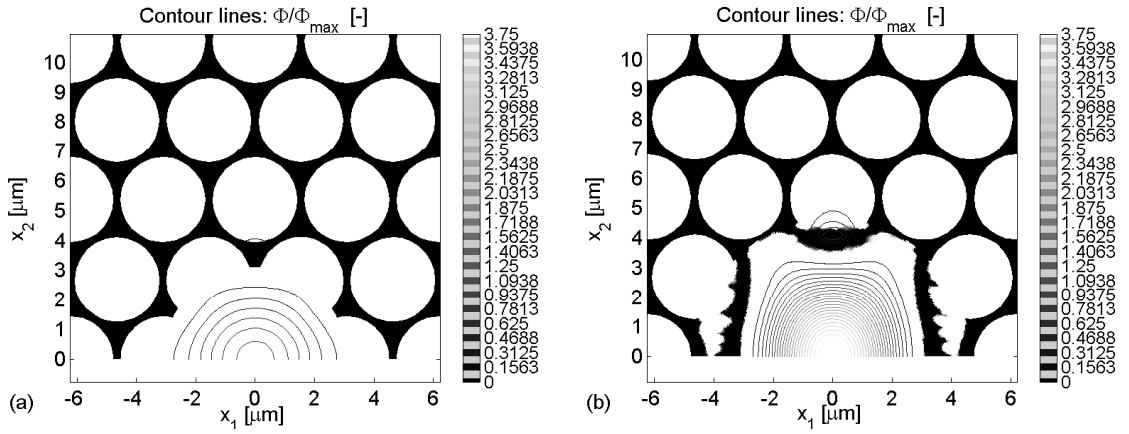

Figure 5.2 The center region of the holey fiber where black indicates silica and white is air. The contour lines show the distribution of the energy measure from the normalized objective function Φ/Φ_{max}. (a): Initial design. (b): Optimized design.

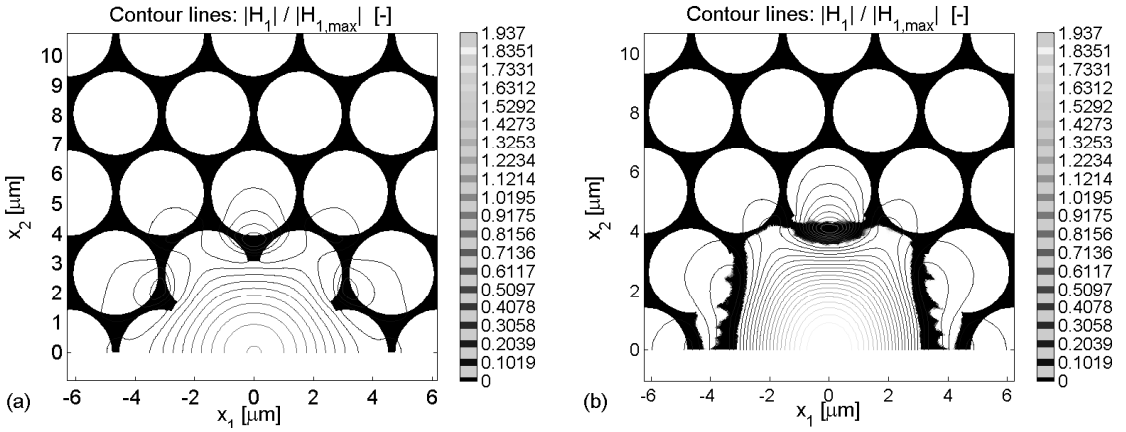

Figure 5.3 The geometry of the center region of the holey fiber where black is silica and white is air. The contour lines indicate the normalized absolute value of the magnetic field $|H_1|/|H_{1,\max}|$. (a): Initial design. (b): Optimized design.

and the peak value in the center has increased compared to the initial design. The magnetic field of the optical mode is mainly polarized in the horizontal direction and the distribution of the normalized field $|H_1|/|H_{1,\max}|$ is plotted with contour lines for the initial and the optimized design in figure 5.3(a) and 5.3(b), respectively. $|H_{1,\max}|$ is the maximum value of $|H_1|$ for the initial design. The field distribution is symmetric around the vertical axis for both the initial and optimized design and like the distribution of the objective function, $|H_1|$ is confined by the vertical walls to the sides and is elongated in the vertical direction after the optimization. For the initial design, concentrations of $|H_1|$ are found where the three fingers are pointing towards the center, but for the optimized design the two field concentrations at the sides has disappeared caused by the forming of the vertical walls. This means that a smaller part of the total field is in the lossy silica material and therefore less energy is absorbed. Thus, the energy flow in the core region can increase. This example shows that the presented method can be employed to improve the energy flow in a holey fiber by reducing the overlap between the optical mode and the lossy cladding.

The optimized design has many small details and will therefore be difficult to fabricate by a drawing process that tends to smoothen the geometry. In order to examine how important the details are for the performance of the fiber and to get designs that are simpler to fabricate, two simplified geometries are constructed and shown in figure 5.4(a) and 5.4(b). The distribution of $\Phi/\Phi_{\max}$ is indicated by the contour lines. Design (a) imitates the optimized design well with tilted side walls and a detailed upper part above the optical wave. The objective function for this case is increased 2.95 times compared to the initial design. The increase is not as big as for the optimized design, but the improvement is still significant. Design (b) is further simplified with vertical side walls and rounded upper part, and Φ is correspondingly smaller and has increased 2.62 times. Thus, these examples show that it is possible

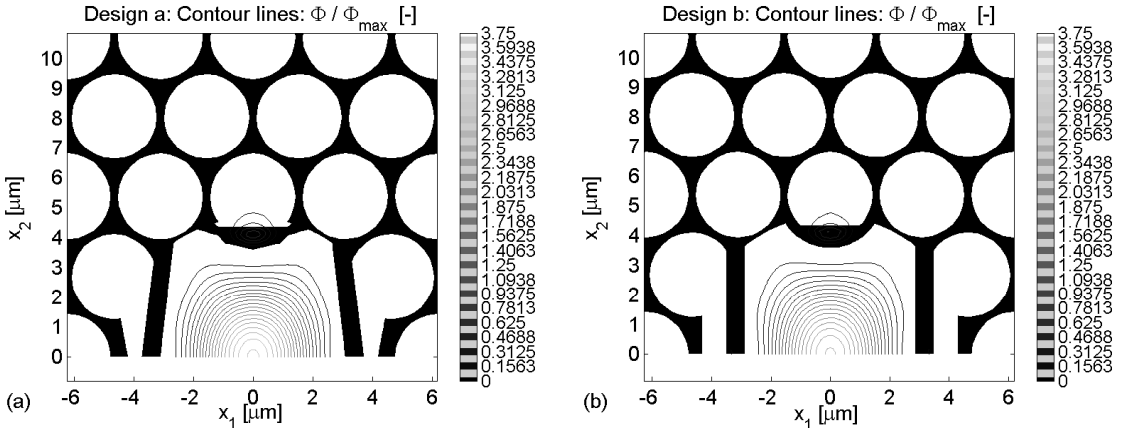

Figure 5.4 Two simplified geometries of the holey fiber inspired from the optimized design. Black is silica and white is air. The contour lines show the distribution of the normalized energy measure from the objective function $\Phi/\Phi_{\max}$.

to design fibers with a simplified geometry inspired from the optimization, which will be easier to fabricate and have a significant improvement of the energy flow. However, the more the geometry deviates from the optimized design the more the performance decreases due to an increased overlap with the cladding.

The presented method can be extended to design other kinds of photonic-crystal fibers, as index-guiding fibers, and other types of objective functions can be tested in order to optimize for dispersion properties and non-linear effects. The optimization can be done for a wavelength range as described in section 3.3 in order to get broadband solutions.

Chapter 6
Design of acousto-optical interaction [P3]-[P7]

An acoustic and an optical wave problem have been studied, respectively, in the two previous chapters and structures have been optimized by the method of topology optimization. In this chapter the last and most complicated wave problem is considered where the acousto-optical interaction between surface acoustic waves and optical waves in channel waveguides is investigated. The chapter gives an overview of the work presented in publication [P3]-[P7].

6.1 Introduction

The propagation of surface acoustic waves (SAW) is confined to a material surface and two main types of waves exist. The Rayleigh wave is polarized in the longitudinal and transverse, vertical directions and the other type is mainly polarized in the shear horizontal direction such as the Bleustein-Gulyaev wave [7]. In piezoelectric materials SAWs can be generated by the inverse piezoelectric effect by interdigital transducers (IDTs), which are arrays of electrode fingers deposited on the surface. The electrode fingers determine the wavelength and the width of the beam as indicated in figure 6.1(a). When the electrode height is small the wave properties of the excited waves are similar to the waves propagating on a free surface. Conventional SAW devices as filters, resonators and sensors as well as the new acousto-optical devices are driven by IDTs with thin electrodes. However, when the aspect ratio of

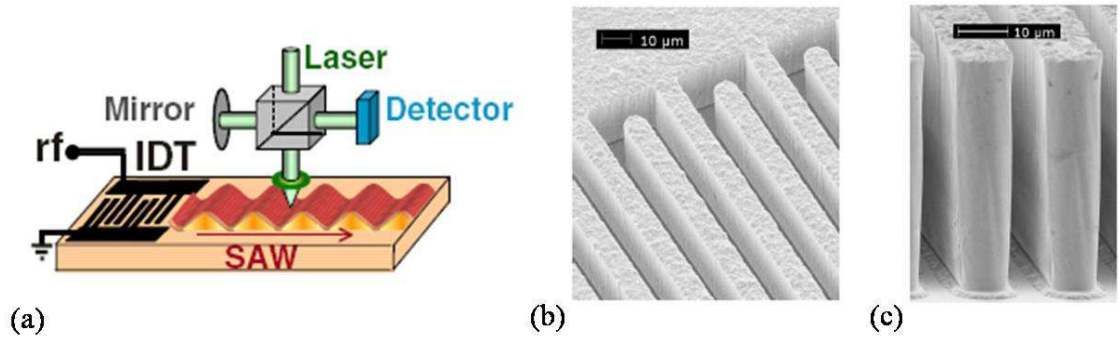

Figure 6.1 Interdigital transducers to generate surface acoustic waves. (a): Double-finger IDT with thin electrodes. The interferometer setup to measure the wave amplitude by a laser is sketched. (M.M. de Lima Jr. et al. [21]). (b) and (c): Scanning electron microscope image of IDT with high aspect ratio electrodes. The substrate is lithium niobate and the electrodes consist of nickel. (V. Laude et al. [81]).

the electrodes increases the SAW properties change significantly, and in [82, 81, 83] numerical and experimental results show a multi-mode SAW propagation and a ten-fold slowing of the phase velocity. The high aspect ratio (HAR) electrodes measured in the experiments are seen in figure 6.1(b) and 6.1(c).

Recently, a Rayleigh wave generated by thin electrodes has been employed to create an optical switch by modulation of optical waves in the two waveguide arms of a Mach-Zehnder interferometer (MZI). A MZI is an optical device consisting of a waveguide that is split into two waveguide arms and after a distance the arms are joined again as illustrated by figure 6.2(a). By sending a Rayleigh wave perpendicular towards the waveguide arms a periodic modulation of the light is obtained. The distance between the waveguide arms is an unequal number of half Rayleigh wavelengths such that when a Rayleigh wave node is present at each waveguide the output light will not change. When a wave crest is located at one waveguide a trough will appear at the other waveguide, and the applied stresses with opposite sign will introduce a refractive index difference in the arms that causes an opposite phase change in them. By constructive and destructive interference the light will be turned on and off periodically with a multiple of the SAW frequency depending on the static phase difference in the two arms, which can be introduced by a length difference between them. Experimental results are reported in [23] and [P3]. For straight electrode fingers a 40% relative modulation was obtained for a GaAs/AlGaAs sample, but only a 0-8% relative modulation was found for a silicon on insulator (SOI) sample.

In this chapter a numerical model is presented in order to study the acousto-optical interaction in a MZI and explain the difference in the experimental results. To model the SAW propagation and the optical modes in the waveguides, it is sufficient to consider a 2D model of a cross-section through the two waveguides and the geometry is seen on figure 6.2(b). Perfectly matched layers (PML) are employed at the domain borders to prevent reflections of the mechanical and electrical disturbances from the SAW. PMLs were introduced for time-harmonic elastic problems in

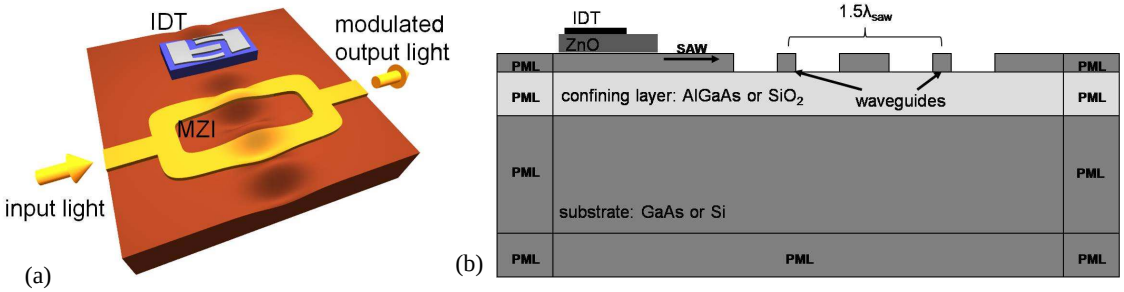

Figure 6.2 Light modulation in a Mach-Zehnder interferometer. (a): 3D geometry of a MZI with a propagating surface acoustic wave (M. van der Poel [P3]). (b): The 2D cross-section through the waveguide arms of the MZI that is used in the simulations.

[26] and are here extended to piezoelectric materials. The Rayleigh wave is generated at the IDT to the left in figure 6.2(b) and propagates in both the left and the right horizontal direction and is absorbed in the PMLs. First the acousto-optical interaction is investigated for the two material cases and a parameter study of the geometry is performed for the SOI case in order to improve the interaction. Then topology optimization, which has successfully been applied to optimize SAW filters and waveguides in elastic materials in [45], is employed to optimize the acousto-optical interaction based on the GaAs/AlGaAs sample.

Finally SAW generation by HAR electrodes is studied. First the electrodes are modeled by a periodic model in order to find the mode shapes and the mechanical energy confinement to the electrodes. Then it is investigated if the acousto-optical interaction can be improved with SAWs generated by HAR electrodes compared to those generated by conventional thin electrodes.

6.2 The acousto-optical model

In a piezoelectric material SAWs are generated by applying an electrical potential to electrode fingers on a material surface. This introduces mechanical deformations in the solid by the inverse piezoelectric effect and the behavior of the piezoelectric material is described by the following model found in [3]. A time-harmonic electrical potential

$$V(x_j, t) = V(x_j)e^{i\omega t}, \tag{6.1}$$

with the angular frequency ω is applied to the electrode. The mechanical strain S_{ij} (assumed small) and the electric field E_j are given by the expressions

$$S_{ij} = \frac{1}{2}\left(\frac{1}{\gamma_j}\frac{\partial u_i}{\partial x_j} + \frac{1}{\gamma_i}\frac{\partial u_j}{\partial x_i}\right) \quad \text{and} \quad E_j = -\frac{1}{\gamma_j}\frac{\partial V}{\partial x_j}, \tag{6.2}$$

where u_i are the displacements. In order to prevent reflections from the sides and bottom of the material, PMLs are employed and the parameter γ_j is an artificial damping at position x_j in the PML given by the expression

$$\gamma_j(x_j) = 1 - i\sigma_j(x_j - x_l)^2. \tag{6.3}$$

Here x_l is the coordinate at the interface between the regular domain and the PML and σ_j is a suitable constant. There is no damping outside the PMLs and here $\gamma_j = 1$. A suitable thickness of the PMLs as well as the value of σ_j must be found by calculations such that both the mechanical and the electrical disturbances are absorbed before reaching the outer boundaries. However, the absorption must also be sufficiently slow as reflections will occur at the interface between the regular domain and the PML if their material properties are not comparable. The mechanical stresses T_{jk} and the electric displacement D_i both depend on the strain and the

electric field according to the constitutive relations

$$T_{jk} = \tilde{c}^E_{jklm} S_{lm} - \tilde{e}^T_{ijk} E_i, \tag{6.4}$$

$$D_i = \tilde{e}_{ijk} S_{jk} + \tilde{\varepsilon}^S_{ij} E_j, \tag{6.5}$$

where $\tilde{c}^E_{jklm}$ are the elastic stiffness constants, $\tilde{e}_{ijk}$ are the piezoelectric stress constants and $\tilde{\varepsilon}^S_{ij}$ are the permittivity constants. The materials are in general anisotropic, and as it is only possible to generate the SAW by the inverse piezoelectric effect in certain directions the material tensors have to be rotated. This is indicated by the tilde above the material tensors. The rotation is done according to Euler's transformation theory as explained in [2]. The two governing equations give the stresses by Newton's second law and the electric displacement from Gauss law

$$\frac{1}{\gamma_j}\frac{\partial T_{ij}}{\partial x_j} = -\rho\omega^2 u_i \quad \text{and} \quad \frac{1}{\gamma_j}\frac{\partial D_j}{\partial x_j} = 0, \tag{6.6}$$

where ρ is the mass density. The piezoelectric model can be solved by a plane formulation obtained by assuming that S_{i3}, S_{3j} and E_3 as well as T_{i3}, T_{3j} and D_3 are equal to zero, which is suitable when simulating Rayleigh waves as they are mainly polarized in the plane. In that case the governing equations are solved for the three unknowns u_1, u_2 and V. When SAWs generated by HAR electrodes are considered, the waves can also have a significant displacement u_3 out of the plane. In that case the model is solved by omitting all derivatives with respect to x_3. Second order Lagrange elements are used for all the unknowns. The implementation in Comsol Multiphysics is done similar to the problems described in [84, 85].

After the mechanical wave is computed by the piezoelectric model described above, the refractive index n_{ij} in the material can be calculated either according to the strain-optical relation [13]

$$\Delta b_{im} b_{mj} = \tilde{p}_{ijkl} S_{kl}, \tag{6.7}$$

where $b_{im} n_{mj} = \delta_{ij}$ and $\tilde{p}_{ijkl}$ are the rotated strain-optical constants, or the stress-optical relation [86]

$$n_{ij} = n^0_{ij} - \tilde{C}_{ijkl} T_{kl}. \tag{6.8}$$

n^0_{ij} is the refractive index in the stress free material and $\tilde{C}_{ijkl}$ are the rotated stress-optical constants. It is assumed that the stress-optical effect is dominant compared to the electro-optical effect, which will be neglected here (see [23]). It is furthermore assumed that the SAW will affect the optical wave, but the optical wave will not influence the SAW. After the SAW induced changes in the refractive index are computed the optical modes in the waveguides are found by solving the eigenvalue problem described in section 5.1. From this the effective refractive indexes of the guided optical modes ν are computed by $n_{\text{eff},\nu} = \beta_\nu / k_0$. The measure of the acousto-optical interaction is defined as

$$\Delta n_{\text{eff},\nu} = |n^{\text{c}}_{\text{eff},\nu} - n^{\text{t}}_{\text{eff},\nu}| / \sqrt{P}, \tag{6.9}$$

where $n^{\mathrm{c}}_{\mathrm{eff},\nu}$ is the case where a surface acoustic wave crest is at the waveguide and $n^{\mathrm{t}}_{\mathrm{eff},\nu}$ is the case where a trough is at the waveguide. The applied electrical power P can be calculated by the expression, see [2],

$$P = \Re \int_{\mathrm{L_{el}}} \frac{V(i\omega D_2 m_2)^*}{2} \mathrm{dL}, \tag{6.10}$$

where $\mathrm{L_{el}}$ corresponds to boundaries with the electrodes and m_2 is the normal vector to the upper surface. The star indicates the complex conjugate and $\Re$ is the real component.

6.3 Modeling surface acoustic waves

To illustrate the performance of the piezoelectric model with the PMLs, a Rayleigh wave is generated by ten double electrode fingers in a GaAs sample with straight surface. The material is rotated 45° around the x_2-axis in order to get the appropriate piezoelectric properties in the propagation direction. An alternating electric potential with magnitude ± 1 V is applied to the electrodes and the resonance frequency is found to be $f = 510$ MHz (where $f = \omega/2\pi$), which is the same as found in experiments, see [87]. On figure 6.3(a) the color scale indicates the displacement u_2 and the surface is deformed with the unified displacements u_1 and u_2 with a scaling factor equal to 1000. The Rayleigh wave is confined to the surface as expected and the correct wavelength defined by the electrodes is obtained. The wave propagates away from the electrodes in the middle and is gradually absorbed in the PMLs at the borders. On figure 6.3(b) the absolute value of u_2 along the upper surface is plotted. A standing wave pattern is generated at the electrodes as the wave here travels in both the left and the right direction. Away from the electrodes the wave is only traveling and the amplitude is therefore nearly constant. It is not constant because the PMLs are not exactly acting as an infinite half space. The electrical potential V is plotted in figure 6.3(c). It is observed that the settings for the PMLs work such that both the mechanical displacements and the electrical potential are absorbed before they reach the outer boundaries. Thus, the results from the piezoelectric model have the expected properties.

6.4 Acousto-optical interaction in a Mach-Zehnder interferometer

This section is an overview of publication [P3]-[P5] where the interaction between a Rayleigh wave and the optical waves in a MZI is studied. The acousto-optical interaction has been investigated experimentally for both a GaAs-/AlGaAs sample and an SOI sample, see [23] and [P3]. For the former case a good performance is obtained, but for the latter case almost no modulation of the optical wave is observed. The described acousto-optical model is here employed to simulate both

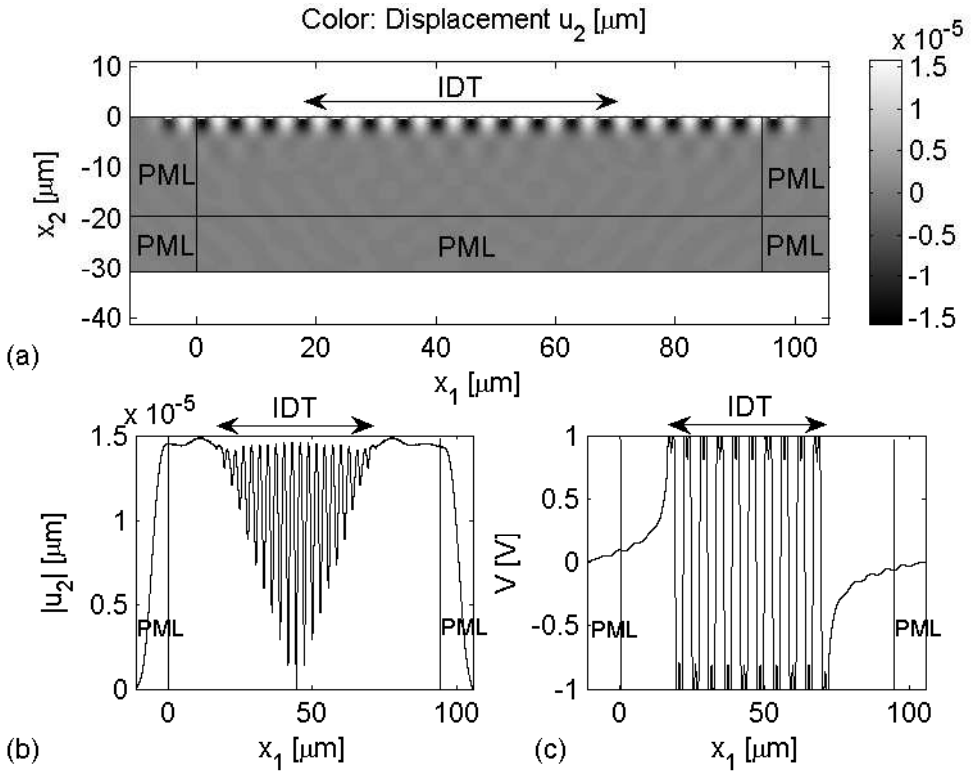

Figure 6.3 Generation of a Rayleigh wave in a GaAs sample. The position of the interdigital transducer (IDT) is indicated. (a): The color indicates the displacement u_2 and the surface is deformed with the unified displacements u_1 and u_2. (b): The absolute amplitude $|u_2|$ along the material surface. (c): The electrical potential V along the material surface.

cases in order to explain the difference in performance. The geometry used in the simulations is sketched in figure 6.2(b). In both cases the SAW is generated by six double electrode finger pairs, and each of the electrodes has a width equal to 0.7 μm and is placed 0.7 μm apart such that the wavelength of the generated SAW is 5.6 μm. To the right the Rayleigh wave will pass through the two waveguides where the optical waves are confined due to the air and the layer below that consists of another material. In the case of the GaAs/AlGaAs sample the confining layer consists of $Al_{0.2}Ga_{0.8}As$, which will be referred to as AlGaAs in the following. The waveguides have the width 1.4 μm and the height 0.3 μm. The driving frequency is $f = 518$ MHz and the optical wavelength is $\lambda_0 = 950$ nm. In the SOI case the substrate and the waveguides are made of Si and the confining layer is SiO_2. These materials are not piezoelectric so the electrodes are placed on top of a ZnO layer from where the generated SAW propagates to the rest of the sample. The waveguides have the width 0.45 μm and the height 0.34 μm. The driving frequency is $f = 630$ MHz and the optical wavelength is $\lambda_0 = 1531$ nm. In [P4] the values of the un-rotated stress-optical constants C_{44}, C_{55} and C_{66} for Si have been ignored

Table 6.1 Refractive index and stress-optical constants from [86].

Material	n_0 [-]	C_{11}, C_{22}, C_{33} [10^{-12} Pa^{-1}]	C_{12}, C_{13}, C_{23} [10^{-12} Pa^{-1}]	C_{44}, C_{55}, C_{66} [10^{-12} Pa^{-1}]
Si	3.42	-11.35	3.65	-12.82

as seen in table III in that paper. The correct material constants are here given in table 6.1. The inclusion of C_{44}, C_{55} and C_{66} does not have any influence on the general conclusions of paper [P4], but the actual values of the interaction have increased. The graphs and results, where the influence of the three components is taken into account, are presented in the following.

When the MZI is designed for acousto-optical interaction the propagation of the Rayleigh wave has to be considered and adjusted. First it is important to be aware that a part of the wave is reflected each time the geometry or the material, that the wave passes through, change. An example is shown in [P3] where the transmission of the Rayleigh wave that passes the two waveguides is measured as function of the etching depth of the material around the waveguides. The transmission decreases drastically after a certain etching depth because the wave is reflected and lost to the bulk material. So in order to get a significant transmission of the Rayleigh wave the changes in geometry and materials must be limited. In the SOI sample an extra change in geometry and material is introduced compared to the GaAs/AlGaAs sample, as the wave has to be generated in a ZnO layer. In addition to the reflections of the Rayleigh wave, its wavelength will also change when the materials are varying along the propagation direction. In the GaAs case this is not a problem as the two materials are so similar that the wavelength is the same through the device. In the SOI case the materials used are not similar and when the wave leaves the ZnO layer the wavelength increases from 5.6 to 7.3 μm. This is a significant reason why the SOI device does not work well, and the distance between the waveguides must be adjusted according to this change in wavelength.

After the Rayleigh wave has been adjusted to the geometry and the materials, the optical properties and the interaction must be considered. First it is verified that the biggest difference in effective refractive index for the fundamental mode $\Delta n_{\text{eff},1}$ appears when one waveguide is influenced by a Rayleigh wave crest and the other is influenced by a trough. The increase of the refractive index $(n_{\text{eff},1} - n_{\text{no}})/\sqrt{P}$ for the SOI case is calculated in the two waveguides for a complete SAW phase passing through the waveguides. n_{no} is the effective refractive index of the fundamental optical mode when no mechanical stresses are applied. The results are plotted in figure 6.4(a) where $\phi_{saw} = 0$ corresponds to a crest in the left waveguide and a trough in the right. It is seen that the biggest difference in $\Delta n_{\text{eff},1}$ is found where a wave crest and a trough is at the waveguides, respectively. This is clarified by plotting the von Mises stress in the sample, see figure 6.4(b). At the surface the von Mises stress is zero at the Rayleigh wave nodes and the biggest values are found

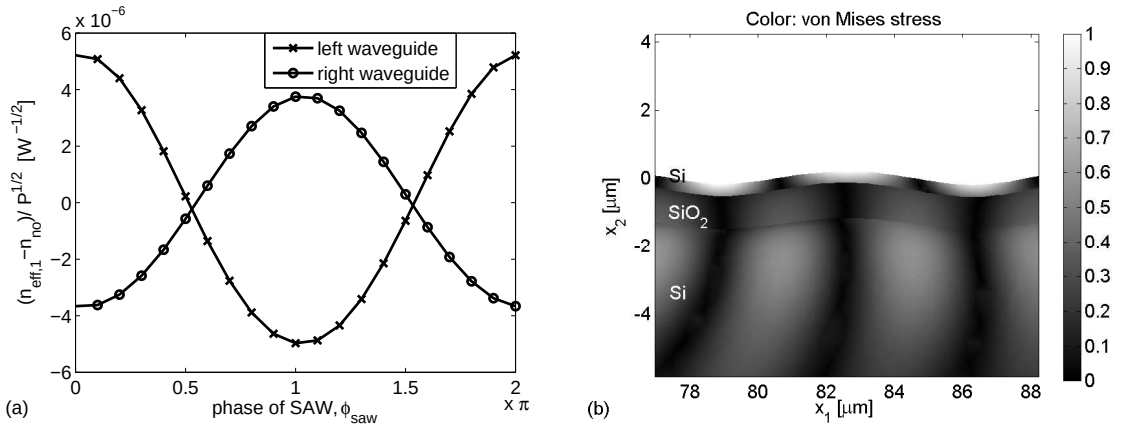

Figure 6.4 Results for the SOI sample. (a): Increase of refractive index $(n_{\text{eff},1}-n_{\text{no}})/\sqrt{P}$ in the two waveguides as function of the SAW phase ϕ_{saw}. $\phi_{saw}=0$ corresponds to a wave crest in the left waveguide and a trough in the right. (b): von Mises stress with arbitrary scale.

at the crests and the troughs. It is observed from figure 6.4(a) that losses due to reflections appear between the waveguides as $(n_{\text{eff},1}-n_{\text{no}})/\sqrt{P}$ in the right waveguide never reaches the extreme values achieved in the left waveguide. It is noted that the values of $(n_{\text{eff},1}-n_{\text{no}})/\sqrt{P}$ are small because of the limited number of electrodes. In experiments several hundred electrode fingers are employed for the wave generation.

In order to understand the acousto-optical interaction it is essential to know the polarization direction of the electric field of the propagating optical modes. An optical mode polarized in a certain direction mainly detects the refractive index and its change in this direction. When designing a device for acousto-optical interaction it is therefore important that the refractive index changes in the polarization direction. The fundamental optical modes for the two different samples are both polarized in the x_1-direction. The waveguide in the GaAs/AlGaAs sample supports one mode and it is of first order. In figure 6.5(a) the increase in refractive index in the x_1-direction, $\Delta n_{11}/\sqrt{P}$, is plotted around one of the waveguides where a Rayleigh wave crest induces stresses. The time averaged power flow in the x_3-direction is indicated by the contour lines with an arbitrary scale. The optical mode has its center in the waveguide and is extending to the substrate below the waveguide. The Rayleigh wave crest is introducing stresses in the entire waveguide area except the upper corners, such that the optical mode is overlapping well with $\Delta n_{11}/\sqrt{P}$. The interaction is $\Delta n_{\text{eff},1}=1.50\cdot 10^{-5}$ W$^{-1/2}$. A similar plot is seen in figure 6.5(b) for the fundamental mode in the SOI sample. In this case the height of the waveguide is bigger compared to the width and therefore the Rayleigh wave only introduces stresses and deformations at the bottom and does not deform the upper part. For that reason $\Delta n_{11}/\sqrt{P}$ only has a significant value at the bottom of the waveguide. Because of the bigger material contrast between the waveguide and the substrate

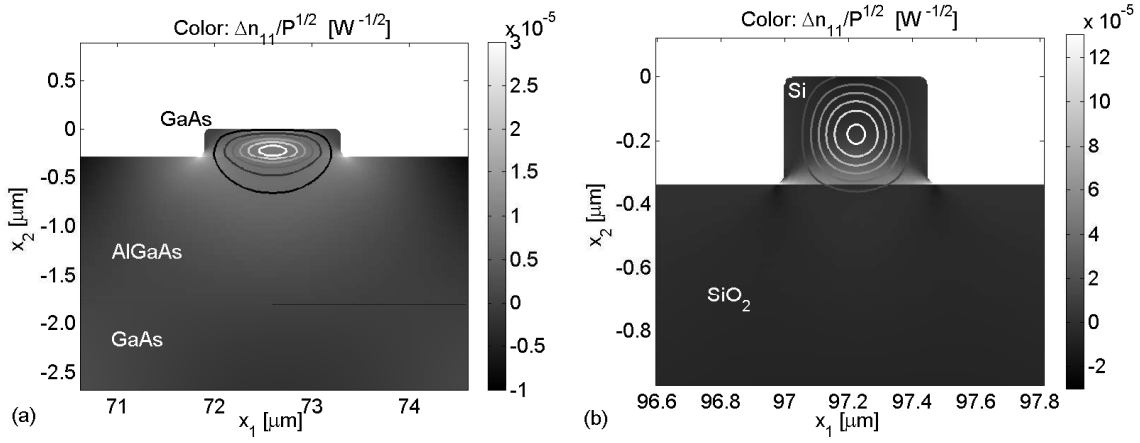

Figure 6.5 Study of acousto-optical interaction in an optical waveguide. The color bars show the refractive index change $\Delta n_{11}/\sqrt{P}$. The time averaged power flow in the x_3-direction of the fundamental mode is indicated by the contour lines with an arbitrary scale. (a): GaAs/AlGaAs sample. (b): SOI sample.

the optical mode is fully confined to the waveguide and its center is placed where $\Delta n_{11}/\sqrt{P}$ is zero. The interaction is $\Delta n_{\text{eff},1} = 8.84 \cdot 10^{-6}$ W$^{-1/2}$, which is less than for the GaAs/AlGaAs case. This shows that the geometry of the waveguide is important for the acousto-optical interaction, and the two examples indicate that it is efficient to have an aspect ratio of the waveguide with a bigger width and a lower height such that the entire waveguide gets deformed as in the GaAs/AlGaAs case. The waveguide of the SOI sample supports another first order mode as well, which is polarized in the x_2-direction. The interaction of this mode is less than the first mode with $\Delta n_{\text{eff},2} = 5.15 \cdot 10^{-6}$ W$^{-1/2}$.

6.4.1 Parameter study of waveguide geometry

The acousto-optical model is now employed to improve the interaction in the SOI sample by varying parameters in the geometry. First the height h of the waveguides is studied and figure 6.6(a) shows the interaction $\Delta n_{\text{eff},\nu}$ as function of h for the two first order modes that the waveguides support. An optimal height $h = 0.19$ μm of the waveguides is found for the mode polarized in the x_1-direction with $\Delta n_{\text{eff},1} = 1.61 \cdot 10^{-5}$ W$^{-1/2}$, which is 1.8 times bigger than for the original height. In figure 6.7(a) $\Delta n_{11}/\sqrt{P}$ is plotted for the optimal height together with the power flow of the fundamental optical mode. As the waveguide has become thinner, the center of the optical mode has moved closer to the surface and is overlapping better with the change in refractive index compared to the original case seen in figure 6.5(b). However, when the height is decreasing the optical wave will be less confined in the waveguide and will be increasingly influenced by the SiO_2 and the air. The air will not contribute to an index difference in the two waveguides and the SiO_2 will have a negative influence on the difference, as the stress-optical constants related

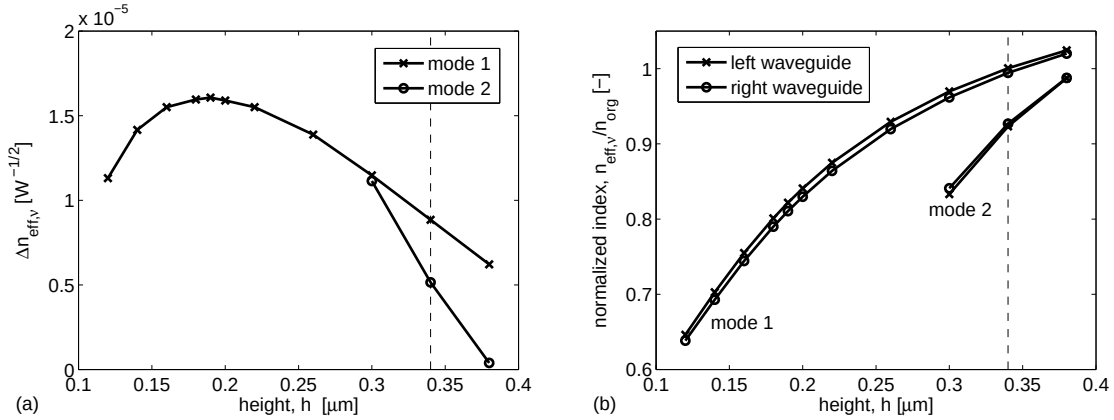

Figure 6.6 Influence of the waveguide height h on the acousto-optical interaction with (- - -) indicating results for the original waveguide geometry. (a): $\Delta n_{\mathrm{eff},\nu}$ for the two first order modes as function of h. (b): Normalized index $n_{\mathrm{eff},\nu}/n_{\mathrm{org}}$ as functions of h.

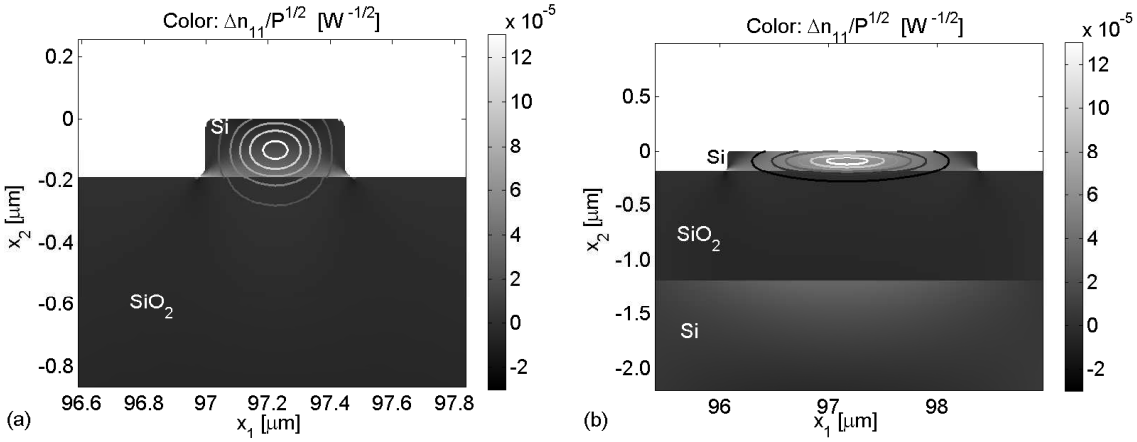

Figure 6.7 Study of acousto-optical interaction in an optical waveguide in the SOI sample. The color bars show $\Delta n_{11}/\sqrt{P}$ and the time averaged power flow in the x_3-direction of the fundamental mode is indicated by the contour lines with an arbitrary scale. (a): For the optimal height $h = 0.19$ μm. (b): For the height $h = 0.19$ μm and the width $w = 2.30$ μm.

to the normal stresses have opposite sign compared to Si. So, if a big part of the optical wave propagates in the air and the SiO_2 the difference between the effective refractive indices in the two waveguides will decrease. The optimal value of h is therefore found as a compromise between how close the center of the optical mode can come to the surface and how confined it is to the waveguide. Figure 6.6(b) shows the effective refractive index as function of h for the two first order modes normalized to the value $n_{\mathrm{eff,org}}$ of the fundamental mode in the left waveguide with a wave crest for the original height. $n_{\mathrm{eff},\nu}$ are in both cases decreasing for decreasing height as less Si, with high refractive index, is used. The waveguide with the original height

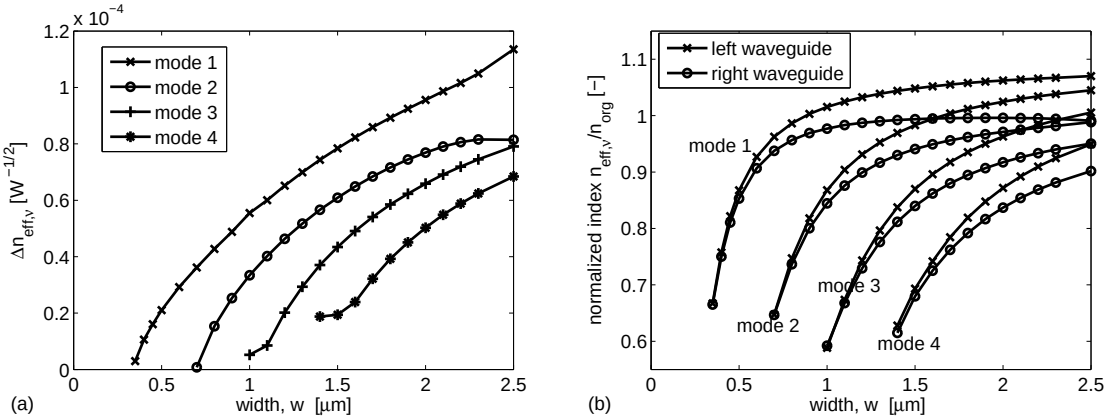

Figure 6.8 Results from a study of the waveguide width w for the optimal height $h = 0.19$ μm. (a): $\Delta n_{\text{eff},\nu}$ of the four lowest order modes as function of w. (b): Normalized index $n_{\text{eff},\nu}/n_{\text{org}}$ as functions of w.

supports the two first order modes whereas the waveguide with the optimal height only supports the mode polarized in the x_1-direction. The interaction is smaller for the mode polarized in the vertical direction.

A study of the width w of the waveguides with the height fixed to $h = 0.19$ μm is seen in figure 6.8(a). $\Delta n_{\text{eff},\nu}$ is plotted for the first four modes, for which the mode order increases with the mode number. $\Delta n_{\text{eff},\nu}$ increases with increasing w for all four modes, but the interaction is biggest for the first order mode. When w is increasing, the confined optical mode will also extend in the horizontal direction and will experience more stresses as long as w is smaller than half a SAW wavelength. The power flow for the first order mode is plotted in figure 6.7(b) for $w = 2.30$ μm and it overlaps well with the change in effective refractive index. The limit for the increase is in principle when w approaches half a SAW wavelength. However, before that the mode in the right waveguide with the SAW trough will start to degenerate into two modes, so the graph is therefore stopped here. The difference in index reaches $1.14 \cdot 10^{-4}$ W$^{-1/2}$, which is more than 12 times bigger than for the original waveguide geometry. When w increases the waveguides will start to support an increasing number of modes, which is also seen on figure 6.8(b) where $n_{\text{eff},i}/n_{\text{org}}$ for the four lowest order modes in the two waveguides are shown as functions of w. The waveguide is single-moded until $w = 0.60$ μm and the interaction is here $2.92 \cdot 10^{-5}$ W$^{-1/2}$, which is 3.3 times bigger than for the original waveguide geometry. This study of the waveguide geometry shows that it is possible to improve the optical modulation by changing the waveguide size such that the mode is moved closer to the surface and extended in the width to experience more stresses. This was also expected when comparing with the GaAs/AlGaAs case as seen in figure 6.5(a).

As the stresses from the Rayleigh wave have their maximum just below the surface, an alternative to changing the waveguide size is to bury the original waveguides

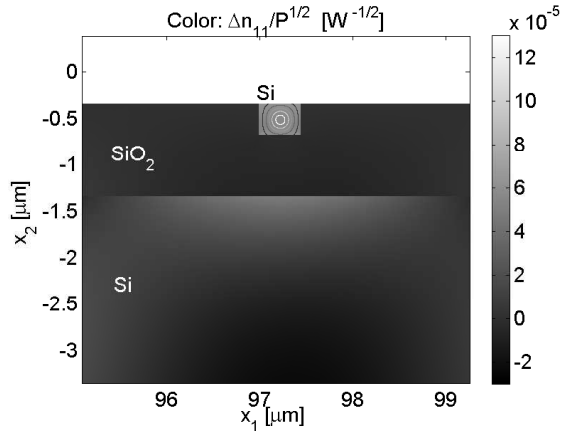

Figure 6.9 Results for the buried waveguide where the color bar indicates $\Delta n_{11}/\sqrt{P}$ close to the optical waveguide. The time averaged power flow in the x_3-direction of the fundamental mode is indicated by the contour lines with an arbitrary scale.

in the SiO_2 layer such that their upper surface is leveled with the substrate surface. The waveguides still support the two first order modes and for the first one polarized in the x_1-direction the interaction is $\Delta n_{\text{eff},1} = 7.16 \cdot 10^{-5}$ $\text{W}^{-1/2}$. This is 8 times bigger than for the original waveguides on top of the surface. The power flow of this optical mode is plotted together with $\Delta n_{11}/\sqrt{P}$ in figure 6.9 and the entire waveguide is now influenced by the change of the refractive index. For the optical mode polarized in the x_2-direction the interaction is $\Delta n_{\text{eff},1} = 3.89 \cdot 10^{-5}$ $\text{W}^{-1/2}$.

From an experimental point of view it is difficult to couple the optical mode to a waveguide if the height is small, and it is more complicated to fabricate a buried waveguide than a ridge waveguide. An alternative design is therefore to introduce a layer of Si next to the waveguide with the height l as seen in figure 6.10(a). This can simply be fabricated by stopping the etching of the Si on the surface before reaching the SiO_2 layer. In this way the optical mode comes closer to the stresses at the surface, but the original height of the Si layer is kept such that the optical mode can be coupled to the waveguide. The interaction $\Delta n_{\text{eff},\nu}$ as function of l is illustrated in figure 6.10(b) for the two first order modes that the waveguide supports. The interaction is increasing for increasing l and it is bigger for the mode polarized in the x_1-direction with $\Delta n_{\text{eff},1} = 1.11 \cdot 10^{-4}$ $\text{W}^{-1/2}$ for $l = 2.5$ μm. This is 12 times bigger than for the original geometry and the increase has the same size as for the improved height and width. For increasing l the mode that is polarized in the x_2-direction is not supported anymore. The power flow of the optical mode and $\Delta n_{11}/\sqrt{P}$ are plotted in figure 6.10(a) for $l = 0.2$ μm. The mode is still confined to the waveguide area and the Si layer, but now the center is below the waveguide where the stresses are big. However, the drawback of this design is, that as the mode has a bigger extension for increasing l the dimensions of other parts in the geometry, as the input waveguides, taperings and splitters, must be correspondingly bigger.

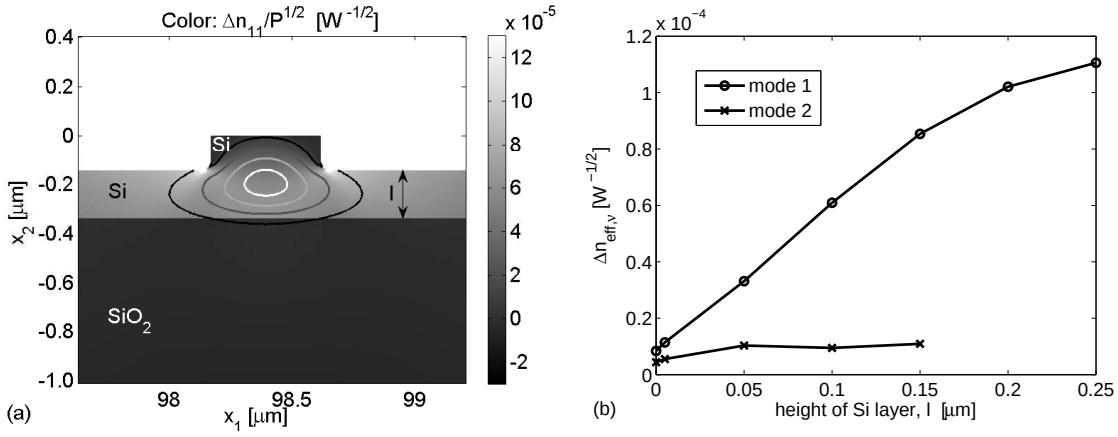

Figure 6.10 Results for the waveguide surrounded by a Si layer with height l. (a): The color bar indicates $\Delta n_{11}/\sqrt{P}$ and the time averaged power flow in the x_3-direction of the fundamental mode is indicated by the contour lines with an arbitrary scale. (b): The acousto-optical interaction $\Delta n_{\text{eff},\nu}$ as function of l for the two first order modes.

The study of the waveguide geometry shows that the acousto-optical interaction in the MZI can be increased significantly compared to the original chosen geometry. Both the Rayleigh wave and the optical wave must be adjusted in order to match well and it is important that the center of the optical mode is close to the substrate surface such that it overlaps the mechanical stresses. When choosing the most suitable geometry different aspects must be taken into account such as the size of the interaction, the fabrication possibilities, the size of the structure and single- and multi-modedness.

Other effects that are not considered in the presented model can have an influence on the interaction. The confinement of the optical mode versus the loss has to be taken into account. When the optical mode gets less confined to the waveguide, as in the case where there is a Si layer next to the waveguide, more energy will be lost to the bulk material. On the other hand, the bigger the dimensions of the waveguide are above the substrate, the more energy can be lost to the air due to irregularities at the surface. The numerical model could also be extended to explore the influence of the mechanical deformations and the temperature on the interaction. Finally, it is important to examine if the polarization direction of the optical mode is unchanged when it propagates along the waveguide. If it changes it can have a significant influence on the interaction. In order to explore this effect a three-dimensional model is required.

The presented results for the SOI sample were calculated with the values of C_{44}, C_{55} and C_{66} taken into account, see table 6.1. This has not influenced the general design conclusions compared to the results in [P4], but the acousto-optical interaction has in general increased. When the stress-optical constants are rotated, the values of C_{44}, C_{55} and C_{66} give a contribution to some of the other components.

The most important change is that the normal component C_{11} is increased around four times. The Rayleigh wave introduces a stress pattern around the waveguide where the normal stresses in the x_1-direction in general have the biggest absolute values. When the values of the interaction for the different waveguide geometries are compared with the values reported in [P4], it shows that they are in general increased around four times - the same as the increase of the C_{11} component. This indicates that the normal stresses in the horizontal direction give the biggest contribution to the acousto-optical interaction in the SOI case.

6.4.2 Topology optimization

Finally, the method of topology optimization is applied to increase the interaction between the Rayleigh wave and the optical mode for the GaAs/AlGaAs sample.

Method

The problem is simplified such that only one waveguide is considered and the rest of the problem setting is the same as described for the GaAs/AlGaAs sample in the beginning of the chapter. During the optimization air and solid material is distributed in a design domain Ω_d below the waveguide such that the objective function Φ is optimized in the output domain Ω_o. The output domain consists of the waveguide combined with an area of the same size just below it, as illustrated at figure 6.11. The design variable ξ takes the value 0 for air and 1 for the solid material, which is AlGaAs in the upper part of Ω_d and GaAs in the lower part. All the material parameters from the piezoelectric and the optical models are interpolated linearly between the two material phases. The purpose of the optimization is to maximize the acousto-optical interaction between the Rayleigh wave and the optical wave. As the fundamental mode in the waveguide is polarized in the x_1-direction it is mainly interesting that the refractive index component n_{11} changes and the change depends on the different strain components - the more the strain components change the more n_{11} changes. The optimization problem is only stated for the piezoelectric model and the aim is to maximize an expression, which depend on the normal strain components. The squared absolute value of the normal strain in the vertical and the horizontal direction, respectively, in the output domain Ω_o have been tested as objective function Φ, as well as their sum. The results obtained for the three cases were similar and in the following the squared absolute value of the normal strain in the vertical direction S_{22} is chosen as Φ. The formulation of the optimization problem is thus given as

$$\max_{\xi} \quad \log(\Phi) = \log\left(\int_{\Omega_\mathrm{o}} |S_{22}(\mathbf{r},\xi(\mathbf{r}))|^2 \mathrm{d}\mathbf{r}\right), \qquad \text{objective function,} \tag{6.11}$$

$$\text{subject to} \quad 0 \leq \xi(\mathbf{r}) \leq 1 \quad \forall\ \mathbf{r} \in \Omega_\mathrm{d}, \qquad \text{design variable bounds.} \tag{6.12}$$

To check that the acousto-optical interaction has indeed improved by the optimization, the optical model is solved for both the initial design and the optimized design.

$\Delta n_{\text{eff},1}$ is then calculated and compared for the two cases. In order to enforce 0-1 designs and avoid mesh-dependent solutions the morphology-based filter on its continuation form is applied. The design variables are discretized by zero order Lagrange elements.

Results

The objective function is maximized and the optimized design is seen in figure 6.11(a) where black represents solid material and white is air. It is almost a 0-1 design and air holes are distributed around the design domain. The objective function is increased with two orders of magnitude and the acousto-optical interaction for the optimized design is $\Delta n_{\text{eff},1} = 1.48 \cdot 10^{-4}$ W$^{-1/2}$, which is almost 10 times higher than for the initial design. The power flow of the optical mode is plotted in figure 6.11(b) together with $\Delta n_{11}/\sqrt{P}$, which has increased by an order of magnitude after the optimization. The refractive index and the interaction have increased because the acoustic wave gets trapped in Ω_{d} and Ω_{o} due to reflections at the air holes. An air hole has furthermore appeared just below the output domain, which is creating strain concentrations that extend to the output domain. A side effect of the optimization is that the optical mode tends to get more confined to the output domain because of the big contrast in refractive index at the air hole next to the output domain.

The example shows that it is possible to improve the acousto-optical interaction by topology optimization where the optimization procedure is based only on the piezoelectric model. Even though a 0-1 design is obtained, it is still difficult to fabricate it with modern fabrication techniques. However, inspired by the optimization

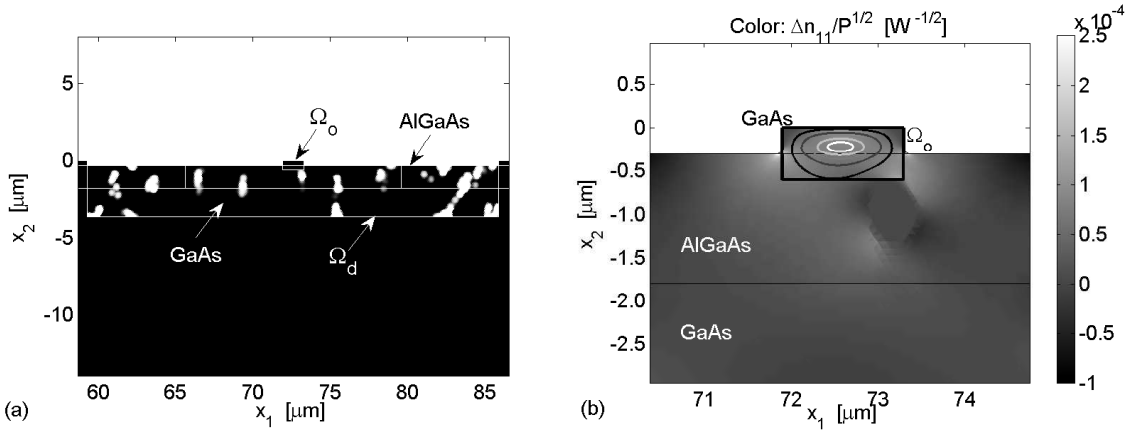

Figure 6.11 Results of the optimization. (a): The optimized design where white is air and black is solid material. (b): The color bar indicates $\Delta n_{11}/\sqrt{P}$ and the time averaged power flow in the x_3-direction of the fundamental mode is shown by the contour lines with an arbitrary scale. The thick line surrounds the output domain Ω_{o}.

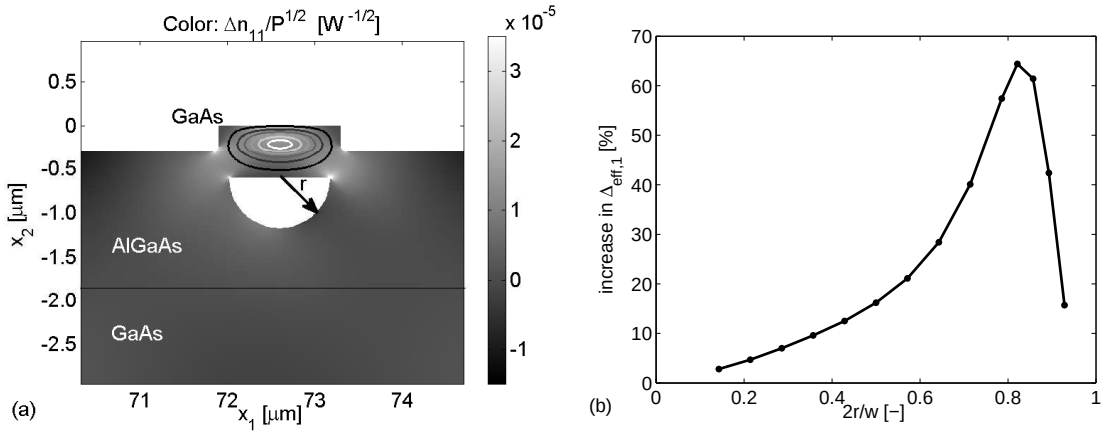

Figure 6.12 Study of the influence of an air hole below the waveguide with radius r. (a): The color bar indicates $\Delta n_{11}/\sqrt{P}$ and the time average power flow in the x_3-direction is shown by the contour lines with an arbitrary scale. (b): Increase in $\Delta n_{\text{eff},1}$ as function of $2r/w$.

a simpler design change can be introduced. The optimization suggests that it as an advantage to have an air hole underneath the output domain. To explore this tendency further an air hole is introduced in the form of a half circle with the radius r, see figure 6.12(a). The increase in $\Delta n_{\text{eff},1}$ as function of $2r/w$, where w is the width of the waveguide, is illustrated by figure 6.12(b). An optimum is obtained around $2r/w = 0.8$ where the interaction has increased with 65% compared to the case without the air hole. When r is increasing two effects will influence the interaction. First, the hole will trap the Rayleigh wave in the waveguide and introduce additional strain concentrations that increase $\Delta n_{11}/\sqrt{P}$, see figure 6.12(a). As r grows, strain is confined more and more to the waveguide above the hole until finally the hole reaches a size, where the Rayleigh wave will be reflected instead. This explains the sudden dip in the graph. The other effect is that the optical mode gets more confined to the waveguide due to the refractive index contrast in the air. The total increase in interaction is small compared to the increase obtained by topology optimization, so the other air holes in the optimized design have an important influence on the performance. To determine if the increased interaction is mainly due to the strains around the hole or due to the better confinement of the optical wave, the interaction $\Delta n_{\text{eff},1}$ is compared for the four cases seen in table 6.2. The value 1

Table 6.2 Increase in acousto-optical interaction $\Delta n_{\text{eff},1}$ compared to the original GaAs/AlGaAs structure without the air hole. The original case corresponds to the value 1.

	optical mode without hole	optical mode with hole
strain without hole	1	1.03
strain with hole	3.29	1.65

corresponds to the original GaAs/AlGaAs structure in figure 6.5(a) where the strain and the optical mode are calculated without the hole. When the strain and the optical mode is found for $2r/w = 0.8$, 1.65 is obtained. Then the strain is calculated without the hole and then the hole is introduced and the optical mode is found. This only gives an increase of a few percent. Finally, the opposite is done where the strain is computed with the hole and the optical mode is calculated with the hole filled. Now the interaction increases more than 2 times, so this indicates that the effect from the strain concentrations is dominant. However, it also indicates that the effect from the strain concentrations and the confinement of the optical mode are counteracting each other.

This shows that the presented optimization method can be employed to improve the acousto-optical interaction and even though the designs are complicated to fabricate, they can be used as inspiration to introduce simpler changes of the initial design. A way to obtain designs that are easier to fabricate is to introduce a constraint that assign the design variables to an entire column that starts at the surface as in [45].

6.5 High aspect ratio electrodes

In the previous sections the acousto-optical model has been employed to study the interaction between a Rayleigh wave and optical waves in channel waveguides. This model is now utilized to investigate SAWs generated by high aspect ratio electrodes. First their mode shapes and the mechanical energy confinement to the electrodes are studied by a periodic model of a unit cell. The obtained results are compared to a model with a finite number of electrodes. Finally, the acousto-optical interaction between the new types of SAWs and an optical wave in a buried channel waveguide is investigated. The section is a summary of the results presented in publication [P6] and [P7].

6.5.1 Periodic structure

First a unit cell is studied with periodic boundary conditions connecting the left and the right boundaries and a PML at the bottom, see figure 6.13. The electrode consists of nickel (Ni) and the substrate is lithium niobate ($LiNbO_3$). The height of the electrode is h and the period of the cell is p. When the aspect ratio of the electrode increases it is possible to excite more mode types than the two that exist for thinner electrodes. Six different modes exist for the aspect ratio $h/2p = 1$ and the mode shapes are plotted in figure 6.13 normalized to the applied electric potential equal to 1 V. Modes with unequal numbers are mainly polarized in the shear horizontal (SH) direction and modes with equal numbers are mainly vertically polarized (VP). All the modes are combinations of a vibration in the electrode and a surface acoustic wave in the substrate. Half of the phase velocity $f \cdot p$, which will be denoted v_p, for increasing aspect ratio is given in figure 6.14(a) for the six modes,

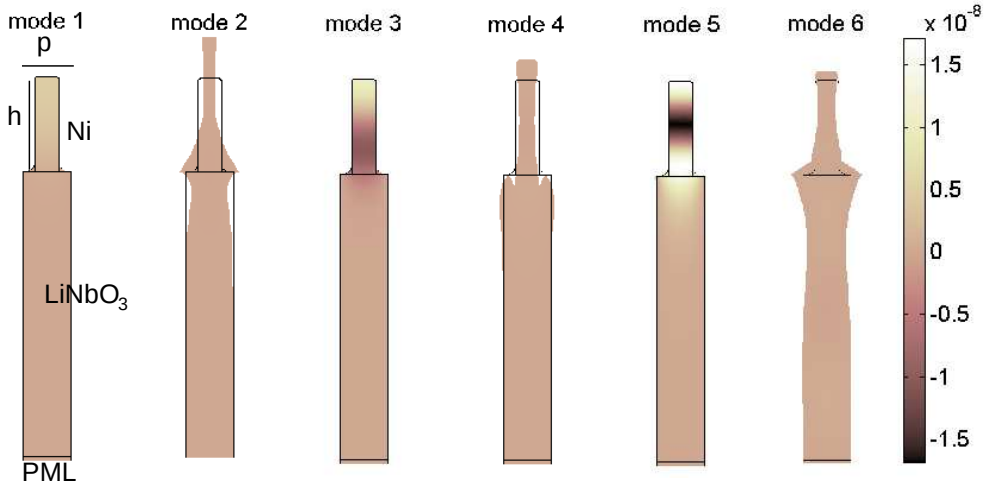

Figure 6.13 The displacements in the structure for each of the six modes at resonance with $h/2p = 1$. u_1 and u_2 are plotted as deformations with an arbitrary scaling factor and u_3 is given by the color bar for all six modes.

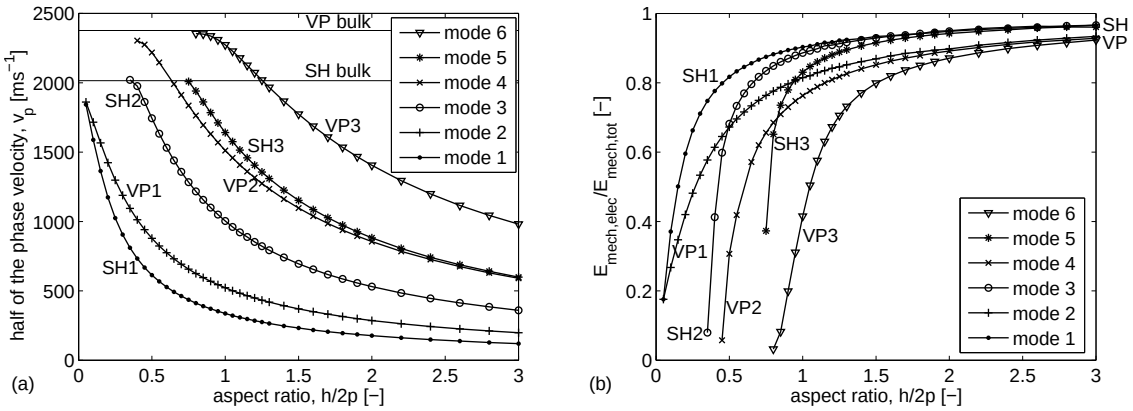

Figure 6.14 Results from the periodic model for the six modes. (a): Half of the phase velocity v_p as function of $h/2p$. The polarization types are indicated along with the limits for the bulk waves. (b): Energy fraction $E_{\mathrm{mech,elec}}/E_{\mathrm{mech,tot}}$ as function of $h/2p$. The limit for the SH modes is 0.97 and the limit for the VP modes is 0.93.

and their polarization direction and the bulk wave limits are indicated. The phase velocity decreases with increasing aspect ratio for all the modes and for mode 1 v_p is decreased up to 15 times. The modes do not appear above their bulk wave limits as they are dissipated to the bulk material. The observed modal shapes in figure 6.13 explain why more and more modes appear in the structure as the aspect ratio increases. When considering the SH modes, which are mainly polarized in the x_3-direction, the mode shapes in the electrode in this direction are of increasing order for increasing mode number. This means that SH1 has a mode shape of order 1,

SH2 has one of order 2 and SH3 has one of order 3. The same is found for the VP modes where the mode shapes have increasing order in the x_1- and x_2-direction. Thus, more modes can exist for larger aspect ratios as the electrode is allowed to vibrate with modes of higher order.

The fraction of mechanical energy in the electrode $E_{\text{mech,elec}}$ with respect to the total mechanical energy in the structure $E_{\text{mech,tot}}$ is plotted in figure 6.14 (b) for the six modes. The energy is more confined to the electrode for increasing aspect ratio. The electrode thus acts as a mechanical resonator, which slows down the SAW velocity because of mechanical energy storage. For modes of the same type, the fraction of mechanical energy in the electrode tends to the same value for increasing aspect ratio. The SH modes tend to a value around 0.97, which is larger than the limit for the VP modes at 0.93. The fact that the limits do not reach 1 explains that the wave is still (slightly) propagating, or rather coupled from one electrode to the other by surface waves. If the energy was fully trapped the surface wave would not propagate at all. For increasing aspect ratio the mode shapes tend to clean cantilever vibrations of slender beams, and the only energy left in the substrate is what connects the cantilever modes to the substrate. Modes of the same polarization type tend to the same energy ratio because they deflect in the same direction where the stiffness in the substrate is the same. As the wavelength gets shorter for increasing mode order for a fixed aspect ratio, the aspect ratio for the higher order modes must be bigger before they reach the energy limits.

6.5.2 Finite structure and acousto-optical interaction

The problem is now extended to a finite structure with twelve electrode pairs by applying PMLs at the vertical borders, see figure 6.15. The electrodes are excited with an alternating electrical potential. The values of the phase velocity and the

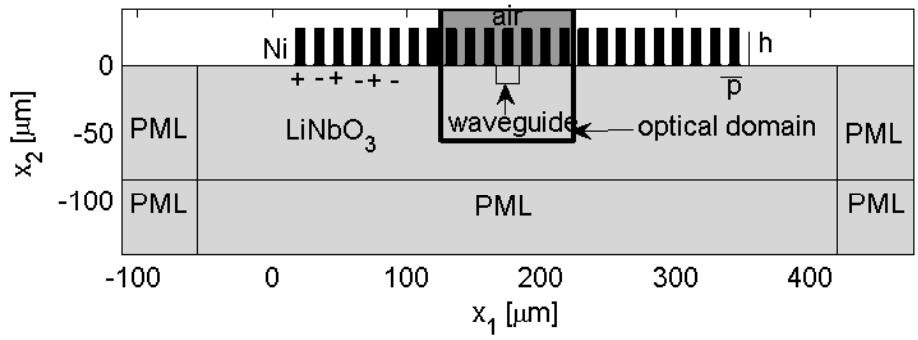

Figure 6.15 The geometry of the acousto-optical problem with Ni electrodes on a $LiNbO_3$ substrate. Perfectly matched layers absorb the waves at the boundaries and the thick square indicates the optical domain.

Table 6.3 Half of the phase velocity v_p and the energy fraction $E_{\text{mech,elec}}/E_{\text{mech,tot}}$ for the periodic and finite structure for the six modes and $h/2p = 1$.

Mode number Mode type		1 SH1	2 VP1	3 SH2	4 VP2	5 SH3	6 VP3
phase velocity	periodic device	337	523	1004	1512	1641	2273
v_p [ms^{-1}]	finite device	337	523	1004	1510	1639	2275
$E_{\text{mech,elec}}/E_{\text{mech,tot}}$	periodic device	90.5	81.7	88.8	76.4	83.1	41.7
[%]	finite device	90.3	81.5	88.5	75.5	82.1	45.0

mechanical energy fraction $E_{\text{mech,elec}}/E_{\text{mech,tot}}$ are in fine agreement for the periodic and the finite model as seen from table 6.3 where the results are listed for $h/2p = 1$. The small deviations in the values are due to energy loss to the bulk material because of the limited number of electrodes in the finite structure.

In order to study acousto-optical interaction, a buried channel waveguide is introduced below one of the electrodes in the waveguide area indicated in figure 6.15. The waveguide is supposed to be created by annealed proton exchange, which will introduce a refractive index variation that can confine optical modes. The eigenvalue problem for the optical modes is solved in the optical area. The waveguide is multi-moded and the two first order modes are considered here. The one polarized in the x_1-direction is denoted optical mode 1 and the one polarized in the x_2-direction is denoted optical mode 2. The acousto-optical interaction $\Delta n_{\text{eff},\nu}$ is calculated for the two optical modes both for the six acoustic modes with $h/2p = 1$ and for the Rayleigh wave excited by thin electrodes with $h/2p = 0.01$. The results are given in table 6.4. The SH modes interact most efficiently with optical mode 1 and the VP modes interact best with optical mode 2. The acousto-optical interaction decreases with increasing mode number within the two different categories of acoustic modes. The six acoustic modes with high aspect ratio electrodes interact better in general

Table 6.4 The difference in effective refractive index for the two first order optical modes influenced by the six acoustic modes with $h/2p = 1$ as well as by the thin electrodes with $h/2p = 0.01$.

	$\Delta n_{\text{eff},1}$ [W$^{-1/2}$]	$\Delta n_{\text{eff},2}$ [W$^{-1/2}$]
mode 1 (SH1)	$1.55 \cdot 10^{-3}$	$8.97 \cdot 10^{-4}$
mode 3 (SH2)	$9.08 \cdot 10^{-5}$	$6.62 \cdot 10^{-5}$
mode 5 (SH3)	$3.08 \cdot 10^{-6}$	$2.50 \cdot 10^{-6}$
mode 2 (VP1)	$7.35 \cdot 10^{-5}$	$7.21 \cdot 10^{-4}$
mode 4 (VP2)	$1.18 \cdot 10^{-5}$	$6.35 \cdot 10^{-5}$
mode 6 (VP3)	$6.49 \cdot 10^{-6}$	$1.38 \cdot 10^{-5}$
thin electrodes	$2.51 \cdot 10^{-6}$	$1.71 \cdot 10^{-6}$

compared to the acoustic mode for the conventional thin electrodes. The interaction is a result of how efficiently the acoustic mode is excited with the applied electrical power and how well the acoustic and optical mode shapes match each other. The acoustic modes of lower order are more efficiently excited by a certain amount of electrical power than the modes of higher order. This fact can be explained by considering the energy confinement to the electrodes in figure 6.14(b). At the energy limits for increasing aspect ratio the energy is concentrated in the electrodes and in the substrate just below where the electrodes are attached. Therefore the stress concentration around the waveguide will be big. As the lower order acoustic modes are closer to the energy limits for $h/2p = 1$ the values of the stresses will be bigger than for the higher order modes. As the structure with high aspect ratio electrodes is more compliant than the almost plane surface with the thin electrodes, more power has to be applied to the thin electrodes in order to get the same stresses. It can therefore be expected that the change in refractive index is biggest for the low order acoustic modes with high aspect ratio electrodes. The other issue is how well the acoustic modes overlap with the optical modes. The optical modes will mainly detect the changes in refractive index in their polarization direction. So for optical mode 1 it is the SAW induced changes of the refractive index in the x_1-direction Δn_{11} that are important. The optical mode 2 must overlap with Δn_{22}. The acoustic modes of the same polarization type all have a similar pattern of changes in refractive index in the different directions around the optical waveguide. As an example $\Delta n_{11}/\sqrt{P}$ is plotted for SH1 in figure 6.16(a) with the power flow of optical mode 1 indicated with contour lines. The same is plotted for the case with the thin electrodes in figure 6.16(b). The change in the refractive index is bigger for SH1 than for the case with the thin electrodes. The SH1 mode overlaps best with the optical mode

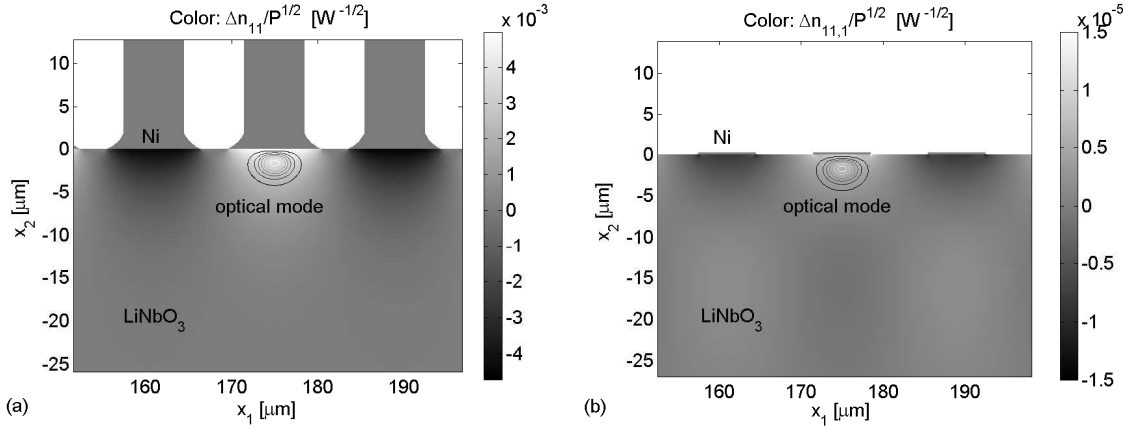

Figure 6.16 Results for the acousto-optical interaction. The color bars show $\Delta n_{11}/\sqrt{P}$ and the time averaged power flow in the x_3-direction of the optical mode 1 is indicated by the contour lines with an arbitrary scale. (a): Results for SH1 with $h/2p = 1$. (b): Results for the thin electrodes with $h/2p = 0.01$.

because changes in $n_{11}/\sqrt{P}$ with the same sign surrounds the mode. $\Delta n_{11}/\sqrt{P}$ for the case with thin electrodes changes sign into the substrate, and therefore a part of the optical mode is overlapping an area where the change in refractive index is zero.

It has thus been proved that the acousto-optical interaction can be increased by the new types of surface acoustic waves generated by HAR electrodes. The problem could be investigated further by a parameter study in order to find the optimal position and size of the waveguide compared to the electrode size. Topology optimization could be applied to the problem to find other and more efficient shapes for the electrodes.

Chapter 7
Concluding remarks

The work presented in this Ph.D. thesis is a contribution to the continuously growing research field of optimization of elastic and optical wave propagation. Three different types of wave devices have been simulated and their performances have been improved either by topology optimization or parameter studies of the geometry. The first problem treated structures for sound reduction, the other was concerned with the energy flow of optical waves in holey fibers, and finally the interaction between surface acoustic waves and optical waves in waveguides was studied. By investigating the waves propagating in the optimized structures, an increased understanding of their physical behavior and the function of the devices were obtained. The acquired knowledge could be employed to fabricate devices with improved efficiency.

It is explained, that even though the three investigated problems describe very different physical phenomena, they can all be described in a similar way by second order differential equations. The time dependency is eliminated as a harmonic time variation can be assumed, and this simplifies the implementation, solving and optimization. The high-level programming language Comsol Multiphysics was found suitable for simulating the studied two-dimensional problems by the finite element method. The implementation time can be reduced with this software, because the differential equations are either predefined or can be specified in a straightforward manner and the discretization, meshing and solving are automated. The code can be extended with Matlab scripting such that studies of geometry parameters and the call to the MMA optimization-algorithm can be performed. The program is however not suited for solving bigger 3D problems due to high memory usage.

The method of topology optimization has successfully been applied to the three types of wave problems. They are defined in a similar way and it was shown that a generic formulation of the optimization problem was suitable for all the wave problems with similar expressions for the objective functions and the interpolation functions. By applying continuation methods and a close-type Heaviside morphology-filter, well defined designs with vanishing gray transition zones at the interfaces between air and solid material were in general obtained. The optimized designs guide and control the propagating waves such that objective function is optimized, and they indicate how much the performance can be increased with unrestricted design freedom. It is therefore concluded that the presented topology optimization method works well for the three wave propagating problems. However, the optimization problems are in general sensitive to factors as the initial guess, move limit, tolerance, filter size and continuation method. So even though essentially the same formulation of the topology optimization can be employed for the considered problems, many different factors must be varied and tested in order to get suitable

designs when optimizing a new problem.

Another disadvantage is that the optimized designs in general are complicated with details comparable to the size of the wavelength. By collaborating with researchers during the project, who work with the fabrication and testing of the SAW structures and optical devices, the experimental limitations could be taken into account. This has led to the study of simplified designs inspired by the optimized results. Their performance were in general not as good as for the optimized designs, but improvements compared to the initial designs were obtained.

In the case of interaction between SAWs and optical waves in waveguides, both mechanical and optical factors have an influence on the performance and can enhance or counteract each other's effects. The simulations with the coupled model are thus crucial in order to understand the acousto-optical interaction and to design the devices. The interaction has been improved by topology optimization based on the piezoelectric model, which resulted in detailed designs that are complicated to fabricate. In contrast to topology optimization, experimental aspects and fabrication issues can be taken directly into consideration when optimizing the interaction by parameter studies of the geometry. The improvements gained by the parameter studies were significant for both thin and high aspect ratio electrodes and the design changes can be introduced in the experimental setups by the existing fabrication techniques.

7.1 Future work

The studied simulation and optimization methods can be exploited further either to improve the studied problems additionally or to extend the methods to other types of wave propagation phenomena.

The problems in this work are simplified in different ways and the focus has in general been on 2D problems. Extensions to 3D problems should be exploited in order to investigate if the optimized structures are similar in 3D or if they are fundamentally different and take advantage of other physical effects. Many types of problems have to be studied by a 3D model as for instance the effects of the optical waves propagating along the photonic-crystal fiber or the waveguide. In order to design structures that guide and control surface acoustic waves in the out of plane direction, as focusing IDTs, a 3D model is necessary as well. The computation time and the use of memory increase significantly with the addition of the third dimension and even though parallel computing is now possible within Comsol Multiphysics, the simulations are still limited to smaller 3D problems. The effects of other physical phenomena as the temperature increase in the SAW devices, the mechanical deformation of the optical waveguides, the sound wave and structure interaction as well as the effect of bending the optical fiber, can be incorporated into the models and the influence on the device performance can be studied.

It is relevant to test the method of topology optimization for other expressions of the objective functions. First of all it can be investigated if the performance of

the studied problems can be improved further by changing the objective function, for instance if a function depending on all the strain components can increase the acousto-optical interaction in the Mach-Zehnder interferometer. Objective functions defined to optimize the structures for other purposes, as optical fibers with specific dispersion properties, can be investigated.

The designs obtained in this work were in general close to be 0-1 designs, but problems with gray transition zones and small details were observed. The applied close-type morphology filter eliminates all air holes with a size below the filter radius, but small details consisting of the solid material are created. Other filter techniques as the method presented in [88], where near-discrete designs were obtained with a defined minimum length scale for both air and solid material, can be tested in order to improve the designs.

The fabrication of structures on micro and nano scale is complicated. The design freedom is limited and irregularities and uncertainties in the final fabricated designs are nearly impossible to prevent. These facts should be taken into account in the topology optimization as extra constraints, for instance by assigning a design variable to an entire column connected to to surface in the MZI as demonstrated in [45]. Another possibility is to design the structures with the techniques for tolerant design as described in [89].

Finally, the numerical results presented in this thesis should be compared to fabricated and characterized versions of the optimized structures to test if their performance are improved in experiments. Designs for the acousto-optical interaction with thin electrodes are being fabricated by the collaborators at the Department of Photonics Engineering at DTU, and at Institute FEMTO-ST in Besançon they have the facilities and are considering to test the improvements of the acousto-optical interaction with the high aspect ratio electrodes.

References

[1] H. Kuttruff, *Room acoustics, 4th edition.* Spon Press, Taylor & Francis Group, 2000.

[2] B. A. Auld, *Acoustic fields and waves in solids, vol. I and II, 1st edition.* Wiley, New York, 1973.

[3] D. Royer and E. Dieulesaint, *Elastic waves in solids, I and II.* Springer, 2000.

[4] L. Rayleigh, "On waves propagating along a plane surface of an elastic solid," *Proc. London Math. Soc.*, vol. 1-17, pp. 4–11, 1885.

[5] P. Curie and J. Curie, "Développement, par pression, de l'électricité polaire dans les cristeux hémièdres à faces inclinées," *C.R. Acad. Sc. Paris*, vol. 92, 1880.

[6] R. M. White and F. W. Voltmer, "Direct piezoelectric coupling to surface elastic waves," *Appl. Phys. Lett.*, vol. 7, no. 12, pp. 314–316, 1965.

[7] K. Y. Hashimoto, *Surface acoustic wave devices in telecommunications, modelling and simulation.* Springer, Berlin, 2000.

[8] S. Takahashi, H. Hirano, T. Kodama, F. Miyashiro, B. Suzuki, A. Onoe, T. Adachi, and K. Fujinuma, "SAW IF filter on $LiTaO_3$ for color TV receivers," *IEEE Trans. Consumer Electron., CE-24*, vol. 3, pp. 337–348, 1978.

[9] K. Shibayama and K. Fujinuma in *Proc. International Symp. on Surface Acoustic Wave Devices for Mobile Communication*, 1992.

[10] U. Wolff, F. L. Dickert, G. K. Fischauer, W. Greibl, and C. C. W. Ruppel, "SAW sensors for harsh environments," *IEEE Sensors Journal*, vol. 1, no. 1, pp. 4–13, 2001.

[11] F. G. Smith and T. A. King, *Optics and photonics, an introduction.* Wiley, New York, 2000.

[12] J. C. Maxwell, "A dynamical theory of the electromagnetic field," *Philosophical Transactions of the Royal Society of London*, vol. 155, pp. 459–512, 1865.

[13] R. Syms and J. Cozens, *Optical guided waves and devices, 1st edition.* McGRAW-Hill, London, 1992.

[14] E. Yablonovitch, "Inhibited spontaneous emission in solid-state physics and electronics," *Phys. Rev. Lett.*, vol. 58, no. 20, pp. 2059–2062, 1987.

[15] S. John, "Strong localization of photons in certain disordered dielectric superlattices," *Phys. Rev. Lett.*, vol. 58, no. 23, pp. 2486–2489, 1987.

[16] T. F. Krauss, R. M. De La Rue, and S. Brand, "Two-dimensional photonic-bandgap structures operating at near-infrared wavelenghts," *Nature*, vol. 383, pp. 699–702, 1996.

[17] J. D. Joannopoulos, S. G. Johnson, J. N. Winn, and R. D. Meade, *Photonic crystals, molding the flow of light, 2nd edition.* Princeton University Press, 2008.

[18] P. Russell, "Photonic crystal fibers," *Science*, vol. 299, no. 5605, pp. 358–362, 2003.

[19] L. Brillouin, "Diffusion de la lumière et des rayons X par un corps transparent homogène, influence de l'agitation thermique," *Ann. Phys.*, vol. 17, pp. 88–122, 1922.

[20] R. Lucas and P. Biquard, "Propriétés optiques des milieux solides et liquides soumis aux vibrations élastiques ultrasonores," *J. Physique*, vol. 10, pp. 464–477, 1922.

[21] M. M. de Lima Jr. and P. V. Santos, "Modulation of photonic structures by surface acoustic waves," *Rep. Prog. Phys.*, vol. 68, pp. 1639–1701, 2005.

[22] C. Gorecki, F. Chollet, E. Bonnotte, and H. Kawakatsu, "Silicon-based integrated interferometer with phase modulation driven by surface acoustic waves," *Opt. Lett.*, vol. 22, no. 23, pp. 1784–1786, 1997.

[23] M. M. de Lima Jr., M. Beck, R. Hey, and P. V. Santos, "Compact Mach-Zehnder acousto-optic modulator," *Appl. Phys. Lett.*, vol. 89, p. 121104, 2006.

[24] M. Beck, M. M. de Lima Jr., and P. V. Santos, "Acousto-optical multiple interference devices," *J. Appl. Phys.*, vol. 103, p. 014505, 2008.

[25] P. De Heyn, *A compact optical frequency shifter using a multi-branch waveguide interferometer.* Master thesis, Department of Information Technology, Ghent University, 2009.

[26] U. Basu and A. K. Chopra, "Perfectly matched layers for time-harmonic elastodynamics of unbounded domains: theory and finite-element implementation," *Comput. Methods Appl. Mech. Eng.*, vol. 192, pp. 1337–1375, 2003.

[27] R. D. Cook, D. S. Malkus, M. E. Plesha, and R. S. Witt, *Concepts and applications of finite element analysis, 4th edition.* Wiley, New York, 2004.

[28] COMSOL Reference Manual for COMSOL 3.5, COMSOL AB, Stockholm, www.comsol.se.

[29] M. P. Bendsøe and N. Kikuchi, "Generating optimal topologies in structural design using a homogenization method," *Comput. Methods Appl. Mech. Engrg.*, vol. 71, pp. 197–224, 1988.

[30] M. P. Bendsøe and O. Sigmund, *Topology optimization, theory, methods and applications*. Springer, Berlin, 2003.

[31] H. L. Thomas, M. Zhou, and U. Schramm, "Issues of commercial optimization software development," *Struct. Multidiscip. Optim.*, vol. 23, pp. 97–110, 2002.

[32] A. R. Díaz and N. Kikuchi, "Solution to shape and topology eigenvalue optimization problems using a homogenization method," *Int. J. Numer. Mech. Eng.*, vol. 35, pp. 1487–1502, 1992.

[33] N. L. Pedersen, "Maximization of eigenvalues using topology optimization," *Struct. Multidisc. Optim.*, vol. 20, no. 1, pp. 2–11, 2000.

[34] J. B. Du and N. Olhoff, "Topological design of freely vibrating continuum structures for maximum values of simple and multiple eigenfrequencies and frequency gaps," *Struct. Multidisc. Optim.*, vol. 34, no. 2, pp. 91–110, 2007.

[35] Z. D. Ma, N. Kikuchi, and H. C. Chen, "Topological design for vibrating structures," *Comput. Methods Appl. Mech. Engrg.*, vol. 121, pp. 259–280, 1995.

[36] C. S. Jog, "Topology design of structures subjected to periodic loading," *J. Sound Vib.*, vol. 253, no. 3, pp. 687–709, 2002.

[37] J. B. Du and N. Olhoff, "Minimization of sound radiation from vibrating bimaterial structures using topology optimization," *Struct. Multidisc. Optim.*, vol. 33, no. 4-5, pp. 305–321, 2007.

[38] N. Olhoff and J. B. Du, "Topological design for minimum dynamic compliance of continuum structures subjected to forced vibration," *Struct. Multidisc. Optim.*, in press, 2009.

[39] O. Sigmund and J. S. Jensen, "Systematic design of phononic band-gap materials and structures by topology optimization," *Phil. Trans. R. Soc. Lond. A*, vol. 361, pp. 1001–1019, 2003.

[40] S. Halkjær, O. Sigmund, and J. S. Jensen, "Inverse design of phononic crystals by topology optimization," *Z. Kristallogr.*, vol. 220, no. 9-10, pp. 895–905, 2005.

[41] S. Halkjær, O. Sigmund, and J. S. Jensen, "Maximizing band gaps in plate structures," *Struct. Multidisc. Optim.*, vol. 32, no. 4, pp. 263–275, 2006.

[42] A. A. Larsen, B. Laksafoss, J. S. Jensen, and O. Sigmund, "Topological material layout in plates for vibration suppression and wave propagation control," *Struct. Multidisc. Optim.*, vol. 37, pp. 585–594, 2009.

[43] M. I. Hussein, K. Hamza, G. M. Hulbert, R. A. Scott, and K. Saitou, "Multiobjective evolutionary optimization of periodic layered materials for desired wave dispersion characteristics," *Struct. Multidisc. Optim.*, vol. 31, no. 1, pp. 60–75, 2006.

[44] J. S. Jensen, "Topology optimization problems for reflection and dissipation of elastic waves," *J. Sound Vib.*, vol. 301, no. 1-2, pp. 319–340, 2007.

[45] C. J. Rupp, A. Evgrafov, K. Maute, and M. L. Dunn, "Design of phononic materials/structures for surface wave devices using topology optimization," *Struct. Multidisc. Optim.*, vol. 34, pp. 111–121, 2007.

[46] E. Wadbro and M. Berggren, "Topology optimization of an acoustic horn," *Comput. Methods Appl. Mech. Engrg.*, vol. 196, no. 1-3, pp. 420–436, 2006.

[47] J. S. Jensen and O. Sigmund, "Systematic design of acoustic devices by topology optimization," in *Proc. of Twelfth International Congress on Sound and Vibration, Lisbon, Portugal*, 2005.

[48] D. Duhamel, "Shape optimization of noise barriers using genetic algorithms," *J. Sound Vib.*, vol. 297, pp. 432–443, 2006.

[49] G. H. Yoon, J. S. Jensen, and O. Sigmund, "Topology optimization of acoustic-structure interaction problems using a mixed finite element formulation," *Int. J. Numer. Meth. Engng.*, vol. 70, pp. 1049–1075, 2007.

[50] S. J. Cox and D. C. Dobson, "Maximizing band gaps in two-dimensional photonic crystals," *SIAM J. Appl. Math.*, vol. 59, no. 6, pp. 2108–2120, 1999.

[51] S. J. Cox and D. C. Dobson, "Band structure optimization of two-dimensional photonic crystals in H-polarization," *J. Computat. Phys.*, vol. 158, pp. 214–224, 2000.

[52] J. S. Jensen and O. Sigmund, "Systematic design of photonic crystal structures using topology optimization: Low-loss waveguide bends," *Appl. Phys. Lett.*, vol. 84, no. 12, pp. 2022–2024, 2004.

[53] J. S. Jensen and O. Sigmund, "Topology optimization of photonic crystal structures: a high-bandwidth low-loss T-junction waveguide," *J. Opt. Soc. Am. B*, vol. 22, no. 6, pp. 1191–1198, 2005.

[54] W. R. Frei, D. A. Tortorelli, and H. T. Johnson, "Topology optimization of a photonic crystal waveguide termination to maximize directional emission," *Appl. Phys. Lett.*, vol. 86, no. 11, p. 111114, 2005.

[55] Y. Tsuji, K. Hirayama, T. Nomura, K. Sato, and S. Nishiwaki, "Design of optical circuit devices based on topology optimization," *IEEE photonics Tehnol. Lett.*, vol. 18, no. 7, pp. 850–852, 2006.

[56] P. I. Borel, A. Harpøth, L. H. Frandsen, M. Kristensen, P. Shi, J. S. Jensen, and O. Sigmund, "Topology optimization and fabrication of photonic crystal structures," *Opt. Exp.*, vol. 12, no. 9, pp. 1996–2001, 2004.

[57] P. I. Borel, L. H. Frandsen, A. Harpøth, M. Kristensen, J. S. Jensen, and O. Sigmund, "Topology optimised broadband photonic crystal Y-splitter," *Electron. Lett.*, vol. 41, no. 2, pp. 69–71, 2005.

[58] N. Ikeda, Y. Sugimoto, Y. Watanabe, N. Ozaki, A. Mizutani, Y. Takata, J. S. Jensen, O. Sigmund, P. I. Borel, M. Kristensen, and K. Asakawa, "Topology optimised photonic crystal waveguide intersections with high-transmittance and low crosstalk," *Electron. Lett.*, vol. 42, no. 18, pp. 1031–1033, 2006.

[59] R. Stainko and O. Sigmund, "Tailoring dispersion properties of photonic crystal waveguides by topology optimization," *Waves in Random and Complex Media*, vol. 17, no. 4, pp. 477–489, 2007.

[60] J. Riishede and O. Sigmund, "Inverse design of dispersion compensating optical fiber using topology optimization," *J. Opt. Soc. Am. B*, vol. 25, no. 1, pp. 88–97, 2008.

[61] K. H. Sun, S. H. Cho, and Y. Y. Kim, "Design optimization of a magnetostrictive patch for maximizing elastic wave transduction in waveguides," *IEEE Trans. Magn.*, vol. 44, no. 10, pp. 2373–2380, 2008.

[62] J. Dahl, J. S. Jensen, and O. Sigmund, "Topology optimization for transient wave propagation problems in one dimension," *Struct. Multidisc. Optim.*, vol. 36, pp. 585–595, 2008.

[63] J. S. Jensen, "Space-time topology optimization for one-dimensional wave propagation," *Comput. Methods Appl. Mech. Engrg*, vol. 198, pp. 705–715, 2009.

[64] J. Jin, *The finite element method in electromagnetics, 2nd edition.* John Wiley & Sons Inc., Berlin, 2002.

[65] D. A. Tortorelli and P. Michaleris, "Design sensitivity analysis: Overview and review," *Inverse Problems in Science and Engineering*, vol. 1, no. 1, pp. 71–105, 1994.

[66] L. H. Olesen, F. Okkels, and H. Bruus, "A high-level programming-language implementation of topology optimization applied to steady-state navier-stokes flow," *Int. J. Numer. Meth. Engng*, vol. 65, pp. 975–1001, 2006.

[67] K. Svanberg, "The method of moving asymptotes - a new method for structural optimization," *Int. J. Numer. Meth. Engng*, vol. 24, pp. 359–373, 1987.

[68] O. Sigmund, "Morphology-based black and white filters for topology optimization," *Struct. Multidisc. Optim.*, vol. 33, pp. 401–424, 2007.

[69] D. N. May and M. M. Osman, "Highway noise barriers: new shapes," *J. Sound Vib.*, vol. 71, no. 1, pp. 73–101, 1980.

[70] D. A. Hutchins, H. W. Jones, and L. T. Russell, "Model studies of barrier performance in the presence of ground surfaces. Part II - Different shapes," *J. Acoust. Soc. Am.*, vol. 75, no. 6, pp. 1817–1826, 1984.

[71] D. C. Hothersall, S. N. Chancler-Wilde, and M. N. Hajmirzae, "Efficiency of single noise barriers," *J. Sound Vib.*, vol. 146, no. 2, pp. 303–322, 1991.

[72] K. Fujiwara, D. C. Hothersall, and C. Kim, "Noise barriers with reactive surfaces," *Applied Acoustics*, vol. 53, no. 4, pp. 255–272, 1998.

[73] A. Habbal, "Nonsmooth shape optimization applied to linear acoustics," *SIAM J. Optim.*, vol. 8, no. 4, pp. 989–1006, 1998.

[74] M. B. Dühring, "Topology optimization of acoustic problems," in *M.P. Bendsøe, N. Olhoff, O. Sigmund (Eds.), IUTAM Symposium on Topological Design Optimization of Structures, Machines and Materials: Status and Perspectives*, Springer, Netherlands, 2006.

[75] T. A. Birks, P. J. Roberts, P. S. J. Russell, D. M. Atkin, and T. J. Shepherd, "Full 2-D photonic bandgaps in silica/air structures," *Electron. Lett.*, vol. 31, no. 22, pp. 1941–1943, 1995.

[76] S. E. Barkou, J. Broeng, and A. Bjarklev, "Silica-air photonic crystal fiber design that permits waveguiding by a true photonic bandgap effect," *Opt. Lett.*, vol. 24, no. 1, pp. 46–48, 1999.

[77] D. Torres, O. Weisberg, G. Shapira, C. Anastassiou, B. Temelkuran, M. Shurgalin, S. A. Jacobs, R. U. Ahmad, T. Wang, U. Kolodny, S. M. Shapshay, Z. Wang, A. K. Devaiah, U. D. Upadhyay, and J. A. Koufman, "OmniGuide photonic bandgap fibers for flexible delivery of CO_2 laser energy for laryngeal and airway surgery," *Proc. of SPIE*, vol. 5686, pp. 310–321, 2005.

[78] P. J. Roberts, F. Couny, H. Sabert, B. J. Mangan, D. P. Williams, L. Farr, M. W. Mason, A. Tomlinson, T. A. Birks, J. C. Knight, and P. S. J. Russell, "Ultimate low loss of hollow-core photonic crystal fibres," *Opt. Exp.*, vol. 13, no. 1, pp. 236–244, 2005.

[79] J. Hu and C. R. Menyuk, "Use of fingers in the core to reduce leakage loss in air-core photonic bandgap fibers," in *Proc. of OFC/NFOEC*, 2007.

[80] T. Murao, K. Saitoh, and M. Koshiba, "Structural optimization of air-guiding photonic bandgap fibers for realizing ultimate low loss waveguides," *J. Lightwave tech.*, vol. 26, no. 12, pp. 1602–1612, 2008.

[81] V. Laude, H. Moubchir, L. Robert, W. Daniau, A. Khelif, and S. Ballandras, "Surface acoustic wave trapping in a periodic array of high aspect ratio electrodes," in *Proc. of 2006 IEEE Ultrasonics Symposium, Vancouver, British Columbia, Canada*, pp. 497–500, 2006.

[82] V. Laude, A. Khelif, T. Pastureaud, and S. Ballandras, "Generally polarized acoustic waves trapped by high aspect ratio electrode gratings at the surface of a piezoelectric material," *J. Appl. Phys.*, vol. 90, no. 5, pp. 2492–2497, 2001.

[83] V. Laude, L. Robert, W. Daniau, A. Khelif, and S. Ballandras, "Surface acoustic wave trapping in a periodic array of mechanical resonators," *Appl. Phys. Lett.*, vol. 89, p. 083515, 2006.

[84] D. B. Carstensen, T. A. Christensen, and M. Willatzen, "Surface Acoustic Wave (SAW) Generation in Wurtzite and Zincblende Piezoelectric Materials.," in *Proc. of the Nordic COMSOL Conference, Lyngby, Denmark*, 2006.

[85] D. B. Carstensen, T. A. Christensen, M. Willatzen, and P. V. Santos, "Modeling of gallium arsenide surface acoustic wave devices," *Electronic Journal, Technical Acoustics*, no. 19, pp. 1–13, 2007.

[86] M. Huang, "Stress effects on the performance of optical waveguides," *Int. J. Solids Struct.*, vol. 40, pp. 1615–1632, 2003.

[87] M. M. de Lima Jr., F. Alsina, W. Seidel, and P. Santos, "Focusing of surface-acoustic-wave fields on (100) GaAs surfaces," *J. Appl. Phys.*, vol. 94, no. 12, pp. 7848–7855, 2003.

[88] J. K. Guest, "Multiphase length scale control in topology optimization," in *Proceedings of the 8th World Congress of Structural and Multidisciplinary Optimization*, (Lisbon, Portugal), 2009.

[89] O. Sigmund, "Manufacturing tolerant topology optimization," *Struct. Multidisc. Optim.*, vol. 25, pp. 227–239, 2009.

Publication [P1]

Acoustic design by topology optimization

Available online at www.sciencedirect.com
ScienceDirect
Journal of Sound and Vibration 317 (2008) 557–575
JOURNAL OF SOUND AND VIBRATION
www.elsevier.com/locate/jsvi

Acoustic design by topology optimization

Maria B. Dühring*, Jakob S. Jensen, Ole Sigmund

Department of Mechanical Engineering, Technical University of Denmark, Nils Koppels Allé, Building 404, DK-2800 Kgs. Lyngby, Denmark

Received 6 November 2007; received in revised form 20 February 2008; accepted 26 March 2008
Handling Editor: C.L. Morfey
Available online 12 May 2008

Abstract

To bring down noise levels in human surroundings is an important issue and a method to reduce noise by means of topology optimization is presented here. The acoustic field is modeled by Helmholtz equation and the topology optimization method is based on continuous material interpolation functions in the density and bulk modulus. The objective function is the squared sound pressure amplitude. First, room acoustic problems are considered and it is shown that the sound level can be reduced in a certain part of the room by an optimized distribution of reflecting material in a design domain along the ceiling or by distribution of absorbing and reflecting material along the walls. We obtain well defined optimized designs for a single frequency or a frequency interval for both 2D and 3D problems when considering low frequencies. Second, it is shown that the method can be applied to design outdoor sound barriers in order to reduce the sound level in the shadow zone behind the barrier. A reduction of up to 10 dB for a single barrier and almost 30 dB when using two barriers are achieved compared to utilizing conventional sound barriers.

1. Introduction

This article describes how topology optimization can be applied to acoustic design either to reduce noise in a certain part of a room or to design sound barriers. The first type of problem has many interesting applications such as reducing engine noise in car cabins at the positions of the driver and the passengers, controlling the noise in industrial halls where people are working at certain locations among noisy machinery or to protect electronic equipment on which sound waves can have a damaging effect. Sound barriers are typically used to reduce traffic noise along roads.

A reduction of noise can be obtained by minimizing the sound pressure, the sound intensity or the reverberation time in the room and optimization can be done either by practical experiments or numerical calculations. One can choose to use active or passive methods. In active noise control the sound is canceled by using techniques from electroacoustics [1], and in passive noise control the optimal shape of the room is found or the noise is reduced by sound absorbers as porous materials, resonators or membrane absorbers [2]. This article is concerned with noise reduction using passive methods by optimized material distributions.

*Corresponding author. Tel.: +45 45254562; fax: +45 45931475.
E-mail address: mbd@mek.dtu.dk (M.B. Dühring).

0022-460X/$ - see front matter © 2008 Elsevier Ltd. All rights reserved.
doi:10.1016/j.jsv.2008.03.042

In Ref. [3] it is studied how the shape of a conference room is influencing the speech intelligibility for 10 different room shapes and with horizontal or sloping ceiling and floor. Distribution of absorbing material has been considered to control different acoustic properties in rooms. In Ref. [4] the speech intelligibility in a class room is improved by optimizing the distribution of a fixed amount of absorbing material. Another type of problem is considered in Ref. [5] where the positioning of absorbing material is used to improve the amplitude response from a loudspeaker in a room and in Ref. [6] the reverberation time is reduced using absorbing material. However, in all four cases a number of fixed configurations are compared—a systematic approach is to use an optimization algorithm. An example of such an approach is presented in Ref. [7] where the depths of a number of rectangular wells along a wall are optimized to improve the low frequency response in a room. Another example is found in Ref. [8] where noise is reduced by optimizing a part of a boundary with shape optimization. In these articles nonintuitive optimized shapes are found, but since only the boundaries can be changed it is not possible to obtain holes in the structure and parts which are not attached to the boundary.

A method that provides as much freedom in the optimized design as possible is topology optimization and it is therefore chosen for this work. This method was developed in the late eighties to find the maximum stiffness material distributions for structures [9]. Since then, the topology optimization method has successfully been applied to other engineering fields such as mechanisms and fluids (see e.g. Ref. [10] for an overview) as well as for wave propagation problems [11]. So far topology optimization has only been applied to a few problems in acoustics. In Refs. [12–14] results are presented for an inverse acoustic horn and an acoustic horn, respectively, and complicated designs are obtained with parts not attached to the boundary. In Refs. [15,16] it is shown how acoustic–structure interaction problems can be treated and in Ref. [17] radiation and scattering of sound from thin-bodies is optimized by genetic algorithms. Topology optimization has also been applied to minimize the sound power radiation from vibrating bi-material plate and pipe structures [18]. In Ref. [19] an example is shown where the shape of a reflection chamber is optimized to reflect waves, first for a single frequency and then for an entire frequency interval. The equation governing the wave propagation is the Helmholtz equation and in the article suitable interpolation functions are suggested to formulate the topology optimization problem. This model is used as the basis for the model in this paper.

The first part of the article describes the acoustic model governed by Helmholtz equation and associated boundary conditions. Design variables and material interpolation functions are introduced and the topology optimization problem is stated with the average of the squared sound pressure amplitude as the objective function and a volume constraint. The model is discretized and solved by the finite element method and the sensitivity analysis needed for the optimization algorithm is described. In the last part, applications of the proposed optimization algorithm are illustrated by three examples. The first problem is to find the optimal shape of a room. A rectangular room in 2 or 3D, bounded by rigid walls, and with a source emitting sinusoidal sound waves is considered. The task is to distribute material in a design domain along the ceiling such that the objective function is minimized in a certain part of the room. In the next example, the problem is changed such that an optimized distribution of reflecting and absorbing material along the walls is generated. In the final example we optimize the shape of outdoor sound barriers, a problem which has been widely studied using both experimental and numerical methods. In Refs. [20,21] experiments with scale models of barriers with various shapes were studied and it was observed that for rigid barriers the T-shaped barrier performed better than other shapes, but Y and arrow shaped barriers were performing almost as good. Also numerical results show the same tendency. In Refs. [22,23] the performance of barriers with different shapes is calculated by a boundary element method and again the T-shaped barrier performed the best. Finally a systematic way of designing barriers utilizing genetic algorithms was proposed in Ref. [24] where optimized designs are obtained which perform better than a straight and a T-shaped barrier for both low and high frequencies. The results obtained here using topology optimization are compared with the results for the low frequency case in Ref. [24] as well as with the straight and T-shaped barriers.

2. Topology optimization for acoustic problems

The problems studied in the first part of this article are of the type illustrated in Fig. 1. The aim is to distribute solid material in the ceiling in order to optimize room acoustics. The room is described by a domain Ω filled with air. The sound comes from a source which is vibrating with the vibrational velocity U such that

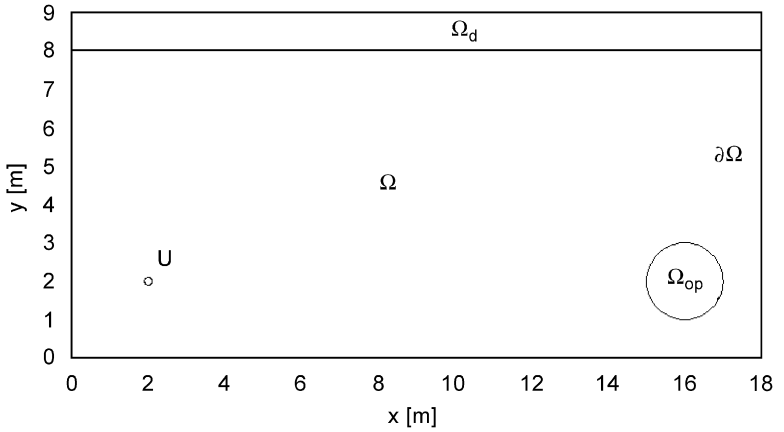

Fig. 1. Dimensions of the rectangular room in 2D with design domain Ω_d, output domain Ω_{op} and a point source with the vibrational velocity U.

sinusoidal sound waves are emitted. In the output domain Ω_{op} the average of the squared sound pressure amplitude is minimized in order to reduce the noise in this area. The minimization is done by finding a proper distribution of air and solid material (scatterer) in the ceiling area (design domain Ω_d).

2.1. The acoustic model

The governing equation of steady-state linear acoustic problems with sinusoidal sound waves of angular frequency ω is the Helmholtz equation [2]

$$\nabla \cdot (\rho^{-1} \nabla \hat{p}) + \omega^2 \kappa^{-1} \hat{p} = 0. \tag{1}$$

The physical sound pressure p is the real part of $\hat{p}$ where $\hat{p}$ appearing in Eq. (1) is the complex sound pressure amplitude which depends on the position $\mathbf{r}$. ρ is the density and κ is the bulk modulus of the acoustic medium and they also depend on $\mathbf{r}$. The design freedom is the pointwise distribution of air and solid material i.e. $\rho = \rho(\mathbf{r})$ and $\kappa = \kappa(\mathbf{r})$ where $\mathbf{r} \in \Omega_d$. For air the material properties are $(\rho, \kappa) = (\rho_1, \kappa_1)$ and for the solid material $(\rho, \kappa) = (\rho_2, \kappa_2)$. The material values used are $\rho_1 = 1.204\,\mathrm{kg\,m^{-3}}$ and $\kappa_1 = 141.921 \times 10^3\,\mathrm{N\,m^{-2}}$ for air and $\rho_2 = 2643.0\,\mathrm{kg\,m^{-3}}$ and $\kappa_2 = 6.87 \times 10^{10}\,\mathrm{N\,m^{-2}}$ for solid material (aluminum). It is convenient to introduce the two nondimensional variables $\tilde{\rho}$ and $\tilde{\kappa}$ defined as

$$\tilde{\rho} = \frac{\rho}{\rho_1} = \begin{cases} 1 & \text{air,} \\ \dfrac{\rho_2}{\rho_1} & \text{solid,} \end{cases} \quad \tilde{\kappa} = \frac{\kappa}{\kappa_1} = \begin{cases} 1 & \text{air,} \\ \dfrac{\kappa_2}{\kappa_1}, & \text{solid.} \end{cases} \tag{2}$$

When Eq. (1) is rescaled with these variables the Helmholtz equation takes the form

$$\nabla \cdot (\tilde{\rho}^{-1} \nabla \hat{p}) + \tilde{\omega}^2 \tilde{\kappa}^{-1} \hat{p} = 0. \tag{3}$$

Here $\tilde{\omega} = \omega / c$ is a scaled angular frequency and $c = \sqrt{\kappa_1 / \rho_1}$ is the speed of sound in air. Finally, two types of boundary conditions are employed

$$\mathbf{n} \cdot (\tilde{\rho}^{-1} \nabla \hat{p}) = 0, \quad \mathbf{n} \cdot (\tilde{\rho}^{-1} \nabla \hat{p}) = -\mathrm{i}\tilde{\omega} U \sqrt{\kappa_1 \rho_1}, \tag{4}$$

where $\mathbf{n}$ is the normal unit vector pointing out of the domain. The first boundary condition describes a perfectly reflecting surface and is employed for the rigid walls of the room. The second boundary condition expresses a vibrating surface with the vibrational velocity U and is used to imitate a near point source emitting sinusoidal sound waves.

2.2. Design variables and material interpolation

The problem of finding the optimal distribution of material is a discrete optimization problem (there should be air or solid material in each point of the design domain), but in order to allow for efficient gradient-based optimization the problem is formulated with continuous material properties that can take any value in between the values for air and solid material. To control the material properties a continuous material indicator field $0 \leqslant \xi(\mathbf{r}) \leqslant 1$ is introduced, where $\xi = 0$ corresponds to air and $\xi = 1$ to solid material:

$$\tilde{\rho}(\xi) = \begin{cases} 1 & \xi = 0, \\ \dfrac{\rho_2}{\rho_1} & \xi = 1, \end{cases} \quad \tilde{\kappa}(\xi) = \begin{cases} 1 & \xi = 0, \\ \dfrac{\kappa_2}{\kappa_1} & \xi = 1. \end{cases} \tag{5}$$

Although ξ is continuous the final design should be as close to discrete ($\xi = 0$ or 1) as possible in order to be well defined. The choice of interpolation functions may aid in avoiding intermediate (gray) material properties in the final design. In Ref. [19] it is suggested to find the interpolation function by looking at a 1D acoustic system where a wave with amplitude of unit magnitude propagates in air and hits an interface to an acoustic medium under normal incidence. Experience shows that good 0–1 designs in general can be obtained if the reflection from the acoustic medium in this system is a smooth function of ξ with nonvanishing slope at $\xi = 1$. This is obtained by interpolating the inverse density and bulk modulus between the two material phases as follows:

$$\tilde{\rho}(\xi)^{-1} = 1 + \xi\left(\left(\frac{\rho_2}{\rho_1}\right)^{-1} - 1\right), \tag{6}$$

$$\tilde{\kappa}(\xi)^{-1} = 1 + \xi\left(\left(\frac{\kappa_2}{\kappa_1}\right)^{-1} - 1\right), \tag{7}$$

which clearly fulfills the discrete values specified in Eq. (5).

2.3. The optimization problem

The purpose of the topology optimization is to minimize the objective function Φ which is the average of the squared sound pressure amplitude in the output domain, Ω_{op}. The formulation of the optimization problem takes the form

$$\min_{\xi} \log(\Phi) = \log\left(\frac{1}{\int_{\Omega_{\text{op}}} \mathrm{d}\mathbf{r}} \int_{\Omega_{\text{op}}} |\hat{p}(\mathbf{r}, \xi(\mathbf{r}))|^2 \mathrm{d}\mathbf{r}\right) \quad \text{objective function,} \tag{8}$$

$$\text{subject to} \quad \frac{1}{\int_{\Omega_d} \mathrm{d}\mathbf{r}} \int_{\Omega_d} \xi(\mathbf{r})\,\mathrm{d}\mathbf{r} - \beta \leqslant 0, \quad \text{volume constraint,} \tag{9}$$

$$0 \leqslant \xi(\mathbf{r}) \leqslant 1 \quad \forall\, \mathbf{r} \in \Omega_d, \quad \text{design variable bounds.} \tag{10}$$

A volume constraint is included to put a limit on the amount of material distributed in the design domain Ω_d in order to save weight and cost. Here β is a volume fraction of allowable material and takes values between 0 and 1, where $\beta = 1$ corresponds to no limit. To obtain better numerical scaling the logarithm is taken to the objective function.

2.4. Discretization and sensitivity analysis

The mathematical model of the physical problem is given by the Helmholtz equation (3) and the boundary conditions (4), and to solve the problem, finite element analysis is used. The complex amplitude field $\hat{p}$ and the design variable field ξ are discretized using sets of finite element basis functions $\{\phi_{i,n}(\mathbf{r})\}$

$$\hat{p}(\mathbf{r}) = \sum_{n=1}^{N} \hat{p}_n \phi_{1,n}(\mathbf{r}), \quad \xi(\mathbf{r}) = \sum_{n=1}^{N_d} \xi_n \phi_{2,n}(\mathbf{r}). \tag{11}$$

The degrees of freedom (dofs) corresponding to the two fields are assembled in the vectors $\hat{\mathbf{p}} = \{\hat{p}_1, \hat{p}_2, \ldots, \hat{p}_N\}^{\mathrm{T}}$ and $\boldsymbol{\xi} = \{\xi_1, \xi_2, \ldots, \xi_{N_d}\}^{\mathrm{T}}$. For the model in 2D a triangular element mesh is employed and tetrahedral elements are used in 3D. Quadratic Lagrange elements are used for the complex pressure amplitude $\hat{p}$ to obtain high accuracy in the solution and for the design variable ξ linear Lagrange elements are utilized.

The commercial program Comsol Multiphysics with Matlab [25] is employed for the finite element analysis. This results in the discretized equation

$$\mathbf{S}\hat{\mathbf{p}} = \mathbf{f}, \tag{12}$$

where $\mathbf{S}$ is the system matrix and $\mathbf{f}$ is the load vector which are both complex valued.

To update the design variables in the optimization algorithm the derivatives with respect to the design variables of the objective and the constraint function must be evaluated. This is possible as the design variable is introduced as a continuous field. The complex sound pressure vector $\hat{\mathbf{p}}$ is via Eq. (12) an implicit function of the design variables, which is written as $\hat{\mathbf{p}}(\boldsymbol{\xi}) = \hat{\mathbf{p}}_R(\boldsymbol{\xi}) + \mathrm{i}\hat{\mathbf{p}}_I(\boldsymbol{\xi})$, where $\hat{\mathbf{p}}_R$ and $\hat{\mathbf{p}}_I$ denote the real and the imaginary part of $\hat{\mathbf{p}}$. Thus the derivative of the objective function $\Phi = \Phi(\hat{\mathbf{p}}_R(\boldsymbol{\xi}), \hat{\mathbf{p}}_I(\boldsymbol{\xi}), \boldsymbol{\xi})$ is given by the following expression found by the chain rule

$$\frac{\mathrm{d}\Phi}{\mathrm{d}\boldsymbol{\xi}} = \frac{\partial\Phi}{\partial\boldsymbol{\xi}} + \frac{\partial\Phi}{\partial\hat{\mathbf{p}}_R}\frac{\partial\hat{\mathbf{p}}_R}{\partial\boldsymbol{\xi}} + \frac{\partial\Phi}{\partial\hat{\mathbf{p}}_I}\frac{\partial\hat{\mathbf{p}}_I}{\partial\boldsymbol{\xi}}. \tag{13}$$

As $\hat{\mathbf{p}}$ is an implicit function of $\boldsymbol{\xi}$ the derivatives $\partial\hat{\mathbf{p}}_R/\partial\boldsymbol{\xi}$ and $\partial\hat{\mathbf{p}}_I/\partial\boldsymbol{\xi}$ are not known directly. The sensitivity analysis is therefore done by employing an adjoint method where the unknown derivatives are eliminated at the expense of determining an adjoint and complex variable field $\boldsymbol{\lambda}$ from the adjoint equation

$$\mathbf{S}^{\mathrm{T}}\boldsymbol{\lambda} = -\left(\frac{\partial\Phi}{\partial\hat{\mathbf{p}}_R} - \mathrm{i}\frac{\partial\Phi}{\partial\hat{\mathbf{p}}_I}\right)^{\mathrm{T}}, \tag{14}$$

where

$$\frac{\partial\Phi}{\partial\hat{\mathbf{p}}_R} - \mathrm{i}\frac{\partial\Phi}{\partial\hat{\mathbf{p}}_I} = \frac{1}{\int_{\Omega_{\mathrm{op}}}\mathrm{d}\mathbf{r}}\int_{\Omega_{\mathrm{op}}}(2\hat{p}_R - \mathrm{i}2\hat{p}_I)\phi_{1,n}\,\mathrm{d}\mathbf{r}. \tag{15}$$

The sensitivity analysis follows the standard adjoint sensitivity approach [26]. For further details of the adjoint sensitivity method applied to wave propagation problems, the reader is referred to Ref. [27]. Eq. (13) for the derivative of the objective function then reduces to

$$\frac{\mathrm{d}\Phi}{\mathrm{d}\boldsymbol{\xi}} = \frac{\partial\Phi}{\partial\boldsymbol{\xi}} + \mathrm{Re}\left(\boldsymbol{\lambda}^{\mathrm{T}}\frac{\partial\mathbf{S}}{\partial\boldsymbol{\xi}}\hat{\mathbf{p}}\right). \tag{16}$$

Finally, the derivative of the constraint function with respect to one of the design variables is

$$\frac{\partial}{\partial\xi_n}\left(\frac{1}{\int_{\Omega_d}\mathrm{d}\mathbf{r}}\int_{\Omega_d}\xi(\mathbf{r})\,\mathrm{d}\mathbf{r} - \beta\right) = \frac{1}{\int_{\Omega_d}\mathrm{d}\mathbf{r}}\int_{\Omega_d}\phi_{2,n}(\mathbf{r})\,\mathrm{d}\mathbf{r}. \tag{17}$$

The vectors $\partial\Phi/\partial\boldsymbol{\xi}$, $\int_{\Omega_{\mathrm{op}}}(2\hat{p}_R - \mathrm{i}2\hat{p}_I)\phi_{1,n}\,\mathrm{d}\mathbf{r}$ and $\int_{\Omega_d}\phi_{2,n}(\mathbf{r})\,\mathrm{d}\mathbf{r}$ as well as the matrix $\partial\mathbf{S}/\partial\boldsymbol{\xi}$ are assembled in Comsol Multiphysics as described in Eq. [28].

2.5. Practical implementation

The optimization problem (8)–(10) is solved using the Method of Moving Asymptotes, MMA [29] which is an algorithm that uses information from the previous iteration steps and gradient information. To fulfill the volume constraint from the first iteration of the optimization procedure the initial design is usually chosen as a uniform distribution of material with the volume fraction β. It should be emphasized that the final design depends both on the initial design and the allowable amount of material to be placed and is therefore dependent on β. Here the best solutions out of several tries will be presented. To make the model more realistic and to minimize local resonance effects a small amount of mass-proportional damping is added.

When the mesh size is decreased the optimization will in general result in mesh-dependent solutions with small details which make the design inconvenient to manufacture. To avoid these problems a morphology-based filter is employed. Such filters make the material properties of an element depend on a function of the design variables in a fixed neighborhood around the element such that the finite design is mesh-independent. Here a close-type morphology-based filter is chosen [30], which has proven efficient for wave-propagation type topology optimization problems. The method results in designs where all holes below the size of the filter (radius $r_{\min}$) have been eliminated. A further advantage of these filter-types is that they help eliminating gray elements in the transition zone between solid and air regions.

3. Results

In this section results are presented for rooms in 2D and 3D as well as for outdoor sound barriers in 2D.

3.1. Optimization of a rectangular room in 2D

The average of the squared sound pressure amplitude is minimized in the output domain Ω_{op} by distributing material in the design domain Ω_d in the rectangular room as shown in Fig. 1. The maximum volume fraction is chosen to $\beta = 0.15$ and the initial design for the optimal design is a uniform distribution of 15% material in the design domain. The vibrational velocity of the pulsating circle is $U = 0.01\,\text{m}\,\text{s}^{-1}$ and the target frequency is $f = 34.56\,\text{Hz}$, $f = \omega/2\pi$, which is a natural frequency for the room with the initial material distribution. The modeling domain is discretized by triangular elements with maximum side length $h_{\max} = 0.3\,\text{m}$ and the filter radius is $r_{\min} = 1.0h_{\max}$. An absolute tolerance of 0.01 on the maximum change of the design variables is used to terminate the optimization loop. The optimized design was found in 281 iterations and the objective function was reduced from 110.9 to 76.1 dB. Fig. 2 shows the optimized design as well as the sound pressure amplitude for the initial and optimized designs. It is clearly seen that in comparison to the initial design the redistributed material in the design domain is influencing the sound pressure in the room such that it has a very low value in the output domain Ω_{op} with a nodal line going through it. The material is placed at the nodal lines for the initial design which is an observation that will be elaborated on later. On the top right of Fig. 2 the frequency response for the initial design and the optimized design are shown, where Φ is plotted as function of the frequency f. In comparison to the initial design, the natural frequencies for the optimized design have changed and the natural frequency, which was equal to the driving frequency for the initial design, has been moved to a lower value. It is noted that the solid material forms small cavities and that there is a tendency for the sound pressure amplitude to be higher in these cavities than outside them. The cavities resemble Helmholtz resonators (see Ref. [2] for a description of a Helmholtz resonator). It should be noted, that even though the filter is used and the value of $r_{\min}$ is varied it is difficult to obtain fully mesh-independent solutions due to many local minima.

In the previous example a low frequency has been used to obtain an optimized design. In the next example the room is optimized for the frequency $f = 4 \times 34.56\,\text{Hz}$, and the quantities $\beta = 0.5$, $h_{\max} = 0.2\,\text{m}$, and $r_{\min} = 1.0h_{\max}$. The optimized design is seen in Fig. 3 where the objective function is decreased from 95.7 to 62.1 dB in 478 iterations. Compared to the design for the lower frequency the design is now a complicated structure with many small features. The reason is that for increasing frequencies the distribution of the sound pressure amplitude in the room gets more complex and the design needed to minimize the objective function will naturally also consist of more complicated details. For higher frequencies well defined designs can still be obtained, but it is hard to get a mesh-independent design as it is very sensitive to discretization, filtering radius, starting guess as well as local minima.

In the next example the optimization is done for $f = 9.39$ and $9.71\,\text{Hz}$ which is less and higher, respectively, than the first natural frequency $9.55\,\text{Hz}$ for the room with the initial design with $\beta = 0.15$. The corresponding mode shape has a vertical nodal line in the middle of the room and high sound pressure amplitude along the walls. The quantities used in both cases are $h_{\max} = 0.3\,\text{m}$ and $r_{\min} = 0.75h_{\max}$. The optimized designs and the corresponding frequency response are seen in Fig. 4. For the case with $f = 9.39\,\text{Hz}$ the solid material is distributed at the corners with the high pressure amplitude and the natural frequency is moved to a higher frequency. However, in the case with $f = 9.71\,\text{Hz}$ the material is placed at the nodal plane in the middle of the

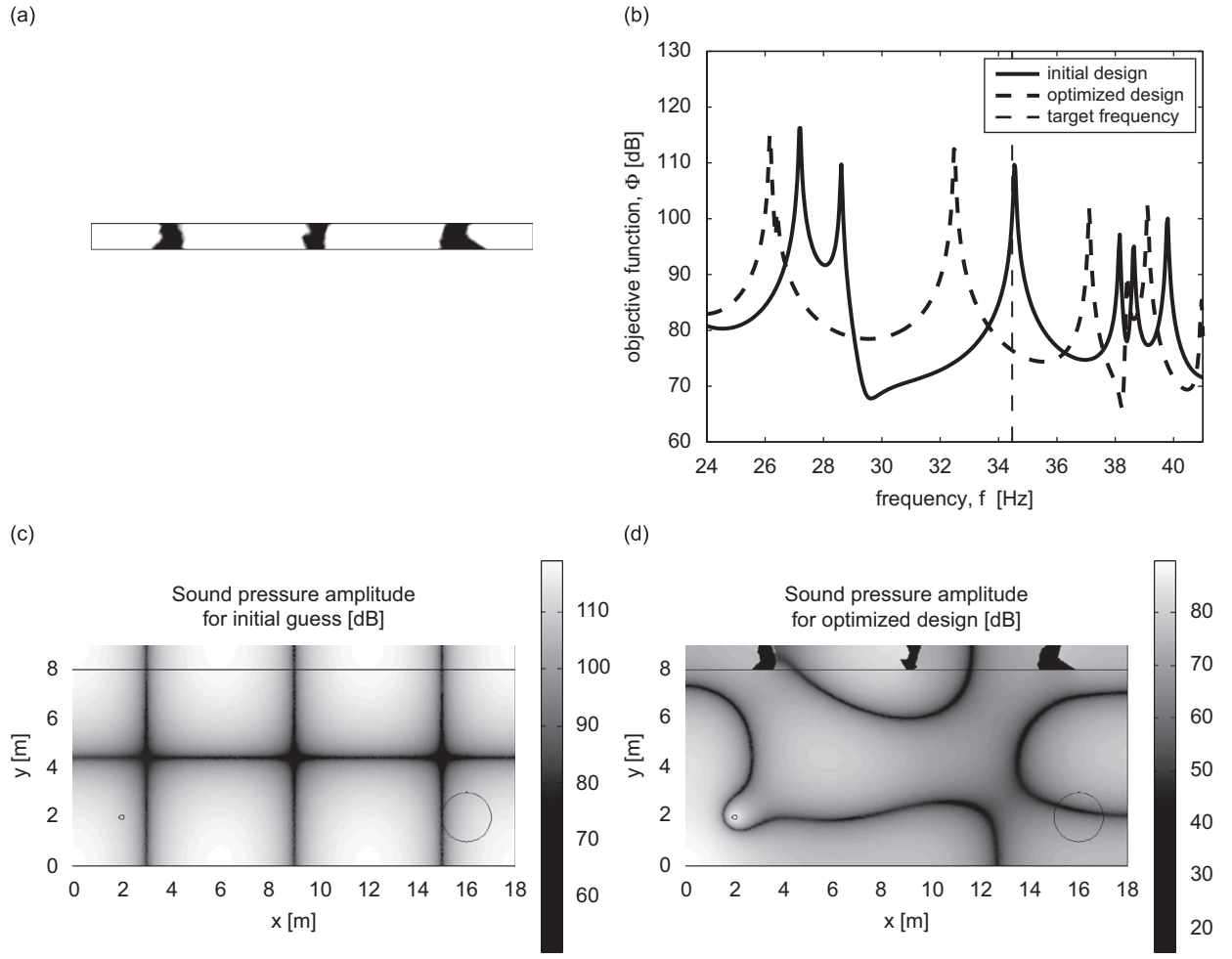

Fig. 2. (a) The optimized ceiling design for target frequency 34.56 Hz; (b) frequency plot for initial and optimized designs; (c) the sound pressure amplitude for initial design; and (d) the sound pressure amplitude for optimized design.

Fig. 3. Optimized design for the rectangular room for the higher target frequency $f = 4 \times 34.56$ Hz.

design domain and the natural frequency is now at a lower value than originally. The same tendency is observed for the example in Fig. 2 where the material is distributed at the nodal lines and the natural frequency is moved to a lower value. The response at the two target frequencies $f = 9.39$ and $f = 9.71$ Hz for both designs, are given in Table 1 and it is noticed that the objective function is minimized most for both frequencies in the case where the solid material is placed at the nodal plane. So for the target frequency which is smaller than the natural frequency the optimization converges to a solution that is not as good as when the other target frequency is used. The explanation is that a natural frequency, which is originally at one side of the driving frequency, can only be moved to a value on the same side during the optimization, else the objective function would have to be increased during a part of the optimization. It is from this example and the example from Fig. 2 concluded, that when optimizing for a driving frequency close to a natural frequency there is a tendency for the material to be distributed at the nodal planes for the initial design when the natural frequency is moved to a lower value. If the natural frequency is moved to a higher value the material is

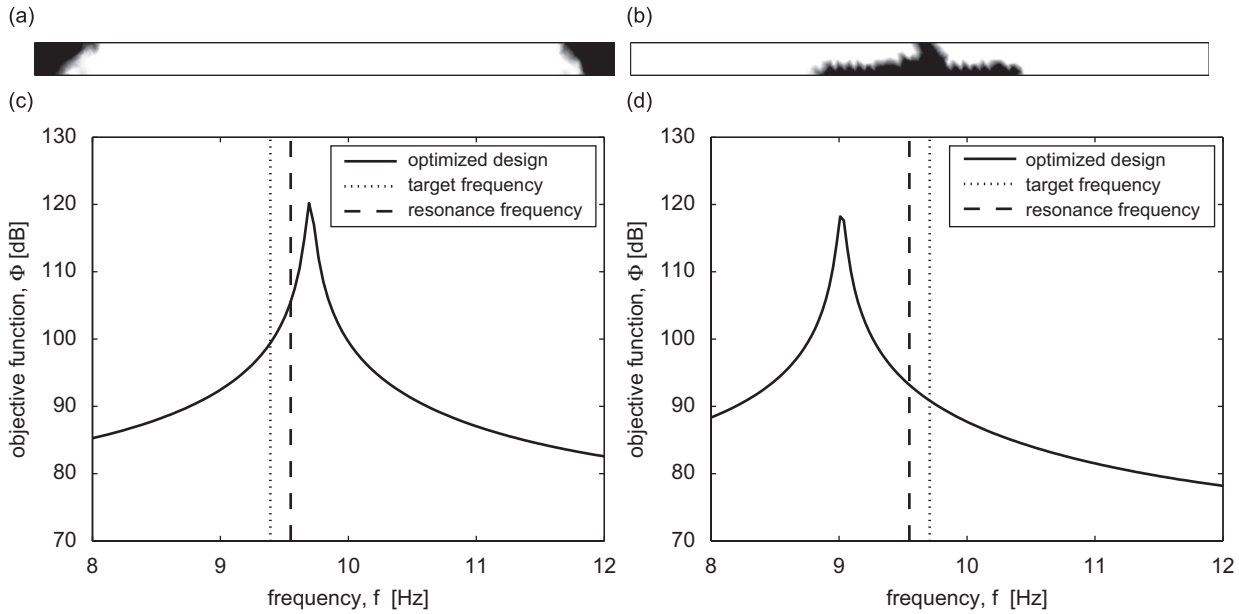

Fig. 4. Optimized design and frequency response after the optimization for two frequencies close to the natural frequency $f = 9.55$ Hz for the room with the initial design: (a) optimized design for $f = 9.39$ Hz; (b) optimized design for $f = 9.71$ Hz; (c) frequency response for the optimized design for $f = 9.39$ Hz; and (d) frequency response for the optimized design for $f = 9.71$ Hz.

Table 1
The value of the objective function for the two frequencies 9.39 and 9.71 Hz for the two designs from Fig. 4

Frequency f (Hz)	Φ for optimized design for $f = 9.39$ Hz (dB)	Φ for optimized design for $f = 9.71$ Hz (dB)
9.39	99.7	96.4
9.71	120.1	90.8

distributed at the high sound pressure amplitudes. The intuitive explanation of this phenomenon is that if a natural frequency has to be decreased it must be made possible for the room to resonate at a lower frequency. Thus the material from the high pressure amplitudes is moved to the nodal planes. If instead the natural frequency has to be increased the system has to be made stiffer at the critical places. In this case the material is removed from the nodal planes and distributed at the high pressure amplitudes. It is difficult to say in general if one of these designs is best for all the frequencies close to the natural frequency and it looks like it depends on how far away the natural frequency can be moved in one of the directions from the considered frequencies. Similar effects have been observed for design of plates subjected to forced vibration [31].

The optimization problem is now changed such that the optimization can be done for an entire frequency interval. The objective is to minimize the sum of responses for a number of target frequencies ω_i in the interval considered as in Eq. [27]. The chosen interval is divided into M equally sized subintervals and the target frequency in each subinterval, which results in the highest value of Φ, is determined. The room is then optimized for the new objective function Ψ which is the sum of Φ evaluated at the determined target frequencies and divided by the number of intervals M to get the average value

$$\min_{\xi} \quad \Psi = \frac{\sum_{\omega_1,\ldots,\omega_M} \max_{\omega_i \in I_i}(\Phi(\omega_i))}{M}, \quad I_1 = [\omega_1; \omega_2[, \ldots, I_M =]\omega_M; \omega_{M+1}]. \tag{18}$$

Here $\omega_{M+1} - \omega_1$ is the entire frequency interval and I_i are the equally sized subintervals. By this optimization procedure Φ is minimized at all the target frequencies and these are updated at regular intervals during the

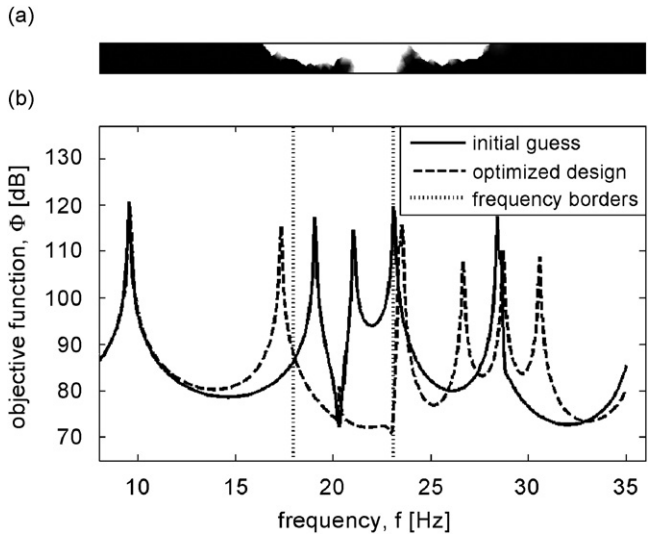

Fig. 5. (a) The optimized design for the frequency interval [18;23] Hz and (b) the frequency response for the initial design and the optimized design.

optimization by approximating the objective function Φ as function of the frequency using Padé expansions, see Ref. [32]. The room from Fig. 1 is then optimized for the frequency interval [18;23] Hz using five target frequencies where the target frequencies are updated every 25th iteration step. The quantities used in the optimization are $\beta = 0.85$, $h_{\max} = 0.3$ m and $r_{\min} = 1.5h_{\max}$. The optimized design obtained after 415 iterations is illustrated in Fig. 5 together with the response curve for the initial design and the optimized design. The objective function is reduced from 111.2 to 75.7 dB. It is seen from the two response curves that the objective function is minimized in the entire interval for the optimized design. Two of the high peaks have been moved out of the interval and the last one has been significantly reduced. The solid material in the optimized design is distributed such that a kind of Helmholtz resonator is formed.

3.2. Optimization of a rectangular room in 3D

The optimization problem is now extended to 3D problems and a rectangular room with the geometry shown in Fig. 6 is considered. We optimize two examples for intervals around the first natural frequency $f = 42.92$ Hz for the room with a vertical nodal plane at $x = 2$ m and high sound pressure amplitude at the end walls at $x = 0$ and 4 m. The quantities used are $\beta = 0.5$, $h_{\max} = 0.4$ m and $r_{\min} = 0.5h_{\max}$ and the target frequencies are updated for each 15 iterations. For the first example the optimization is done for the interval [41.5;44.5] Hz and one target frequency. After 252 iterations the objective function Ψ is reduced from 115.2 to 81.6 dB. The optimized design and the response for the initial design and the optimized design are seen in Fig. 7. It is observed that the solid material is distributed at the walls with high sound pressure amplitude and that the natural frequency has been moved to a higher value outside the interval. For the next example the frequency interval is extended to [40.5;45.5] Hz and four target frequencies are used. Ψ is minimized from 96.6 to 46.9 dB in 218 iterations and the results are illustrated in Fig. 8. In this case most of the solid material is distributed at the nodal plane around $x = 2$ m rather than at the two shorter walls opposite to the previous example. From the response curve in Fig. 8 it is seen that the first natural frequency is not contained in the interval after the optimization and instead a natural frequency has appeared at a lower value. These two examples show that if the frequency interval is slightly changed, the optimization can converge to two very different, in fact opposite designs. The optimized designs here depend on what side of the interval the first natural frequency is moved to after the optimization. The best design in this case is the design where the solid material is placed at low pressure amplitude for the initial design. The two examples here can thus be interpreted as an extension to 3D of the examples in Fig. 4.

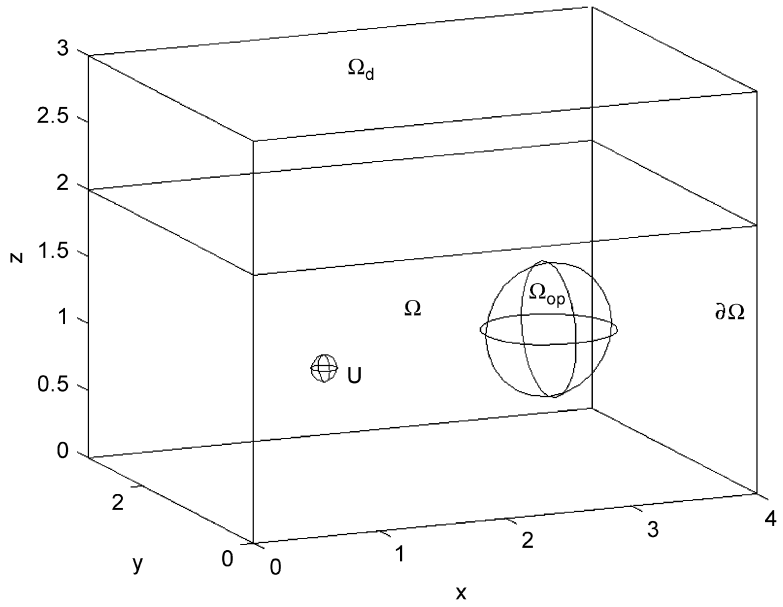

Fig. 6. The dimensions of the rectangular room in 3D with the design domain Ω_d, the output domain Ω_{op} and the point source with the vibrational velocity U.

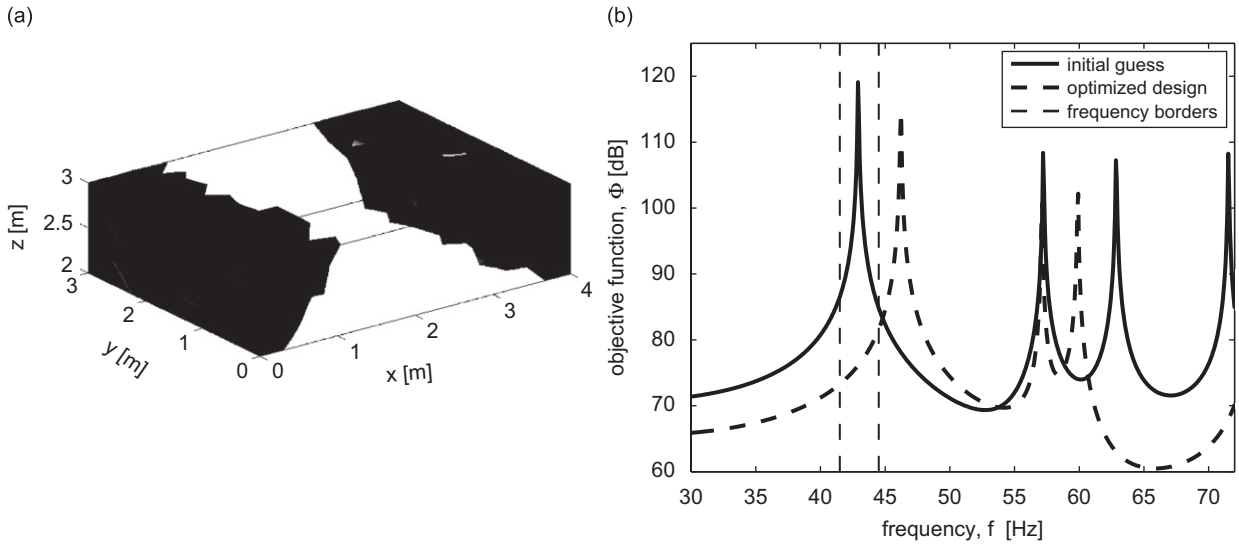

Fig. 7. Results of the optimization for the frequency interval [41.5;44.5] Hz with one target frequency: (a) the optimized design and (b) the frequency response for the initial design and the optimized design.

3.3. Distribution of absorbing and reflecting material along the walls

An alternative way of reducing noise in a room is to use absorbing material along the walls. This type of design will in general be easier to manufacture and install compared to placing solid material and therefore also cheaper. For this reason the optimization problem is now changed such that the goal is to find the distribution of absorbing and reflecting material along the boundaries of a room which minimizes the objective function. The problem is similar to the previous one, but there are some differences. The degrees of freedom describing the boundary conditions are used as design variables and the sound field is now governed

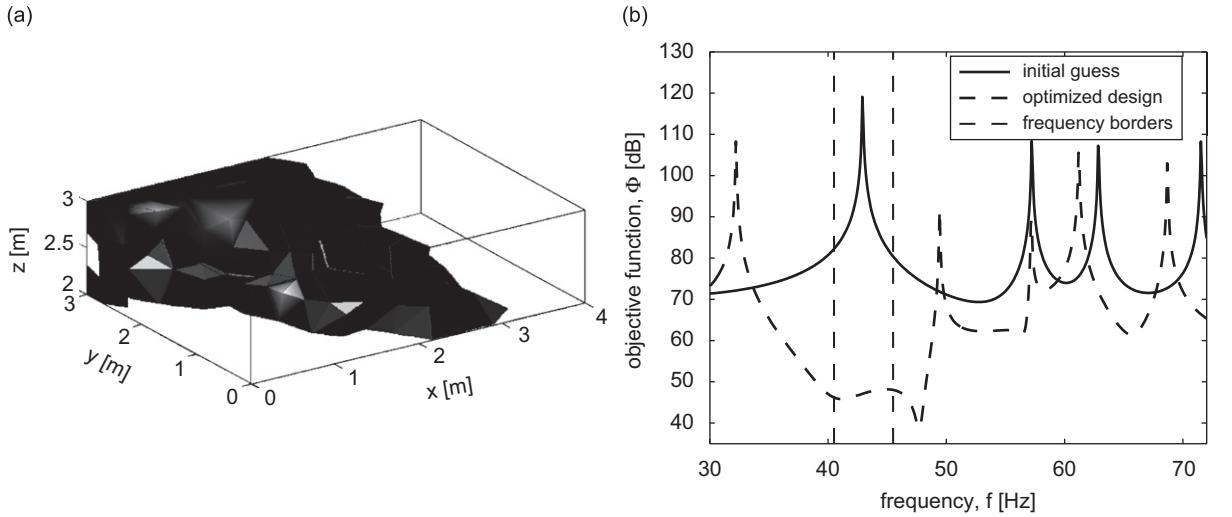

Fig. 8. Results of the optimization for the frequency interval [40.5;45.5] Hz with four target frequencies: (a) the optimized design and (b) the frequency response for the initial design and the optimized design.

by Helmholtz equation for a homogeneous medium. The material properties for air in the room are ρ_a and κ_a and it is assumed that there is no damping effect in the air. The material on the boundaries is inhomogeneous and the optimized design is a distribution of the usual reflecting material described by ρ_2 and κ_2 and an absorbing material with the properties $\rho_1 = 3.04\,\mathrm{kg\,m^{-3}}$ and $\kappa_1 = 7.90 \times 10^5\,\mathrm{N\,m^{-2}}$. The absorbing material has an absorption coefficient equal to 0.1 which could be realized in practice by a cork sheet with the thickness of a few millimeters. It is then convenient to use the new variables

$$\tilde{\rho} = \frac{\rho}{\rho_a} = \begin{cases} \dfrac{\rho_1}{\rho_a} & \text{absorbing,} \\ \dfrac{\rho_2}{\rho_a} & \text{reflecting,} \end{cases} \qquad \tilde{\kappa} = \frac{\kappa}{\kappa_a} = \begin{cases} \dfrac{\kappa_1}{\kappa_a} & \text{absorbing,} \\ \dfrac{\kappa_2}{\kappa_a} & \text{reflecting.} \end{cases} \tag{19}$$

With this rescaling the acoustic model for the problem takes the form

$$\nabla^2 \hat{p} + \tilde{\omega}^2 \hat{p} = 0 \quad \text{Helmholtz equation,} \tag{20}$$

$$-\mathbf{n} \cdot \nabla \hat{p} = \frac{\mathrm{i}\tilde{\omega}\sqrt{\kappa_a \rho_a}}{Z(\mathbf{r})} \hat{p}, \quad \text{b.c. for surface with impedance } Z \tag{21}$$

$$-\mathbf{n} \cdot \nabla \hat{p} = \mathrm{i}\tilde{\omega}\sqrt{\kappa_a \rho_a}\, U, \quad \text{b.c. for pulsating surface.} \tag{22}$$

The inhomogeneities on the walls are described in the boundary condition (21) by the impedance boundary $Z(\mathbf{r}) = \rho_a c_a \sqrt{\tilde{\kappa}(\mathbf{r})\tilde{\rho}(\mathbf{r})}$. The impedance boundary condition is only strictly valid for plane waves of normal incidence but is used for simplicity in this work. The material interpolation functions for $\tilde{\rho}(\xi)$ and $\tilde{\kappa}(\xi)$ must now satisfy the requirements

$$\tilde{\rho}(\xi) = \begin{cases} \dfrac{\rho_1}{\rho_a} & \xi = 0, \\ \dfrac{\rho_2}{\rho_a} & \xi = 1, \end{cases} \qquad \tilde{\kappa}(\xi) = \begin{cases} \dfrac{\kappa_1}{\kappa_a}, & \xi = 0, \\ \dfrac{\kappa_2}{\kappa_a}, & \xi = 1, \end{cases} \tag{23}$$

and again interpolation functions in the inverse material properties are used

$$\tilde{\rho}(\xi)^{-1} = \left(\frac{\rho_1}{\rho_a}\right)^{-1} + \xi\left(\left(\frac{\rho_2}{\rho_a}\right)^{-1} - \left(\frac{\rho_1}{\rho_a}\right)^{-1}\right), \tag{24}$$

$$\tilde{\kappa}(\xi)^{-1} = \left(\frac{\kappa_1}{\kappa_a}\right)^{-1} + \xi\left(\left(\frac{\kappa_2}{\kappa_a}\right)^{-1} - \left(\frac{\kappa_1}{\kappa_a}\right)^{-1}\right). \tag{25}$$

The optimization problem has the same form as Eqs. (8)–(10), except that an area constraint is used instead of a volume constraint

$$-\frac{1}{\int_{\Omega_d} \mathrm{d}\mathbf{r}} \int_{\Omega_d} \xi(\mathbf{r})\,\mathrm{d}\mathbf{r} + \beta \leqslant 0, \tag{26}$$

where the amount of reflecting material must be at least the fraction β.

3.3.1. Results for 2D and 3D problems

Calculations have shown that when optimizing for a single frequency the absorbing material is in general placed where the sound pressure amplitude is highest, as one would expect. However, when optimizing for a frequency interval it gets more difficult to predict the design intuitively and in this case it is necessary to use topology optimization to get an optimized solution. In the following example the room in 2D is optimized for the frequency interval [38;43] Hz with seven target frequencies. The quantities used are $\beta = 0.5$, $h_{\max} = 0.3$ m, $r_{\min} = 0.5h_{\max}$ and the number of iterations between the updates of the target frequencies is 20. The optimized design and the response curve before and after the optimization are seen in Fig. 9. In 135 iterations the objective function Ψ is reduced from 80.3 to 78.8 dB and it is seen from the figure that the response curve for the optimized design in general lies beneath the curve for the initial design. Five mode shapes have an influence in this frequency interval and it is therefore difficult to predict the optimized design. Three of the mode shapes have two horizontal nodal planes and from the design in Fig. 9 it is seen that at these nodal planes there is no absorbing material. However, it is difficult to predict anything on the horizontal boundaries, but as none of the mode shapes have nodal planes in the corners it is obvious that some absorbing material will be placed here and this is also observed in the design.

In the next example a rectangular room in 3D with the length 4 m, the width 3 m and the height 2.5 m is optimized for the interval [79.5;90.5] Hz and seven target frequencies. The quantities used are $\beta = 0.5$, $h_{\max} = 0.4$ m, $r_{\min} = 0.5h_{\max}$ and the target frequencies are updated for each 15th iteration. The results in Fig. 10 are obtained after 197 iterations and Ψ is reduced from 67.7 to 66.1 dB. From the response curves it is seen that Φ is reduced in most of the interval. It is also observed that the natural frequency around 80 Hz has

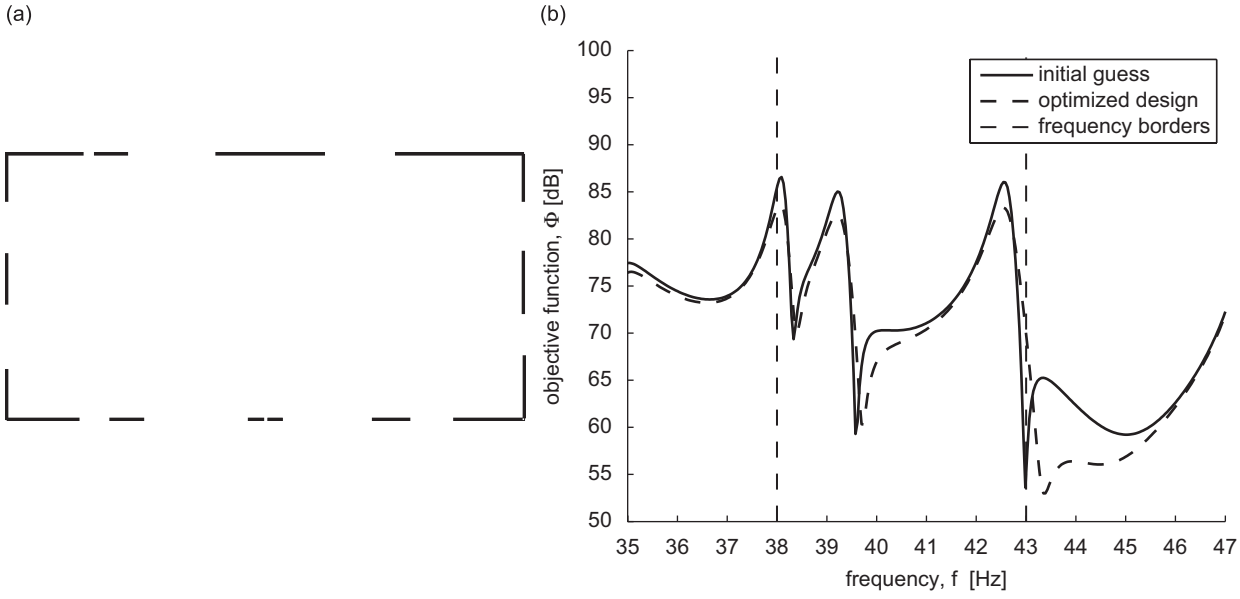

Fig. 9. Results of the optimization for the frequency interval [38;43] Hz with seven target frequencies and $\beta = 0.5$: (a) the optimized design where solid lines denote damped boundaries and (b) the response curve for the initial design and the optimized design.

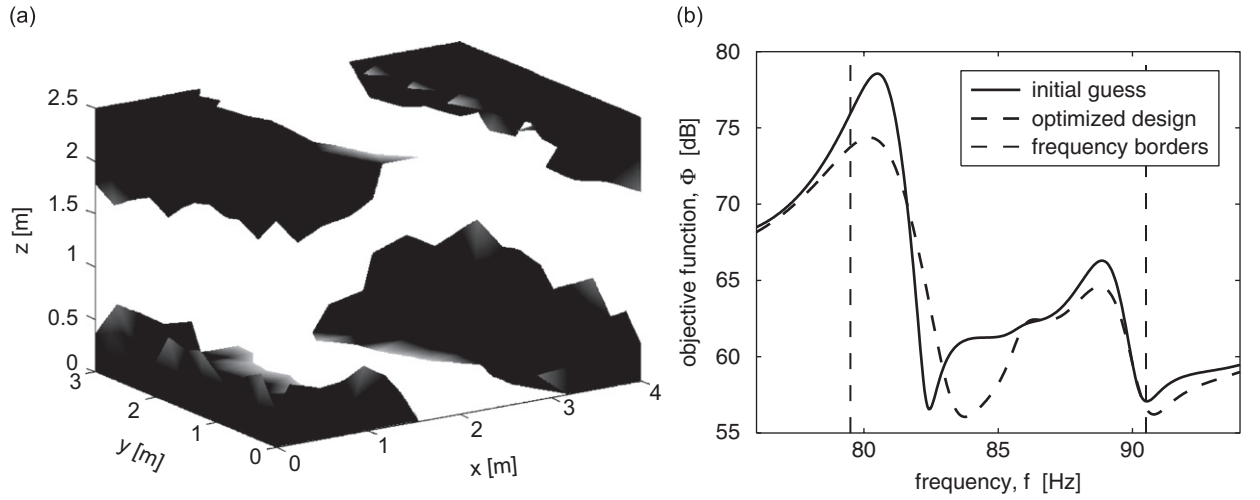

Fig. 10. Results of the optimization for the frequency interval [79.5;90.5] Hz with seven target frequencies: (a) the optimized design and (b) the response curve for the initial design and the optimized design.

the highest response in the interval and it is therefore expected that in order to minimize Ψ the absorbing material should be distributed where the sound pressure amplitude is high in the mode shape corresponding to the mentioned natural frequency. The associated mode shape has a nodal plane for $x = 2$ m and $z = 1.25$ m and as seen from the optimized design, reflecting material is distributed here, whereas the absorbing material is placed in the corners with high sound pressure amplitude, as expected.

Thus topology optimization appears as an efficient method to find an optimized distribution of reflecting and absorbing material in a room for an interval of relatively low frequencies.

3.4. Design of sound barriers

In this section topology optimization is employed to design outdoor sound barriers and the problem setting is illustrated in Fig. 11. The design domain Ω_d is 0.5×2 m and the sound source is placed at the ground 5 m in front of the barrier with the radius 0.1 m. The output domain Ω_{op} is a circle with center (9.25,1.25) m and radius 0.35 m. The ground is reflecting and to describe an outdoor situation with an unbounded medium the other boundaries are absorbing with the Sommerfeld radiation condition

$$\mathbf{n} \cdot (\hat{\rho}^{-1}(\mathbf{r}) \nabla \hat{p}(\mathbf{r})) = \mathrm{i}\tilde{\omega} \hat{p}(\mathbf{r}). \tag{27}$$

The geometry of the optimization problem is the same as in Ref. [24] where sound barriers are designed using a boundary element method and genetic algorithms for both low and high frequencies. The output domain Ω_{op} used here contains all the control points from the small output domain in that paper. As the optimization algorithm is most suitable for low frequencies the results will be compared to the results in Ref. [24] only for the frequency $f = 125$ Hz. The performance of the optimized designs will in each case be compared to the performance of a straight barrier and a T-shaped barrier with the dimensions as indicated in Fig. 12. The optimization is done for the two octave band center frequencies 63 and 125 Hz, respectively, and in both cases $h_{\max}$ is equal to 0.02 m in the design domain and 0.3 m in the rest of the domain. In the first case $r_{\min} = 1.5h_{\max}$ is used and in the second case $r_{\min} = 3.5h_{\max}$ is used. With these parameters the number of design variables is around 5500 which is more than in Ref. [24]. In Table 2 the value of the objective function for the T-shaped barrier and the optimized barrier are given relative to the straight barrier for each of the two frequencies. It is first of all observed that the T-shaped barrier is performing better than the straight barrier in both cases as expected from the references and that the reduction in the case $f = 125$ Hz is 0.9 dB — exactly as reported in Eq. [24]. The first two examples are for the frequency 63 Hz. The first is with $\beta = 0.24$ which is the same amount of material as in the T-shaped barrier. It is seen that a reduction of 5.88 dB is obtained compared to the straight barrier. By increasing the amount of material in the initial design to $\beta = 0.9$ it is possible to obtain

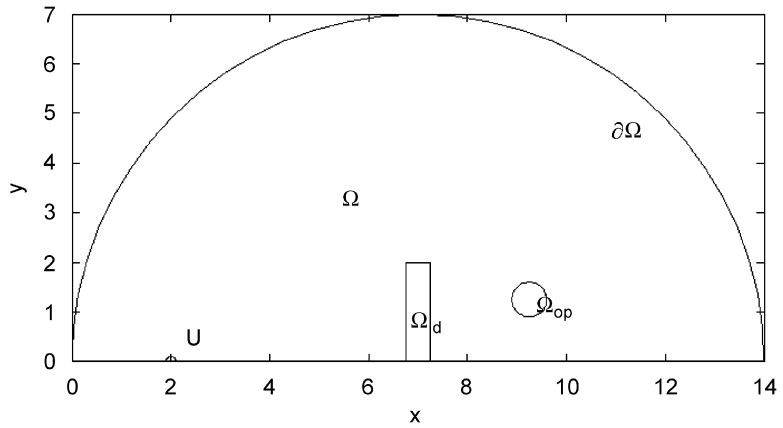

Fig. 11. The geometry for the sound barrier problem in 2D with the design domain Ω_d, the output domain Ω_{op} and the point source with the vibrational velocity U.

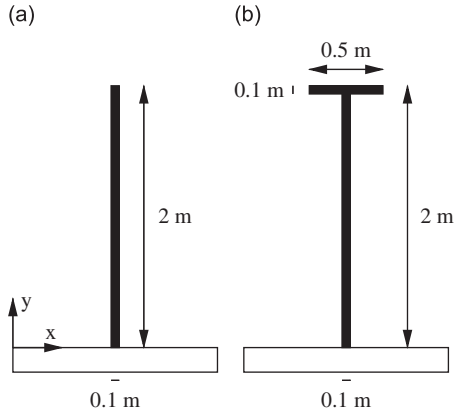

Fig. 12. The dimensions of the barriers with which the performance of the optimized sound barriers will be compared: (a) straight barrier and (b) T-shaped barrier.

Table 2
The value of the objective function for the T-shaped barrier and the optimized barrier relative to the straight barrier for each of the two frequencies

Frequency f (Hz)	Straight Φ (dB)	T-shape $\Delta\Phi$ (dB)	Optimized $\Delta\Phi$ (dB) $\beta = 0.24$	Optimized $\Delta\Phi$ (dB) $\beta = 0.90$
63	68.25	−1.70	−5.88	−7.04
125	70.02	−0.90		−9.13

a further reduction of the objective function of more than one dB as more reflecting material can be distributed. Note, however, that the amount of material used in the optimized design is well below the limit of 90%. In Fig. 13 the designs for $f = 63$ Hz with the two different values of β are shown. The two designs are different, but in both cases they look like modified T-shapes and cavities are formed that act as Helmholtz resonators at each side of the barriers. The optimization for the frequency 125 Hz is then done for $\beta = 0.9$ and the result can be compared to the result in Ref. [24]. The reduction of the objective function is here 9.13 dB, which is a few dB less than in Ref. [24], but the objective function is here minimized over an entire domain and not only over a few point as in that reference. In Fig. 14 the optimized design for $f = 125$ Hz is given together with the distribution of the sound pressure amplitude. The design obtained is different from the

Fig. 13. The optimized designs for the target frequency $f = 63$ Hz: (a) with volume fraction $\beta = 0.24$ and (b) with volume fraction $\beta = 0.9$.

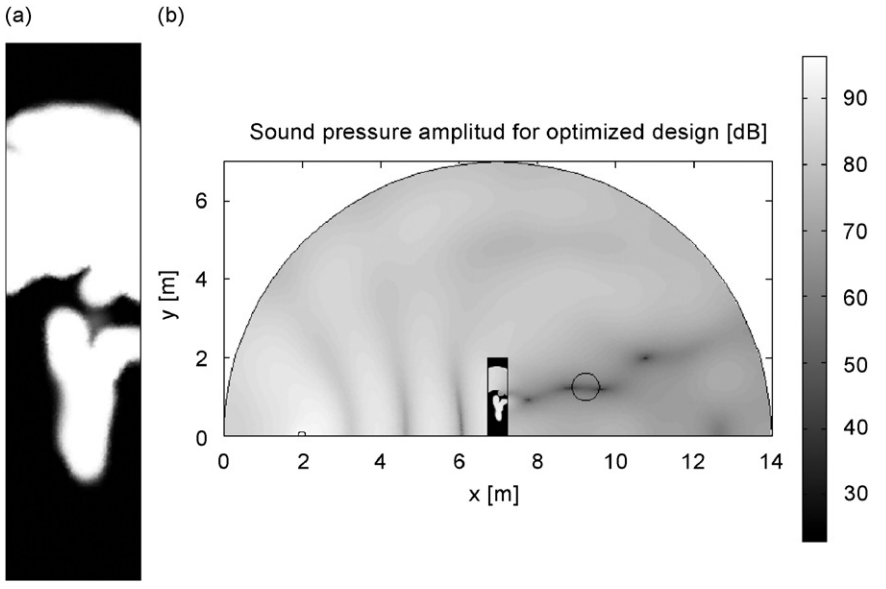

Fig. 14. (a) The optimized design for the target frequency $f = 125$ Hz and $\beta = 0.9$ and (b) The distribution of the sound pressure amplitude for the optimized design.

design in Ref. [24] with a Helmholtz resonator formed at the edge pointing away from the source where the sound pressure amplitude is high. From these results it is observed that the designs for the two frequencies are very different and the reduction achieved is bigger the higher the frequency is. This tendency is expected,

because the distribution of the sound pressure amplitude gets more complicated for higher frequencies and therefore a detailed optimized design can have more influence.

In the next example the optimization is done for the frequency interval [63;125] Hz with seven target frequencies which are updated every 25th iteration step. The quantities $\beta = 0.9$, $h_{\max} = 0.02$ m in the design domain and $r_{\min} = 2.5h_{\max}$ are used. The objective function Ψ is reduced from 71.4 to 64.4 dB after 889 iterations and in Fig. 15 the optimized design is seen to the left. The design has a cavity on both vertical edges as in the cases for $f = 63$ Hz. To the right Φ as function of the frequency f is plotted for the optimized design as well as for the straight and the T-shaped barrier. In the entire interval the optimized design is performing better than the two others with a few dB. So these examples show that the topology optimization method presented here is suitable for designing sound barriers for both a single frequency and frequency intervals.

Usually sound barriers are used on both sides of a sound source, for instance along roads. So to see how this influences the optimized results the problem is modified such that a sound barrier is introduced on both sides of the sound source. Again the optimization domain is placed behind the right barrier. The size of the barriers and the output domain as well as the distances between the source, the barriers and the design domain are the same as in the previous examples. Here $f = 125$ Hz is used and $h_{\max}$ is equal to 0.05 m in the design domain. The objective function for the same problem but with straight barriers is 64.1 dB and with T-shaped barriers the objective function is slightly reduced to 63.9 dB. To get the optimized design $\beta = 0.4$ and $r_{\min} = 3.0h_{\max}$ are employed and after 609 iterations the objective function is reduced with 27.9 to 36.1 dB compared to the example with the T-shaped barriers. The results of the optimization are shown in Fig. 16. The optimized designs for the two barriers are different and the material has been moved to a position such that a destructive interference pattern between the source and the right barrier is created. This has the effect that the sound pressure in the direction of the output domain is reduced. As more material can be distributed to control the sound as compared to the case with only one barrier the objective function is reduced more, and as noted, another effect of reducing the sound is being utilized. Inspired by this result the example with the T-barriers is recalculated where the inner edges of the columns, that are pointing towards the source, are moved to the inner edges of the optimized designs. For this case it is possible to get an objective function equal to 54.2 dB. This value is not reduced as much as for the optimized designs, but it is reduced with almost 10 dB compared to the case where the T-shaped barriers were in their original position. This shows that topology optimization can be employed to find new designs of sound barriers as well as to get inspiration to find an efficient position of conventional sound barriers.

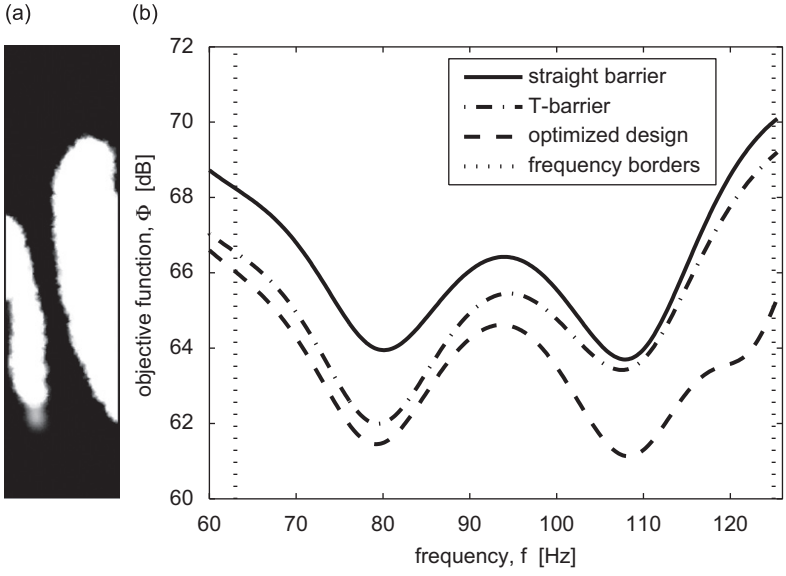

Fig. 15. Results of the optimization for the frequency interval [63;125] Hz with seven target frequencies: (a) the optimized design and (b) the distribution of sound pressure amplitude for the optimized design.

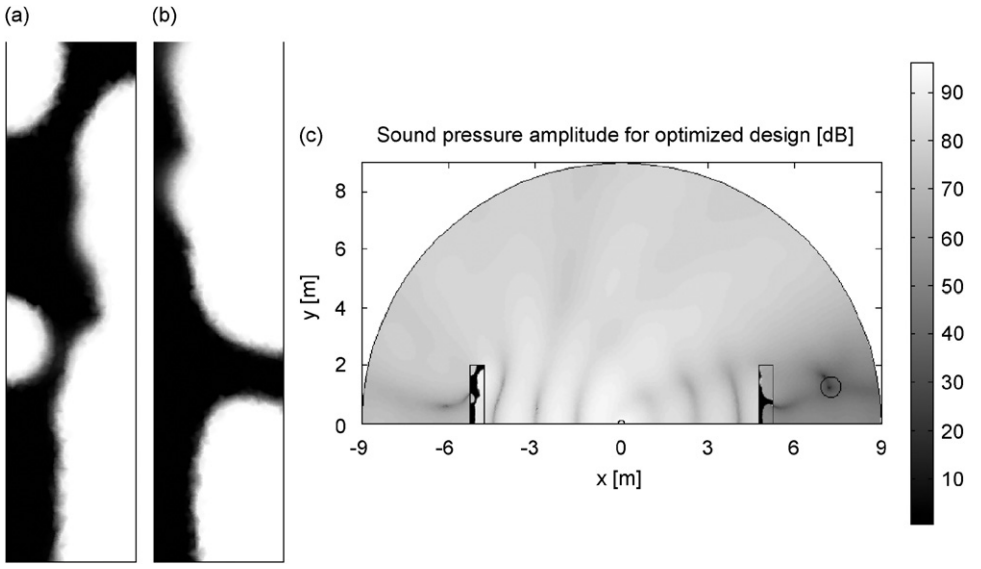

Fig. 16. (a) The optimized design with two sound barriers and one optimization domain for the target frequency $f = 125\,\text{Hz}$ and (b) the distribution of the sound pressure amplitude for the optimized design.

4. Conclusion

In this article it was shown that topology optimization can be employed to minimize the squared sound pressure amplitude in a certain part of a room and behind noise barriers by distribution of air, reflecting or absorbing material in a chosen design domain. The method is based on continuous material interpolation functions in the inverse density and bulk modulus and was developed for problems in both 2D and 3D.

It was shown that the method in general is suitable for low frequencies where well-defined designs can be obtained for a single frequency or a frequency interval. However, it was observed that it could be difficult to obtain mesh-independent designs, hence an image morphology-based filter was used to eliminate small details and grey scale domains. For higher frequencies the method is not suitable, mainly due to problems with obtaining a sufficiently fine finite element mesh, but also due to problems with too many local minima.

For the first type of problem, where reflecting material is distributed in a design domain along the ceiling, it was noted that small cavities acting as Helmholtz resonators were formed. It was also observed that the optimized designs were dependent on wether a natural frequency close to a driving frequency was increased or decreased. If a natural frequency was moved to a lower value, the solid material was removed from the high pressure amplitudes and redistributed at the nodal planes for the initial design such that the system was able to resonate at a lower frequency. The opposite happened when a natural frequency was moved to a higher value. In this case the material was redistributed at the high pressure amplitudes in order to make it more difficult for the system to resonate.

The second type of problem was concerned with the distribution of reflecting and absorbing material along the walls. In general the material was distributed at high pressure amplitudes to minimize the objective function and the method therefore appeared suitable for minimizing the objective function for bigger intervals with more mode shapes for which the design cannot be predicted easily. However, as most mode shapes have high pressure amplitudes in the corners a tendency for the absorbing material to be placed here was observed.

It was finally shown that the method can be utilized to design outdoor sound barriers where the objective function in the shadow zone was reduced with up to 10 dB with one barrier and with almost 30 dB with two barriers compared to conventional types. In the cases with one barrier cavities were again formed that were acting as Helmholtz resonators. In the case with the design of two barriers the material was placed such that a destructive interference pattern was formed resulting in a high noise reduction.

As the designs in general are sensitive to the choice of driving frequency or frequency interval as well as other factors as the choice of the volume fraction β and the filter size, it is recommended to choose the driving

frequency or the frequency interval carefully and to do more optimizations with several parameter combinations to obtain the best possible design.

Acknowledgments

This work received support from the Eurohorcs/ESF European Young Investigator Award (EURYI, www.esf.org/euryi) through the grant "Synthesis and topology optimization of optomechanical systems" and from the Danish Center for Scientific Computing (DCSC). Also support from the EU Network of Excellence ePIXnet is gratefully acknowledged.

References

[1] S.J. Elliot, P.A. Nelson, The active control of sound, *Electronics & Communication Engineering Journal* 2 (1990) 127–136.
[2] H. Kuttruff, *Room Acoustics*, fourth ed., Spon Press, Taylor & Francis Group, 2000, ISBN 0-419-24580-4.
[3] A.L. Rayna, J. Sancho, Technical note: the influence of a room shape on speech intelligibility in rooms with varying ambient noise levels, *Noise Control Engineering Journal* 31 (1988) 173–179.
[4] R. Reich, J. Bradley, Optimizing classroom acoustics using computer model studies, *Canadian Acoustics/Acoustique Canadienne* 26 (1998) 15–21.
[5] X. Shen, Y. Shen, J. Zhou, Optimization of the location of the loudspeaker and absorption material in a small room, *Applied Acoustics* 65 (2004) 791–806.
[6] V. Easwaran, A. Craggs, An application of acoustic finite models to finding the reverberation times of irregular rooms, *Acta Acustica* 82 (1996) 54–64.
[7] X. Zhu, Z. Zhu, J. Cheng, Using optimized surface modifications to improve low frequency response in a room, *Applied Acoustics* 65 (2004) 841–860.
[8] A. Habbal, Nonsmooth shape optimization applied to linear acoustics, *Society for Industrial and Applied Mathematics* 8 (1998) 989–1006.
[9] M.P. Bendsøe, N. Kikuchi, Generating optimal topologies in optimal design using a homogenization method, *Computer Methods in Applied Mechanics and Engineering* 71 (1988) 197–224.
[10] M.P. Bendsøe, O. Sigmund, *Topology Optimization, Theory, Methods and Applications*, Springer, Berlin, 2003 ISBN 3-540-42992-1.
[11] J.S. Jensen, O. Sigmund, Systematic design of phononic band-gap materials and structures by topology optimization, *Philosophical Transactions of the Royal Society London, Series A (Mathematical, Physical and Engineering Sciences)* 361 (2003) 1001–1019.
[12] O. Sigmund, J.S. Jensen, A. Gersborg-Hansen, R.B. Haber, Topology optimization in wave-propagation and flow problems, *Warsaw International Seminar on Design and Optimal Modelling*, WISDOM 2004, Warsaw, 2004, pp. 45–54.
[13] O. Sigmund, J.S. Jensen, Design of acoustic devices by topology optimization, *Short Paper of the Fifth World Congress on Structural and Multidisciplinary Optimization*, WCSMO5, Venice, 2003, pp. 267–268.
[14] E. Wadbro, M. Berggren, Topology optimization of an acoustic horn, *Computer Methods in Applied Mechanics and Engineering* 196 (2006) 420–436.
[15] G.H. Yoon, J.S. Jensen, O. Sigmund, Topology optimization of acoustic-structure interaction problems using a mixed finite element formulation, *International Journal for Numerical Methods in Engineering* 70 (2007) 1049–1075.
[16] J. Luo, H.C. Gea, Optimal stiffener design for interior sound reduction using a topology optimization based approach, *Journal of Vibration and Acoustics* 125 (2003) 267–273.
[17] J. Lee, S. Wang, Shape design sensitivity analysis for the radiated noise from the thin-body, *Journal of Sound and Vibration* 261 (2003) 895–910.
[18] J. Du, N. Olhoff, Minimization of sound radiation from vibrating bi-material structures using topology optimization, *Structural and Multidisciplinary Optimization* 33 (2007) 305–321.
[19] J.S. Jensen, O. Sigmund, Systematic design of acoustic devises by topology optimization, *Twelfth International Congress on Sound and Vibration*, Lisbon, 2005.
[20] D.N. May, M.M. Osman, Highway noise barriers: new shapes, *Journal of Sound and Vibration* 71 (1980) 73–101.
[21] D.A. Hutchins, H.W. Jones, Model studies of barrier performance in the presence of ground surfaces. Part II—different shapes, *Journal of Acoustic Society of America* 75 (1984) 1817–1826.
[22] D.C. Hothersall, S.N. Chancler-Wilde, M.N. Hajmirzae, Efficiency of single noise barriers, *Journal of Sound and Vibration* 146 (1991) 303–322.
[23] K. Fujiwara, D.C. Hothersall, C. Kim, Noise barriers with reactive surfaces, *Applied Acoustics* 53 (1998) 255–272.
[24] D. Duhamel, Shape optimization of noise barriers using genetic algorithms, *Journal of Sound and Vibration* 297 (2006) 432–443.
[25] *FEMLAB Reference Manual for FEMLAB 3.2*. COMSOL AB, Stockholm, www.comsol.se.
[26] D.A. Tortorelli, P. Michaleris, Design sensitivity analysis: overview and review, *Inverse Problems in Engineering* 1 (1994) 71–105.
[27] J.S. Jensen, O. Sigmund, Topology optimization of photonic crystal structures: a high bandwidth low loss T-junction waveguide, *Journal of the Optical Society of America B–Optical Physics* 22 (2005) 1191–1198.

[28] L.H. Olesen, F. Okkels, H. Bruus, A high-level programming-language implementation of topology optimization applied to steady-state Navier-Stokes flow, *International Journal for Numerical Methods in Engineering* 65 (2006) 975–1001.
[29] K. Svanberg, The method of moving asymptotes—a new method for structural optimization, *International Journal for Numerical Methods in Engineering* 24 (1987) 359–373.
[30] O. Sigmund, Morphology-based black and white filters for topology optimization, *Structural and Multidisciplinary Optimization* 33 (2007) 401–424.
[31] N. Olhoff, J. Du, Topological design for minimum dynamic compliance of continuum structures subjected to forced vibration, *Structural and Multidisciplinary Optimization*, in press, 2008.
[32] J. Jin, *The Finite Element Method in Electromagnetics*, second ed., John Wiley & Sons Inc., New York, 2002 ISBN 0-471-43818-9.

Publication [P2]

Design of photonic-bandgap fibers by topology optimization

Design of photonic-bandgap fibers by topology optimization

M. B. Dühring*, O. Sigmund* and T. Feurer**

* Department of Mechanical Engineering, Solid Mechanics, Technical University of Denmark, 2800 Kgs. Lyngby, Denmark.

** Institute of Applied Physics, University of Bern, 3012 Bern, Switzerland.

Abstract

A method based on topology optimization is presented to design the cross section of hollow core photonic-bandgap fibers for minimizing the energy loss by material absorption. The optical problem is modeled by the time-harmonic wave equation and solved with the finite element program Comsol Multiphysics. The optimization is based on continuous material interpolation functions between the refractive indices and is carried out by the Method of Moving Asymptotes. An example illustrates the performance of the method where air and silica are redistributed around the core such that the overlap between the magnetic field distribution and the lossy silica material is reduced and the energy flow is increased 375% in the core. Simplified designs inspired from the optimized geometry are presented, which will be easier to fabricate. The energy flow is increased up to almost 300% for these cases.

Keywords: finite element analysis, wave equation, photonic-crystal fiber, morphology filter, Comsol Multiphysics, optimized design

1 Introduction

Photonic crystals were first described in the two papers [1, 2] from 1987. They consist of periodically structured dielectric materials in one, two or three dimensions that can prohibit the propagation of electromagnetic waves at certain frequencies such that band gaps are created. Point and line defects can be introduced in the structures to localize and guide optical waves. The first 2D photonic crystal was fabricated for optical wavelengths in 1996, see [3], and applications are found in filters, splitters or resonant cavities, see [4]. Another application of the photonic crystal is the photonic-crystal fiber developed in the 1990s [5, 6]. Conventionally, optical fibers are made as step-index fibers where an index difference between the core and the cladding confines the optical wave to the core region [7]. These types of fibers are extensively used in telecommunication. In contrast to the conventional optical fibers, the optical wave in photonic-crystal fibers is guided in a core region surrounded by a 1D or 2D periodic structured material, see [8, 4] for an overview. Depending on the periodic structure the wave is confined either by index guiding or the band-gap effect. Because of the band-gap effect it is possible to guide the optical wave in an air core such that losses and unwanted dispersion and nonlinear effects from the bulk materials can be reduced. The first photonic-crystal fibers were produced for commercial purposes in 2000 and are fabricated by a drawing process.

In this work holey fibers are considered, which denote photonic-crystal fibers with air cores surrounded by periodic arrays of air holes. The cladding material is typically silica as it is suitable for fabrication with the drawing process. However, silica has higher loss for most optical wavelengths away from 1.55 μm, which is used in telecommunication. For optical wavelengths in general the photonic-crystal fibers are therefore not convenient for long fiber links, but rather for short distance applications. An example of a short distance application is laser surgery where wavelengths between 2-10 μm are used for various purposes in medical application as drilling holes in teeth and tissue removal. Lasers directed by mirrors are normally used for these purposes, but by employing fibers it will furthermore be possible to do surgery inside the body without opening it. A first example of

photonic-crystal fibers used for medical purposes is found in [9] where a 1D, rotational symmetric, photonic-crystal fiber is employed for laryngeal and airway surgery. However, as the silica is lossy at these optical wavelengths it is important to design the cross sections such that the losses in the cladding material are as small as possible.

Low loss photonic-bandgap fibers have been designed by parameter studies in various papers [10, 11, 12, 13, 14], where geometry parameters as the core size, the thickness and shape of the core boundary, the air filling fraction and the size of the fingers pointing towards the core have been varied. In the present work, we suggest to use topology optimization in order to design low loss holey fibers with cladding material that itself is lossy. Topology optimization is a computer based method and was originally developed in 1988 to maximize the stiffness of structures for a limited amount of material [15]. The method has since then been developed and applied to other engineering fields as mechanism design, heat transfer and fluid flow problems, see [16] for an introduction to the method and the different applications. By topology optimization air and solid material can be distributed freely in a design domain and the size and the number of the holes are determined. The method therefore offers more freedom in the design than obtained by size and shape optimization alone. The method was extended to electromagnetic wave propagation problems in 1999 where photonic-bandgap materials were designed in [17] for plane waves. Structures as bends and splitters based on 2D band-gap materials were designed in [18, 19] for single frequencies or frequency intervals. Planar photonic-crystal waveguide components optimized for low loss and high bandwidth and transmission have been fabricated and characterized, see [20, 21]. The tailoring of dispersion properties by topology optimization is considered for photonic-crystal waveguides in [22] and for step-index optical fibers in [23].

In this work we extend the method of topology optimization to holey fibers. The aim is to design the cross section of the fiber for a fixed wavelength relevant for medical purposes in order to optimize the energy flow through the core region. The optical model and optimization problem are described in section 2. An example of the performance of the method is given in section 3 and simplified designs inspired from the optimized geometry are studied.

2 Description of the optimization problem

2.1 The optical model

The optimization problem is based on a photonic-bandgap fiber with the geometry indicated in figure 1. It is a holey fiber where the optical wave is guided in a hollow core region, which is surrounded by a two-dimensional periodic cladding of air holes and silica at IR wavelengths. Silica is a highly lossy material and the goal of the optimization is to improve the energy transport in the core region, or in other words, to modify the mode profile such that its overlap with the silica becomes as small as possible. This is done by redistributing air and silica in the design domain Ω_{d} such that the objective function Φ, which is an expression related to the power flow, is optimized in the inner part of the core region denoted Ω_{c}.

It is assumed that the propagating optical modes of order ν have harmonic solutions on the form

$$H_{p,\nu}(x_1, x_2, x_3) = H_{p,\nu}(x_1, x_2) e^{-i\beta_\nu x_3}, \tag{1}$$

where $H_{p,\nu}$ is the magnetic field of the optical wave and β_ν is the propagation constant for a given optical mode ν. In the following only the guided mode is considered and therefore the notation with ν is omitted. The magnetic field is entered into the time-harmonic wave equation

$$e_{ijk} \frac{\partial}{\partial x_j} \left(n^{-2} e_{knp} \frac{\partial H_p}{\partial x_n} \right) - k_0^2 H_i = 0, \tag{2}$$

where k_0 is the free space propagation constant and e_{ijk} is the alternating symbol. As the energy of guided optical modes is concentrated in the core region, it can be assumed that the electric field

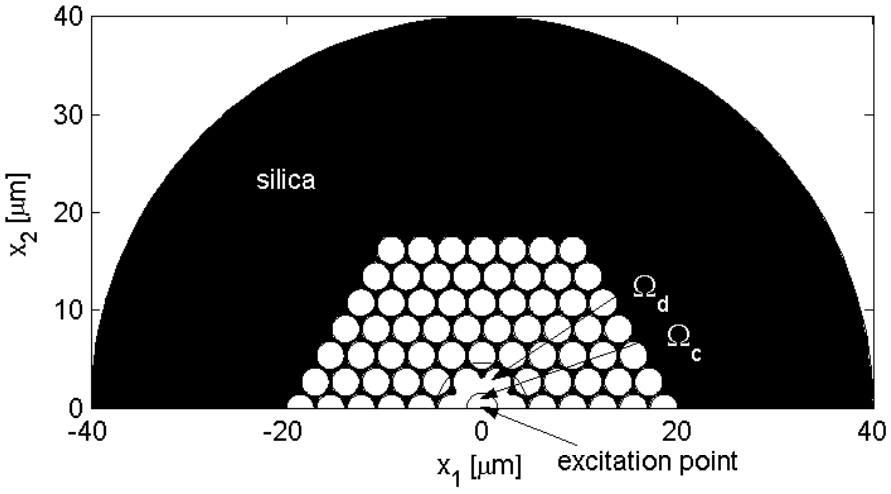

Figure 1: Geometry of the photonic-crystal fiber used in the optimization. Black indicates silica and white is air. The design domain is Ω_{d} and Ω_{c} is the core region where the objective function is optimized.

is zero at the outer boundary of the fiber and the perfect electric conductor boundary condition is applied. The guided mode for the geometry used here is twofold symmetric and therefore only half the geometry is needed. At the symmetry border the perfect electric conductor is applied as well, such that the electric field is polarized in the vertical direction.

For the given value of k_0 the propagation constant β for the guided mode is found by solving the wave equation as an eigenvalue problem. In order to define the problem for the topology optimization β is first computed. Then the wave equation is solved in a time-harmonic way where both k_0 and β are fixed, and the guided mode is excited by introducing a small half-circle in the middle of the fiber where a magnetic forcing term in the horizontal direction is applied. To get a realistic problem for the topology optimization, material damping is introduced in the silica cladding by adding an imaginary part to the refractive index. This means that the magnetic field components are complex valued.

The mathematical model of the optical problem is solved by finite element analysis. The complex fields H_j are discretized using sets of finite element basis functions $\{\phi_{j,n}(\mathbf{r})\}$

$$H_j(\mathbf{r}) = \sum_{n=1}^{N} H_{j,n}\phi_{j,n}(\mathbf{r}). \tag{3}$$

The degrees of freedom are assembled in the vectors $\mathbf{H}_j = \{H_{j,1}, H_{j,2}, ...H_{j,N}\}^T$. A triangular element mesh is employed and vector elements are used for H_1 and H_2 in order to avoid spurious modes. Second order Lagrange elements are used for H_3. The optical model is solved by the commercial finite element program Comsol Multiphysics with Matlab [24] with the module "Perpendicular waves, hybrid-mode waves" for the three magnetic field components. This results in the discretized equations for the time-harmonic problem used in the topology optimization

$$\sum_{j=1}^{3} \mathbf{S}_{kj}\mathbf{H}_j = \mathbf{f}_k, \tag{4}$$

where $\mathbf{S}_{kj}$ is the complex system matrix and $\mathbf{f}_k$ is the load vector. The problem in (4) is solved as one system in Comsol Multiphysics.

2.2 Design variables and material interpolation

The problem of finding an optimized distribution of material is a discrete optimization problem, and there should be air or solid material in each point of the design domain. However, in order to allow for efficient gradient-based optimization the problem is formulated with continuous material properties that can take any value in between the values for air and solid material. To control the material properties a continuous material indicator field $0 \leq \xi(\mathbf{r}) \leq 1$ is introduced, where $\xi = 0$ corresponds to air and $\xi = 1$ to silica material. The refractive index is interpolated linearly between the two material phases

$$n(\xi) = n_{\mathrm{a}} + \xi(n_{\mathrm{s}} - n_{\mathrm{a}}). \tag{5}$$

Although ξ is continuous, the final design should be as close to discrete ($\xi = 0$ or $\xi = 1$) as possible in order to be well defined and such a design will be denoted 0-1 in the following. This is done by employing a morphology-based filter as described in subsection 2.5.

2.3 The optimization problem

The purpose of the topology optimization is to maximize the energy flow through the hollow core, and thereby indirectly minimizing the energy loss in the glass material. The flow should be maximized if the optical mode is concentrated in the air region. The objective function Φ is based on an energy measure similar to the expression for the power flow in the x_3-direction. It is maximized in the inner core region Ω_{c} by redistributing air and silica in the design domain Ω_{d} that surrounds the core region, see figure 1. The component H_3 is not included in the expression since its value is several orders of magnitude smaller than those of H_1 and H_2. The formulation of the optimization problem takes the form

$$\max_{\xi} \ \log(\Phi) = \log \int_{\Omega_{\mathrm{c}}} \sum_{j=1}^{2} |H_j(\mathbf{r}, \xi(\mathbf{r}))|^2 \mathrm{d}\mathbf{r}, \qquad \text{objective function} \tag{6}$$

$$\text{subject to } \ 0 \leq \xi(\mathbf{r}) \leq 1 \quad \forall \ \mathbf{r} \in \Omega_{\mathrm{d}}, \qquad \text{design variable bounds} \tag{7}$$

The logarithm to the objective function is used in order to obtain better numerical scaling for the optimization process.

2.4 Sensitivity analysis

In order to update the design variables by a gradient based optimization algorithm, the derivatives of the objective function with respect to the design variables must be computed. This is possible as the design variable is introduced as a continuous field. The design variable field ξ is therefore discretized in a similar way as the dependent fields

$$\xi(\mathbf{r}) = \sum_{n=1}^{N_d} \xi_n \phi_{4,n}(\mathbf{r}). \tag{8}$$

The degrees of freedom are assembled in the vector $\boldsymbol{\xi} = \{\xi_1, \xi_2, ...\xi_{N_d}\}^T$. Zero order Lagrange elements are used and N_d is therefore typically smaller than N. The complex magnetic field vector $\mathbf{H}_k$ is via (4) an implicit function of the design variables, which is written as $\mathbf{H}_k(\boldsymbol{\xi}) = \mathbf{H}_k^R(\boldsymbol{\xi}) + i\mathbf{H}_k^I(\boldsymbol{\xi})$, where $\mathbf{H}_k^R$ and $\mathbf{H}_k^I$ denote the real and the imaginary part of $\mathbf{H}_k$. Thus the derivative of the objective function $\Phi = \Phi(\mathbf{H}_k^R(\boldsymbol{\xi}), \mathbf{H}_k^I(\boldsymbol{\xi}), \boldsymbol{\xi})$ is given by the following expression found by the chain rule

$$\frac{\mathrm{d}\Phi}{\mathrm{d}\boldsymbol{\xi}} = \frac{\partial \Phi}{\partial \boldsymbol{\xi}} + \sum_{k=1}^{3} \left(\frac{\partial \Phi}{\partial \mathbf{H}_k^R} \frac{\partial \mathbf{H}_k^R}{\partial \boldsymbol{\xi}} + \frac{\partial \Phi}{\partial \mathbf{H}_k^I} \frac{\partial \mathbf{H}_k^I}{\partial \boldsymbol{\xi}} \right). \tag{9}$$

Note, that derivatives with respect to $\mathbf{H}_3^R$ and $\mathbf{H}_3^I$ are zero. As $\mathbf{H}_k$ is an implicit function of $\boldsymbol{\xi}$ the derivatives $\partial \mathbf{H}_k^R / \partial \boldsymbol{\xi}$ and $\partial \mathbf{H}_k^I / \partial \boldsymbol{\xi}$ are not known directly. The sensitivity analysis is therefore done by employing an adjoint method where the unknown derivatives are eliminated at the expense of determining adjoint and complex variable fields $\boldsymbol{\lambda}_j$ from the adjoint equation

$$\sum_{j=1}^{3} \mathbf{S}_{kj} \boldsymbol{\lambda}_j = \left(\frac{\partial \Phi}{\partial \mathbf{H}_k^R} - i \frac{\partial \Phi}{\partial \mathbf{H}_k^I} \right)^T, \tag{10}$$

where

$$\frac{\partial \Phi}{\partial \mathbf{H}_{k,n}^R} - i \frac{\partial \Phi}{\partial \mathbf{H}_{k,n}^I} = \int_{\Omega_\mathrm{c}} (2H_k^R - i2H_k^I) \phi_{k,n} \mathrm{d}\mathbf{r}. \tag{11}$$

The sensitivity analysis follows the standard adjoint sensitivity approach [25]. For further details of the adjoint sensitivity method applied to wave propagation problems, the reader is referred to [18]. Equation (9) for the derivative of the objective function then reduces to

$$\frac{\mathrm{d}\Phi}{\mathrm{d}\boldsymbol{\xi}} = \frac{\partial \Phi}{\partial \boldsymbol{\xi}} + \sum_{k=1}^{3} \Re \left(\boldsymbol{\lambda}_k^T \sum_{j=1}^{3} \frac{\partial \mathbf{S}_{kj}}{\partial \boldsymbol{\xi}} \mathbf{H}_j \right). \tag{12}$$

The vectors $\partial \Phi / \partial \boldsymbol{\xi}$ and $\int_{\Omega_\mathrm{c}} (2H_k^R - i2H_k^I) \phi_{k,n} \mathrm{d}\mathbf{r}$ as well as the matrix $\partial \mathbf{S}_{kj} / \partial \boldsymbol{\xi}$ are assembled in Comsol Multiphysics as described in [26]. Similar to the problem in (4), the expression in (10) can be solved as one system.

2.5 Practical implementation

The optimization problem defined by (6)-(7) is solved using the Method of Moving Asymptotes, [27]. This is an algorithm well suited to solve problems with a high number of degrees of freedom and it employs information from the previous iteration steps and gradient information.

When the mesh size is decreased the optimization will in general result in mesh-dependent solutions with small details, which make the resulting design inconvenient to manufacture. To avoid this problems a morphology-based filter is employed. Such filters make the material properties of an element depend on a function of the design variables in a fixed neighborhood around the element, such that the finite design is mesh-independent. Here a Heaviside close-type morphology-based filter is chosen [28], which has proven efficient for wave-propagation type topology optimization problems, see for instance [29]. The method results in designs where all holes below the size of the filter (radius r) have been eliminated. A further advantage of these filter-types is that they help eliminating gray elements in the transition zone between solid and air regions.

The problem studied is non-unique with a number of local optima that typically originate from local resonance effects. To prevent convergence to these local optima a continuation method is applied where the original problem is modified to a smoother problem. In wave problems it has been shown that a strong artificial damping will smooth out the response [30, 18] and this idea is applied to the problem. A strong material damping is therefore applied in the beginning of the optimization and after convergence of the modified problem or after a fixed number of iterations the problem is gradually changed back to the original one with a realistic damping.

3 Results

Now the method described above is applied to optimize the energy flow in a holey fiber with the geometry shown in figure 1 as the initial guess. The geometry is taken from [12] and is adapted to have a band gap for the optical wavelength in free space $\lambda_0 = 2$ μm. The geometry consists of six air hole rings around the hollow core. The pitch, which denotes the distance between the center of

two air holes, is $\Lambda = 3.1$ μm, the hole diameter over the pitch ratio is $d/\Lambda = 0.92$ and the diameter is $d = 2.852$ μm. The radius of the air core in the center is $R = \Lambda$. The core region Ω_c where the objective function is optimized has the radius $0.5R$, and the design domain Ω_d is defined by the area between the two half circles with radius equal to $0.5R$ and $1.5R$, respectively. The half circle at the center where the source is applied is equal to $0.05R$. The maximum element size is 0.1 μm in Ω_d and 0.8 μm in the rest of the domain. The refractive indexes for the chosen wavelength are $n_a = 1$ for air and $n_s = 1.43791 + 0.0001i$ for silica, where the imaginary part in n_s causes absorption and is denoted as the absorbing coefficient α_s. Before the optimization, a band-gap check is performed with the commercial program BandSolve, see [31]. The band diagram is calculated for the periodic structure with $k_0\Lambda$ as function of $k_3\Lambda$, where k_3 is the propagation constant in the x_3-direction. The point $(k_3\Lambda, k_0\Lambda) = (9.5127, 9.73894)$ for the fundamental mode was shown to be in the calculated band gap. The wave equation (2) is then solved as an eigenvalue problem with the absorption coefficient α_s equal to zero and the propagating constant β for the guided mode is found, which is used together with the fixed value of $k_0 = 2\pi/\lambda_0$ to solve the model by employing the forcing term.

3.1 Study of the optimized design

The optimization is performed with the filter radius $r = 0.15$ μm, a move limit equal to 0.05 for the maximum change in the design variables in each iteration step and the absolute tolerance 0.01 to terminate the optimization. The continuation method for the damping is applied such that α_s is equal to 1 when the optimization starts and is reduced by a factor 10 after 100 iterations or if the tolerance is satisfied. This is repeated until α_s reaches the value 0.0001. Introducing the damping lowers and widens the peak at resonance as seen on figure 2 where $\log(\Phi/\Phi_{\text{init}})$ is plotted as function of λ_0 for increasing α_s. Φ_{init} is the value of the objective function for the initial design. The resonance is kept at the original wavelength $\lambda_0 = 2$ μm for the low values of α_s, but is slightly shifted to higher wavelengths for the two highest values of α_s such that the optimization starts away from resonance. The optimized design is found in 316 iterations and the objective function Φ is increased 375% compared to the initial design. In figure 2, $\log(\Phi/\Phi_{\text{init}})$ as function of λ_0 is compared for the initial and the optimized design. The wavelength at resonance is the same before and after the optimization and the peak value has increased for the optimized design. In figure 3(a) and 3(b) the initial and optimized design are plotted, respectively, and the distribution of the energy measure from the objective function normalized with the maximal value for the initial design, $\Phi_{\max}$, is indicated with the contour lines. The optimized design is close to a 0-1 design and all parts are

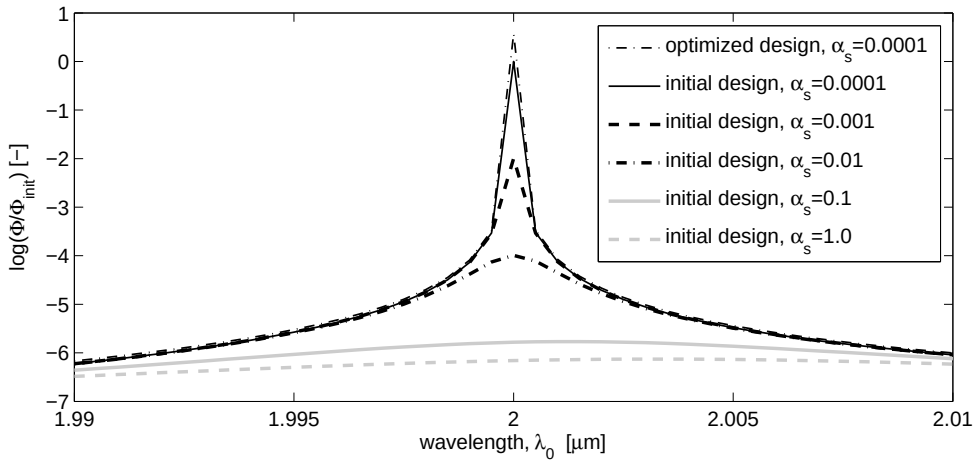

Figure 2: The logarithm to the normalized objective function Φ/Φ_{init} as function of the optical wavelength λ_0 is indicated both for the initial design with different values of the absorption coefficient α_s and for the optimized design with $\alpha_s = 0.0001$.

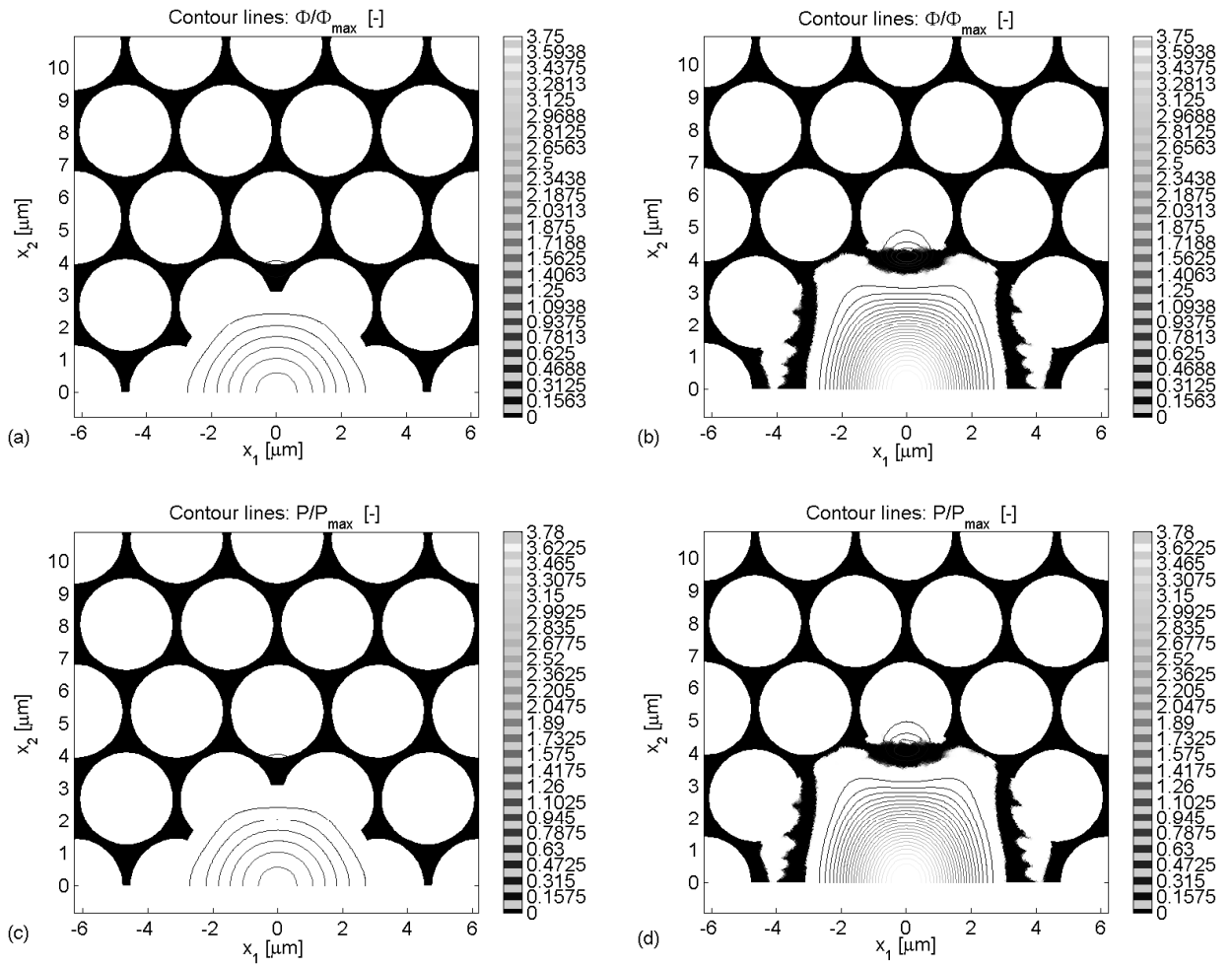

Figure 3: The center region of the holey fiber where black indicates silica and white is air. (a) and (b): The contour lines show the distribution of the normalized energy measure from the objective function $\Phi/\Phi_{\max}$ in the initial and the optimized design, respectively. (c) and (d): The normalized time average power flow $P/P_{\max}$ in the x_3-direction is indicated by the contour lines for the initial and the optimized design, respectively.

connected, which is important due to fabrication issues. The design is almost symmetric around a vertical axis, which has not been enforced in the optimization. The small deviation from symmetry is most likely due to the unstructured mesh, which is not symmetric. Compared to the initial design the objective function in the optimized design has been redistributed, such that the modes shape is extending more in the vertical direction and the peak value in the center has increased. The time average power flow P in the x_3-direction, normalized with the maximum value $P_{\max}$ for the initial design, is plotted on figure 3(c) and 3(d) for the initial and the optimized design, respectively. The shape of the modes are in good agreement with the distribution of the energy measure from the objective function in figure 3(a) and 3(b), and their ratio of magnitude is also similar. Compared to the initial design the integral of P in Ω_c has increased 378% for the optimized design. So the same improvement is obtained for Φ and P when Φ is used as the objective function.

In order to explain that the objective function has increased, the absolute value of the magnetic fields H_1 and H_2 are considered. Both fields are symmetric around the vertical axis before and after the optimization and $|H_1|/|H_{1,\max}|$ is plotted with contour lines for the initial and optimized design in figure 4(a) and 4(b), respectively. $|H_{1,\max}|$ is the maximum value of $|H_1|$ for the initial design. Like the distribution of the objective function, $|H_1|$ is confined by the vertical walls to the sides and is elongated in the vertical direction. In the initial design concentrations of $|H_1|$ are found where the

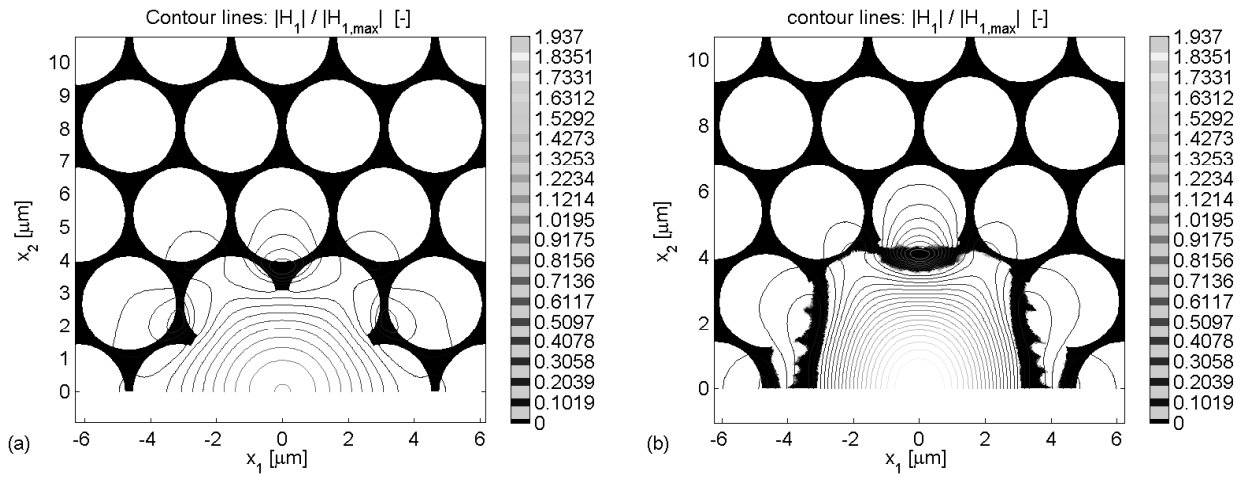

Figure 4: The geometry of the center region of the holey fiber where black is silica and white is air. The contour lines indicate the normalized absolute value of the magnetic field $|H_1|/|H_{1,\max}|$. (a): Initial design. (b): Optimized design.

three fingers are pointing towards the center. In the optimized design the two field concentrations at the sides has disappeared because of the forming of the vertical walls. This means that a smaller part of the total field is in the lossy silica material and therefore less energy is absorbed and the energy flow in the core region is increased. Similar tendencies are found for $|H_2|$, but as its values are an order of magnitude lower than for $|H_1|$, the plots are not included here.

When the outer radius of the design domain is increased to $1.65R$ the optimized design is essentially not changed and the objective function is also increased 375% as with the original radius. This indicates that the optimized design is not so sensitive to the outer radius of the design domain in this range.

3.2 Study of simplified designs

The previous example shows that the presented method can be employed to design holey fibers such that the overlap between the magnetic field and the lossy material is deceased and the energy flow in the core region is increased. The optimized design, however, has many small details that will be difficult to fabricate as the drawing process tends to smoothen the interface between air and silica. Especially the walls pointing away from the center have small details and spikes that appear due to the filter radius r. When a bigger value of r is used these walls get more smooth, but a gray transition zone of intermediate materials has a tendency to appear between the silica and the air. In order to examine how important the details are for the performance and to get designs that are simpler to fabricate, four simplified geometries with the main features of the optimized design are constructed. The wave equation (2) is solved as an eigenvalue problem for each of the designs and the propagating constant β_1 for the guided mode is found. The model is then solved with the forcing term and α_s equal to zero. The simplified designs denoted (a) to (d) are seen in figure 5(a) to 5(d) and the distribution of $\Phi/\Phi_{\max}$ is indicated by the contour lines with the same scale as for the initial and optimized design in figure 3(a) and 3(b). The level of details imitating the optimized design is decreasing for the four designs and the improvement of the objective function Φ and the average power flow P compared to the initial design is decreasing accordingly, see table 1. Design (a) has tilted walls to the sides and a detailed layout at the top part above the mode, which represent the details of the optimized design well. The objective function is improved almost 300% compared to the initial design, which is not as much as for the optimized design, so the smaller details do have an influence on the performance. Design (b) has been further modified by simplifying the geometry above the optical mode and by vertically cutting off the structures behind the side walls. The side

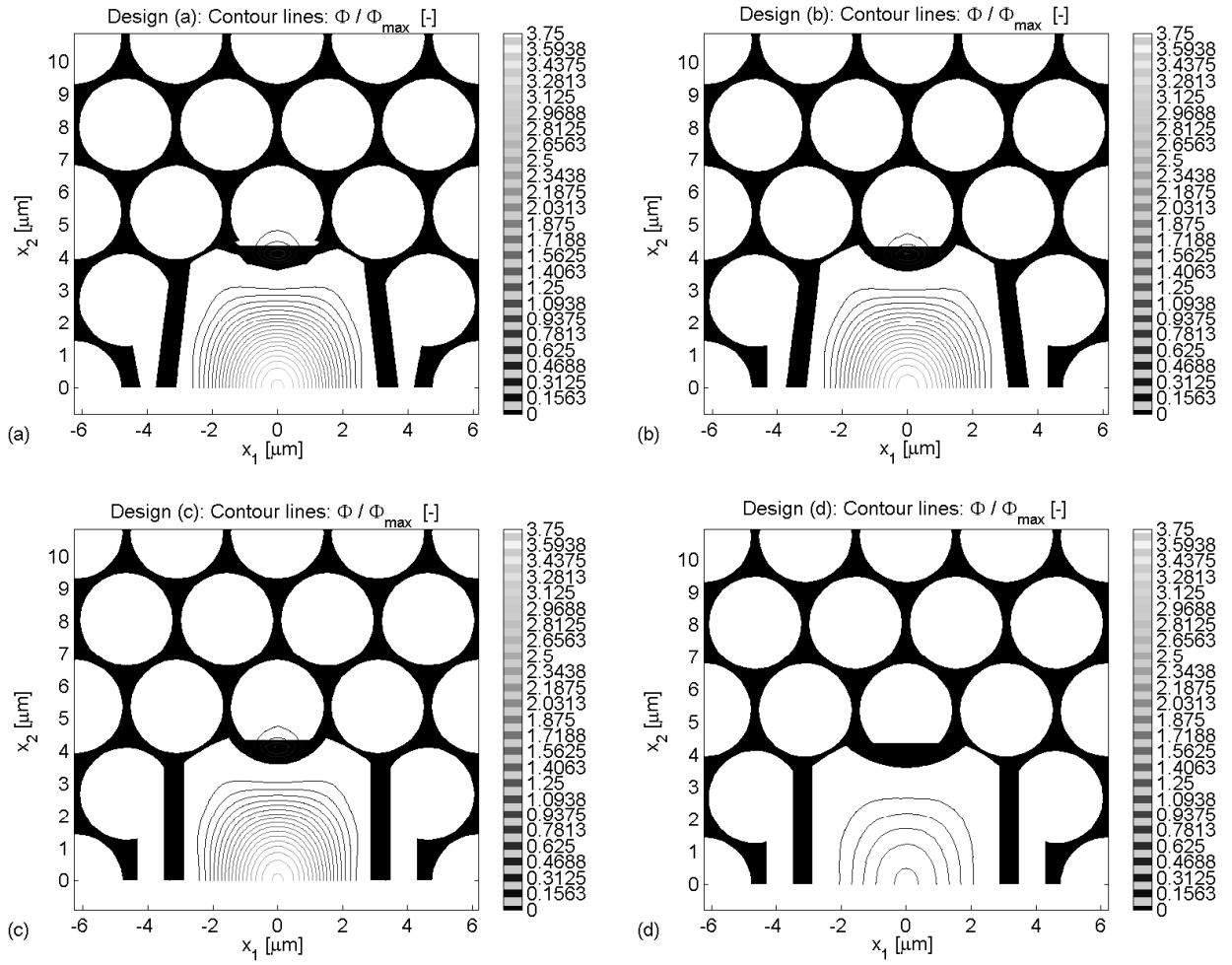

Figure 5: Four simplified geometries of the holey fiber inspired from the optimized design. Black is silica and white is air. The contour lines show the distribution of the energy measure from the normalized objective function $\Phi/\Phi_{\max}$.

Table 1: The increase of the objective function Φ and the time average power flow P in the x_3-direction for the optimized design and the four simplified designs compared to the values for the initial design.

design	optimized	(a)	(b)	(c)	(d)
Φ/Φ_{init} [%]	375	295	269	262	80
P/P_{init} [%]	378	297	271	264	80

walls are furthermore adjusted to be vertical in design (c). Design (b) and (c) almost have the same improvement of Φ, which is a little less than for design (a). So the exact layout of the top part and the tilted walls do not have a big influence on the performance compared to design (a), and all three designs have a similar mode shape. Finally, the top part is made more massive in design (d) and this detail has a significant influence on the performance that now is worse than the initial design, due to increased overlap between the magnetic field and the silica cladding. This shows that the design of the top part is important and must not fill out too much space such that the mode is prohibited to extend to the upper corners.

The examples show that it is possible to design fibers with a simplified geometry inspired from the optimization, which will be simpler to fabricate and still have a significant improvement of the performance. However, the more the geometry deviates from the optimized design the more the

performance will decrease and some details, as the layout of the top part, are crucial.

4 Conclusion

A method to optimize the energy flow trough the core of a holey photonic-crystal fiber based on topology optimization has been presented. As the cladding material is lossy, the aim is to design the cross section of the fiber such that the mode shape is overlapping the cladding as little as possible. The optical model is based on the time-harmonic wave equation for the magnetic field. Matching values for the propagation constant and the optical wavelength are employed in order to solve the wave equation in a time-harmonic way where the wave is exited by a magnetic force in the center of the fiber. The topology optimization is based on linear interpolation functions between the refractive indices and the objective function is the sum of the squared absolute value of the magnetic fields in the plane. A close type morphology filter and a continuation method based on the damping are applied to obtain appropriate designs.

The performance of the method is illustrated by an example where a 0-1 design is obtained, which is symmetric about a vertical axis in contrast to the 60 degree symmetry of the initial design. The objective function is increased 375% because the optimized design changes the distribution of the magnetic field such that its overlap with the lossy cladding material is decreased. It is shown, that by maximizing the objective function the time-average power flow in the propagation direction is increased 378% times, and its distribution in the initial and the optimized design is similar to the distribution of the energy measure form the objective function. Thus, the same improvement is obtained for power flow and the objective function. It is furthermore shown that simplified designs with the main features from the optimized design can be created, which are simpler to fabricate. The improvement is decreasing when the simplified designs deviate more from the optimized design.

Further work encompasses the inclusion of a symmetry constraint around the vertical axis and a study of other types of filters to further eliminate small details and the gray transition zones at the air/cladding interfaces. Methods to optimize for tolerant designs are relevant to apply, see [32], as the drawing process tends to smooth out the details in the design. Optimization of wavelength intervals to obtain broadband solutions can be performed by the method described in [18]. Finally, the method can be extended to other types of photonic-crystal fibers, as fibers where the light is confined by index guiding, and to other objective functions where dispersion properties and non-linear effects are optimized.

5 Acknowledgements

This work received support from the Eurohorcs/ESF European Young Investigator Award (EURYI, www.esf.org/euryi) through the grant "Synthesis and topology optimization of optomechanical systems" and from the Danish Center for Scientific Computing (DCSC). Also support from the EU Network of Excellence ePIXnet is gratefully acknowledged. The authors are thankful to Jakob S. Jensen from the Department of Mechanical Engineering, Technical University of Denmark, for helpful discussions related to the presented work.

References

[1] E. Yablonovitch, Inhibited spontaneous emission in solid-state physics and electronics, *Phys. Rev. Lett.*, 58, 20, 2059-2062, 1987.

[2] S. John, Strong localization of photons in certain disordered dielectric superlattices, *Phys. Rev. Lett.*, 58, 23, 2486-2489, 1987.

[3] T.F. Krauss, R.M. De La Rue and S. Brand, Two-dimensional photonic-bandgap structures operating at near-infrared wavelenghts, Nature, 383, 699-702, 1996.

[4] J.D. Joannopoulos, S.G. Johnson, J.N. Winn and R.D. Meade, Photonic crystals, molding the flow of light, 2nd edition, Princeton University Press, 2008.

[5] T.A. Birks, P.J. Roberts, P.St.J. Russell, D.M. Atkin and T.J. Shepherd, Full 2-D photonic bandgaps in silica/air structures, *Electron. Lett.*, 31, 22, 1941-1943, 1995.

[6] S.E. Barkou, J. Broeng and A. Bjarklev, Silica-air photonic crystal fiber design that permits waveguiding by a true photonic bandgap effect, *Opt. Lett.*, 24, 1, 46-48, 1999.

[7] R. Syms and J. Cozens, *Optical guided waves and devices*, 1st ed., McGraw-Hill, 1992.

[8] P. Russell, Photonic crystal fibers, *Science*, 299, 5605, 358-362, 2003.

[9] D. Torres, O. Weisberg, G. Shapira, C. Anastassiou, B. Temelkuran, M. Shurgalin, S.A. Jacobs, R.U. Ahmad, T. Wang, U. Kolodny, S.M. Shapshay, Z. Wang, A.K. Devaiah, U.D. Upadhyay and J.A. Koufman, OmniGuide photonic bandgap fibers for flexible delivery of CO_2 laser energy for laryngeal and airway surgery, *Proc. of SPIE*, 5686, 310-321, 2005.

[10] H.K. Kim, J. Shin, S. Fan, M.J.F. Digonnet and G.S. Kino, Designing air-core photonic-bandgap fibers free of surface modes, *IEEE J. Quantum Electron.*, 40, 5, 551-556, 2004.

[11] P.J. Roberts, F. Couney, H. Sabert, B.J. Mangan, D.P. Williams, L. Farr, M.W. Mason, A. Tomlinson, T.A. Birks, J.C. Knight and P.St.J. Russell, Ultimate low loss of hollow-core photonic crystal fibres, *Opt. Exp.*, 13, 1, 236-244, 2005.

[12] J. Hu and C.R. Menyuk, Use of fingers in the core to reduce leakage loss in air-core photonic bandgap fibers, *Proc. of OFC/NFOEC*, 2007.

[13] R. Amezcua-Correa, N.G.R. Broderick, M.N. Petrovich, F. Poletti and D.J. Richardson, Design of 7 and 19 cells core air-guiding photonic crystal fibers for low-loss, wide bandwidth and dispersion controlled operation, *Opt. Exp.*, 15, 26, 17577-17586, 2007.

[14] T. Murao, K. Saitoh and M. Koshiba, Structural optimization of air-guiding photonic bandgap fibers for realizing ultimate low loss waveguides, *J. Lightwave tech.*, 26, 12, 1602-1612, 2008.

[15] M. P. Bendsøe and N. Kikuchi, Generating optimal topologies in structural design using a homogenization method, *Comp. Meth. Appl. Mech. Engrg.*, 71, 197-224, 1988.

[16] M.P. Bendsøe and O. Sigmund, Topology optimization, theory, methods and applications, Springer, Berlin, 2003.

[17] S.J. Cox and D.C. Dobson, Maximizing band gaps in two-dimensional photonic crystals, *SIAM J. Appl. Math.*, 59, 6, 2108-2120, 1999.

[18] J.S. Jensen and O. Sigmund, Topology optimization of photonic crystal structures: A high bandwidth low loss T-junction waveguide, *J. Opt. Soc. Am. B* 22, 1191-1198, 2005.

[19] Y. Tsuji, K. Hirayama, T. Nomura, K. Sato, and S. Nishiwaki, Design of optical circuit devices based on topology optimization, *IEEE photonics Tehnol. Lett.*, 18, 7, 850-852, 2006.

[20] P.I. Borel, A. Harpøth, L.H. Frandsen, M. Kristensen, P. Shi, J.S. Jensen and O. Sigmund, Topology optimization and fabrication of photonic crystal structures, *Opt. Exp.*, 12, 9, 1996-2001, 2004.

[21] P.I. Borel, L.H. Frandsen, A. Harpøth, M. Kristensen, J.S. Jensen and O. Sigmund, Topology optimised broadband photonic crystal Y-splitter, *Electron. Lett.*, 41, 2, 69-71, 2005.

[22] R. Stainko and O. Sigmund, Tailoring dispersion properties of photonic crystal waveguuides by topology optimization, *Waves in Random and Complex Media*, 17, 4, 477-489, 2007.

[23] J. Riishede and O. Sigmund, Inverse design of dispersion compensating optical fiber using topology optimization, *J. Opt. Soc. Am. B*, 25, 1, 88-97, 2008.

[24] COMSOL Reference Manual for COMSOL 3.5. COMSOL AB, Stockholm, www.comsol.se.

[25] D.A. Tortorelli and P. Michaleris, Design sensitivity analysis: overview and review, *Inverse Problems in Science and Engineering* 1, 1, 71-105, 1994.

[26] L.H. Olesen, F. Okkels and H. Bruus, A high-level programming-language implementation of topology optimization applied to steady-state Navier-Stokes flow, *Int. J. Numer. Meth. Engng* 65, 975-1001, 2006.

[27] K. Svanberg, The method of moving asymptotes - a new method for structural optimization, *Int. J. Numer. Meth. Engng* 24, 359-373, 1987.

[28] O. Sigmund, Morphology-based black and white filters for topology optimization, *Struct. Multidisc. Optim.* 33, 401-424, 2007.

[29] M.B. Dühring, J.S. Jensen and O. Sigmund, Acoustic design by topology optimization, *J. Sound Vib.*, 317, 557-575, 2008.

[30] O. Sigmund and J.S. Jensen, Systematic design of phononic band-gap materials and structures by topology optimization, *Phil. Trans. R. Soc. Lond. A*, 361, 1001-1019, 2003.

[31] www.rsoftdesign.com

[32] O. Sigmund, Manufacturing tolerant topology optimization, *Acta. Mech. Sin.*, 25, 227-239, 2009.

Publication [P3]

Surface acoustic wave driven light modulation

Surface acoustic wave driven light modulation

Mike van der Poel (1), Markus Beck (2), Maria B. Dühring (3), Maurício M. de Lima (4), Lars H. Frandsen (1), Christophe Peucheret (1), Ole Sigmund (3), Uwe Jahn (2), Jørn M. Hvam (1), and Paulo Santos (2)
1) COM-DTU, NanoDTU, Technical University of Denmark, DK-2800 Kgs. Lyngby, Denmark 2) Paul-Drude Institut für Festkörperfysik, D-10117 Berlin, Germany, 3) Department of Mechanical Engineering, NanoDTU, Technical University of Denmark, DK-2800 Kgs. Lyngby, Denmark, 4) Material Science Institute, University of Valencia, 46071 Valencia, Spain

Abstract: *Si and GaAs Mach-Zehnder type light modulators with surface acoustic wave (SAW) excitation are demonstrated. Relative modulation depths of 40% at 950 nm and 5% at 1550 nm in the GaAs and Si samples respectively are achieved at SAW frequency around 600 MHz. Active area dimensions are down to 20 x 20 μm.*

Introduction

Compact, integrated light modulation devices are essential components in many photonic applications and have received large attention in recent years [1-4]. Of particular interest is the realization of modulation functionality in the Si material system [3-5] as this has the potential for seamless integration with electronics.

An important class of light modulators work by achieving uneven phase shifting of the light in the two arms of a Mazh-Zehnder interferometer (MZI). The change in relative phase and resulting constructive or destructive interference of the light waves at the exit port is the mechanism behind the light modulation. The principle of the phase change can be based upon shifting of the modal index of the guided wave by utilizing e.g. the thermo-optic [2], the electro-optical effect [3] or the Kerr effect [4].

In this paper we present light modulation in compact Si and GaAs [1] MZI devices with phase shifting resulting from surface acoustic wave (SAW) modulation of the waveguides.

SAW modulator

A SAW consists of a strain field propagating along the surface of a solid. The field strength decays towards the bulk with the wavelength as the characteristic decay length. The SAW field can be excited by applying an electrical RF field to an interdigital transducer (IDT) on a piezo electric material. The SAW strain field results in a periodic refractive index modulation $\Delta n \sin(\omega_{SAW} t)$ in the material, where ω_{SAW} is the SAW angular frequency. This is the primary

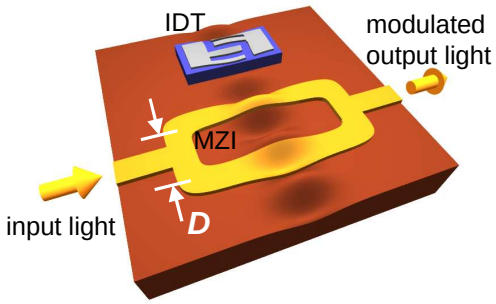

Fig. 1: Schematic representation of an MZI device with SAW modulation. Separation of the MZI arms, *D*, is an odd number of half SAW wavelenghts, so that tbhe SAW field modulates the two arms in opposite phase.

mechanism behind the optical phase change $\Delta\phi_1$ and $\Delta\phi_2$ in arm 1 and 2 of a SAW based MZI modulator respectively. For an interaction length L, the light waves of common angular frequency ω in arm 1 and 2 of the MZI undergo a harmonic phase shift of magnitude $\Delta\phi_{1,2} = \omega\Delta n_{1,2} L/c$, where c is the speed of light in vacuum. The index change is proportional to the strength of the SAW strain field and thus changes sign during a SAW cycle. We note that it follows from this, that the induced phase shift is proportional to the square root of the SAW power.

In the experiments reported here, we use a SAW propagating perpendicularly to a MZI with arm spacing D corresponding to an odd number of half SAW waves (fig. 1). In this configuration, the SAW results in a modal index variation of opposite phase in the two arms thus increasing the phase difference of the two light waves when combined at the exit port of the MZI device. Besides the acoustic phase moulation, the light field at the exit port also dependends on the static phase difference $\Delta\phi_s$ between the two interferometer arms. A path-length difference in the two arms of Δx results in a static phase difference $\Delta\phi_s = \omega n \Delta x/c$, where n is the modal index of the guided light. We write the electrical field E_{out} of the light at the exit port as

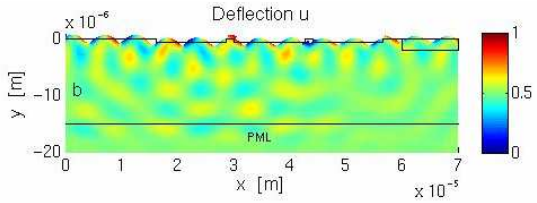

Fig. 2: SAW propagating in the MZI from the left to the right. The colorbar indicates the deflections in the x-direction.

$$E_{out} = \frac{E_0}{2}\{\sin[\omega t - \Delta\phi_1 \sin(\omega_{SAW} t)] + \sin[\omega t - \Delta\phi_2 \sin(\omega_{SAW} t - \pi/2) - \Delta\phi_s]\}, \quad (1)$$

where E_0 is the electrical field amplitude at the MZI input.

The light modulation in a MZI device as described above [1] depends strongly on the static phase difference between the two interferometer arms. For a small amplitude of the phase modulation $\Delta\phi_{1,2}$, for instance, the maximum modulation at the SAW frequency is achieved with a static phase difference $\Delta\phi_s = \pi/2$, while $\Delta\phi_s = 0$ or π results in no modulation at the SAW frequency and instead a modulation at twice the SAW frequency.

SAW modelling

To understand and improve the interaction of the SAW elastic field with the optical field in the waveguides a numerical model of the MZI is made. The SAW generation by IDTs is modeled using a 2D finite-element model of a piezoelectric, inhomogeneous material implemented in the high-level programming language 'Comsol Multiphysics'. To prevent unwanted reflections of the SAW from the boundaries of the calculation domain perfectly matched layers [6] are employed to absorb the elastic and electric field at the sides and at the bottom of the domain. The solution of this model gives the stresses in the material introduced by the SAW, from which the associated change in refractive index in the two wave guides can be calculated. This model is successively coupled to an optical model where the time independent wave equation is solved as an eigenvalue problem giving the effective refractive index of the fundamental mode in the waveguides.

With this numerical model the propagation of the SAW in the MZI can be studied. In fig. 2, a SAW is generated at the left part of the surface and propagating in the right direction through a GaAs MZI. It is observed that a part of the SAW propagates through the MZI and another part is redirected into the bulk substrate because of the disturbance at the surface caused by the wave guides. Figure 3 shows the

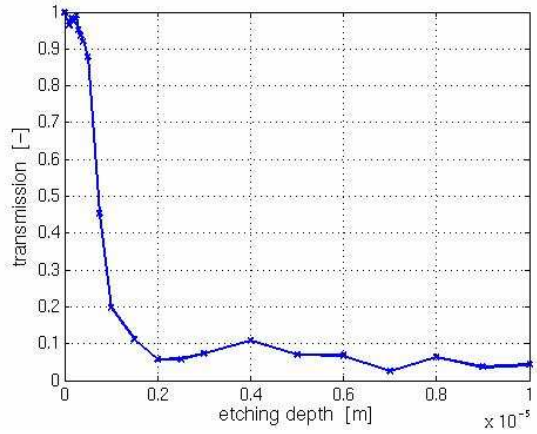

Fig. 3: The transmission of the SAW as function of the etching depth.

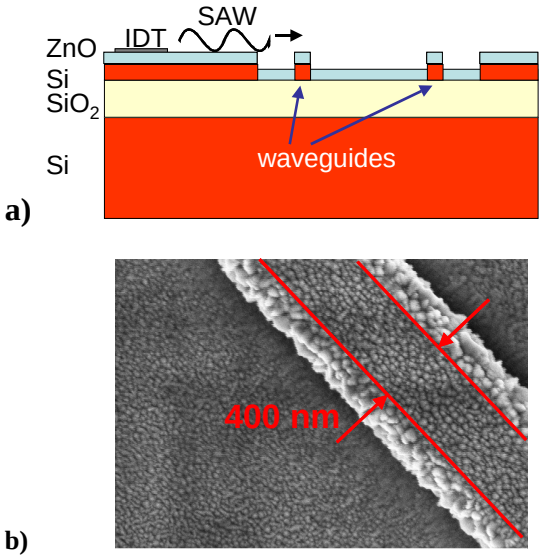

Fig. 4: a) Schematic edge view of SOI wafer with waveguides. b) SEM micrograph with top view of 400 nm ridge waveguide covered with ZnO.

transmission of the SAW (calculated as the part of the deflections in the x-direction that reaches the marked rectangle in the right corner of the domain in fig. 1) as function of the etching depth. It is seen that for small etching depths almost the entire SAW is transmitted, but for larger depths most of the SAW energy will be reflected back or disappear into the bulk substrate.

This model can be used to simulate the acousto-optical interaction in the MZI from the experiments and by a parameter study of the geometry it can be determined how the geometry should be changed in order to improve the optical modulation.

Devices

Devices based upon the Si and GaAs material system have been fabricated.

The GaAs MZI devices were fabricated on a (Al,Ga)As waveguide structure grown by molecular beam epitaxy on a GaAs (100) wafer. The waveguide core consists of a 300-nm-thick GaAs core grown on a 1500-nm-thick $Al_{0.2}Ga_{0.8}As$ cladding layer. The acoustic waves were generated by a split-finger IDT with an aperture of 120 μm and operating at an acoustic wavelength λ_{SAW}=5.6 μm. The waveguides were fabricated by combining contact optical lithography with plasma etching. Further details of the fabrication process can be found in Ref. [1].

The Si based samples were made on a Si-on-insulator (SOI) wafer with a top 340 nm thick Si layer. 400 nm wide single-mode ridge waveguides were defined by electron-beam lithography (fig. 4a). Si itself is not a piezo electrical material: for the electric SAW excitation, the sample is covered with a 500 nm layer of piezoelectric ZnO before IDT deposition. Scanning electron microscopy (SEM) of the sample after ZnO deposition (fig. 4b) shows a corrugated surface with ZnO crystallites grown from all surfaces. This is ex-

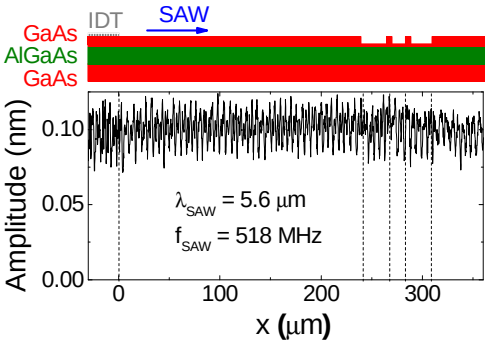

Fig. 5: Transmission of a SAW across the GaAs MZI structure.

pected to lead to the undesirable effect of increased 1) optical waveguide losses and 2) scattering of the SAW wave at Si etch steps. The former is discussed in a section below. To investigate the latter, we perform interferometric measurements of sample surface displacement. Fig. 5 shows interferometric measurements of the amplitude of the acoustic wave normal to the surface in similar structures on a GaAs/AlGaAs sample. Consistent with the calculations discussed above, the reflections of the wave at the grooves and ridges of the structure are small. In the SOI structures, we observe considerably stronger reflections.

Modulation experiments

The optical properties of the GaAs MZI devices were measured by coupling light to the cleaved edge of the waveguides using a tapered fiber and collecting the transmitted light using a microscope objective. As a light source, we used a CW superluminescence diode with peak emission at 950 nm and full width of half maximum of approx. 50 nm. The transmitted intensity was detected with a time resolution of 300 ps using a Si avalanche photodiode. Fig. 6 compares the time dependence of the transmitted intensity (normal-

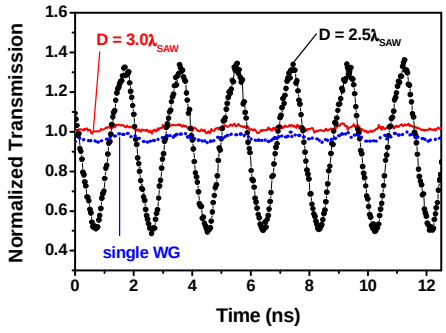

Fig. 6: Transmission of MZI devices with waveguide separation D = 3 λ_{SAW} (solid line) and 2.5 λ_{SAW} (dots). The dotted line shows the transmission in a control structure where the MZI arms have been replaced by a single waveguide. All measurements were carried out by coupling an RF-power P_{IDT}=60 mW to the IDTs.

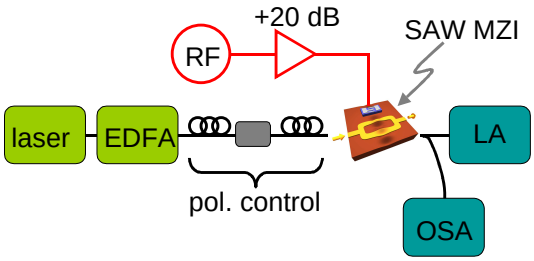

Fig.7: Experimental setup for characterizing SOI modulator.

ized to the transmission in the absence of acoustic excitation) of devices with distances *D* between the MZI arms of 3 λ_{SAW} (solid line) and 2.5 λ_{SAW} (dots). All measurements were carried out by coupling an rf-power P_{IDT}=60 mW to the IDTs. For the devices with 3 λ_{SAW}, as well as in control structures where the MZI arms have been replaced by a single waveguide (dotted line in fig. 6), the relative modulation does not exceed 2 %. In devices with D = 2.5 $\lambda_{SAW,}$ where the MZI arms are excited with opposite acoustic phases, the relative modulation reaches 40 %. These results demonstrate the large modulation performance achieved by the simultaneous out-of-phase modulation of the MZI arms. By employing focusing IDTs, we were able to further increase the performance and to reduce the length of the MZI arms down to approx. 15 µm. [1].

The experimental setup of the modulation experiments carried out on the SOI devices can be summarized as follows (fig. 7): A fiber-coupled, tunable CW laser and Er doped fiber amplifier (EDFA) was used as light source in the wavelength range 1530-1580 nm. A polarization controller was used to achieve transverse-electric (TE) polarized light before using a tapered fiber to couple the light into the MZI device under test. Modulation properties of the light output from the MZI were then analyzed using a lightwave analyzer (LA).

The MZI were deliberately made with a path length difference in the two interferometer arms of 34 µm so as to have a wavelength-dependent static phase

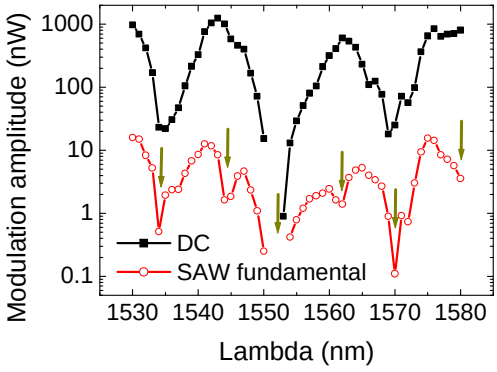

Fig. 8: Transmission (black line, filled symbols) and modulation (red line, open symbols) spectrum of SOI MZI with arm separation of *D*=4.5λ_{SAW}. RF power to IDTs P_{RF}= 50 mW.

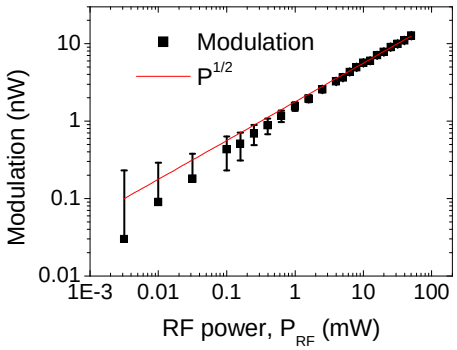

Fig. 9: Modulationamplitude at SAW frequency vs. RF power to the IDT, P_{RF}.

$\Delta\phi_s = \omega n \Delta x/c$ as mentioned above. This results in a sinusoidally varying DC transmission spectrum of the device (fig. 8). The overall transmission of the device at constructive interference at the exit port was about –20 dB. This poor performance is primarily ascribed to the two T-splitters in the MZI. These topology-optimized ridge-waveguide splitters [7] were designed without ZnO coverage in mind. We also believe that the deviations from a sinusoidal transmission spectrum are due to the T-splitters.

The MZI had an arm separation of D=4.5λ_{SAW} corresponding to an out-of-phase phase-change in the two interferometer arms when SAW modulation is applied to the device. It follows from eq. 1 that the modulation spectrum at the SAW frequency will display minima at both the DC transmission maxima and minima in agreement with fig. 8 (minima marked with arrows). Furthermore it is concluded from eq. 1, that the observed modulation at the SAW fundamental frequency is consistent with a refractive change of 2.3×10^{-5}. This value is also consistent with the absence of measurable higher harmonics in the modulated light at all wavelengths. The relative modulation in the investigated wavelength range varied from 0% to 8%. Finally, we mention that the modulation amplitude vs. RF power was measured, and a reasonable agreement with the expected $P_{SAW}^{1/2}$ dependency, as demonstrated in fig. 9.

Conclusion

SAW-driven MZI is a promising technology for compact light modulators in integrated semiconductor platforms such as Si and GaAs.

Acknowledgments

This project is supported by the EU network of excellence ePIXnet. Mike van der Poel acknowledges support from the Danish Research Council.

References

1 M. M. de Lima, Jr., M. Beck, R. Hey, and P. V. Santos, Appl. Phys. Lett., vol. 89, p. 121104, 2006.
2 E. A. Camargo, H. M. H. Chong, and R. M. De La Rue, Opt. Express, vol. 12, p. 588, 2004.
3 R. S. Jacobsen et al., Nature, vol. 44, p. 199, 2006.
4 M. Hochberg et al., Nature Mater., vol. 5, p. 703, 2006.
5 M. Lipson, J. Lightwave Techn., vol. 23, p. 4222, 2005.
6 U. Basu and A. K. Chopra,, Comput. Methods Appl. Mech. Engrg., vol. 192, p. 1337 (2003).
7 L. H. Frandsen, paper CMV4, Conference of Lasers and Electro-Optics (CLEO), 2006.

Publication [P4]

Improving the acousto-optical interaction in a Mach-Zehnder interferometer

Improving the acousto-optical interaction in a Mach–Zehnder interferometer

Maria B. Dühring[a] and Ole Sigmund
Department of Mechanical Engineering, Solid Mechanics, Technical University of Denmark, 2800 Lyngby, Denmark

(Received 2 December 2008; accepted 1 March 2009; published online 22 April 2009)

A method for modeling the interaction of the mechanical field from a surface acoustic wave and the optical field in the waveguides of a Mach–Zehnder interferometer is presented. The surface acoustic wave is generated by an interdigital transducer using a linear elastic plane model of a piezoelectric, inhomogeneous material, and reflections from the boundaries are avoided by applying perfectly matched layers. The optical modes in the waveguides are modeled by time-harmonic wave equations for the magnetic field. The two models are coupled using stress-optical relations and the change in effective refractive index introduced in the Mach–Zehnder interferometer arms by the stresses from the surface acoustic wave is calculated. It is then shown that the effective refractive index of the fundamental optical mode increases at a surface acoustic wave crest and decreases at a trough. The height and the width of the waveguides are varied for a silicon on insulator sample, and it is shown that the difference in effective refractive index between the waveguides can be increased 12 times for the right choice of waveguide size such that the optical modulation is improved. The difference is four times bigger if the waveguides are kept single moded. It is furthermore shown that the difference increases more than ten times when the waveguides are buried below the surface, where the mechanical stresses have their maximum, and in the case where two interdigital transducers are used the difference is increased 1.5 times. © *2009 American Institute of Physics*. [DOI: 10.1063/1.3114552]

I. INTRODUCTION

In the last four decades, surface acoustic waves (SAWs) have received increasing attention and have found use in a range of different applications. One type of SAW, also known as a Rayleigh wave, is defined as elastic vibrations that propagate along a material surface and consists of a longitudinal and a shear component.[1] There is almost no decay of the amplitude along the propagation direction, but there is exponential decay into the bulk material such that most of the energy density is confined within one wavelength of the surface. In piezoelectric materials the elastic field is accompanied by an electric field, and in these materials it was suggested by White and Voltmer[2] in 1965 to generate SAWs by interdigital transducers (IDTs) by the inverse piezoelectric effect. Since then, SAWs have been widely used in electromechanical filters and resonators in telecommunication as well as in oscillators and sensors.[3–5] In recent years another application of SAWs has been introduced, which is modulation of optical waves for signal generation in semiconductor structures.[6,7] Experimental results are reported in Refs. 8 and 9 for a compact and monolithic modulator consisting of a SAW driven Mach–Zehnder interferometer (MZI). The relative modulation obtained with waveguides of GaAs on an AlGaAs layer and with straight IDTs exceeded 40%. However, for silicon waveguides on a silica layer, materials which are easier to work with and common in optical components, only a relative modulation between 0% and 8 % was obtained. Here a general finite element model for calculating the acousto-optical interaction between SAWs and optical waves is presented and it is employed to improve the modulation of the optical wave in the silicon on insulator (SOI) MZI. The interaction is simulated by coupling a model of a piezoelectric material with an optical model where the effective refractive indices for the propagating optical modes can be calculated by solving the in-plane time-harmonic wave equation. Finite element simulation of SAWs in a piezoelectric material has been discussed by others for both stratified, periodic structures[10,11] as well as for finite domains with straight surfaces and a single piezoelectric material.[12] In this work the periodic model presented in Ref. 11 for a piezoelectric material is used for a stratified structure and is furthermore extended to finite structures by employing perfectly matched layers (PMLs),[13] which surround the SAW device such that reflections from the domain boundaries are avoided. With this model it is possible to simulate nonperiodic SAW devices on a stratified structure. A description of the MZI problem and the coupled acousto-optical model is found in Sec. II. In Sec. III results on the SAW generation and the optical modes are presented and it is shown how the optical modulation in the MZI can be improved by changing the height and width of the waveguides and introducing other changes in the structure. Section IV concludes the article and suggests further work.

II. THE ACOUSTO-OPTICAL MODEL

A. Problem description

In this work a numerical model of SAW driven light modulation in a MZI is presented. A MZI is an optical device consisting of a ridge waveguide that is split into two waveguide arms and after a distance the arms are joined into one

[a]Electronic mail: mbd@mek.dtu.dk.

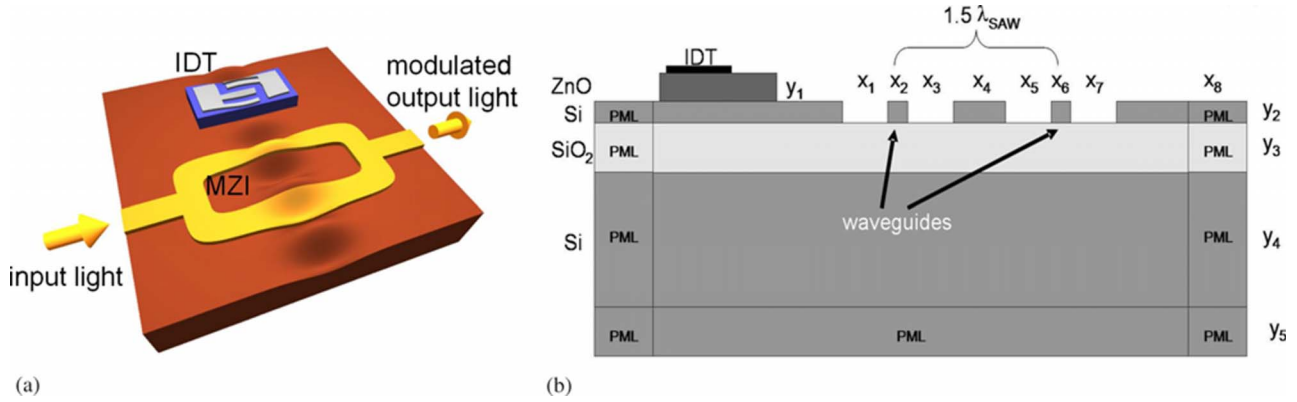

FIG. 1. (Color online) Light modulation in a MZI with a SAW generated by an IDT. (a) Three dimensional geometry of a MZI with a propagating SAW ([van der Poel (Ref. 9)]. (b) A 2D cross section through the waveguide arms of the MZI, which is used in the simulations. The SAW is absorbed in PMLs at the boundaries. The dimensions indicated in are in microns given by $x_1=2.77$, $x_2=0.45$, $x_3=2.79$, $x_4=2.39$, $x_5=2.77$, $x_6=0.45$, $x_7=2.79$, $x_8=15.0$, $y_1=0.5$, $y_2=2.34$, $y_3=1.0$, $y_4=16.8$, and $y_5=15.0$.

waveguide again as illustrated by Fig. 1(a). When a SAW is propagating perpendicular to the waveguide arms it is possible to obtain a periodic modulation of the light. When the distance between the waveguide arms is an unequal number of half SAW wavelengths, different situations will occur. At one point in time, a wave node will be present at each waveguide and the output light will not change. In another point in time, a wave crest will be located at one waveguide, whereas a trough will appear at the other waveguide. The applied stresses with opposite sign will introduce a refractive index difference in the arms, which causes an opposite phase change in them. By constructive and destructive interferences the light will be turned on and off periodically with a multiplum of the SAW frequency depending on the static phase difference in the two arms, which can be introduced by a length difference between them. To model the SAW propagation and the optical modes in the waveguides, it is sufficient to consider a two dimensional (2D) model of a cross section of the two waveguides as seen on Fig. 1(b). The SAW is generated at the IDT to the left and propagates in both the left and the right horizontal direction and is absorbed in the PMLs. To the right the SAW will pass through the two waveguides. To simulate the acousto-optical interaction in the MZI a model describing the SAW generation in a piezoelectric material is coupled with an optical model describing the propagation of the light waves in the waveguides. It is assumed that the stress-optical effect is dominant compared to the electro-optical effect, which will be neglected here (see Ref. 8). It is furthermore assumed that the SAW will affect the optical wave, but the optical wave will not influence the SAW, so the problem is solved by first calculating the stresses in the MZI introduced by the SAW. Then the change in refractive index in the materials due to the stresses can be calculated, and finally by solving the optical model the effective refractive index of the different possible light modes can be determined. The mathematical model, which is solved by the commercial finite element program COMSOL MULTIPHYSICS,[14] is described in the following subsections.

B. The piezoelectric model

The SAW is generated in a piezoelectric material by applying an electric potential to the electrode fingers of the IDT on the surface of the solid. The applied electric field will introduce mechanical displacements in the solid by the inverse piezoelectric effect. The behavior of the piezoelectric material is described by the following model as found in Ref. 15. The mechanical strain S_{ij} is for small displacements given by the tensor expression

$$S_{ij} = \frac{1}{2}\left(\frac{\partial u_i}{\partial x_j} + \frac{\partial u_j}{\partial x_i}\right), \tag{1}$$

where u_i are the displacements and x_i are the coordinates. The stresses T_{ij} have to fulfill Newton's second law for a dynamic problem. The SAW is generated by applying a harmonic electric potential V to the electrodes given by

$$V(x_j,t) = V(x_j)e^{i\omega_{\mathrm{SAW}}t}, \tag{2}$$

where ω_{SAW} is the angular frequency of the potential driving the SAW and t is the time. As the electric field is harmonic, the strain and stresses will vary harmonically as well and Newton's second law takes the form

$$\frac{\partial T_{ij}}{\partial x_j} = -\rho\omega_{\mathrm{SAW}}^2 u_i, \tag{3}$$

where ρ is the density of the material. The electrical behavior of the material is described by Maxwell's equations for the electric field. It is assumed that there are no free electric charges in the material, so Gauss' law reduces to

$$\frac{\partial D_j}{\partial x_j} = 0, \tag{4}$$

where D_j is the electric displacement. The electric field E_j can be derived from a scalar potential as in electrostatic problems, and Faraday's law then states

$$E_j = -\frac{\partial V}{\partial x_j}. \tag{5}$$

The mechanical stresses and the electric displacement both depend on the strain and the electric field by the constitutive relations

$$T_{jk} = \tilde{c}^E_{jklm} S_{lm} - \tilde{e}^T_{ijk} E_i, \tag{6}$$

$$D_i = \tilde{e}_{ijk} S_{jk} + \tilde{\varepsilon}^S_{ij} E_j, \tag{7}$$

where $\tilde{c}^E_{jklm}$ are the elastic stiffness constants, $\tilde{e}_{ijk}$ are the piezoelectric stress constants, and $\tilde{\varepsilon}^S_{ij}$ are the permittivity constants. The materials are, in general, anisotropic, and as it is only possible to generate the SAW by the inverse piezoelectric effect in certain directions, the material tensors have to be rotated. This is indicated by the tilde above the material tensors. The rotation is done according to Euler's transformation theory as explained in Ref. 16. Here the relation between the original directional vector r_j and the rotated vector $\hat{r}_i$ is given by

$$\hat{r}_i = a_{ij} r_j, \tag{8}$$

where a_{ij} is the transformation matrix given by the Euler angles φ_1, φ_2, and φ_3, where the crystal axes are rotated clockwise about the x_3-axis, then the x_2-axis, and finally the x_3-axis again. The material property matrices can then be transformed by the transformation matrix a_{ij} and the Bold matrix M_{ijmn} as follows:

$$\tilde{c}^E_{ijkl} = M_{ijmn} M_{klpq} c^E_{mnpq}, \quad \tilde{e}_{ijk} = a_{il} M_{jkmn} e_{lmn},$$

and

$$\tilde{\varepsilon}^S_{ij} = a_{ik} a_{jl} \varepsilon^S_{kl}. \tag{9}$$

At the boundaries, both mechanical and electrical conditions must be specified to solve the problem. Considering the mechanical conditions the upper surface is stress-free and the sides and the bottom are clamped outside the PMLs,

$$\text{stress free surface:} \quad T_{jk} m_k = 0, \tag{10}$$

$$\text{clamped surface:} \quad u_i = 0, \tag{11}$$

where m_k is the normal unit vector pointing out of the surface. At the upper surface there are no charges and therefore electric insulation occurs, meaning that the normal component of the electric displacement is zero. At the sides and at the bottom of the domain it is assumed that the electric potential is zero, whereas at the interface between the electrodes and the substrate the potential is V_p at the positively charged electrodes and $-V_p$ at the negatively charged electrodes. The electrical boundary conditions are summarized below,

$$\text{electric insulation:} \quad D_i m_i = 0, \tag{12}$$

$$\text{zero potential:} \quad V = 0, \tag{13}$$

$$\text{applied positive potential:} \quad V = V_p, \tag{14}$$

$$\text{applied negative potential:} \quad V = -V_p. \tag{15}$$

The piezoelectric problem is solved by a plane formulation obtained by setting S_{i3}, S_{3j} and E_3 as well as T_{i3}, T_{3j}, and D_j equal to zero. The governing equations (3) and (4) are solved simultaneously to find the three unknowns u_1, u_2, and V.

1. PMLs

To prevent reflections of the SAW from the outer boundaries, which will disturb the wave propagation, PMLs are applied around the regular domain as illustrated on Fig. 1(b). In Ref. 13 PMLs are introduced for time-harmonic elastodynamic problems and are now extended to piezoelectric materials. The PMLs have the property that the mechanical and the electrical disturbances are gradually absorbed in the layers before they reach the outer boundaries. In this way there are no reflections that can disturb the propagation of the SAW and an infinite domain is thus simulated by a finite domain. An artificial damping γ_j at position x_j in the PMLs is introduced on the form

$$\gamma_j(x_j) = 1 - i\sigma_j (x_j - x_l)^2, \tag{16}$$

where x_l is the coordinate at the interface between the regular domain and the PML and σ_j is a suitable constant. The damping is introduced in the expressions for the strain and the electric field,

$$S_{ij} = \frac{1}{2}\left(\frac{1}{\gamma_j}\frac{\partial u_i}{\partial x_j} + \frac{1}{\gamma_i}\frac{\partial u_j}{\partial x_i}\right) \quad \text{and} \quad E_j = -\frac{1}{\gamma_j}\frac{\partial V}{\partial x_j}, \tag{17}$$

as well as in the governing equations for the piezoelectric material

$$\frac{1}{\gamma_j}\frac{\partial T_{ij}}{\partial x_j} = -\rho\omega^2 u_i \quad \text{and} \quad \frac{1}{\gamma_j}\frac{\partial D_i}{\partial x_j} = 0. \tag{18}$$

There is no damping outside the PMLs and here $\gamma_j = 1$. A suitable thickness of the PMLs as well as the value of σ_j must be found by numerical experiments such that both the mechanical and electrical disturbances are absorbed before reaching the outer boundaries. However, the absorption must also be sufficiently slow as reflections will occur at the interface between the regular domain and the PML if their material properties are not comparable.

C. The optical model

After the mechanical stresses in the material have been computed by the piezoelectric model described above, the refractive index n_{ij} in the stressed material can be calculated according to the stress-optical relation[17]

$$n_{ij} = n^0_{ij} - \tilde{C}_{ijkl} T_{kl}, \tag{19}$$

where n^0_{ij} is the refractive index in the stress-free material. $\tilde{C}_{ijkl}$ are the rotated stress-optical constants obtained by the expression

TABLE I. The elastic stiffness constants (10^{11} N m^{-2}) and the density (kg m^{-3}) for the materials used in the piezoelectric model.

Material	c_{11}^E	c_{12}^E	c_{13}^E	c_{22}^E	c_{23}^E	c_{33}^E	c_{44}^E	c_{55}^E	c_{66}^E	ρ
GaAs	1.183	0.532	0.532	1.183	0.532	1.183	0.595	0.595	0.595	5316.5
Si	1.660	0.639	0.639	1.660	0.639	1.660	0.796	0.796	0.796	2330
SiO_2	0.785	0.161	0.161	0.785	0.161	0.785	0.312	0.312	0.312	2200
ZnO	2.090	1.205	1.046	2.096	1.046	2.106	0.423	0.423	0.4455	5665

$$\tilde{C}_{ijkl} = M_{ijmn} M_{klpq} C_{mnpq}. \tag{20}$$

For a given optical mode of order ν and with the out of plane propagation constant β_ν, the effective refractive index $n_{\text{eff},\nu}$ is defined as

$$n_{\text{eff},\nu} = \beta_\nu / k_0, \tag{21}$$

where k_0 is the free space propagation constant. It is assumed that the propagating optical modes have harmonic solutions on the form

$$H_{p,\nu}(x_1, x_2, x_3) = H_{p,\nu}(x_1, x_2) e^{-i\beta_\nu x_3}, \tag{22}$$

where $H_{p,\nu}$ is the magnetic field of the optical wave. The governing equation for the magnetic field is thus the time-harmonic wave equation

$$e_{ijk} \frac{\partial}{\partial x_j} \left(b_{kl} b_{lm} e_{mnp} \frac{\partial H_p}{\partial x_n} \right) - k_0^2 H_p = 0, \tag{23}$$

where e_{ijk} here is the alternating symbol and $b_{ik} n_{kj} = \delta_{ij}$. For a given value of k_0, the propagation constant β_ν for the possible modes is found by solving the wave equation as an eigenvalue problem, whereby the effective refractive indices can be obtained. In this work the set of equations are reduced such that the model is only solved for the transverse components of the magnetic fields H_1 and H_2. As the energy of the lower order optical modes is concentrated in the waveguides, the calculation domain, where the eigenvalue problem is solved, can be reduced to a smaller area around each of the waveguides. At the boundary of such a domain it is assumed that the magnetic field is zero as the energy density quickly decays outside the waveguide, thus the boundary condition is

$$e_{ijk} H_j m_k = 0, \tag{24}$$

where e_{ijk} again is the alternating symbol and m_k is the normal unit vector pointing out of the surface.

III. RESULTS

In this section results are presented for the SAW propagation, the optical waves in the waveguides, and their acousto-optical interaction.

A. Simulation of SAWs

The piezoelectric model is first employed to solve the propagation of a SAW in a GaAs sample with straight surface to show that the model performs as expected. The SAW is generated by ten double electrode finger pairs. Each of the electrodes has a width equal to 0.7 μm and is placed 0.7 μm apart such that the wavelength of the generated SAW is 5.6 μm. GaAs is a piezoelectric material with cubic crystal structure. The material constants used in the piezoelectric model are given in Tables I and II and are here given in the usual matrix form for compactness reasons. The frequency is $f_{\text{SAW}} = 510$ MHz (where $f_{\text{SAW}} = \omega_{\text{SAW}} / 2\pi$) and the applied electric potential is $V_p = 1$ V. The constant σ_j controlling the damping in the PMLs is set to 10^{10}. GaAs is piezoelectric in the [110] direction, so for the SAW to propagate in this direction the material tensors have to be rotated by the angle $\varphi_2 = \pi/4$. Second order Lagrange elements are used for all the calculations. In Fig. 2(a) the displacement u_2 in the x_2-direction is plotted in the domain with a displacment scaling factor set to 1000, and it is seen that the SAW is generated at the electrodes and propagates away from them to the right and the left. In the PMLs the wave is gradually absorbed. The same results are illustrated at Fig. 2(b) where the absolute amplitude abs(u_2) is plotted along the material surface. It is seen how a standing wave is generated at the electrodes because the SAW here travels in both directions. Away from the electrodes the SAW is a traveling wave and therefore the amplitude is nearly constant. It is also seen how the SAW is absorbed in the PMLs. In Fig. 3(a) the displacements u_1 and u_2 are plotted as function of the depth for $x_1 = 85$ μm. It is seen that the displacements are concentrated within one SAW wavelength of the surface as expected. Below the surface they have smaller oscillations. This is due to the finite depth and the use of the PMLs that are not exactly acting as an infinite domain. On Fig. 3(b) the absolute amplitude abs(u_2) normalized with the square root of the applied electric power P is plotted as function of the frequency f_{SAW} at a point on the surface to the right of the

TABLE II. The piezoelectric stress constants and the permittivity constants for the materials used in the piezoelectric model.

Material	e_{14} (C m^{-2})	e_{15} (C m^{-2})	e_{24} (C m^{-2})	e_{25} (C m^{-2})	e_{31} (C m^{-2})	e_{32} (C m^{-2})	e_{33} (C m^{-2})	e_{36} (C m^{-2})	ε_{11}^S (10^{-11} F m)	ε_{22}^S (10^{-11} F m)	ε_{33}^S (10^{-11} F m)
GaAs	−0.160	0	0	−0.160	0	0	0	−0.160	9.735	9.735	9.735
Si	0	0	0	0	0	0	0	0	11.5	11.5	11.5
SiO_2	0	0	0	0	0	0	0	0	2.37	2.37	2.37
ZnO	0	−0.480	−0.480	0	−0.573	−0.573	1.321	0	7.38	7.38	7.83

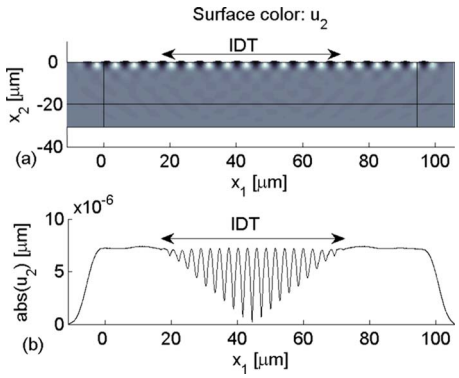

FIG. 2. (Color online) Generation of a SAW in a GaAs sample by the piezoelectric model. The position of the IDT is indicated. (a) The color indicates the displacement u_2 and the shape of the surface is deformed with the unified displacements u_1 and u_2. (b) The graph shows the absolute amplitude abs(u_2) along the material surface as function of x_1

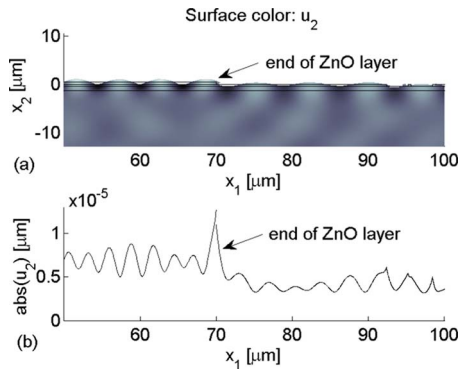

FIG. 4. (Color online) Generation of SAWs in a SOI sample by the piezoelectric model. The results are given to the right of the IDT. (a) The color indicates the displacement u_2 and the shape of the surface is deformed with the unified displacements u_1 and u_2. (b) The graph shows the absolute amplitude abs(u_2) along the material surface as function of x_1.

IDT for the frequency interval of 210–810 MHz for 10 and 20 electrode pairs, respectively. The power P is calculated by the expression[16]

$$P = \Re \int_{L_{\mathrm{el}}} \frac{V(i\omega D_2 m_2)^*}{2} dL, \tag{25}$$

where L_{el} corresponds to boundaries with the electrodes and m_2 is the normal vector to the upper surface. Figure 3(b) shows that the highest value of abs(u_2)/$\sqrt{P}$ appears at f_{SAW} =510 MHz, which corresponds to the frequency found by experiments for a GaAs sample, see Ref. 18. Hence, these results show that the piezoelectric model performs as expected for generation of SAWs. It can also be observed from Fig. 3(b) that when the number of electrode pairs increases, the bandwidth decreases as more of the applied energy is confined to the SAW and consequently the amplitude increases. For twice as many fingers the bandwidth is halved, which is expected as the bandwidth is inversely proportional to the number of finger pairs (see Ref. 15). In practical constructions several hundred finger pairs are used in order to generate a strong SAW. For computational reasons only a fraction of the finger pairs can be used in these calculations. This means that a SAW with a smaller amplitude as in practice is used and the acousto-optical interaction is therefore also smaller than in experiments. However, the same physical effects are expected, which is discussed further in Sec. III C 1.

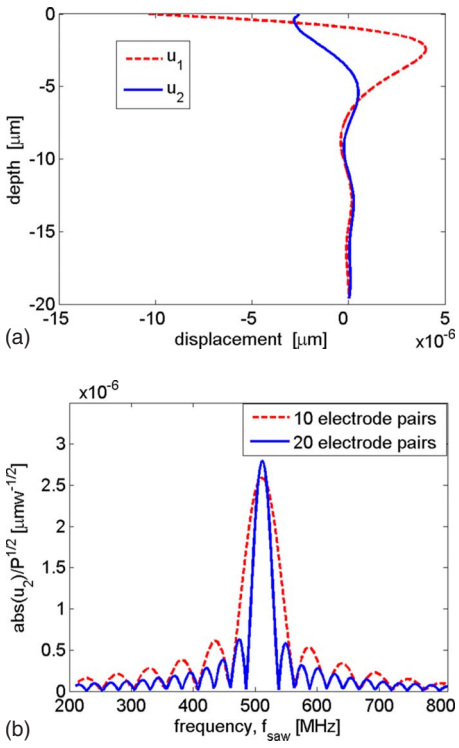

FIG. 3. (Color online) Results for the SAW in the GaAs substrate. (a) Displacements u_1 and u_2 as function of depth at position x_1=85 μm. (b) The absolute amplitude abs(u_2) normalized with the square root of the electrical power P as function of the frequency f_{saw} for 10 and 20 electrode pairs.

In Refs. 8 and 9 results for the acousto-optical modulation in a MZI with GaAs waveguides on a $Al_{0.2}Ga_{0.8}As$ layer were presented as well as results for a MZI with Si waveguides on a SiO_2 layer. In the first case a relative modulation of 40% was obtained with straight waveguides, but for the SOI sample the modulation was only between 0% and 8%. In this work attention is given to the SOI sample in order to understand the unsatisfactory performance and what can be done to improve the modulation. As Si is not piezoelectric the SAW is generated in a ZnO layer on top of the Si from which the SAW propagates toward the rest of the sample with the optical waveguides. The geometry is indicated on Fig. 1(b). The IDT consists of double double finger electrode pairs where each of the electrodes again has a width of 0.7 μm such that the wavelength of the generated SAW is 5.6 μm. The material constants for Si, SiO_2, and ZnO used in the piezoelectric model are given in Tables I and II. The applied potential is V_p=1 V and it is driven with the frequency f_{SAW}=630 MHz. After numerical experiments the constant σ_j in the PMLs is set to 10^{10}. All the materials are rotated with $\varphi_2=\pi/4$ such that the SAW propagates along the [110] direction. In Fig. 4(a) a zoom of the displacements u_2 around the end of the ZnO layer is plotted and it is seen how the wave is generated at the electrodes to the left and propagates from the ZnO layer to the rest of the sample with the waveguides to the right. In Fig. 4(b) the absolute ampli-

TABLE III. Stress-optical constants (Ref. 19).

Material	n_0 (-)	C_{11}, C_{22}, C_{33} (10^{-12} Pa^{-1})	C_{12}, C_{13}, C_{23} (10^{-12} Pa^{-1})	C_{44}, C_{55}, C_{66} (10^{-12} Pa^{-1})
Si	3.42	−11.35	3.65	0
SiO_2	1.46	0.65	4.50	−3.85

tude abs(u_2) is plotted along the material surface. From the two figures it is seen that there is a decrease in amplitude when the SAW propagates out in the Si/SiO_2 layer. In the ZnO layer the amplitude has a magnitude of around 0.8×10^{-5} μm. In the Si/SiO_2 layer the amplitude is almost halved and has a size around 0.5×10^{-5} μm—only 60% of the amplitude in the ZnO. So the SAW looses energy because of reflections and a change in material with different impedances. It is noted that smaller oscillations in the amplitude occur, and these indicate that standing waves appear in the device due to reflections from the discontinuity of the surface. Another reason for the poor modulation is that the wavelength of the SAW is 5.6 μm in the ZnO layer as expected from the size of the electrodes. However, when the SAW continuous to the Si/SiO_2 layer, the amplitude drops and the wavelength increases to approximately 7.3 μm—an increase of approximately 30%. This means that the two waveguides are no longer placed a multiple of half wavelengths apart, so to obtain a better modulation this distance must be corrected. To improve the model further it is necessary to examine how the SAW interacts with the optical wave in the waveguides, so the coupled acousto-optical model must be used.

B. Simulation of optical waves

In this section results for the optical eigenvalue problem are presented for the SOI MZI when x_4 from Fig. 1(b) is corrected to 4.94 μm such that there are 1.5 SAW wavelengths between the center of the waveguides. The free space wavelength of the optical wave is set to $\lambda_0 = 1531$ nm. The material constants for Si and SiO_2 used in the optical model are given in Table III. For air simply the refractive index $n_0 = 1$ is used. The size of the optical calculation domain is 5×4 μm. Figure 5 shows the x_3-component of the time averaged power flow of the fundamental mode in the waveguides when no stresses are applied.

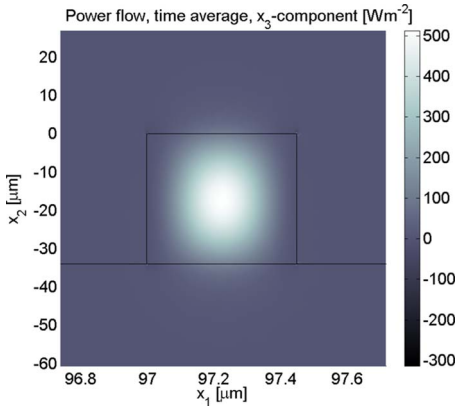

FIG. 5. (Color online) The x_3-component of the time averaged power flow of the fundamental mode in the waveguides when no stresses are applied.

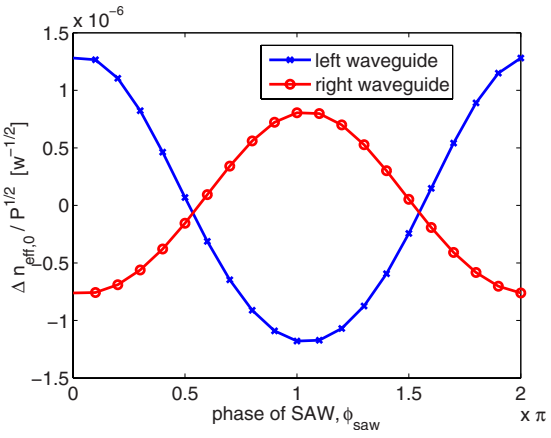

FIG. 6. (Color online) Change in the effective refractive index $n_{\text{eff},0}/\sqrt{P}$ of the fundamental mode in the two waveguides normalized by the square root of the power P as function of the SAW phase ϕ_{SAW}. $\phi_{\text{SAW}}=0$ corresponds to a wave crest in the left waveguide and a trough in the right.

eraged power flow of the fundamental mode in the waveguide obtained by solving the eigenvalue problem when no stresses are applied. The power flow is confined to the waveguide. Calculations are now done when stresses from the SAW are applied to the MZI and the resulting effective refractive indices are normalized with the square root of the applied electrical power P. To verify that the biggest difference in effective refractive index for the fundamental mode $n_{\text{eff},0}$ appears when one waveguide is influenced by a wave crest and the other is influenced by a wave trough, the change $\Delta n_{\text{eff},0}/\sqrt{P}$ is calculated in the two waveguides for a complete SAW phase passing through the waveguides. The results are seen on Fig. 6 where $\phi_{\text{SAW}}=0$ corresponds to a wave crest in the left waveguide and a trough in the right. It is verified from the two graphs that the biggest difference in effective refractive index $(n^l_{\text{eff},0}-n^r_{\text{eff},0})/\sqrt{P}$ between the left and the right waveguide is at the expected positions of the SAW with the value of 2.00×10^{-6} W$^{-1/2}$. It is also observed that there are losses between the waveguides due to reflections as $\Delta n_{\text{eff},0}/\sqrt{P}$ in the right waveguide never reaches the extreme values achieved in the left waveguide. Again, it is emphasized that the values of $\Delta n_{\text{eff},0}/\sqrt{P}$ are small, which is due to the limited numbers of electrodes used.

C. Increasing the difference in effective refractive index between the waveguides

In this subsection suggestions on how to change the geometry in order to increase the difference in effective refractive index $n_{\text{eff},0}$ between the waveguides are presented. An increased difference will improve the light modulation.

1. Changing the waveguide size

In this study the height and the width of the waveguides are changed. Figure 7(a) shows the difference in effective refractive index $(n^l_{\text{eff},0}-n^r_{\text{eff},0})/\sqrt{P}$ as function of the height h when a wave crest appears at the left waveguide and a trough at the right waveguide. The calculations are done for both the original case with six electrode pairs and for 12 electrode pairs. It is observed that there is an optimal height of the

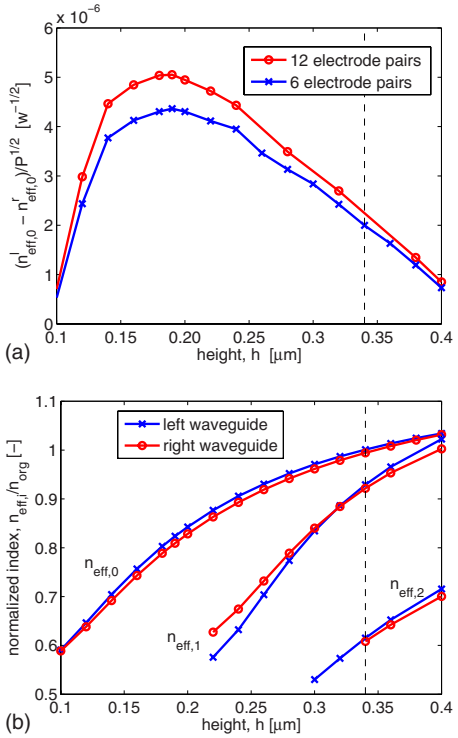

FIG. 7. (Color online) Results for a study of the height h of the waveguides with (- - -) indicating the results for the original waveguide geometry. (a) Difference in effective refractive index $(n^l_{\mathrm{eff},0}-n^r_{\mathrm{eff},0})/\sqrt{P}$ of the fundamental mode between the two waveguides as function of h for 6 and 12 electrode pairs. (b) The effective refractive index $n_{\mathrm{eff},i}$ for the three lowest order modes in the waveguides normalized to the value $n_{\mathrm{eff,org}}$ of the fundamental mode in the left waveguide for the original geometry as functions of h.

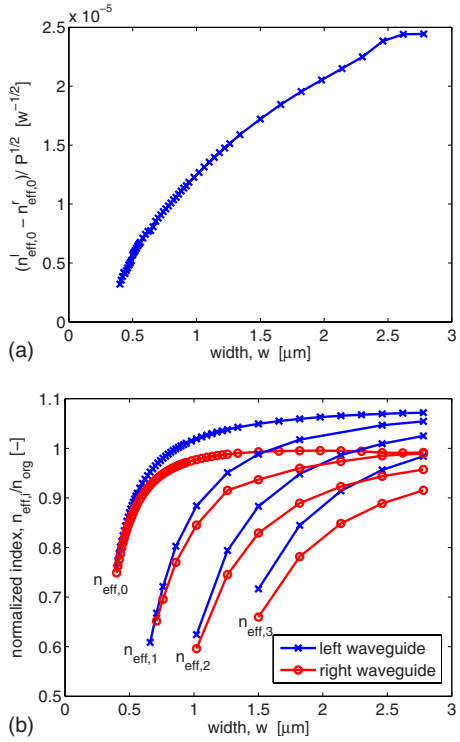

FIG. 8. (Color online) Results for a study of the waveguide width w for the optimal height h=0.19 μm. (a) Difference in effective refractive index $(n^l_{\mathrm{eff},0}-n^r_{\mathrm{eff},0})/\sqrt{P}$ of the fundamental mode between the two waveguides as function of w. (b) The effective refractive index $n_{\mathrm{eff},i}$ for the four lowest order modes in the waveguides normalized to the value $n_{\mathrm{eff,org}}$ of the fundamental mode in the left waveguide for the original geometry as functions of w.

waveguides for which the biggest difference in $n_{\mathrm{eff},0}$ is obtained. The optimal height is for both 6 and 12 electrode pairs found to be 0.19 μm with a difference in index equal to 4.36×10^{-6} $\mathrm{W}^{-1/2}$ for 6 electrode pairs, 2.2 times bigger than for the original height. The reason for this optimum is first of all that when the height of the waveguides decreases the reflections of the SAW due to the interruptions at the surface will be reduced and the stresses in the waveguides will be bigger. With a smaller height the center of the optical wave will move closer to the SiO_2 surface and will experience larger stresses as the biggest stresses of a SAW are found just below the surface of the material and not at the surface, see Fig. 3(a). However, when the height is too small, the optical wave will be less confined in the waveguide and will be increasingly influenced by the SiO_2 and the air. The air will for obvious reasons not contribute to an index difference in the two waveguides and the SiO_2 will have a negative influence on the difference. This is seen from the signs of the stress-optical constants. For Si the stress-optical constant with the biggest numerical value has a negative sign and therefore the refractive index will mainly increase for positive stresses. For SiO_2 C_{11}, C_{12}, C_{13} C_{22}, C_{23}, and C_{33}, which will relate to the normal stresses, all have a positive sign and here the refractive index will mainly decrease for positive stresses. So, if a big part of the optical wave propagates in the air and the SiO_2, the difference between the effective refractive indices will decrease. The graph on Fig. 7(a) therefore shows an optimal height of the waveguides, which is a solution of a nontrivial interaction of how much the SAW is reflected and how close the center of the optical wave can get to the SiO_2 surface and still be well confined in the waveguide. The fact that the same optimal height is found for both 6 and 12 electrode pairs indicates that the design conclusions are independent of the number of electrode pairs. An increase in electrodes will just increase the difference in $n_{\mathrm{eff},0}$, which is expected as more of the applied energy will be confined to the SAW. Figure 7(b) shows the effective refractive index for the zero, first, and second order mode normalized to the value $n_{\mathrm{eff,org}}$ of the fundamental mode in the left waveguide for the original height as functions of h. $n_{\mathrm{eff},i}$ are in all cases decreasing for decreasing height as less Si, with high refractive index, is used. The waveguide with the original height supports the three lowest order modes, whereas for the optimal height the waveguide is single moded.

A study of the width of the waveguide is then done with the height fixed to the optimal height h=0.19 μm and the difference in index between the two waveguides is seen on Fig. 8(a). The difference in $n_{\mathrm{eff},0}$ increases with increasing w. This can be explained by observing how the mode changes. When w is increasing the confined optical mode will also increase in the horizontal direction. This means that the mode will experience more stresses as long as w is smaller than half a SAW wavelength. At the same time the mode is also getting less confined to the waveguide, meaning that it will be more influenced by the surrounding materials, which

will have a negative influence on the index change as discussed above. However, this effect is smaller than the positive effect from the increased stresses in the waveguide. The limit for the increase is when w approaches half a SAW wavelength, where the change in $n_{\mathrm{eff},0}$ slowly stops to increase. However, before that the mode in the right waveguide with the SAW trough will start to degenerate into two modes, so the graph is therefore stopped there. The difference in index is now 2.44×10^{-5} $\mathrm{W}^{-1/2}$, which is more than 12 times bigger than for the original waveguide geometry. However, when w is increasing the waveguides will start to be multimoded again as seen on Fig. 8(b). Here $n_{\mathrm{eff},i}/n_{\mathrm{org}}$ for the first four lowest order modes in the two waveguides are shown as functions of w. The waveguide is single moded until $w=0.64$ μm and the difference in index is here 7.76×10^{-6} $\mathrm{W}^{-1/2}$, which is almost four times bigger than for the original waveguide geometry. This shows that it is possible to improve the optical modulation by changing the waveguide size such that the mode is moved closer to the surface and extended in the width to experience more stresses.

It is noted that even though the optimal height found is optimal for the original width, it is not certain that this height is optimal when the width is changed afterwards. As the optical modes change when the waveguide geometry is varied, it is not straightforward to apply a systematic optimization algorithm. Instead an extended parameter study has to be performed in order to find the height and width that are optimal together. This, however, is beyond the scope of the paper.

2. Other device structures

Alternative to changing the size of the waveguides, other device structures can be thought of to improve the acousto-optical modulation. As the stresses from the SAW have their maximum just below the surface, it is expected that the acousto-optical interaction is increased if the waveguides are buried in the SiO_2 layer instead of being placed above the layer. A calculation is carried out with the original waveguide size, but with the waveguides placed such that their upper surface is leveled with the substrate surface. The difference in effective refractive index is 2.14×10^{-5} $\mathrm{W}^{-1/2}$, which is more than ten times bigger than for the original waveguides on top of the surface. So with buried waveguides it is possible to improve the modulation drastically.

Another idea is to use an IDT at each side of the MZI arms. The two SAWs will be reflected back toward the waveguides when reaching the opposite IDT and a standing wave pattern will appear, which is expected to have enhanced amplitude compared to the original traveling wave. The distance between the two IDTs is tuned such that the standing wave achieves its maximum amplitude. The waveguides have the original size and eight electrode pairs are used in each IDT. The difference in effective refractive index is calculated for the case with the electric potential applied at one IDT for double fingers, the potential applied at both IDTs for double and single fingers and the results are scaled by the squared applied power, see Table IV. It is seen that the difference in effective refractive index is increased when two IDTs are used, as expected, and that the difference in index is more than 1.5 times bigger than for one IDT when using double fingers. The effect is small, but is expected to be bigger when more electrodes are used.

TABLE IV. Results for the difference in effective refractive index $(n^l_{\mathrm{eff},0}-n^r_{\mathrm{eff},0})/\sqrt{P}$ for different combinations of IDT numbers and single and double electrode fingers, $(\mathrm{W}^{-1/2})$.

	1 IDT (double fingers)	2 IDTs (double fingers)	2 IDTs (single fingers)
$\frac{n^l_{\mathrm{eff},0}-n^r_{\mathrm{eff},0}}{\sqrt{P}}$	1.93×10^{-6}	3.04×10^{-6}	2.34×10^{-6}

IV. CONCLUSION

This work presents a general finite element method to calculate the acousto-optical interaction between a SAW and optical waves in waveguides in a finite device.

The SAW is generated by an IDT using a piezoelectric model for an inhomogeneous material implemented in the high-level programming language COMSOL MULTIPHYSICS, where reflections from the boundaries are avoided by PMLs. Results of the SAW generation in a GaAs sample are presented, which show that the model works satisfactory as SAWs are generated at the electrodes and are absorbed in the PMLs. The frequency, which gives the biggest amplitude, is found to be the same as in experiments.

This model is then coupled to a model of the optical waves in the waveguides of a SOI MZI where the optical modes are found by solving the time-harmonic wave equation. By applying stresses from a SAW, it is shown that the effective refractive index of the fundamental optical mode has its maximum value for a SAW crest and minimum value for a SAW trough, as is expected.

This coupled finite element model is then employed to study geometry changes in the SOI MZI in order to increase the difference in effective refractive index in the two waveguide arms such that the optical modulation in the device is improved. A study of the height of the waveguides shows that an optimal height exists for the device, which is a result of a nontrivial compromise of how much the SAW is reflected, because of the interrupted surface, and how close the center of the optical wave can get to the SiO_2 surface and still be well confined in the waveguide. The difference in effective refractive index is approximately 2.2 times bigger for the optimal height and the waveguides have become single moded. The same optimal height is found when the number of electrode pairs in the IDT is doubled and this indicates that the design results in this work are independent of the number of electrode pairs. The width of the waveguides is then studied for the optimal height. The difference in effective refractive index increases for increasing width as the optical mode is influenced by increasing stresses from the SAW until the width reaches half a SAW wavelength. The difference in effective refractive index is 12 times bigger than for the original geometry, and if the waveguide has to stay single moded the difference is approximately four times bigger. The stresses of the SAW have their maximum just below the surface and a calculation where the

waveguides with the original size are buried below the surface shows that the difference in effective refractive index can be increased more than ten times by this change. Finally, it is tested if a standing wave created by two IDTs can improve the interaction. When double finger electrodes are used the difference in effective refractive index is 1.5 times bigger than the original case, and for single fingers it is 1.2 times bigger.

Further work includes a study of other geometry parameters as the height of the different layers as well as employing an optimization method as topology optimization (see Refs. 20 and 21) to improve certain parts of the geometry such as the shape of the waveguides and structures in between them.

ACKNOWLEDGMENTS

This work is supported by the European FP6 research project ePIXnet—*European Network of Excellence on Photonic Integrated Components and Circuits*. The authors thank the partners from the joint research group of ePIXnet *Photonic Switches and Modulators based on Surface Acoustic Waves* Paulo V. Santos and Markus Beck from Paul-Drude-Institut für Festkörperelektronik, Berlin, Germany and Mike van der Poel from Department of Photonics Engineering, Technical University of Denmark, for valuable input related to the model presented.

The authors are grateful to Jakob S. Jensen from the Department of Mechanical Engineering and Martin P. Bendsøe from the Department of Mathematics, Technical University of Denmark, for helpful discussions related to the presented work.

The support from Euro-horcs/ESF European Young Investigator Award (EURYI) through the grant *Synthesis and Topology Optimization of Optomechanical Systems* as well as from the Danish Center for Scientific Computing (DCSC) is gratefully acknowledged.

[1] K.-Y. Hashimoto, *Surface Acoustic Wave Devices in Telecommunications, Modeling and Simulation* (Springer, Berlin, 2000).
[2] R. M. White and F. W. Voltmer, Appl. Phys. Lett. **7**, 314 (1965).
[3] S. Takahashi, H. Hirano, T. Kodama, F. Miyashiro, B. Suzuki, A. Onoe, T. Adachi, and K. Fujinuma, IEEE Trans. Consum. Electron. **CE-24**, 337 (1978).
[4] Proceedings of the International Symposium on Surface Acoustic Wave Devices for Mobile Communication, 1992, edited by K. Shibayama and K. Fujinuma (unpublished).
[5] U. Wolff, F. L. Dickert, G. K. Fischauer, W. Greibl, and C. C. W. Ruppel, IEEE Sens. J. **1**(1), 4 (2001).
[6] C. Gorecki, F. Chollet, E. Bonnotte, and H. Kawakatsu, Opt. Lett. **22**, 1784 (1997).
[7] M. M. de Lima, Jr., and P. V. Santos, Rep. Prog. Phys. **68**, 1639 (2005).
[8] M. M. de Lima, Jr., M. Beck, R. Hey, and P. V. Santos, Appl. Phys. Lett. **89**, 121104 (2006).
[9] M. van der Poel, M. Beck, M. B. Dühring, M. M. de Lima, Jr., L. H. Frandsen, C. Peucheret, O. Sigmund, U. Jahn, J. M. Hwam, and P. V. Santos, Proceedings of European Conference on Integrated Optics and Technical Exhibition, Copenhagen, Denmark, 25–27 April 2007 (unpublished).
[10] S. Ballandras, M. Wilm, P.-F. Edora, A. Soufyana, V. Laude, W. Steichen, and R. Lardat, J. Appl. Phys. **93**, 702 (2003).
[11] D. B. Carstensen, T. A. Christensen, and M. Willatzen, Proceedings of the Nordic COMSOL Conference, Denmark, 2006 (unpublished).
[12] J. Wang and J. Lin, J. Intell. Mater. Syst. Struct. **16**, 623 (2005).
[13] U. Basu and A. Chopra, Comput. Methods Appl. Mech. Eng. **192**, 1337 (2003).
[14] COMSOL Reference Manual for COMSOL 3.3A, COMSOL AB, Stockholm, www.comsol.se.
[15] D. Royer and E. Dieulesaint, *Elastic Waves in Solids I*, 1st ed. (Springer, New York, 2000).
[16] B. A. Auld, *Acoustic Fields and Waves in Solids, Volume I*, 1st ed. (Wiley, New York, 1973).
[17] R. Syms and J. Cozens, *Optical Guided Waves and Devices*, 1st ed. (McGraw-Hill, New York, 1992).
[18] M. M. de Lima, Jr., F. Alsina, W. Seidel, and P. V. Santos, J. Appl. Phys. **94**, 7848 (2003).
[19] M. Huang, Int. J. Solids Struct. **40**, 1615 (2003).
[20] M. P. Bendsøe and O. Sigmund, *Topology Optimization, Theory, Methods and Applications* (Springer-Verlag, Berlin, 2003).
[21] J. S. Jensen and O. Sigmund, Appl. Phys. Lett. **84**, 2022 (2004).

Publication [P5]

Design of acousto-optical devices by topology optimization

8th World Congress on Structural and Multidisciplinary Optimization
June 1-5, 2009, Lisbon, Portugal

Design of acousto-optical devices by topology optimization

Maria B. Dühring

Department of Mechanical Engineering, Solid Mechanics, Technical University of Denmark, Nils Koppels Allé, Building 404, DK-2800 Kgs. Lyngby, Denmark, mbd@mek.dtu.dk

1. Abstract
In resent years it has been shown experimentally that it is possible to modulate optical waves in waveguides by surface acoustic waves and a theoretical study shows that the modulation can be improved by changing the waveguide geometry. Here a method to improve the acousto-optical interaction by means of topology optimization is presented. The surface acoustic waves are generated by interdigital transducers in a 2D piezoelectric model, which is coupled to an optical model where the optical mode in the waveguide is found by solving the time-harmonic wave equation for the magnetic field. Only the piezoelectric model is used in the optimization and the objective function is the squared absolute value of the strain in the vertical direction in the waveguide. The objective function is maximized by distributing air and solid material in an area below the waveguide. The optical model is solved for the initial and the optimized design and the measure of the acousto-optical interaction is the difference in effective refractive index for the fundamental mode between the two cases where a surface acoustic wave crest is in the waveguide and a trough is in the waveguide, which is then normalized with the squared applied electric power. It is here shown that the acousto-optical interaction can be increased almost 10 times by redistribution of solid material and air in the design domain.
2. Keywords: Rayleigh waves, piezoelectricity, perfectly matched layers, optical waveguide, strain-optical relation.

3. Introduction

This work elaborates on how to improve the acousto-optical interaction between a surface acoustic wave (SAW), also known as a Rayleigh wave, and an optical wave in a waveguide by topology optimization. SAWs are elastic vibrations that propagate along a material surface with most of their energy density concentrated at the surface. In piezoelectric materials it is possible to generate the SAW by the inverse piezoelectric effect by applying an electric potential to interdigital transducers at the material surface [1]. SAWs are now used in filters and resonators in telecommunication [2]. A new application is modulation of optical waves for signal generation in semiconductor structures [3]. In [4, 5] experimental results are reported for a compact and monolithic modulator consisting of a SAW driven Mach-Zehnder interferometer and a relative modulation up to 40 % was obtained with straight interdigital transducer fingers. A finite element model where a piezoelectric model is coupled to a optical model for the mode in the waveguide was introduced in [6] in order to simulate the acousto-optical interaction is such a device. By varying some of the geometry parameters as the width and the height of the waveguide it is shown that it is possible to improve the acousto-optical interaction. A potential new way of improving the interaction with a high freedom in the design is to use topology optimization. This is a gradient based optimization method that has proven efficient in optimizing a wide range of static and dynamic problems in engineering [7]. Recently, this method has been extended to problems in acoustic wave propagation problems [8, 9, 10, 11] as well as to photonic problems [12, 13]. Topology optimization has been applied in [14] to design surface acoustic wave filters and waveguides in 2 and 3 dimensions in elastic materials. Here the coupled piezoelectric and optical model from [6] is employed in a topology optimization approach where the optimization is employed to the piezoelectric model only, and the optical model is solved for the initial design and the optimized design in order to check that the acousto-optical interaction indeed has improved. In section 4 the acousto-optical model is described as well as the topology optimization approach. In section 5 results are presented for interaction between a SAW and an optical wave in a ridge waveguide.

4. Topology optimization method for acousto-optical problems

The problem studied in this article is illustrated in Figure. 1. The size of the waveguide and the material layers are the same as in the experiments presented in [4, 5] with a waveguide of GaAs on top of a $Al_{0.2}Ga_{0.8}As$ layer, which will further on be referred to as AlGaAs for simplicity. Both materials are

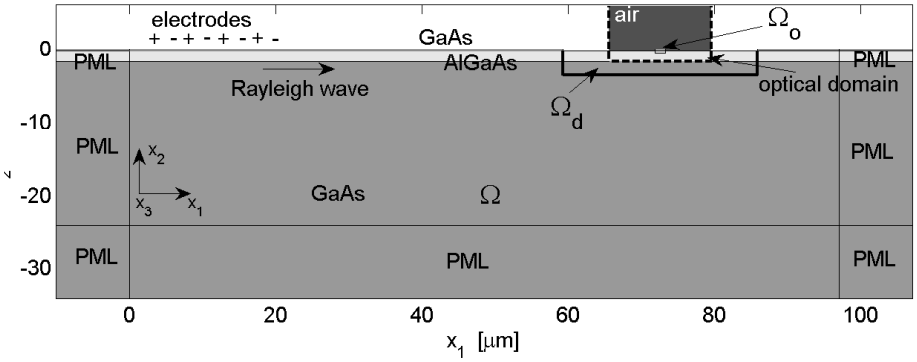

Figure 1: The geometry used in the topology optimization problem. The design domain Ω_d below the waveguide is indicated with the thick lines and the optical area where the optical model is solved is indicated by the dashed lines. The objective function is evaluated in the output domain Ω_o. The surface acoustic wave is generated at the electrodes and are absorbed in perfectly matched layers before they reach the outer boundaries.

piezoelectric. The aim is here to distribute air and solid material in the structure in order to optimize the acousto-optical interaction. The structure is described by a domain Ω filled with solid material. The SAW is generated by the inverse piezoelectric effect by applying an alternating electric potential to electrodes on top of the surface as indicated to the left on Figure 1. The SAW then propagates in the left and the right horizontal direction and is absorbed in the perfectly matched layers (PML), see [6, 15]. To the right of the electrodes the SAW will pass through an optical waveguide at the surface where light propagates in the x_3-direction. To simulate the acousto-optical interaction in the waveguide a model describing the SAW generation in a piezoelectric material is coupled with an optical model describing the propagation of the optical wave in the waveguide. It is assumed that the strain-optical effect is dominant compared to the electro-optical effect, which will be neglected here, see [4]. It is furthermore assumed that the SAW will affect the optical wave, but the optical wave will not influence the SAW, so the problem is solved by first calculating the mechanical strain introduced by the SAW. Then the change in refractive index in the materials due to the strain can be calculated by the strain-optical relation and finally, by solving the optical model, the effective refractive index of the different possible light modes can be determined. The mathematical model is described in the following subsections. In the output domain Ω_o the objective function Φ is maximized in order to improve the acousto-optical interaction in the waveguide. The maximization is done by finding a proper distribution of air and solid material in the area below the waveguide (design domain Ω_d).

4.1. The Piezoelectric Model

The applied electric potential will introduce mechanical deformations in the solid by the inverse piezoelectric effect. The behavior of the piezoelectric material is described by the following model as found in [16]. A time-harmonic electric potential

$$V(x_j, t) = V(x_j)e^{i\omega_\mathrm{saw}t}, \tag{1}$$

with the angular frequency ω_saw is applied to the electrodes. The mechanical strain S_{ij} and the electric field E_j are given by the expressions

$$S_{ij} = \frac{1}{2}\left(\frac{1}{\gamma_j}\frac{\partial u_i}{\partial x_j} + \frac{1}{\gamma_i}\frac{\partial u_j}{\partial x_i}\right) \quad \text{and} \quad E_j = -\frac{1}{\gamma_j}\frac{\partial V}{\partial x_j}, \tag{2}$$

where u_i are the displacements and x_i are the coordinates. (Note that Einstein notation is not used in Eq.(2).) The parameter γ_j is an artificial damping at position x_j in the PML given by the expression

$$\gamma_j(x_j) = 1 - i\sigma_j(x_j - x_l)^2, \tag{3}$$

where x_l is the coordinate at the interface between the regular domain and the PML and σ_j is a suitable constant. There is no damping outside the PMLs and here $\gamma_j = 1$. A suitable thickness of the PMLs as

well as the value of σ_j must be found by calculations such that both the mechanical and the electrical disturbances are absorbed before reaching the outer boundaries. However, the absorption must also be sufficiently slow as reflections will occur at the interface between the regular domain and the PML if their material properties are not comparable. The mechanical stresses T_{jk} and the electric displacement D_i both depend on the strain and the electric field according to the constitutive relations

$$T_{jk} = \tilde{c}^E_{jklm} S_{lm} - \tilde{e}^T_{ijk} E_i, \tag{4}$$

$$D_i = \tilde{e}_{ijk} S_{jk} + \tilde{\varepsilon}^S_{ij} E_j, \tag{5}$$

where $\tilde{c}^E_{jklm}$ are the elastic stiffness constants, $\tilde{e}_{ijk}$ are the piezoelectric stress constants and $\tilde{\varepsilon}^S_{ij}$ are the permittivity constants. The materials are in general anisotropic and as it is only possible to generate the SAW by the inverse piezoelectric effect in certain directions, the material tensors have to be rotated. This is indicated by the tilde above the material tensors. The rotation is done according to Eulers transformation theory as explained in [17]. Here the relation between the original directional vector r_j and the rotated vector $\hat{r}_i$ is given by

$$\hat{r}_i = a_{ij} r_j, \tag{6}$$

where a_{ij} is the transformation matrix given by the Euler angles φ_1, φ_2 and φ_3 where the crystal axis are rotated clockwise about the x_3-axis, then the x_2-axis and finally the x_3-axis again. The material property matrices can then be transformed by the transformation matrix a_{ij} and the Bold matrix M_{ijmn} as follows

$$\begin{aligned} \tilde{c}^E_{ijkl} =& M_{ijmn} M_{klpq} c^E_{mnpq}, \quad \tilde{e}_{ijk} = a_{il} M_{jkmn} e_{lmn} \\ & \text{and} \quad \tilde{\varepsilon}^S_{ij} = a_{ik} a_{jl} \varepsilon^S_{kl}. \end{aligned} \tag{7}$$

The governing equations give the stresses by Newton's second law and the electric displacement from Gauss law

$$\frac{1}{\gamma_j} \frac{\partial T_{ij}}{\partial x_j} = -\rho \omega^2_{\text{saw}} u_i \quad \text{and} \quad \frac{1}{\gamma_j} \frac{\partial D_i}{\partial x_j} = 0, \tag{8}$$

where ρ is the density of the material.

Both mechanical and electrical boundary conditions must be specified to solve the problem. Considering the mechanical conditions the upper surface is stress free and the bottom is clamped

$$\text{stress free surface :} \qquad T_{jk} m_k = 0, \tag{9}$$

$$\text{clamped surface :} \qquad u_i = 0, \tag{10}$$

where m_k is the normal unit vector pointing out of the surface. At the upper surface there are no charges and therefore electric insulation occurs, meaning that the normal component of the electric displacement is zero. At the bottom of the domain it is assumed that the electric potential is zero and at the electrodes the potential is V_p. The electrical boundary conditions are summarized as follows

$$\text{electrical insulation :} \qquad D_i m_i = 0, \tag{11}$$

$$\text{zero potential :} \qquad V = 0, \tag{12}$$

$$\text{applied positive potential :} \qquad V = V_p, \tag{13}$$

$$\text{applied negative potential :} \qquad V = -V_p. \tag{14}$$

The piezoelectric problem is solved by a plane formulation obtained by setting S_{i3}, S_{3j} and E_3 as well as T_{i3}, T_{3j} and D_3 equal to zero. The two governing equations (8) are solved simultaneously to find the unknowns u_1, u_2 and V.

4.2. The Optical Model

After the mechanical strain in the material has been computed by the piezoelectric model described above the refractive index n_{ij} in the strained material can be calculated according to the strain-optical relation [18]

$$\Delta \frac{1}{n^2_{ij}} = \tilde{p}_{ijkl} S_{kl}, \tag{15}$$

where $\tilde{p}_{ijkl}$ are the rotated strain-optical constants obtained by the expression

$$\tilde{p}_{ijkl} = M_{ijmn} M_{klpq} p_{mnpq}. \tag{16}$$

For a given optical mode of order ν and with the propagation constant β_ν the effective refractive index $n_{\text{eff},\nu}$ is defined as

$$n_{\text{eff},\nu} = \beta_\nu / k_0, \tag{17}$$

where k_0 is the free space propagation constant. It is assumed that the propagating optical modes have harmonic solutions on the form

$$H_{p,\nu}(x_1, x_2, x_3) = H_{p,\nu}(x_1, x_2) e^{-i\beta_\nu x_3}, \tag{18}$$

where $H_{p,\nu}$ is the magnetic field of the optical wave. The governing equation for the magnetic field is thus the time-harmonic wave equation

$$e_{ijk} \frac{\partial}{\partial x_j} \left(b_{kl} b_{lm} e_{mnp} \frac{\partial H_p}{\partial x_n} \right) - k_0^2 H_p = 0, \tag{19}$$

where e_{ijk} here is the alternating symbol and $b_{ik} n_{kj} = \delta_{ij}$. For a given value of k_0 the propagation constant β_ν for the possible modes are found by solving the wave equation as an eigenvalue problem, whereby the effective refractive indices can be obtained. In this work the set of equations are reduced such that the model is only solved for the transverse components of the magnetic field H_1 and H_2. As the energy of the lower order optical modes is concentrated in the waveguides the calculation domain, where the eigenvalue problem is solved, can be reduced to a smaller optical area around the waveguide as indicated by the dashed lines in Figure 1. At the boundary of such a domain it is assumed that the magnetic field is zero as the energy density quickly decays outside the waveguide, thus the boundary condition is

$$e_{ijk} H_j m_k = 0, \tag{20}$$

where e_{ijk} again is the alternating symbol and m_k is the normal unit vector pointing out of the surface. The coupled model is solved by the commercial finite element program Comsol Multiphysics with Matlab [19].

4.3. Design variables and material interpolation

The problem of finding an optimized distribution of material is a discrete optimization problem (there should be air or solid material in each point of the design domain), but in order to allow for efficient gradient-based optimization the problem is formulated with continuous material properties that can take any value in between the values for air and solid material. To control the material properties a continuous material indicator field $0 \leq \xi(\mathbf{r}) \leq 1$ is introduced, where $\xi = 0$ corresponds to air and $\xi = 1$ to solid material. If μ describes any of the material parameters in the model, introducing the design variable means that

$$\mu(\xi) = \begin{cases} \mu_{\text{a}}, & \xi = 0 \\ \mu_{\text{s}}, & \xi = 1 \end{cases}, \tag{21}$$

where μ_{a} represents the material values for air and μ_{s} the material values for solid material. Although ξ is continuous, the final design should be as close to discrete ($\xi = 0$ or $\xi = 1$) as possible in order to be well defined. This is done by employing a morphology-based filter as described in subsection 4.6. The material parameters are interpolated linearly between the two material phases

$$\mu(\xi) = \mu_{\text{a}} + \xi(\mu_{\text{s}} - \mu_{\text{a}}), \tag{22}$$

which clearly fulfills the discrete values specified in Eq.(21).

4.4. The optimization problem

The purpose of the topology optimization is to maximize the acousto-optical interaction between the SAW and the optical wave. The fundamental mode in the waveguide is polarized in the x_1-direction so it primarily senses the refractive index in this direction. Therefore it is mainly interesting that the

refractive index component n_{11} changes and the change depends on the different strain components - the more the strain components change the more n_{11} changes. The optimization problem is only stated for the piezoelectric model and the aim is to maximize an expression, which is dependent on one of the normal strain components. The objective function Φ is thus chosen as the squared absolute value of the normal strain in the vertical direction in the output domain Ω_{o} and the formulation of the optimization problem takes the form

$$\max_{\xi} \quad \log(\Phi) = \log\left(\int_{\Omega_{\mathrm{op}}} |S_2(\mathbf{r}, \xi(\mathbf{r}))|^2 \mathrm{d}\mathbf{r}\right), \qquad \text{objective function,} \tag{23}$$

$$\text{subject to} \quad 0 \leq \xi(\mathbf{r}) \leq 1 \quad \forall\ \mathbf{r} \in \Omega_{\mathrm{d}}, \qquad \text{design variable bounds.} \tag{24}$$

To obtain better numerical scaling the logarithm of the objective function is used. To check that the acousto-optical interaction has indeed improved by the optimization the optical model is solved for both the initial design and the optimized design for the case where a wave crest is at the waveguide and half a SAW phase later where a wave trough is at the waveguide. For these two cases the difference in effective refractive index for the fundamental mode $\Delta n_{\mathrm{eff},1}$ will take the biggest value possible for the initial design as shown in [6]. $\Delta n_{\mathrm{eff},1}$ is normalized with the squared applied electric power P and this is then defined as the measure for the acousto-optical interaction, see [6] for the expression for P. So the final goal of the optimization is to increase this measure.

4.5. Discretization and sensitivity analysis

The mathematical model of the acousto-optical problem is solved by finite element analysis. For the piezoelectric model the displacement-electric potential vector is defined as $\mathbf{w} = [w_1, w_2, w_3] = [u_1, u_2, V]$. The complex fields w_i and the design variable field ξ are discretized using sets of finite element basis functions $\{\phi_{i,n}(\mathbf{r})\}$

$$w_i(\mathbf{r}) = \sum_{n=1}^{N} w_{i,n}\phi_{i,n}(\mathbf{r}), \quad \xi(\mathbf{r}) = \sum_{n=1}^{N_d} \xi_n \phi_{4,n}(\mathbf{r}). \tag{25}$$

The degrees of freedom corresponding to the four fields are assembled in the vectors $\mathbf{w}_i = \{w_{i,1}, w_{i,2}, ...w_{i,N}\}^T$ and $\boldsymbol{\xi} = \{\xi_1, \xi_2, ...\xi_{N_d}\}^T$. A triangular element mesh is employed and second order Lagrange elements are used for the complex fields w_i to obtain high accuracy in the solution and for the design variable ξ zero order Lagrange elements are utilized. The commercial program Comsol Multiphysics with Matlab is employed for the finite element analysis. This results in the discretized equations

$$\sum_{i=1}^{3} \mathbf{K}_{ji}\mathbf{w}_i = \mathbf{f}_j, \tag{26}$$

where $\mathbf{K}_{ji}$ is the system matrix and $\mathbf{f}_j$ is the load vector, both being complex valued due to the PMLs.

To update the design variables in the optimization algorithm the derivatives with respect to the design variables of the objective function must be evaluated. This is possible as the design variable is introduced as a separate field. The objective function depends on the complex field vector $\mathbf{w}_2$, which is via Eq.(26) an implicit function of the design variables and can be written as $\mathbf{w}_2(\boldsymbol{\xi}) = \mathbf{w}_2^R(\boldsymbol{\xi}) + i\mathbf{w}_2^I(\boldsymbol{\xi})$, where $\mathbf{w}_2^R$ and $\mathbf{w}_2^I$ denote the real and the imaginary part of $\mathbf{w}_2$, respectively. Thus the derivative of the objective function $\Phi = \Phi(\mathbf{w}_2^R(\boldsymbol{\xi}), \mathbf{w}_2^I(\boldsymbol{\xi}), \boldsymbol{\xi})$ is given by the following expression found by the chain rule

$$\frac{\mathrm{d}\Phi}{\mathrm{d}\boldsymbol{\xi}} = \frac{\partial\Phi}{\partial\boldsymbol{\xi}} + \frac{\partial\Phi}{\partial\mathbf{w}_2^R}\frac{\partial\mathbf{w}_2^R}{\partial\boldsymbol{\xi}} + \frac{\partial\Phi}{\partial\mathbf{w}_2^I}\frac{\partial\mathbf{w}_2^I}{\partial\boldsymbol{\xi}}. \tag{27}$$

As $\mathbf{w}_2$ is an implicit function of $\boldsymbol{\xi}$ the derivatives $\partial\mathbf{w}_2^R/\partial\boldsymbol{\xi}$ and $\partial\mathbf{w}_2^I/\partial\boldsymbol{\xi}$ are not known directly. The sensitivity analysis is therefore done by employing an adjoint method where the unknown derivatives are eliminated at the expense of determining an adjoint and complex variable field $\boldsymbol{\lambda}$ from the adjoint equation

$$\mathbf{K}_{j2}\boldsymbol{\lambda} = -\left(\frac{\partial\Phi}{\partial\mathbf{w}_2^R} - i\frac{\partial\Phi}{\partial\mathbf{w}_2^I}\right), \tag{28}$$

where

$$\frac{\partial \Phi}{\partial \mathbf{w}_{2,n}^R} - i\frac{\partial \Phi}{\partial \mathbf{w}_{2,n}^I} = \int_{\Omega_{\text{op}}} \left(2\frac{\partial w_2^R}{\partial x_2} - i2\frac{\partial w_2^I}{\partial x_2}\right)\frac{\partial \phi_{2,n}}{\partial x_2}\mathrm{d}\mathbf{r} = \int_{\Omega_{\text{op}}} \left(2S_2^R - i2S_2^I\right)\frac{\partial \phi_{2,n}}{\partial x_2}\mathrm{d}\mathbf{r}. \tag{29}$$

The sensitivity analysis follows the standard adjoint sensitivity approach [20]. For further details of the adjoint sensitivity method applied to wave propagation problems, the reader is referred to [12]. Eq.(27) for the derivative of the objective function then reduces to

$$\frac{\mathrm{d}\Phi}{\mathrm{d}\boldsymbol{\xi}} = \frac{\partial \Phi}{\partial \boldsymbol{\xi}} + \mathrm{Re}\left(\boldsymbol{\lambda}^T \frac{\partial \mathbf{K}_{j2}}{\partial \boldsymbol{\xi}}\mathbf{w}_2\right). \tag{30}$$

The vectors $\partial\Phi/\partial\boldsymbol{\xi}$ and $\int_{\Omega_{\text{op}}}\left(2S_2^R - i2S_2^I\right)\frac{\partial\phi_{2,n}}{\partial x_2}\mathrm{d}\mathbf{r}$ as well as the matrix $\partial\mathbf{K}_{j2}/\partial\boldsymbol{\xi}$ are assembled in Comsol Multiphysics as described in [21].

4.6. Practical implementation

The optimization problem Eq.(23)-(24) is solved using the Method of Moving Asymptotes, MMA [22], which is an algorithm that uses information from the previous iteration steps and gradient information.

When the mesh size is decreased the optimization will in general result in mesh-dependent solutions with small details, which make the design inconvenient to manufacture. To avoid these problems a morphology-based filter is employed. Such filters make the material properties of an element depend on a function of the design variables in a fixed neighborhood around the element such that the finite design is mesh-independent. Here a Heaviside close-type morphology-based filter is chosen [23], which has proven efficient for wave-propagation type topology optimization problems, see for instance [11]. The method results in designs where all holes below the size of the filter (radius r_{min}) have been eliminated. A further advantage of these filter-types is that they help eliminating gray elements in the transition zone between solid and air regions.

5. Results

Results are now presented for the problem shown in Figure 1. The SAW is generated by 6 double electrode finger pairs. Each of the electrodes has a width equal to 0.7 μm and is placed 0.7 μm apart such that the wavelength of the generated SAW is 5.6 μm. The waveguide is placed at the surface and has the width 1.4 μm and the height 0.3 μm. The output domain Ω_{o} consists of the waveguide and an area just below the waveguide with the same size, in order to increase the possibility that the waveguide will still be able to confine an optical mode after the optimization. The materials GaAs and AlGaAs are piezoelectric with cubic crystal structure. The material constants used in the piezoelectric model are given in Table 1 and are here given in the usual matrix form for compactness reasons. For the SAW to propagate in the piezoelectric direction the material tensors have to be rotated by the angle $\varphi_2 = \pi/4$. The frequency is $f_{\text{saw}} = 518$ MHz (where $f_{\text{saw}} = \omega_{\text{saw}}/2\pi$), which is the resonance frequency. The constant σ_j controlling the damping in the PMLs is set to 10^{10}. Elements with maximum side length $e_1 = 0.6$ μm are used in the domain except in the design domain where it is $e_2 = 0.1$ μm and in the output domain where it is $e_3 = 0.02$ μm. The optical model is solved both for the initial design, where the design domain is filled with solid material, and for the optimized design in order to compare the acousto-optical interaction. The free space wavelength of the optical wave is set to $\lambda_0 = 950$ nm and the material constants for GaAs and AlGaAs used in the optical model are given in Table 2. For air simply the refractive index $n_0 = 1$ is used. The logarithm to the objective function for the initial design is found to be $\Phi = -19.99$ and the acousto-optical interaction measure is $\Delta n_{\text{eff},1}/\sqrt{(P)} = 1.500 \cdot 10^{-5}$. Note that these values are low do the the limited numbers of electrodes, in practice several hundred electrode fingers are employed to generate a SAW.

Table 1: The elastic stiffness constants, the density, the piezoelectric stress constants and the permittivity constants for the materials used in the piezoelectric model.

Material	c_{11}^E,c_{22}^E,c_{33}^E [10^{11} Nm^{-2}]	c_{12}^E,c_{13}^E,c_{23}^E [10^{11} Nm^{-2}]	c_{44}^E,c_{55}^E,c_{66}^E [10^{11} Nm^{-2}]	ρ [kgm^{-3}]	e_{14},e_{25},e_{36} [Cm^{-2}]	ε_{11}^S,ε_{22}^S,ε_{33}^S [10^{-11} Fm]
GaAs	1.1830	0.5320	0.5950	5316.5	-0.160	9.735
AlGaAs	1.1868	0.5396	0.5938	5005.2	-0.152	9.446

Table 2: Refractive index and strain-optical constants for the materials used in the optical model.

Material	n_0 [-]	p_{11}, p_{22}, p_{33} [10^{-12} Pa^{-1}]	p_{12}, p_{13}, p_{23} [10^{-12} Pa^{-1}]	p_{44}, p_{55}, p_{66} [10^{-12} Pa^{-1}]
GaAs	3.545	-0.165	-0.14	-0.072
AlGaAs	3.394	-0.165	-0.14	-0.072

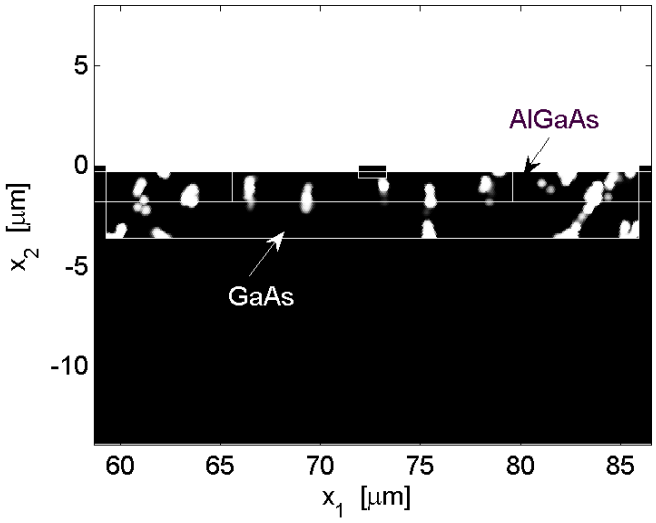

Figure 2: The optimized design below the waveguide. Black color represents solid material and white color represents air.

The objective function Φ is then maximized in the output domain Ω_{op} by distributing air and solid material in the design domain Ω_{d} where solid material refers to AlGaAs in the upper part of Ω_{d} and GaAs in the lower part. The filter radius is $r_{\min} = 2.5e_2$, an absolute tolerance of 0.01 on the maximum change of the design variables is used to terminate the optimization loop and a move limit for the design variables equal to 0.2 is used. The optimized design was found in 692 iterations and the logarithm to the objective function was increased to -17.39 - i.e. more than 2 orders of magnitude. Figure 2 shows the optimized design where black represents solid material and white represents air. The design is almost a pure black and white design and compared to the initial design air holes around the design domain have appeared. On Figure 3 the distribution of Φ normalized with $\sqrt{P}$ is plotted close to the waveguide for the original design and the optimized design, respectively, together with the air holes represented with white color. It is seen that in comparison to the initial design the redistributed material in the design domain is influencing Φ such that it has a higher value in the output domain Ω_{o}. This happens because the SAW gets trapped in the design and output domain because of reflections at the air holes. An air hole is created just below the output domain, which is creating some strain concentrations that are also extending to the output domain such that the strain here is increased. When solving the optical model for the optimized design the acousto-optical interaction is found to be $\Delta n_{\text{eff},1}/\sqrt{(P)} = 1.480 \cdot 10^{-4}$, which is 9.9 times higher than for the initial design. As the fundamental optical mode is polarized in the x_1-direction it is important that the change in n_{11} is as big as possible and $\Delta n_{11}/\sqrt{P}$ is plotted for the initial design and the optimized design in Figure 4. The change in $n_{11}/\sqrt{P}$ is an order of magnitude bigger for the optimized design compared to the initial design, which explains that $\Delta n_{\text{eff},1}/\sqrt{P}$ has increased. In Figure 4 the optical mode is indicated with contour lines and it is seen that the mode is confined to the waveguide both before and after the optimization. It is observed that a side benefit of the optimization is that the optical mode tends to get more confined to the output domain because of the big contrast in refractive index at the air hole next to the output domain.

This example shows that it is possible to improve the acousto-optical interaction between a SAW and an optical wave in a waveguide by topology optimization where the objective function is based only on

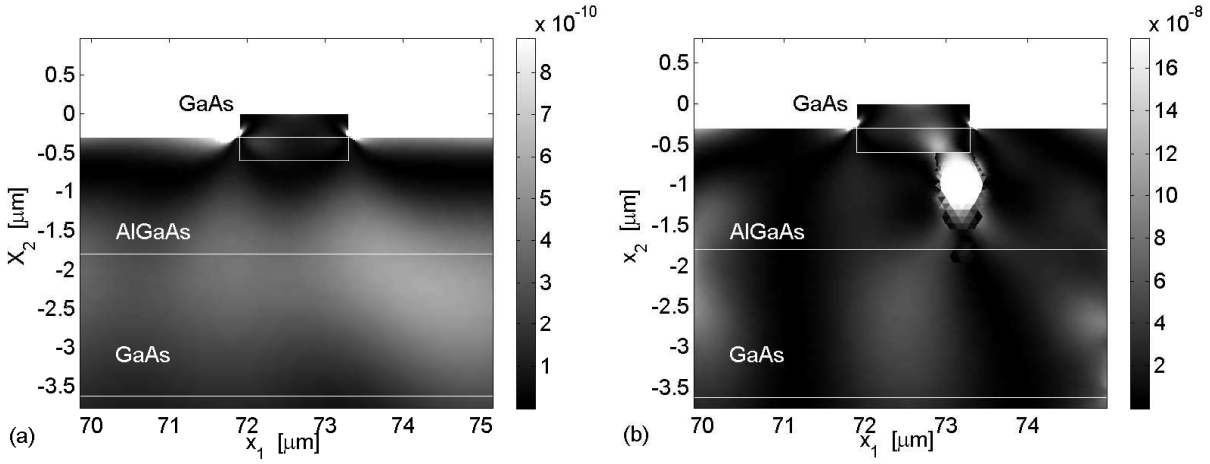

Figure 3: The distribution of the objective function Φ normalized with $\sqrt{P}$ close to the optical waveguide. (a): Initial design. (b): Optimized design where air holes are represented with white color.

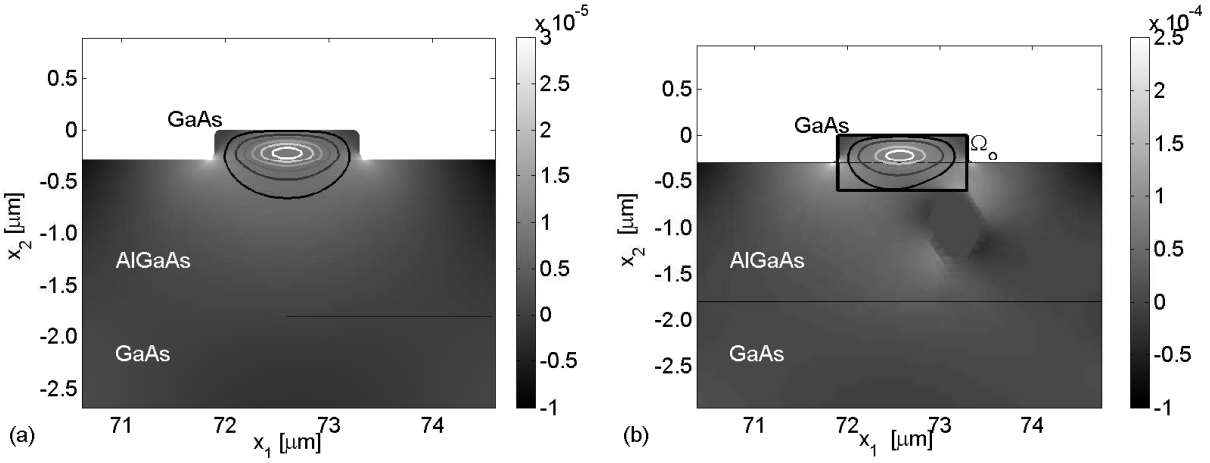

Figure 4: The color bar indicates the distribution of the change in the refractive index component Δn_{11} normalized with $\sqrt{P}$ close to the optical waveguide. The fundamental mode in the waveguide is indicated with contour lines. (a): Initial design. (b): Optimized design.

the piezoelectric model. However, due to the objective function, which is only dependent on S_2, some debatable mechanisms can appear in the design as the air hole close to the waveguide. This can on one hand create strain concentrations that can increase the objective function, but on the other hand air holes are areas where there is no periodic change in the refractive index components and these can also guide the optical wave, which is clearly unwanted. So it might not always be an advantage to have air holes close to the waveguide as the optical mode can extend out of the output domain. Holes close to the waveguide can be prevented by moving the design domain further away from the waveguide or try out other objective functions that both depend on the strain components and the strain-optical constants such that n_{11} is optimized more directly.

The optimized design almost consists of solid material and air, but it will still be difficult to fabricate it with modern fabrication technics. To make designs that are easier to fabricate the optimization could be done with the constraint that the design variables are assigned to an entire column that starts at the surface as in [14].

6. Conclusion and future work

It was here shown that the method of topology optimization can be employed to improve the acousto-optical interaction between a surface acoustic wave and an optical wave in a waveguide. The SAW generation is modeled by a 2D piezoelectric model, which is coupled to an optical model for the optical

mode in the waveguide. The topology optimization approach is based on the piezoelectric model and the objective function is the squared absolute value of the normal strain in the vertical direction. It vas shown that the objective function could be increased more than 2 orders of magnitude by the optimization where several smaller air holes were created in the design domain that initially consisted of solid material. The effect of the air holes is to trap the SAW in the design domain close to the waveguide and to make strain concentrations around the holes that extend into the waveguide. The increased strain concentration in the waveguide changes the refractive index components such that the periodic difference in effective refractive index for the fundamental guided mode, as the SAW passes the waveguide, is increased 10 times compared to the initial design. So the topology optimization approach is a promising method to improve acousto-optical interaction.

Further work includes testing of other objective functions that depend both on the strain components and the strain-optical constants such that the refractive index component in the horizontal direction is optimized directly. Finally, the constraint, that the design variables are assigned to entire columns starting at the surface, can be introduced in order to get designs that are easier to fabricate.

7. Acknowledgements

This work received support from the Eurohorcs/ESF European Young Investigator Award (EURYI, www.esf.org/euryi) through the grant "Synthesis and topology optimization of optomechanical systems" and from the Danish Center for Scientific Computing (DCSC). Also support from the EU Network of Excellence ePIXnet is gratefully acknowledged. The author is thankful to Ole Sigmund and Jakob S. Jensen from the Department of Mechanical Engineering, Technical University of Denmark, for helpful discussions related to the presented work.

8. References

[**1**] R.M. White and F.W. Voltmer, *Applied Physics Letters*, 17, 314-316, 1965.

[**2**] K.-Y. Hashimoto, *Surface acoustic wave devices in telecommunications, modeling and simulation*, Springer, Berlin, 2000.

[**3**] M.M. de Lima Jr. and P.V. Santos, Modulation of photonic structures by surface acoustic waves. *Reports on Progress in Physics*, 68, 1639-1701, 2005.

[**4**] M.M. de Lima Jr., M. Beck, R. Hey and P.V. Santos, Compact Mach-Zehnder acousto-optic modulator, *Applied Physics Letters*, 89, 121104, 2006.

[**5**] M. van der Poel, M. Beck, M.B. Dühring, M.M. de Lima, Jr., L.H. Frandsen, C. Peucheret, O. Sigmund, U. Jahn, J.M. Hwam and P.V. Santos, *proceedings of European Conference on Integrated Optics and Technical Exhibition*, Copenhagen, Denmark, April 25-27, 2007.

[**6**] M.B. Dühring and O. Sigmund, Improving the acousto-optical interaction in a Mach-Zehnder interferometer, *Journal of Applied Physics*, in press, 2009.

[**7**] M.P. Bendsøe and O. Sigmund, *Topology optimization, theory, methods and applications*, Springer Verlag Berlin, 2003, ISBN 3-540-42992-1.

[**8**] E. Wadbro and M. Berggren, Topology optimization of an acoustic horn, *Computer Methods in Applied Mechanics and Engineering* 196, 420-436, 2006.

[**9**] G.H. Yoon, J.S. Jensen and O. Sigmund, Topology optimization of acoustic-structure interaction problems using a mixed finite element formulation, *International Journal for Numerical Methods in Engineering* 70, 1049-1075, 2007.

[**10**] J. Du and N. Olhoff, Minimization of sound radiation from vibrating bi-material structures using topology optimization, *Structural and Multidisciplinary Optimization*, 33, 305-321, 2007.

[**11**] M.B. Dühring, J.S. Jensen and O. Sigmund, Acoustic design by topology optimization, *Journal of Sound and Vibration*, 317, 557-575, 2008.

[**12**] J.S. Jensen and O. Sigmund, Topology optimization of photonic crystal structures: A high bandwidth low loss T-junction waveguide, *Journal of the Optical Society of America B-Optical physics* 22, 1191–1198 2005.

[**13**] R. Stainko and O. Sigmund, Tailoring dispersion properties of photonic crystal waveguuides by topology optimization, *Waves in Random and Complex Media*, 17, 4, 477-489, 2007.

[**14**] C.J. Rupp, A. Evgrafov, K. Maute and M.L. Dunn, Design of phononic materials/structures for surface wave devices using topology optimization, *Struct. Multidisc. Optim.*, 34, 111-121, 2007.

[**15**] U. Basu, and A. Chopra Perfectly matched layers for the time-harmonic elastodynamics of unbounded domains: theory and finite-element implementation. *Computer Methods in Applied Mechanics and Engineering*, 192, 1337-1375, 2003.

[**16**] D. Royer and E. Dieulesaint, *Elastic Waves in Solids I.*, 1st ed., Springer, 2000.

[**17**] B.A. Auld, *Acoustic fields and waves in solids. volume 1*, John Wiley & Sons, 1973.

[**18**] R. Syms and J. Cozens, *Optical guided waves and devices*, 1st ed., McGraw-Hill, 1992.

[**19**] COMSOL Reference Manual for COMSOL 3.5. COMSOL AB, Stockholm, www.comsol.se.

[**20**] D.A. Tortorelli and P. Michaleris, Design sensitivity analysis: overview and review, *Inverse Problems in Engineering* 1, 71-105, 1994.

[**21**] L.H. Olesen, F. Okkels and H. Bruus, A high-level programming-language implementation of topology optimization applied to steady-state Navier-Stokes flow, *International Journal for Numerical Methods in Engineering* 65, 975-1001, 2006.

[**22**] K. Svanberg, The method of moving asymptotes - a new method for structural optimization, *International Journal for Numerical Methods in Engineering* 24, 359-373, 1987.

[**23**] O. Sigmund, Morphology-based black and white filters for topology optimization, *Structural and Multidisciplinary Optimization* 33, 401-424, 2007.

Publication [P6]

Energy storage and dispersion of surface acoustic waves trapped in a periodic array of mechanical resonators

Energy storage and dispersion of surface acoustic waves trapped in a periodic array of mechanical resonators

Maria B. Dühring,[1,a)] Vincent Laude,[2] and Abdelkrim Khelif[2]
[1]*Department of Mechanical Engineering, Solid Mechanics, Technical University of Denmark, 2800 Lyngby, Denmark*
[2]*Institut FEMTO-ST, Université de Franche-Comté, CNRS, ENSMM, UTBM, 32 avenue de l'Observatoire, F-25044 Besançon, France*

(Received 12 January 2009; accepted 25 February 2009; published online 4 May 2009)

It has been shown previously that surface acoustic waves can be efficiently trapped and slowed by steep ridges on a piezoelectric substrate, giving rise to two families of shear-horizontal and vertically polarized surface waves. The mechanisms of energy storage and dispersion are explored by using the finite element method to model surface acoustic waves generated by high aspect ratio electrodes. A periodic model is proposed including a perfectly matched layer to simulate radiation conditions away from the sources, from which the modal distributions are found. The ratio of the mechanical energy confined to the electrode as compared to the total mechanical energy is calculated and is found to be increasing for increasing aspect ratio and to tend to a definite limit for the two families of surface waves. This observation is in support of the interpretation that high aspect ratio electrodes act as resonators storing mechanical energy. These resonators are evanescently coupled by the surface. The dispersion diagram is presented and shows very low group velocities as the wave vector approaches the limit of the first Brillouin zone. © *2009 American Institute of Physics*. [DOI: 10.1063/1.3114543]

I. INTRODUCTION

Surface acoustic wave (SAW) transduction by the use of interdigital transducers[1] (IDTs) is a widespread technique for the electrical transduction in piezoelectric materials. SAWs are elastic waves that propagate along a material surface with most of their energy density concentrated at the surface.[2] In most practical cases, for example, for the design of classical resonators, filters, and sensors,[3–5] only the electrical properties of the IDT are of interest. In these applications SAWs are generated by IDTs with limited electrode height such that the SAW mode properties do not differ appreciably from those of a free or a fully metallized surface, except for the periodic aspects of wave propagation. For instance, propagation remains only slightly dispersive and the polarization of surface waves is relatively unaltered. In Ref. 6, however, it was shown theoretically by a finite element method (FEM)/boundary element method algorithm that the SAW properties are significantly changed when high aspect ratio (HAR) electrodes are used instead. Multimode SAW propagation was found and up to a tenfold slowing of the SAW phase velocity was obtained. These results were confirmed by experiments.[7] Recently, related work has been performed using the finite element and finite difference time domain method as well as experiments to show how band gaps and resonances change for increasing stub height in a plate with a periodic stubbed surface.[8,9]

The FEM/boundary element method is widely used for obtaining the harmonic admittance[10] as well as the harmonic displacements under the electrodes of a periodic infinite array of electrodes on a piezoelectic substrate.[6,11,12] An alternative method is to use directly the FEM with appropriate periodic boundary conditions.[13] The difficulty in this case, however, is to account for the semi-infinite nature of the substrate, which can result in oversized meshes and then impractical calculations. Here we introduce a full finite element model of a piezoelectric, anisotropic material to simulate the HAR electrodes utilizing periodic boundary conditions. A perfectly matched layer (PML) is employed at the bottom to absorb the acoustic and electric disturbances propagating away from the surface.[14–17] With this model it is possible to obtain the mode shape of all the resonances for the periodic structure such that it can be explained how the vibration of the surface interacts with the electrode for the different modes. We then use the model to calculate the mechanical energy stored in the electrode compared to the mechanical energy in the total structure in order to explain why the phase velocity is slowed down for increasing electrode aspect ratio. Finally, the dispersion and group velocity of the different modes are reported.

II. THE ACOUSTIC MODEL

A two dimensional (2D) periodic model of an electrode array on the surface of a piezoelectric material is used. The unit cell and the computational domain are illustrated in Fig. 1. The electrode consists of nickel (Ni) and is placed on a substrate of Y+128 cut lithium niobate, $LiNbO_3$. Material constants for lithium niobate are taken from Ref. 18, and for nickel, Young's modulus $E=200$ GPa and Poisson's ratio $\nu=0.31$ are used. The width of the electrode is a and the height is h. The parameter $p=2a$ is the acoustic period in the problem and is of the order of a few microns in applications. The SAW is generated by applying an alternating electrical

a)Electronic mail: mbd@mek.dtu.dk.

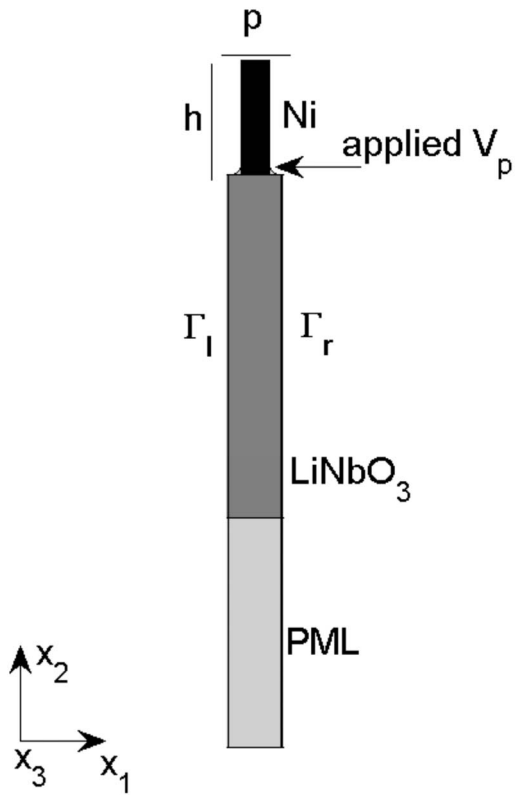

FIG. 1. The geometry of the unit cell with periodic boundary conditions and period p. The electrode consists of nickel and has the height h. The substrate is lithium niobate and a PML is placed at the bottom. The electric potential V_p is applied at the interface between the electrode and the substrate.

potential to the HAR electrodes. This is modeled by applying a positive potential to the electrode in the unit cell and then using periodic boundaries with opposite sign. As the metal is supposed to be perfectly conducting, the electrical potential needs only to be applied at the interface between Ni and $LiNbO_3$. To prevent reflections of the SAW from the bottom, a PML (Ref. 14) is applied as illustrated on Fig. 1. In Ref. 15, PMLs are introduced for time-harmonic elastodynamic problems and are extended to piezoelectric materials in Refs. 16 and 17. The PMLs have the property that the mechanical and electrical disturbances are gradually absorbed in the layers before they reach the outer boundaries. In this way there are no reflections that can disturb the propagation of the SAW.

The applied electric potential will introduce mechanical deformations in the solid by the inverse piezoelectric effect and the behavior of the piezoelectric material is described by the following model as found in Ref. 19. A time-harmonic electric potential

$$V(x_j,t) = V(x_j)e^{i\omega t}, \tag{1}$$

with the angular frequency ω, is applied to the electrode. The mechanical strain S_{ij} and the electric field E_j are given by the expressions

$$S_{ij} = \frac{1}{2}\left(\frac{1}{\gamma_j}\frac{\partial u_i}{\partial x_j} + \frac{1}{\gamma_i}\frac{\partial u_j}{\partial x_i}\right) \quad \text{and} \quad E_j = -\frac{1}{\gamma_j}\frac{\partial V}{\partial x_j}, \tag{2}$$

where u_i are the displacements and x_i are the coordinates. Note that the Einstein notation is not applied in the expressions in Eq. (2). The parameter γ_j is an artificial damping at position x_j in the PML. As the PML is added at the bottom of the structure only γ_2 is different from 1 and is given by the expression

$$\gamma_2(x_2) = 1 - i\sigma_2(x_2 - x_l)^2, \tag{3}$$

where x_l is the coordinate at the interface between the regular domain and the PML and σ_2 is a suitable constant. There is no damping outside the PMLs and here $\gamma_2 = 1$. A suitable thickness of the PML as well as the value of σ_2 must be found by calculations such that both the mechanical and electrical disturbances are absorbed before reaching the outer boundaries. However, the absorption must also be sufficiently slow as reflections will occur at the interface between the regular domain and the PML if their material properties are not comparable. The mechanical stresses T_{jk} and the electric displacement D_i both depend on the strain and the electric field according to the constitutive relations

$$T_{jk} = \tilde{c}^E_{jklm}S_{lm} - \tilde{e}^T_{ijk}E_i, \tag{4}$$

$$D_i = \tilde{e}_{ijk}S_{jk} + \tilde{\varepsilon}^S_{ij}E_j, \tag{5}$$

where $\tilde{c}^E_{jklm}$ are the elastic stiffness constants, $\tilde{e}_{ijk}$ are the piezoelectric stress constants, and $\tilde{\varepsilon}^S_{ij}$ are the permittivity constants. The materials are, in general, anisotropic, and as it is only possible to generate the SAW by the inverse piezoelectric effect in certain directions the material tensors have to be rotated. This is indicated by the tilde above the material tensors. The rotation is done according to Euler's transformation theory as explained in Ref. 20. Here the relation between the original directional vector r_j and the rotated vector $\hat{r}_i$ is given by

$$\hat{r}_i = a_{ij}r_j, \tag{6}$$

where a_{ij} is the transformation matrix given by the Euler angles φ_1, φ_2, and φ_3, where the crystal axes are rotated clockwise about the x_3-axis, then the x_2-axis, and finally the x_3-axis again. The material property matrices can then be transformed by the transformation matrix a_{ij} and the Bond stress transformation matrix M_{ijmn} (the derivation procedure of M_{ijmn} is defined in Ref. 20) as follows:

$$\tilde{c}^E_{ijkl} = M_{ijmn}M_{klpq}c^E_{mnpq}, \quad \tilde{e}_{ijk} = a_{il}M_{jkmn}e_{lmn} \quad \text{and} \tag{7}$$

$$\tilde{\varepsilon}^S_{ij} = a_{ik}a_{jl}\varepsilon^S_{kl}.$$

The governing equations give the stresses by Newton's second law and the electric displacement from Gauss law,

$$\frac{1}{\gamma_j}\frac{\partial T_{ij}}{\partial x_j} = -\rho\omega^2 u_i \quad \text{and} \quad \frac{1}{\gamma_j}\frac{\partial D_i}{\partial x_j} = 0, \tag{8}$$

where ρ is the density of the material. Note again that the Einstein notation is not applied in Eq. (8).

Both mechanical and electrical boundary conditions must be specified to solve the problem. Considering the mechanical conditions, the upper surface is stress-free and the bottom is clamped,

$$\text{streess free surface:} \quad T_{jk}m_k = 0, \tag{9}$$

$$\text{clamped surface:} \quad u_i = 0, \tag{10}$$

where m_k is the normal unit vector pointing out of the surface. At the upper surface, there are no charges and therefore electric insulation occurs, meaning that the normal component of the electric displacement is zero. At the bottom of the domain it is assumed that the electric potential is zero, whereas at the interface between the electrodes and the substrate the potential is V_p. The electrical boundary conditions are summarized as follows:

$$\text{electrical insulation:} \quad D_i m_i = 0, \tag{11}$$

$$\text{zero potential:} \quad V = 0, \tag{12}$$

$$\text{applied positive potential:} \quad V = V_p. \tag{13}$$

Periodic boundary conditions must be induced for u_i and $u_{i,j}$ as well as for V and $V_{,j}$ at the boundaries Γ_l and Γ_r, see Fig. 1. When u_l represents these quantities on the left boundary Γ_l and u_r the quantities on the right boundary Γ_r, the induced periodic boundary conditions take the form

$$u_r(x_j) = u_l(x_j)e^{-ik2p}, \tag{14}$$

where k is the phase propagation constant of the SAW.[21] When looking at the case with an alternating electric potential, $k=\pi/2p$ is used.

The piezoelectric problem is solved by a plane formulation obtained by setting S_{i3} and E_3 as well as T_{i3} and D_3 equal to zero. The governing equations (8) are solved simultaneously to find the dependent variables u_1, u_2, u_3, and V. The model with the PML described above is directly implemented in the partial differential equation application mode of COMSOL MULTIPHYSICS, which is a commercial finite element program.[22] Second order Lagrange elements are used for all dependent variables.

III. RESULTS

In this section, results are presented for the periodic model of the HAR electrodes.

A. Polarization of HAR IDT modes

One HAR electrode with periodic boundary conditions is considered. The computational domain is illustrated on Fig. 1 where $p=1.4$ μm is used for definiteness. A harmonic electric potential of $V_p=1$ V is applied to excite the device and the resonance frequencies are found by integrating the deflections along the substrate surface for a frequency range. The first six modes are examined. Three of the modes are found to be mainly polarized in the shear-horizontal (SH) direction and the other three modes to be mainly vertically polarized (VP). In Fig. 2, the half phase velocity fp (where $f=\omega/2\pi$ is the frequency) of these six modes is plotted versus the aspect ratio of the electrode $h/2p$ and the polarization types are indicated. It is seen that the phase velocity is decreasing with increasing aspect ratio for all the modes. The decrease gets bigger for decreasing mode number, and for mode 1 fp is decreased up to 15 times. These modes and their polarization as well as the phase velocity dependence of increasing aspect ratio are in fine agreement with the results presented in Ref. 7, where the modes were found by a combined FEM/boundary element method algorithm. The SH and VP bulk wave limits are marked in Fig. 2 as well and the modes do not appear above these limits as they are dissipated to the bulk.

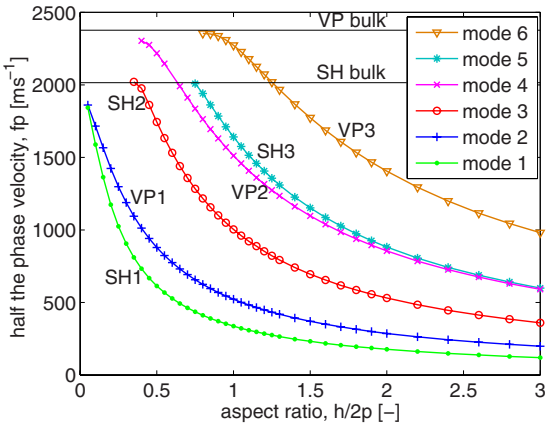

FIG. 2. (Color online) Half of the phase velocity fp as function of $h/2p$ for the six first modes for $kp=\pi/2$. The polarization types are indicated along with the limits for the bulk waves.

One advantage of using a pure finite element model is that it is easy to plot the displacement fields in the entire structure. Examples are given in Fig. 3 where the deflections u_1, u_2, and u_3 in the x_1-, x_2-, and x_3-directions are plotted for the six modes for $h/2p=1$. These plots clearly show that all modes of the structure are, in fact, the combination of a vibration in the electrode and of a surface wave in the substrate. The first five modes are fully confined to the surface, whereas mode 6 is leaking into the substrate. The different scaling on the color bars on Fig. 2 indicates the dominant polarization directions for the six modes. In order to clarify these polarizations, a plot for each mode is made in Fig. 4 where the deformations u_1 and u_2 in the x_1- and x_2-directions are plotted with a scaling factor to emphasize in-plane deformations, and the deflection u_3 in the x_3-direction is indicated by the color bar. The plots are focused on the electrode and the regular part of the substrate. The observed modal shapes explain why more and more modes appear in the structure as the aspect ratio increases. When SH-type modes are considered, which are mainly polarized in the x_3-direction, it is observed that the mode shapes in the electrode in this direction are of increasing order for increasing mode number, such that SH1 has a mode shape of order 1, SH2 has one of order 2, and SH3 has one of order 3. The same is found for the modes of VP type where VP1 has a mode of order 1, VP2 has a mode of order 2, and VP3 has a mode of order 3 in both the x_1- and x_2-directions. Thus, for larger aspect ratios, more modes can exist as the electrode is allowed to vibrate with modes of higher order.

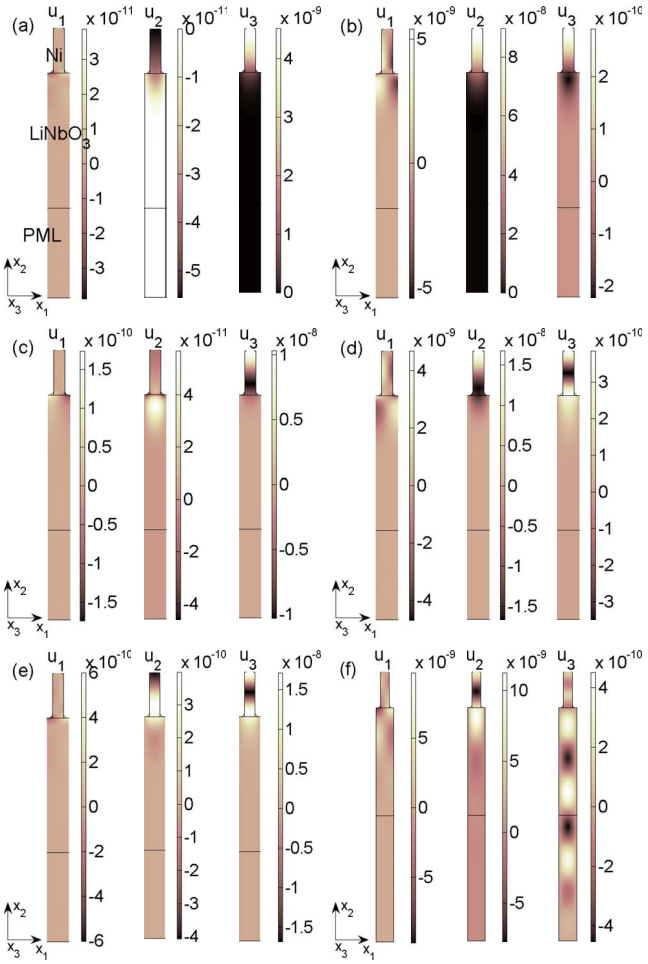

FIG. 3. (Color online) The deflections u_1, u_2, and u_3 at resonance with $h/2p=1$ and $kp=\pi/2$. All deflections are normalized to $V_p=1$ V. (a) Mode 1, (b) mode 2, (c) mode 3, (d) mode 4, (e) mode 5, and (f) mode 6.

B. Mechanical energy storage

To explain the slowing down of the wave velocity, the mechanical energy distribution in the structure is calculated. The mechanical energy is the sum of the stored strain and kinetic energy and the mechanical flux flowing into the PML at the bottom. Expressions for these quantities are given, for instance, in Ref. 20. The fraction of the mechanical energy in the electrode compared to the total mechanical energy in the structure is plotted in Fig. 5. Here it is observed that the energy is more confined to the electrode for increasing aspect ratio. The electrode thus acts as a mechanical resonator, which slows down the SAW velocity because of mechanical energy storage. For modes of the same type, the fraction of mechanical energy in the electrode tends to the same value for increasing aspect ratio. The SH types tend to a value around 0.97, which is larger than the limit for the VP types, about 0.93. The fact that the limits do not reach 1 explains that the wave is still (slightly) propagating or rather coupled from one electrode to the other by surface waves. If the energy was fully trapped then the surface waves would not propagate at all. For increasing aspect ratios the modes are more and more clean cantilever vibrations in the electrode and the only energy left in the substrate is what connects the cantilever modes to the substrate. Modes of the same polarization type deflect in the same direction in the substrate, so the stiffness in the substrate for these modes is the same. This explains why modes of the same type tend to the same energy ratio. The observation that the limit for SH is bigger than the limit for VP is not obvious as SH waves as, e.g., Love waves or leaky-SAW penetrates deeper in the substrate than Rayleigh waves. However, it indicates that the effective mechanical stiffness at the surface is bigger for the VP modes than for the SH modes. This is also confirmed when comparing the rotated stiffness constants in these directions.

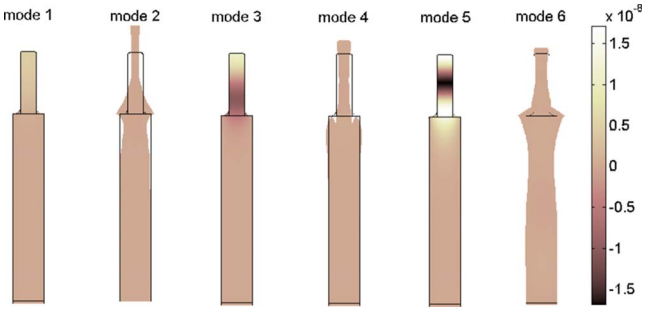

FIG. 4. (Color online) The deflections in the structure for each of the six modes at resonance with $h/2p=1$ and $kp=\pi/2$ normalized to $V_p=1$ V. The deflections u_1 and u_2 are given with an arbitrary scaling factor and u_3 is given by the color bar for all six modes.

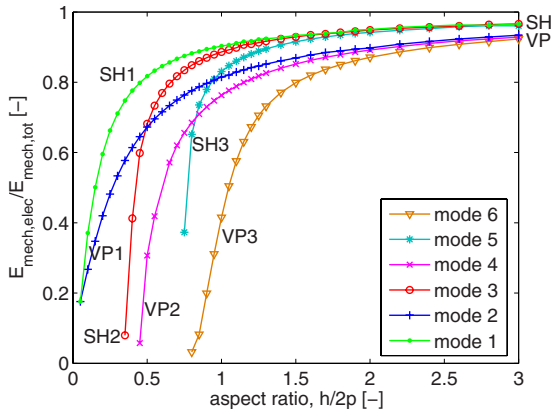

FIG. 5. (Color online) Fraction of mechanical energy in the electrode with respect to the total energy in the structure, as a function of the aspect ratio $h/2p$ for the first six modes. The propagation constant is $kp=\pi/2$. The limit for the SH-type modes is 97% and the limit for the VP-type modes is 93%.

C. Dispersion and group velocity of HAR IDT modes

A dispersion diagram can be obtained by plotting the frequency as a function of the propagation constant or wave vector. Dispersion tells if the phase velocity is dependent on frequency and is important to know in order to describe propagation in the periodic structure. The normal Rayleigh wave excited by conventional thin electrodes is almost dispersionless and will give a straight line in the diagram just below the straight line corresponding to the slowest shear bulk wave.[10] The dispersion properties for HAR electrodes are different as illustrated at Fig. 6 where half the phase velocity fp is plotted as function of kp [where the propagation constant k comes from expression (14)] for $h/2p=1$. When the wave vector approaches the X point of the Bril-

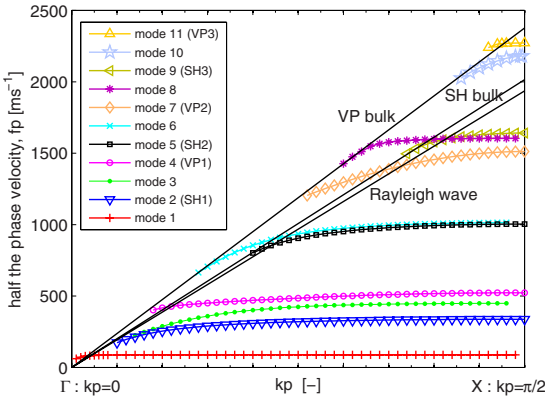

FIG. 6. (Color online) Band diagram for $h/2p=1$ obtained by plotting half the phase velocity fp as function of kp.

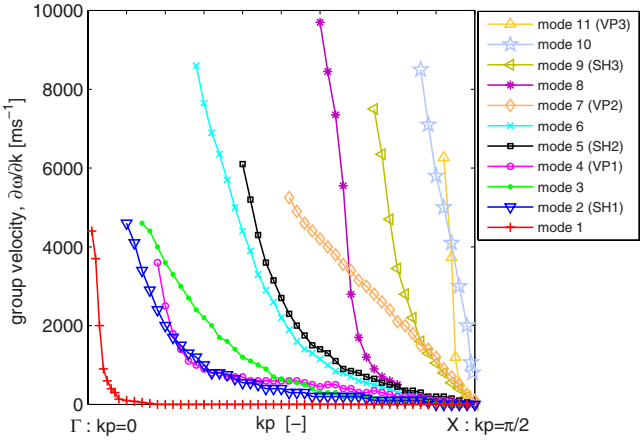

FIG. 7. (Color online) The group velocity $v_g=\partial\omega/\partial k$ as function of kp for $h/2p=1$.

louin zone, all bands become flatter and flatter, which means that the group velocity tends to zero. Then the elastic energy is almost not propagating and is mostly stored in the HAR electrodes. In Fig. 6 the straight lines for the Rayleigh wave as well as the lines for the SH and VP bulk waves are indicated. It is seen that the bands for the SH modes and the VP modes stop at their bulk limits as the waves are dissipated into the bulk material. In the dispersion region following the lowest bulk shear velocity (or Rayleigh SAW) there is an interaction between the Rayleigh SAW and the discrete mechanical modes of the HAR electrodes. When moving away from this line, the interaction between the resonators and SAW reduces (flatband) and the substrate mostly plays the role of a connecting medium for the HAR resonators. The dispersion diagram also shows that there exist 11 modes outside the Brillouin zone limit X. The deflections of these additional modes get insignificant when approaching the X point limit and here only the six resonant modes are found in practice to respect the electrical condition and the periodic boundary conditions at the same time. Also in experiments with such structures, only the six resonant modes will be found for alternating electrical potential excitation.[7] Other values of kp could be selected by using more than two fingers per wavelength in the IDT. For instance, $kp=2\pi/3$ and $kp=\pi/2$ would be obtained with three or four fingers per wavelength, respectively.

The group velocity is calculated from the band diagram by the expression

$$v_g = \frac{\partial \omega}{\partial k}. \tag{15}$$

The results are shown on Fig. 7 where v_g is plotted as function of kp. The group velocity tends to zero for all 11 modes when the wave vector approaches the point X. This means that the velocity of information carried by groups of waves of similar frequencies in the HAR electrodes tends to zero. What is remarkable here is that close to zero group velocity can also be obtained for wave vectors away from the Brillouin zone boundary. This property is more pronounced for modes with smaller orders and is equally true for SH and VP modes.

IV. CONCLUSION AND FURTHER WORK

This paper elaborates on how to model SAWs generated by high aspect ratio electrodes. It is explained how SAWs propagating in HAR electrode arrays can be computed by employing a 2D model of a piezoelectric, anisotropic material where reflections at the bottom are avoided by a PML. Results are presented for a unit cell with one HAR electrode with periodic boundary conditions. The first six resonant modes are studied and the phase velocity is found to decrease up to 15 times with increasing height. By plotting deflections in all three directions for each mode, it is shown that the movement consists of a combined SAW in the substrate and vibration in the electrode. Three of the modes are mainly polarized in the SH direction and the three other modes are mainly VP. The deflection plots show that the reason for more and more modes to exist is that for increasing mode number the mode shapes have increasing order. The ratio of mechanical energy confined to the electrodes compared to the total mechanical energy is calculated and increases for increasing electrode height. This indicates that the electrode acts as a mechanical resonator, slowing down the SAW velocity because of mechanical energy storage. The modes of SH type go to the same limit around 0.97 and the modes of VP type go to a limit around 0.93. The band diagram for the structure is calculated and shows strong dispersion for the 11 existing modes where the bands get flatter and flatter when reaching the X point of the first Brillouin zone. Finally, the group velocity is calculated for the 11 modes and shown to tend to zero when reaching the X point for all the modes.

Further work includes the consideration of finite HAR SAW resonators, where mechanical energy storage would be used to avoid leakage outside the transducer. We are also considering using HAR IDTs for efficient acousto-optical interactions in planar optical waveguides.

ACKNOWLEDGMENTS

This work is supported by the European FP6 research project ePIXnet—*European Network of Excellence on Photonic Integrated Components and Circuits*. The authors thank the partners from the joint research group of ePIXnet *Photo-*

nic Switches and Modulators Based on Surface Acoustic Waves Paulo V. Santos and Markus Beck from Paul-Drude-Institut für Festkörperelektronik, Berlin, Germany, and Mike van der Poel from Department of Photonics Engineering, Technical University of Denmark, for valuable input related to the model presented.

The authors are grateful to Ole Sigmund and Jakob S. Jensen from the Department of Mechanical Engineering and Martin P. Bendse from the Department of Mathematics, Technical University of Denmark for helpful discussions related to the presented work.

The support from Euro-horcs/ESF European Young Investigator Award (EURYI) through the grant *Synthesis and Topology Optimization of Optomechanical Systems* as well as from the Danish Center for Scientific Computing (DCSC) is gratefully acknowledged.

[1]R. M. White and F. W. Voltmer, Appl. Phys. Lett. **7**, 314 (1965).
[2]K.-Y. Hashimoto, *Surface Acoustic Wave Devices in Telecommunications, Modeling and Simulation* (Springer, Berlin, 2000).
[3]S. Takahashi, H. Hirano, T. Kodama, F. Miyashiro, B. Suzuki, A. Onoe, T. Adachi, and K. Fujinuma, IEEE Trans. Consum. Electron. **CE-24**, 337 (1978).
[4]Proceedings of the International Symposium on Surface Acoustic Wave Devices for Mobile Communication, 1992, edited by K. Shibayama and K. Fujinuma (unpublished).
[5]U. Wolff, F. L. Dickert, G. K. Fischauer, W. Greibl, and C. C. W. Ruppel, IEEE Sens. J. **1**, 4 (2001).
[6]V. Laude, A. Khelif, T. Pastureaud, and S. Ballandras, J. Appl. Phys. **90**, 2492 (2001).
[7]V. Laude, L. Robert, W. Daniau, A. Khelif, and S. Ballandras, Appl. Phys. Lett. **89**, 083515 (2006).
[8]T.-T. Wu, Z.-G. Huang, T.-C. Tsai, and T.-C. Wu, Appl. Phys. Lett. **93**, 111902 (2008).
[9]Y. Pennec, B. Djafari-Rouhani, H. Larabi, J. O. Vasseur, and A. C. Hladky-Hennion, Phys. Rev. B **78**, 104105 (2008).
[10]Y. Zhang, J. Desbois, and L. Boyer, IEEE Trans. Ultrason. Ferroelectr. Freq. Control **40**, 183 (1993).
[11]G. Endoh, K. Hashimoto, and M. Yamaguchi, Jpn. J. Appl. Phys., Part 1 **34**, 2638 (1995).
[12]Y. Fusero, S. Ballandras, J. Desbois, J.-M. Hodé, and P. Ventura, IEEE Trans. Ultrason. Ferroelectr. Freq. Control **49**, 805 (2002).
[13]S. Ballandras, M. Wilm, P. F. Edoa, A. Soufyane, V. Laude, W. Steichen, and R. Lardat, J. Appl. Phys. **93**, 702 (2003).
[14]J.-P. Berenger, J. Comput. Phys. **114**, 185 (1994).
[15]U. Basu and A. Chopra, Comput. Methods Appl. Mech. Eng. **192**, 1337 (2003).
[16]M. B. Dühring, Proceedings of 7th World Congress of Structural and Multidisciplinary Optimization, Seoul, Korea, COEX, 2007 (unpublished).
[17]M. B. Dühring and O. Sigmund, J. Appl. Phys. (in press).
[18]G. Kovacs, M. Anhorn, H. E. Engan, G. Visintini, and C. C. W. Ruppel, Proc.-IEEE Ultrason. Symp. **1**, 435 (1990).
[19]D. Royer and E. Dieulesaint, *Elastic Waves in Solids*, 1st ed. (Springer, New York, 2000).
[20]B. A. Auld, *Acoustic Fields and Waves in Solids*, 1st ed. (Wiley, New York, 1973).
[21]M. Hofer, R. Lerch, N. Finger, G. Kovacs, J. Schøberl, S. Zaglmayr, and U. Langer, WCCM V, Fifth World Congress on Computational Mechanics, Vienna, Austria, 7–12 July 2002 (unpublished).
[22]COMSOL Reference, Manual for COMSOL 3.3A, COMSOL AB, Stockholm, www.comsol.se.

Publication [P7]

Improving surface acousto-optical interaction by high aspect ratio electrodes

Improving surface acousto-optical interaction by high aspect ratio electrodes

Maria B. Dühring*
Department of Mechanical Engineering, Solid Mechanics, Technical University of Denmark, 2800 Kgs. Lyngby, Denmark.

Vincent Laude and Abdelkrim Khelif
Institut FEMTO-ST, Université de Franche-Comté, CNRS, ENSMM, UTBM; 32 avenue de l'Observatoire, F-25044, Besançon, France

The acousto-optical interaction of an optical wave confined inside a waveguide and a surface acoustic wave launched by an interdigital transducer (IDT) at the surface of a piezoelectric material is considered. The IDT with high aspect ratio electrodes supports several acoustic modes that are strongly confined to the surface, causing a significant increase in the strain underneath the surface. A finite element method is employed to model the surface acoustic waves generated by a finite length IDT with twelve electrode pairs, and subsequently to study their interaction with an optical wave propagating in a waveguide buried in the lithium niobate substrate supporting the electrodes. The interaction can be increased up to 600 times using these new types of surface acoustic waves as compared to using a conventional IDT with thin electrodes. This result could find applications in improved acousto-optical integrated modulators.

Keywords: surface acoustic waves, piezoelectricity, finite element analysis, perfectly matched layers, acousto-optical modulator

I. INTRODUCTION

This paper is concerned with surface acoustic waves (SAW) generated by high aspect ratio (HAR) electrodes and their use for improving integrated acousto-optical modulators. SAWs are elastic waves that propagate along a material surface with most of their energy density concentrated at the surface [1]. Two main types of SAWs exist. One type is the Rayleigh wave, which is mainly polarized in the vertical and longitudinal direction, and the other type includes surface waves that are mostly polarized in the shear horizontal direction, such as the Bleustein-Gulyaev wave or the leaky surface acoustic waves of lithium tantalate and lithium niobate. In piezoelectric materials the elastic field is accompanied by an electric field and SAWs can be generated by interdigital transducers (IDT) by the inverse piezoelectric effect. SAWs are extensively used in electromechanical filters and resonators for telecommunication as well as in oscillators and sensors [2–4]. A new application is modulation of optical waves, see Ref. [5] for an overview, and in Refs. [6–8] experimental results for a compact and monolithic modulator consisting of a SAW driven Mach-Zehnder interferometer (MZI) are presented. A coupled piezoelectric and optical finite element model is introduced in Ref. [9], which is employed to calculate and improve the acousto-optical interaction in such a modulator by a parameter study of the geometry. In these applications SAWs are generated by IDTs with limited electrode height such that the SAW mode properties are similar to the propagation on a free surface. In Ref. [10] it was shown theoretically by a combined finite element and boundary element method that the SAW properties are significantly changed when high aspect ratio (HAR) electrodes are used instead. Multimode SAW propagation was found and up to a tenfold slowing of the SAW velocity was obtained. Experimental results are presented in Ref. [11] and a fine agreement between numerical and experimental results was found. In order to plot the mode shapes we introduced a finite element model of a piezoelectric, anisotropic material in Ref. [12] to simulate the HAR electrodes utilizing periodic boundary conditions. A perfectly matched layer (PML) was employed at the bottom to absorb the mechanical and electrical disturbances propagating away from the surface [9, 13]. A fine agreement was found between this new model and the previous results in Refs. [10, 11]. With this model it was possible to obtain the mode shape of all the resonances for the periodic structure and it was observed that each mode shape consisted of a combined vibration at the surface and in the electrode. The mechanical energy confinement to the electrodes was calculated and it was observed that it increases with increasing aspect ratio. This indicates that the phase velocity is slowed down because of energy storage in the electrodes.

In this work we modify the periodic model to examine the structure with a finite number of HAR electrodes by employing PMLs at the vertical borders. The resonance frequencies and the energy confinement to the electrodes are compared for the periodic and finite model in order to validate the finite model and a fine agreement is obtained. The finite HAR device is then employed to calculate the acousto-optical interaction in an optical waveguide based on the acousto-optical model from Ref. [9]. The two first order optical modes are matched with the first six acoustic modes at the surface where the acoustic strain energy

*Electronic address: mbd@mek.dtu.dk

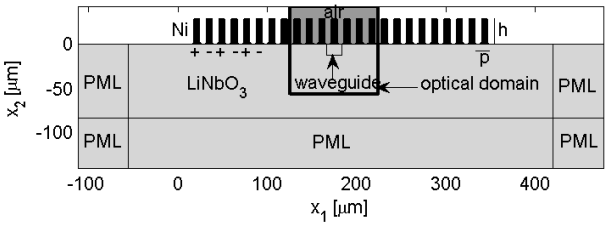

FIG. 1: The geometry of the acousto-optical problem with Ni electrodes on a $LiNbO_3$ substrate. Perfectly matched layers absorb the waves at the boundaries and the thick line indicates the optical domain.

has a high confinement. The acoustic strain is first calculated by the piezoelectric model, which is then coupled to a model of the optical wave. From this coupled model it is possible to calculate the difference in effective refractive index between the two cases where a negative and a positive electric potential, respectively, are applied to the electrode above the waveguide. This is a measure for how efficient each acoustic mode interact with the optical modes. The results of the acousto-optical interaction with the HAR electrodes are compared to similar results for a conventional device with thin electrodes, and it is concluded that the interaction can be increased more than 600 times for the new types of waves.

II. THE ACOUSTO-OPTICAL MODEL

The finite model for computing the interaction between SAWs generated by HAR electrodes and a optical wave in a waveguide is described in this section and is similar to the model from Ref. [9].

A. Problem Description

The 2D computational domain is illustrated in Fig. 1. The electrodes consist of nickel (Ni) and are placed on top of a substrate of Y+128 degrees cut lithium niobate ($LiNbO_3$). The width of the electrodes is a and the height is h. The parameter $p = 2a$ is the period in the problem and is of the order of a few microns in applications. The SAW is generated by applying an alternating electrical potential to the HAR electrodes as indicated at the left electrodes in Fig. 1. The metal is assumed to be perfectly conducting such that the electrical potential only needs to be applied at the interface between Ni and ($LiNbO_3$). The SAW then propagates in the left and the right horizontal direction and both the mechanical and electrical disturbances are absorbed in the PMLs. The SAW passes through an optical waveguide in the middle where light propagates out of the plane in the x_3-direction. To simulate the acousto-optical interaction in the waveguide, a model describing the SAW generation in a piezoelectric material is coupled with an optical model describing the propagation of the optical wave in the waveguide. It is assumed that the strain-optical effect is dominant compared to the electro-optical effect, which will be neglected here [7]. It is furthermore assumed that the SAW will affect the optical wave, but the optical wave will not influence the SAW, so the problem is solved by first calculating the mechanical strain introduced by the SAW. Then the change in refractive index in the materials due to the strain can be calculated by the strain-optical relation, and finally by solving the optical model the effective refractive index of the different possible light modes can be determined. The mathematical model is described in the following subsections.

B. The Piezoelectric Model

The applied electric potential will introduce mechanical displacements in the solid by the inverse piezoelectric effect. The behavior of the piezoelectric material is described by the following model, as found in Ref. [14]. A time-harmonic electrical potential

$$V(x_j, t) = V(x_j)e^{i\omega t}, \tag{1}$$

with the angular frequency ω is applied to the electrodes, x_j are the coordinates and t is the time. The mechanical strain S_{ij}, assumed small, and the electric field E_j are given by the expressions

$$S_{ij} = \frac{1}{2}\left(\frac{1}{\gamma_j}\frac{\partial u_i}{\partial x_j} + \frac{1}{\gamma_i}\frac{\partial u_j}{\partial x_i}\right) \quad \text{and} \quad E_j = -\frac{1}{\gamma_j}\frac{\partial V}{\partial x_j}, \tag{2}$$

where u_i are the displacements. Note that the Einstein notation is not applied in (2). The parameter γ_j is an artificial damping at position x_j in the PML given by the expression

$$\gamma_j(x_j) = 1 - i\sigma_j(x_j - x_l)^2, \tag{3}$$

where x_l is the coordinate at the interface between the regular domain and the PML and σ_j is a suitable constant. There is no damping outside the PMLs and here $\gamma_j = 1$. The mechanical stresses T_{jk} and the electric displacement D_i both depend on the strain and the electric field according to the constitutive relations

$$T_{jk} = \tilde{c}^E_{jklm}S_{lm} - \tilde{e}^T_{ijk}E_i, \tag{4}$$

$$D_i = \tilde{e}_{ijk}S_{jk} + \tilde{\varepsilon}^S_{ij}E_j, \tag{5}$$

where $\tilde{c}^E_{jklm}$ are the elastic stiffness constants, $\tilde{e}_{ijk}$ are the piezoelectric stress constants and $\tilde{\varepsilon}^S_{ij}$ are the permittivity constants. The material tensors are rotated according to Eulers transformation theory [15] to get the proper

piezoelectric directions. This is indicated by the tilde above the material tensors. The two governing equations give the stresses by Newton's second law and the electric displacement from Gauss law

$$\frac{1}{\gamma_j}\frac{\partial T_{ij}}{\partial x_j} = -\rho\omega^2 u_i \quad \text{and} \quad \frac{1}{\gamma_j}\frac{\partial D_j}{\partial x_j} = 0, \tag{6}$$

where ρ is the density of the material. The governing equations are second order differential equations for u_j and V. Mechanical and electrical boundary conditions must be specified. Considering the mechanical conditions the upper surface is stress free and the vertical sides and the bottom are clamped

$$\text{stress free surface :} \qquad T_{jk}m_k = 0, \tag{7}$$

$$\text{clamped surface :} \qquad u_i = 0, \tag{8}$$

where m_k is the normal unit vector pointing out of the surface. At the upper surface there are no charges and therefore electric insulation occurs, meaning that the normal component of the electric displacement is zero. At the bottom and to the sides of the domain it is assumed that the electrical potential is zero whereas at the interface between the electrodes and the substrate the potential is $\pm V_p$. The electrical boundary conditions are summarized as follows

$$\text{electrical insulation :} \qquad D_i m_i = 0, \tag{9}$$

$$\text{zero potential :} \qquad V = 0, \tag{10}$$

$$\text{applied positive potential :} \qquad V = V_p, \tag{11}$$

$$\text{applied negative potential :} \qquad V = -V_p. \tag{12}$$

The piezoelectric problem is solved by a plane formulation obtained by omitting all derivatives with respect to x_3. The two governing equations (6) are solved simultaneously to find the four unknowns u_1, u_2, u_3 and V.

C. The Optical Model

After the mechanical strain in the material is computed by the piezoelectric model the refractive index n_{ij} in the strained material can be calculated according to the strain-optical relation [16]

$$\Delta b_{ik} b_{kj} = \tilde{p}_{ijlm} S_{lm}, \tag{13}$$

where $\tilde{p}_{ijlm}$ are the rotated strain-optical constants and $b_{ik}n_{kj} = \delta_{ij}$. For a given optical mode of order ν with the propagation constant β_ν the effective refractive index $n_{\text{eff},\nu}$ is defined as

$$n_{\text{eff},\nu} = \beta_\nu / k_0, \tag{14}$$

where k_0 is the free space propagation constant. It is assumed that the propagating optical modes have harmonic solutions on the form

$$H_{p,\nu}(x_1, x_2, x_3) = H_{p,\nu}(x_1, x_2) e^{-i\beta_\nu x_3}, \tag{15}$$

where $H_{p,\nu}$ are the magnetic field components of the optical wave. The governing equations for the magnetic field are the time-harmonic wave equations

$$e_{ijk}\frac{\partial}{\partial x_j}\left(b_{kl}b_{lm}e_{mnp}\frac{\partial H_p}{\partial x_n}\right) - k_0^2 H_i = 0, \tag{16}$$

where e_{ijk} here is the alternating symbol. For a given value of k_0 the propagation constant β_ν for the possible modes are found by solving the wave equations as an eigenvalue problem, whereby the effective refractive indices are obtained. In this work the set of equations are reduced such that the model is only solved for the transverse components of the magnetic field H_1 and H_2. As the energy of the lower order optical modes is concentrated in the waveguide, the optical domain (where the eigenvalue problem is solved) can be reduced to a smaller area around the waveguide, see Fig. 1. At the boundary of this optical domain it is assumed that the magnetic field is zero as the energy density quickly decays outside the waveguide. Thus, the perfectly magnetic conductor boundary condition is applied

$$e_{ijk}H_j m_k = 0, \tag{17}$$

where e_{ijk} again is the alternating symbol.

D. Practical implementation

The coupled model is solved by the commercial finite element program Comsol Multiphysics with Matlab [17]. This program is designed for modeling engineering problems described by partial differential equations and it is possible to combine different physical models and solve multiphysics problems. The models can be defined by writing conventional differential equations directly or it is possible to use the application modes, which are templates for specific physical problems with the appropriate equations and variables predefined. In this work the piezoelectric model is implemented in the general form where the governing equations and boundary conditions are written on divergence form. The optical problems are solved using the perpendicular waves, hybrid-mode waves, application mode. The problems are discretized by a triangular element mesh and second order Lagrange elements are employed. A sufficient number of elements must be used in wave problems in order to resolve the waves and obtain convergence, which typically means that at least 5-6 second order elements per wavelength must be employed. In the studied problem the geometry is complicated and a coupled model is used, so a fine mesh is employed where the wavelength of the vibration in the electrodes for the highest frequency is discretized by at least 10 elements. For $a = 7$ μm, a maximum element size of 1.5 μm is used except in the waveguide area where 0.25 μm is used, see Fig. 1. For the piezoelectric model it has been tested that the results for the phase velocity and the mechanical energy did not change for a

finer mesh. For the coupled model it was furthermore ensured that the values of the refractive indices did not change for a finer mesh and for a bigger optical domain.

III. RESULTS

The SAWs generated by HAR electrodes by the finite model are first compared to the results obtained by the periodic model from Ref. [12]. The finite model is then employed to calculate the acousto-optical interaction in an optical waveguide.

A. Simulation of Surface Acoustic Waves - Comparison between a Periodic and a Finite Model

The SAWs are generated by Ni electrodes placed on top of the Y+128 degrees cut $LiNbO_3$ substrate where the material matrices are rotated 128 degrees around the x_1-axis. Material constants for $LiNbO_3$ are taken from Ref. [18]. Young's modulus for Ni is $E = 200$ GPa and Poisson's ratio is $\nu = 0.31$. The results for the SAWs obtained by the finite model are first compared to the results found by studying the unit cell with one electrode from Ref. [12]. The geometry is illustrated in Fig. 2 where the height of the substrate is $6p$. A PML is placed at the bottom of the domain with the hight $4p$ and periodic boundary conditions connect the left- and right-hand side boundaries of the substrate. An electrical potential of 1 V was applied to excite the device and it is found that an increasing number of modes can be excited for increasing aspect ratio and six modes exist for $h/2p = 1$. Three of the modes are mainly polarized in the shear horizontal (SH) direction and the other three modes are mainly vertically polarized (VP). Examples are given in Fig. 2(a) and 2(b) where the displacements u_1, u_2 and u_3 in the x_1-, x_2- and x_3-direction are plotted for mode 3 and 4 at resonance. These plots clearly show that the modes are in fact a combination of a vibration in the electrode and a surface wave. It is also verified that mode 3 has a SH polarization and that mode 4 has a VP polarization, note the different scaling on the color bars. By plotting the mode shapes it was found that the electrodes vibrate with modes of increasing order such that mode 3, which is also denoted SH2, vibrates in the x_3-direction with a mode shape of order 2 and mode 4 (VP2) vibrates in the x_1- and x_2-direction with a mode shape of order 2 as well. So it is possible for more and more modes to exist for larger aspect ratio as the electrodes vibrate with modes of higher order. In Ref. [12] the mechanical energy in the structure was calculated, which is the sum of the stored strain and kinetic energy and the mechanical flux flowing into the PML at the bottom. The expressions are given in Ref. [15]. The fraction of mechanical energy in the electrode $E_{\mathrm{mech,elec}}$ with respect to the total mechanical energy in the structure $E_{\mathrm{mech,tot}}$ is repeated in Fig. 3(b) for the aspect ratios $h/2p \in [0.05 : 3]$ for the later discussion in subsection III C. The mechanical energy gets more confined to the electrode for increasing aspect ratio. Thus, the electrode acts as a mechanical resonator, which slows down the SAW velocity because of mechanical energy storage. The modes of the same type tend to the same fraction of mechanical energy in the electrode for increasing aspect ratio because the movement tend to the clean cantilever vibration for slender beams. The only energy left in the substrate is what connects the cantilever modes to the substrate and as modes of the same polarization type deflect in the same direction in the substrate the stiffness in the substrate for these modes is the same. For modes of higher order the aspect ratio must be bigger before the energy fraction limit is reached, as the wavelength of the vibration is shorter for the same aspect ratio.

Now the wave propagation is studied in the finite device, which is modeled by introducing PMLs at the vertical borders and at the bottom of the substrate as illustrated in Fig. 1. The device has 24 electrodes and is excited with an alternating potential of $+1$ V and -1 V. The aspect ratio $h/2p = 1$ is chosen for the remaining part of the paper. Two examples of the displacement fields for mode 3 (SH2) and 4 (VP2) at resonance are given in Fig. 4. Mode 3 is the SH-type, so displacement u_3 is dominant and is plotted in Fig. 4(a). Mode 4 is the VP-type, displacements u_1 and u_2 are dominant and u_2 is shown in Fig. 4(c). Compared to the plots for the periodic model in Fig. 2 it can now be seen how the vibrations are build up and are strongest in the middle. It can also be seen, most clearly for mode 4, how a SAW is propagating away from the electrodes and is absorbed in the PMLs. The two zooms of the area around the electrodes in Fig. 4(b) and 4(d) show that the displacement patterns are the same as for the periodic model shown in Fig. 2(a) and 2(b). In order to compare the results for the periodic and the finite model half of the phase velocity fp for the six modes are given in Table I for both cases, where f represents the resonance frequency. It is seen that the phase velocities are identical for the first three modes and only deviate slightly for the last three modes. So the resonances for the modes are in fine agreement for the periodic and finite model. Finally, the fraction of mechanical energy stored in the electrodes compared to the total mechanical energy in the structure is given in Table I for the periodic and finite case. All the energy ratios for the finite device are close to the ratios for the periodic device, but they are deviating more with increasing mode number.

These results show that the periodic and finite model appear to be in fine agreement. A tendency is that the values as the phase velocity and the mechanical energy ratio deviates more and more from the periodic device, which can be explained by the mode shapes getting increasingly complicated with increasing mode number and more energy is lost to bulk waves for the finite structure.

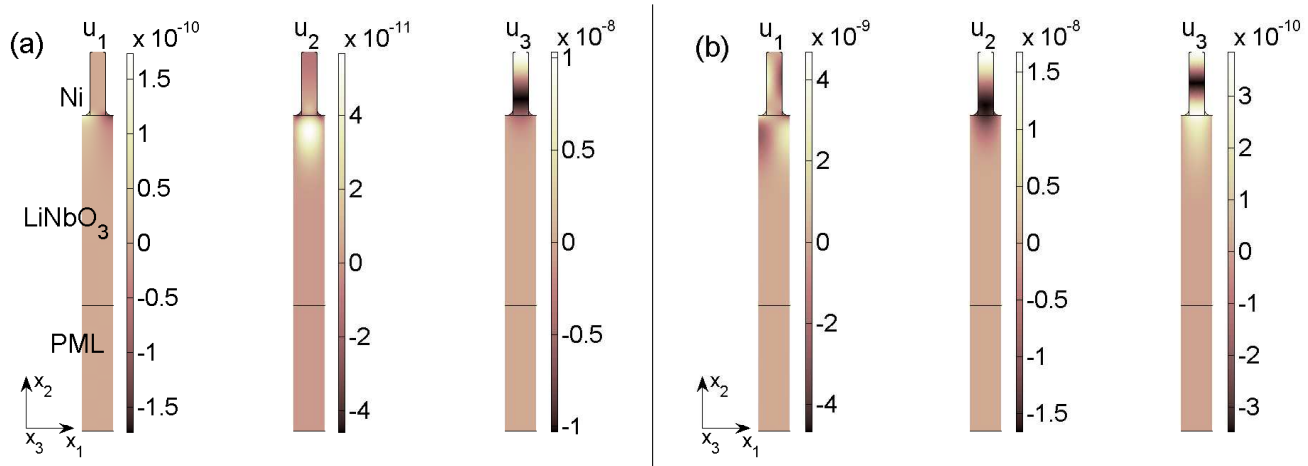

FIG. 2: The displacements u_1, u_2 and u_3 at resonance with $h/2p = 1$. (a): Displacements for mode 3 (SH2) for $fp = 1004$ ms^{-1}. (b): Displacements for mode 4 (VP2) for $fp = 1512$ ms^{-1}.

TABLE I: Half of the phase velocity fp and the energy fraction $E_{\text{mech,elec}}/E_{\text{mech,tot}}$ for the periodic and finite problem for the six modes and $h/2p = 1$.

Mode number		1	2	3	4	5	6
Mode type		SH1	VP1	SH2	VP2	SH3	VP3
phase velocity	periodic device	337	523	1004	1512	1641	2273
fp [ms^{-1}]	finite device	337	523	1004	1510	1639	2275
$E_{\text{mech,elec}}/E_{\text{mech,tot}}$	periodic device	90.5	81.7	88.8	76.4	83.1	41.7
[%]	finite device	90.3	81.5	88.5	75.5	82.1	45.0

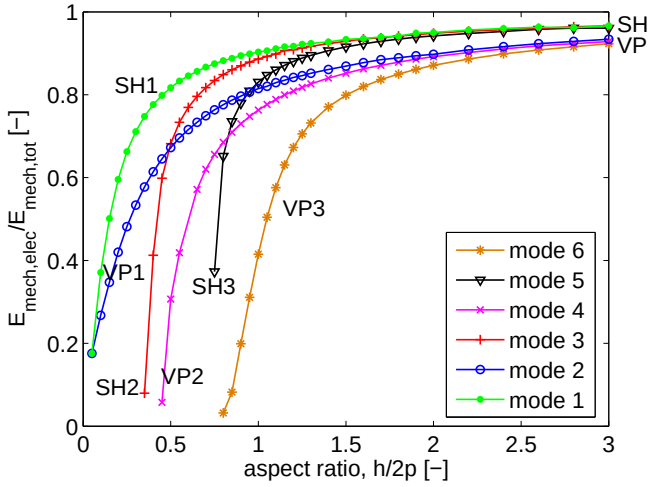

FIG. 3: Energy fraction $E_{\text{mech,elec}}/E_{\text{mech,tot}}$ as a function of $h/2p$ for the six modes computed by the periodic model.

B. Simulation of Optical Waves

Results are now presented for the optical eigenvalue problem described in subsection II C. The optical waveguide is supposed to be created by annealed proton exchange [19] and the analytical expression for the refractive index distribution $n(x_1, x_2)$ is

$$n(x_1, x_2) = 2.138 + 0.0289e^{-\frac{(x_2 \cdot 10^6)^2}{12.5} - \frac{(x_1 - 1.7500 \cdot 10^{-4}) \cdot 10^6)^2}{15.68}}. \quad (18)$$

The unit for x_1 and x_2 is meter. The refractive index distribution given by (18) is illustrated by Fig. 5(a) and it creates a waveguide that can confine an optical mode. The free space wavelength of the optical wave is set to $\lambda_0 = 1.55$ μm - the wavelength used in telecommunication. The refractive index constant for $LiNbO_3$ is $n_{\text{Li}} = 2.138$ and the strain-optical constants are found in Ref. [14]. The refractive index for Ni is set to $n_{\text{Ni}} = 3.5 + 6i$ according to Ref. [20]. It is assumed that n_{Ni} is not changed by the applied strain as the optical mode has almost no energy in the Ni electrode and therefore the acousto-optical modulation has no contribution from the electrode strain. For air simply $n_{\text{air}} = 1$ is used. Fig. 5(b) shows the x_3- component of the time averaged power flow of the fundamental mode in the waveguide obtained by solving the eigenvalue problem when no strain is applied (for V_p =0 V). The power flow is confined to the waveguide and the effective refractive index is found to be $n_{\text{eff},1} = 2.148 + 7.858 \cdot 10^{-5} i$. The real part is between the highest value of the refractive index in the waveguide and the value in the substrate, as expected. The small imaginary part is the attenuation and has a value because of

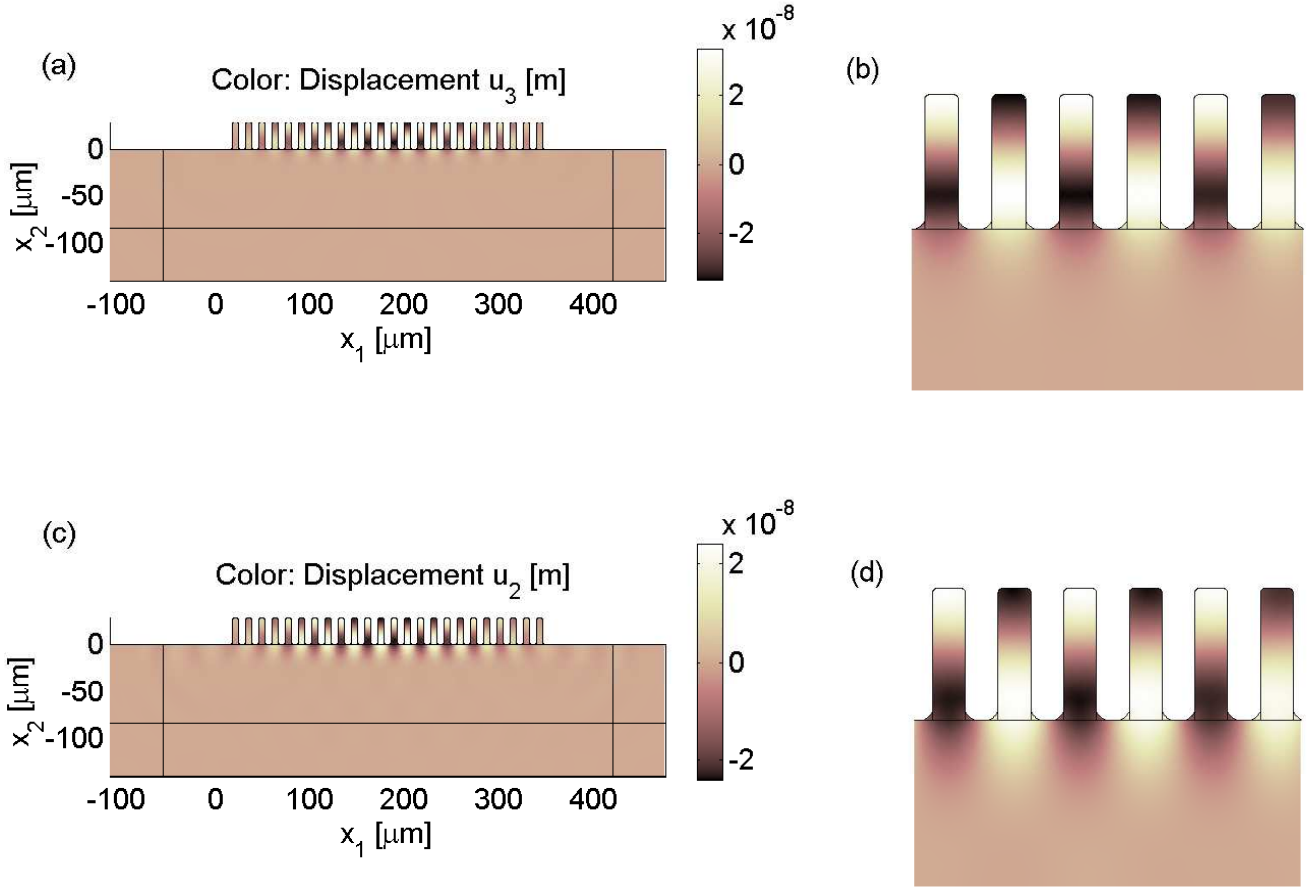

FIG. 4: Results for the finite model at resonance with $h/2p = 1$. (a) and (b): The displacements u_3 for mode 3 (SH2) with $fp = 1004$ ms^{-1}. (c) and (d): The displacements u_2 for mode 4 (VP2) with $fp = 1510$ ms^{-1}.

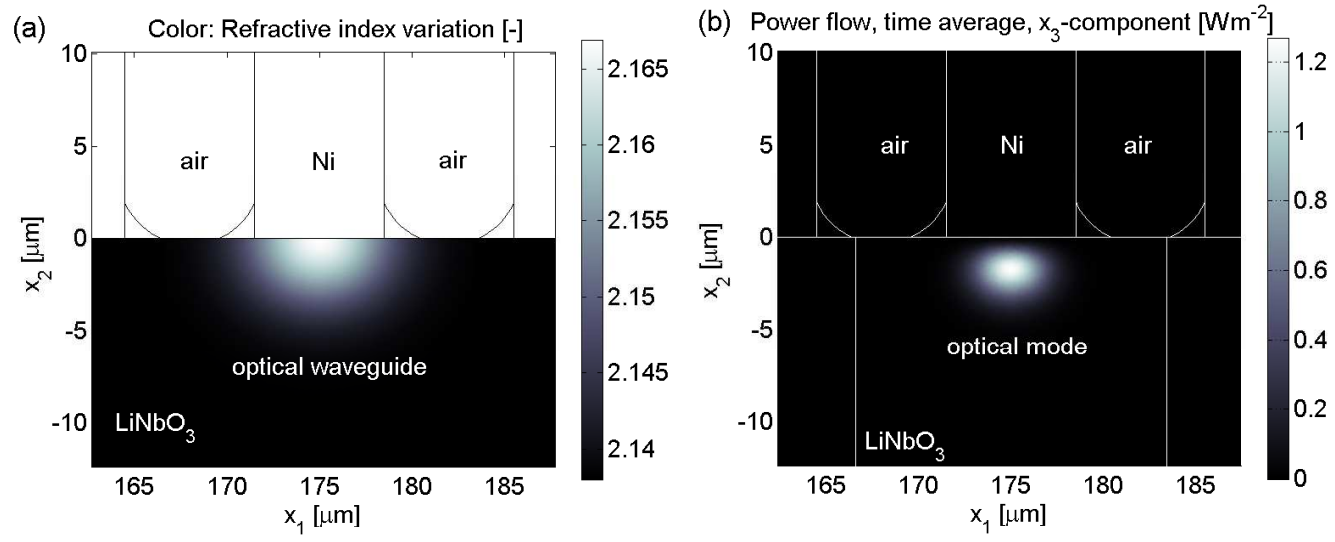

FIG. 5: Results for the optical model with $h/2p = 1$. (a): The refractive index variation in the waveguide. (b): The distribution of the x_3-component of the time averaged power flow for the fundamental mode in the waveguide with arbitrary scale when no strain is applied.

TABLE II: The difference in effective refractive index for the two first order optical modes for the six acoustic modes with $h/2p = 1$ as well as for the thin electrodes with $h/2p = 0.01$.

	$\Delta n_{\text{eff},1}/\sqrt{P}$ [W$^{-1/2}$]	$\Delta n_{\text{eff},2}/\sqrt{P}$ [W$^{-1/2}$]
mode 1 (SH1)	$1.55 \cdot 10^{-3}$	$8.97 \cdot 10^{-4}$
mode 3 (SH2)	$9.08 \cdot 10^{-5}$	$6.62 \cdot 10^{-5}$
mode 5 (SH3)	$3.08 \cdot 10^{-6}$	$2.50 \cdot 10^{-6}$
mode 2 (VP1)	$7.35 \cdot 10^{-5}$	$7.21 \cdot 10^{-4}$
mode 4 (VP2)	$1.18 \cdot 10^{-5}$	$6.35 \cdot 10^{-5}$
mode 6 (VP3)	$6.49 \cdot 10^{-6}$	$1.38 \cdot 10^{-5}$
thin electrodes	$2.51 \cdot 10^{-6}$	$1.71 \cdot 10^{-6}$

the imaginary part in the refractive index in the Ni electrodes that absorb energy from the system. The fundamental mode is mainly polarized in the x_1-direction. The waveguide supports several modes and the next mode is also a first order mode with a similar mode shape. It is mainly polarized in the x_2-direction with the effective refractive index $n_{\text{eff},2} = 2.147 + 6.090 \cdot 10^{-4}i$.

C. Improving the Acousto-Optical Interaction

The coupled acousto-optical model is now solved for each of the six acoustic modes for the case where a wave crest is at the waveguide and a wave trough is at the waveguide, respectively. In the following, only the real part of the effective refractive index is considered and the change between the two extreme cases is given as

$$\Delta n_{\text{eff},j} = |n^{\text{c}}_{\text{eff},j} - n^{\text{t}}_{\text{eff},j}|, \tag{19}$$

where j is 1 for the mode that is polarized in the x_1-direction and 2 for the mode polarized in the x_2-direction. The modes will be denoted optical mode 1 and 2. The superscript c in (19) indicates the value at a wave crest and t the value at a trough. The difference $\Delta n_{\text{eff},j}$ is normalized to the square root of the time averaged applied electric power P calculated by the following expression found in [15]

$$P = \Re \int_{\text{L}_{\text{el}}} \frac{V(i\omega D_2 m_2)^*}{2} \text{dL}, \tag{20}$$

where L_{el} corresponds to the interfaces between the electrodes and the substrate and m_2 is the normal vector to these interfaces. The star indicates the complex conjugate. The results are reported in Table II for the six acoustic modes and for thin electrodes with $h/2p = 0.01$ for both optical mode 1 and 2. The tendency is that the SH modes interact most efficiently with optical mode 1 and the VP modes interact best with optical mode 2. The acousto-optical interaction decreases with increasing mode number within the two different categories of acoustic modes. The six acoustic modes with high aspect ratio electrodes interact better in general compared to the acoustic mode for the conventional thin electrodes. The interaction is a result of how efficiently the acoustic mode is excited with the applied electrical power and how well the acoustic and optical modes match each other. The calculations show that the acoustic modes of lower order are more efficiently excited by a certain amount of electrical power than the modes of higher order such that larger values of the strain and hence bigger change in refractive index for lower order modes are obtained. A reason for this tendency is that for higher aspect ratios the movement of the structure tend to clean cantilever vibrations with the mechanical energy concentrated in the electrodes and just below them where they are attached to the substrate. The graphs in Fig. 3 show that the lower order acoustic modes are closer to this limit for $h/2p = 1$ and therefore more strain is concentrated in the area just below the electrodes. As the structure with high aspect ratio electrodes is more compliant than the almost plane surface with the thin electrodes more power has to be applied to the thin electrode in order to get the same strain. It can therefore be expected that the change in refractive index is biggest for the low order acoustic modes with high aspect ratio electrodes.

The other important question is how well the acoustic modes match with the optical modes, in other words how well the changes in refractive index and the optical modes overlap. The optical modes will mainly detect the changes in refractive index in their polarization direction. So for optical mode 1, it is the SAW induced changes of the refractive index in the horizontal direction Δn_{11} that are important. Optical mode 2 must overlap with Δn_{22}. The acoustic modes of the same polarization type all have a similar pattern of changes in refractive index around the optical waveguide. As an example $\Delta n_{11}/\sqrt{P}$ is plotted for SH1 in Fig. 6(a) with the power flow of optical mode 1 indicated with contour lines. $\Delta n_{22}/\sqrt{P}$ is plotted with optical mode 2 in Fig. 6(b). When these two figures are compared it is seen that $\Delta n_{11}/\sqrt{P}$ has bigger values than $\Delta n_{22}/\sqrt{P}$, but the distribution of these parameters have a similar pattern that both match the optical modes well. This is a tendency for all the SH modes. However, for SH modes of higher order the wave patterns tend to go deeper into the substrate and therefor the strain concentrations are not as big around the waveguide. The same is plotted for VP1 in Fig. 6(c) and 6(d), note the different color scales. In this case $\Delta n_{22}/\sqrt{P}$ has the biggest values and the distribution overlap well with the optical mode. $\Delta n_{11}/\sqrt{P}$ does not overlap so well, as it has a pattern where $\Delta n_{11}/\sqrt{P}$ changes sign into the depth. A part of optical mode 1 is therefore overlapping with $\Delta n_{11}/\sqrt{P}$ close to zero. This is also a tendency for all the VP modes. Thus, the mode patterns explain that the interaction is different for the SH and VP modes with respect to the polarization direction of the optical mode. The interaction is most efficient for SH1 with optical mode 1 and it is more than 600 times bigger than for the case with the thin electrodes. In Fig. 7(a) and 7(b) the change in refractive index $\Delta n_{11}/\sqrt{P}$ and $\Delta n_{22}/\sqrt{P}$ are plotted for

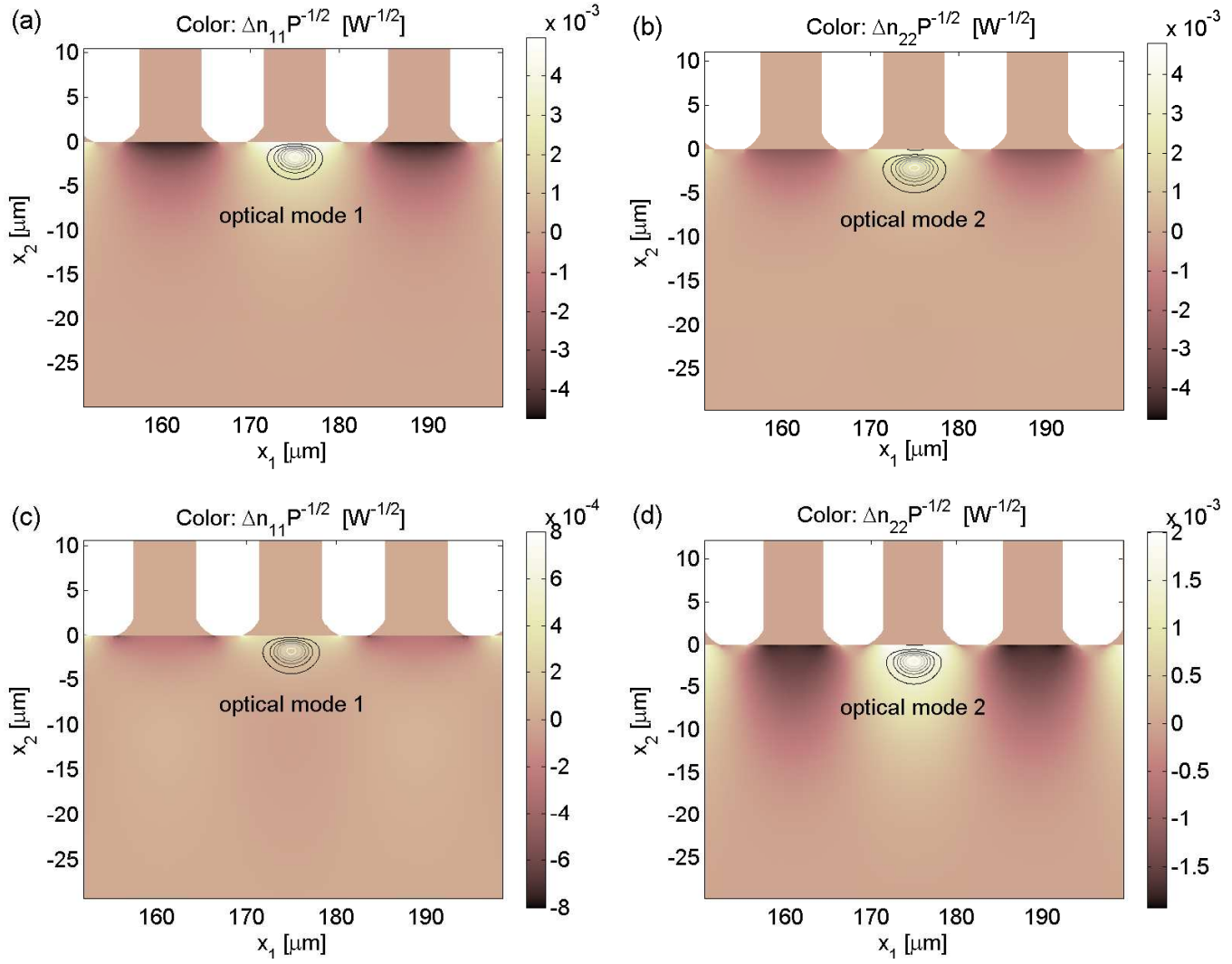

FIG. 6: Results for the acousto-optical interaction with $h/2p = 1$. The color scales indicate the refractive index change and the contour lines illustrate the power flow of the optical modes. (a): Acoustic mode 1 (SH1) and optical mode 1. (b): Acoustic mode 1 (SH1) and optical mode 2. (c): Acoustic mode 2 (VP1) and optical mode 1. (d): Acoustic mode 2 (VP1) and optical mode 2.

the case with thin electrodes, respectively. It is seen that the changes are small compared to the acoustic modes SH1 and VP1 in Fig. 6 and that the overlap with the optical modes is not as good. In the case with the overlap between $\Delta n_{22}/\sqrt{P}$ and optical mode 2 the center of the optical mode is where the change in refractive index is zero.

The results show that it is possible to get a more efficient acousto-optical interaction with the new types of SAWs compared to using conventional IDTs, where Rayleigh-type waves are generated. It is important to know how well the acoustic mode is excited for the applied electrical power in order to get bigger changes in refractive index. The distribution of the change in refractive index in the different directions must match an optical mode polarized in a certain direction. In this work the SH modes overlap the horizontally polarized optical mode best and the VP modes match best with the optical mode, which is vertically polarized. The stronger modulation of the optical waves could improve the modulation efficiency in structures like acousto-optical multiple interference devices. The concept of these devices are presented in Ref. [21] where several MZIs are combined in parallel or series in order to design ON/OFF switching, pulse shapers and frequency converters.

IV. CONCLUSION AND FURTHER WORK

In this paper, surface acoustic waves are generated by high aspect ratio electrodes and the interaction with optical waves in a waveguide is studied in order to improve

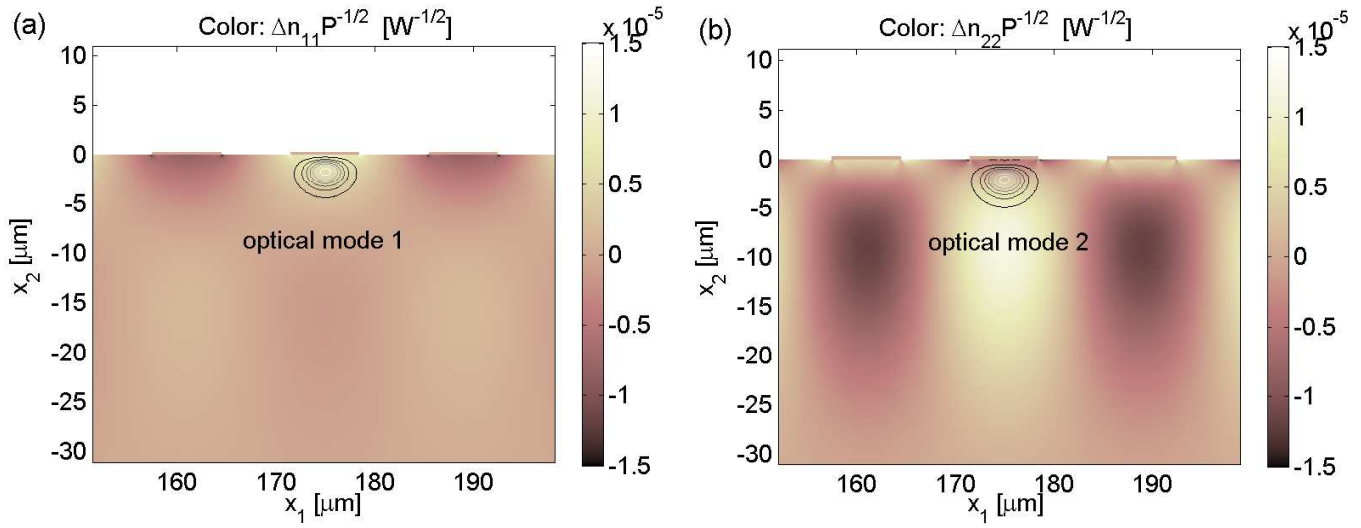

FIG. 7: Results for the acousto-optical interaction with $h/2p = 0.01$. The color scales indicate the refractive index change and the contour lines illustrate the power flow of the optical modes. (a): Optical mode 1. (b): Optical mode 2.

integrated acousto-optical modulators. It is explained how the SAWs can be generated by HAR electrodes by employing a 2D model of a piezoelectric, anisotropic material where reflections from the boundaries are avoided by PMLs. This model is then coupled to a model of the optical wave such that the change in effective refractive index introduced in the waveguide by the strain from the SAWs can be calculated.

A finite model with twelve electrode pairs is considered and six different acoustic modes can be generated for the chosen aspect ratio of the electrodes. A fine agreement for the modes shapes, the resonance frequencies and the mechanical energy confinement to the electrodes is found between the finite model and the periodic model studied in Refs. [12]. The finite model is then employed to study the acousto-optical interaction in a waveguide. The optical modes in the waveguide are found by solving the time-harmonic wave equation. By applying strain from the six acoustic modes for the case where a wave crest is at the waveguide and a trough is at the waveguide, the difference in effective refractive index normalized with the square root of the applied electrical power is found for the two first order optical modes. The efficiency of the interaction depends on how well the acoustic mode is excited and how good the acoustic and the optical modes are overlapping. The interaction decreases with increasing number of acoustic mode, and the modes polarized in the shear horizontal direction interact best with the optical wave polarized in the horizontal direction and the vertical polarized acoustic modes interact best with the vertical polarized optical mode. Compared to the case with the conventional thin electrodes, the acousto-optical interaction can be increased more than 600 times with the new type of SAWs.

Further work includes a study of the optimal position and size of the waveguide compared to the electrode size. Also the optimal aspect ratio for each of the six modes can be explored and it is expected that the interaction will increase with increasing aspect ratio, as less power has to be applied to obtain certain strain values and the mechanical energy is more concentrated around the electrodes.

V. ACKNOWLEDGEMENTS

This work is supported by the European FP6 research project ePIXnet - *European Network of Excellence on Photonic Integrated Components and Circuits*. The authors are grateful to Ole Sigmund and Jakob S. Jensen from the Department of Mechanical Engineering and Martin P. Bendsøe from the Department of Mathematics, Technical University of Denmark, for helpful discussions related to the presented work. The support from Eurohorcs/ESF European Young Investigator Award (EURYI) through the grant *Synthesis and topology optimization of optomechanical systems* as well as the Danish Center for Scientific Computing is gratefully acknowledged.

[1] K.-Y. Hashimoto, *Surface Acoustic Wave Devices in Telecommunications, Modelling and Simulation*, Springer Berlin, (2000).

[2] S. Takahashi, H. Hirano, T. Kodama, F. Miyashiro, B.

Suzuki, A. Onoe, T. Adachi and K. Fujinuma, IEEE Trans. Consumer Electron., CE-24, **3**, 337 (1978).
[3] K. Shibayama and K. Fujinuma (eds), Proc. International Symp. on Surface Acoustic Wave Devices for Mobile Communication, (1992).
[4] U. Wolff, F. L. Dickert, G. K. Fischauer, W. Greibl and C. C. W. Ruppel, IEEE Journal, **1(1)**, 4 (2001).
[5] M. M. de Lima, Jr. and P. V. Santos, Rep. Prog. Phys., **68**, 1639 (2005).
[6] C. Gorecki, F. Chollet, E. Bonnotte and H. Kawakatsu, Opt. Lett., **22**, 1784 (1997).
[7] M. M. de Lima, Jr., M. Beck, R. Hey and P. V. Santos, Appl. Phys. Lett., **89**, 121104 (2006).
[8] M. van der Poel, M. Beck, M. B. Dühring, M. M. de Lima, Jr., L. H. Frandsen, C. Peucheret, O. Sigmund, U. Jahn, J. M. Hwam and P. V. Santos, proceedings of European Conference on Integrated Optics and Technical Exhibition, April 25-27, 2007, Copenhagen, Denmark.
[9] M. B. Dühring and O. Sigmund, J. Appl. Phys., **105**, 083529 (2009).
[10] V. Laude, A. Khelif, T. Pastureaud and S. Ballandras, J. Appl. Phys., **90**, 2492 (2001).
[11] V. Laude, L. Robert, W. Daniau, A. Khelif and S. Ballandras, Appl. Phys. Lett., **89**, 083515 (2006).
[12] M. B. Dühring, V. Laude and A. Khelif, J. Appl. Phys., **105**, 093504 (2009).
[13] U. Basu and A. Chopra, Comput. Methods Appl. Mech. Eng., **192**, 1337 (2003).
[14] D. Royer and E. Dieulesaint, *Elastic Waves in Solids*, 1st ed. Springer, New York, (2000).
[15] B. A. Auld, *Acoustic Fields and Waves in Solids*, 1st ed. Wiley, New York, (1973).
[16] R. Syms and J. Cozens, *Optical Guided Waves and Devices*, 1st ed., McGraw-Hill, New York (1992).
[17] COMSOL Reference Manual for COMSOL 3.3a. COMSOL AB, Stockholm, www.comsol.se.
[18] G. Kovacs, M. Anhorn, H. E. Engan, G. Visintini and C. C. W Ruppel, IEEE Ultrason. Symp. Proc., **1**, 435 (1990).
[19] M. L. Bortz and M. M. Fejer, Opt. Lett., **16**, 1844 (1991).
[20] M. A. Ordal, R. J. Bell, R. W. Alexander, L. L. Long and M. R. Querry, W. Applied Optics, **24**, 4493 (1985).
[21] M. Beck, M. M. de Lima Jr. and P. V. Santos, J. Appl. Phys., **103**, 014505 (2008).

DTU Mechanical Engineering
Section of Solid Mechanics
Technical University of Denmark

Nils Koppels Allé, Bld. 404
DK- 2800 Kgs. Lyngby
Denmark
Phone (+45) 45 25 42 50
Fax (+45) 45 93 14 75
www.mek.dtu.dk
ISBN: 978-87-89502-86-1

DCAMM
Danish Center for Applied Mathematics and Mechanics

Nils Koppels Allé, Bld. 404
DK-2800 Kgs. Lyngby
Denmark
Phone (+45) 4525 4250
Fax (+45) 4593 1475
www.dcamm.dk
ISSN: 0903-1685